

ISSN 1573-160X

Vol. 31, Iss. 5 September – October 2024



Physical Oceanography

<http://physical-oceanography.ru/>



ISSN 1573-160X

Vol. 31, no. 5. 2024
September – October

Founded in January 1987

Publication frequency: 6
issues per year

Physical Oceanography

Scientific and theoretical journal

FOUNDER AND PUBLISHER:

Federal State Budget Scientific Institution

Federal Research Centre

“Marine Hydrophysical Institute of RAS”

Peer reviewed scientific journal.

The Journal publishes original research results, review articles (at the editorial board's request) and brief reports on the following sections of hydrophysics:

- thermohydrodynamics of the ocean and atmosphere;
- analysis of observational results and methods of calculation of ocean hydrophysical fields;
- experimental and expeditionary studies;
- satellite hydrophysics;
- mathematical modelling of marine systems;
- automation of scientific research of the seas and oceans.

Objectives

- familiarisation of the world and Russian scientific community with the results of theoretical, experimental and expeditionary studies of the World Ocean;
- exchange of scientific information, experience, research and observation data with specialists from different regions of the country and abroad;
- increase of publication activity of national authors, rating of scientific organisations of Russia and level of national publications in the world scientific community according to their citation data;
- theoretical and practical assistance to scientists in preparing articles for printing that meet modern requirements of publication and scientific ethics;
- strengthening the popularity and authority of the publication, increasing the number of regular subscribers

The Journal is indexed in:

Google Scholar
Web of Science (ESCI)
Scopus

journal@mhi-ras.ru

<http://physical-oceanography.ru/>

Founder, Publisher and Editorial Office address:

2, Kapitanskaya St., Sevastopol, 299011

Russia

Phone, fax: + 7 (8692) 54-02-23

EDITORIAL BOARD

- Sergey K. Konovalov** – Editor-in-Chief, Director of FSBSI FRC MHI, corresponding member of RAS, Dr.Sci. (Geogr.), ORCID ID: 0000-0002-5200-8448, secretary@mhi-ras.ru (Sevastopol, Russia)
- Vladimir N. Belokopytov** – Deputy Editor-in-Chief, Head of Department of FSBSI FRC MHI, Dr.Sci. (Geogr.), ORCID ID: 0000-0003-4699-9588 (Sevastopol, Russia)
- Aleksandr I. Kubryakov** – Deputy Editor-in-Chief, Chief Scientist Researcher of FSBSI FRC MHI, Dr.Sci. (Phys.-Math.), ORCID ID: 0000-0003-1899-9230, ResearcherID: F-8959-2014, (Sevastopol, Russia)
- Igor K. Ivashchenko** – Executive Editor, Senior Scientist of FSBSI FRC MHI, Ph.D. (Econ.), (Sevastopol, Russia)
- Yuri V. Artamonov** – Head Scientist Researcher of FSBSI FRC MHI, Dr.Sci. (Geogr.), ResearcherID: AAC-6651-2020 (Sevastopol, Russia)
- Sergey V. Berdnikov** – Director of FRC SSC of RAS, Dr.Sci. (Geogr.), ORCID ID: 0000-0002-3095-5532 (Rostov-on-Don, Russia)
- Valery G. Bondur** – Scientific Supervisor of ISR "AEROCOSMOS", academician of RAS, Dr.Sci. (Techn.), ORCID ID: 0000-0002-2049-6176 (Moscow, Russia)
- Demuri I. Demetrasvili** – Head of the sector of mathematical modeling of geophysical processes of sea and atmosphere, the Nodia Institute of Geophysics of the Javakhishvili Tbilisi State University, Dr.Sci. (Phys.-Math.), ORCID ID: 0000-0002-4789-4852 (Tbilisi, Georgia)
- Sergey A. Dobrolyubov** – Dean of Faculty of Geography of MSU, academician of RAS, Dr.Sci. (Geogr.), prof., ResearcherID: A-9688-2012 (Moscow, Russia)
- Grigory I. Dolgikh** – Director of POI FEB of RAS, Dr.Sci. (Phys.-Math.), academician of RAS, prof., ORCID ID: 0000-0002-2806-3834 (Vladivostok, Russia)
- Vladimir A. Dulov** – Head of Laboratory of FSBSI FRC MHI, Dr.Sci. (Phys.-Math.), prof., ORCID ID: 0000-0002-0038-7255, (Sevastopol, Russia)
- Vladimir V. Efimov** – Head of Department of FSBSI FRC MHI, Dr.Sci. (Phys.-Math.), prof., ResearcherID: P-2063-2017, (Sevastopol, Russia)
- Vladimir V. Fomin** – Head of Department of FSBSI FRC MHI, Dr.Sci. (Phys.-Math.), ORCID ID: 0000-0002-9070-4460, (Sevastopol, Russia)
- Isaac Gertman** – Head of the Physical Oceanography Department of Israel Oceanographic & Limnological Research, Head of IOLR data center ISRAMAR, Ph.D. (Geogr.), ORCID ID: 0000-0002-6953-6722 (Haifa, Israel)
- Dmitry G. Gryazin** – Head of Department, Chief Metrologist of SRC of the "Concern CSRI Elektropribor" JSC, Dr.Sci. (Techn.), prof. of Mechatronics of ITMO University, Scopus AuthorID: 25638150600, (Saint Petersburg, Russia)
- Rashit A. Ibraev** – Chief Scientist Researcher of INM of RAS, corresponding member of RAS, Dr.Sci. (Phys.-Math.), ORCID ID: 0000-0002-9099-4541 (Moscow, Russia)
- Vasily V. Knysh** – Head Scientist Researcher of FSBSI FRC MHI, Dr.Sci. (Phys.-Math.), prof., ResearcherID: B-3603-2018 (Sevastopol, Russia)
- Gennady K. Korotaev** – Scientific Supervisor of FSBSI FRC MHI, corresponding member of RAS, Dr.Sci. (Phys.-Math.), prof., ResearcherID: K-3408-2017 (Sevastopol, Russia)
- Vladimir N. Kudryavtsev** – Executive Director of Satellite Oceanography Laboratory of RSHU, Dr.Sci. (Phys.-Math.), prof., ResearcherID: G-1502-2014 (Saint Petersburg)
- Michael E. G. Lee** – Head of Department of FSBSI FRC MHI, Dr.Sci. (Phys.-Math.), prof., ORCID ID: 0000-0002-2292-1877 (Sevastopol, Russia)
- Gennady G. Matishov** – Deputy President of RAS, Deputy academician-Secretary of the Department of Earth Sciences of Supervisor of RAS – Head of the Oceanology, Atmospheric Physics and Geography Section, Scientific Supervisor of SSC of RAS, Supervisor of MMBI KSC of RAS, academician of RAS, Dr.Sci. (Geogr.), prof., ORCID ID: 0000-0003-4430-5220 (Rostov-on-Don, Russia)
- Nikolay A. Rimski-Korsakov** – Deputy Director (Marine Engineering) of FSBSI P.P. Shirshov IO of RAS, Dr.Sci. (Techn.), ResearcherID: K-8378-2017 (Moscow, Russia)
- Angelo Rubino** – Professor of Ca' Foscari University, Ph.D. (Phys. Oceanogr.), ORCID ID: 0000-0003-3857-4811 (Venice, Italy)
- Anatoly S. Samodurov** – Head of Department of FSBSI FRC MHI, Dr.Sci. (Phys.-Math.), ResearcherID: V-8642-2017 (Sevastopol, Russia)
- Georgy I. Shapiro** – Head of Plymouth Ocean Forecasting Centre of the University of Plymouth, Dr.Sci. (Phys.-Math.), prof. in Phys. Oceanogr., (Plymouth, Great Britain)
- Naum B. Shapiro** – Head Scientist Researcher of FSBSI FRC MHI, Dr.Sci. (Phys.-Math.), ResearcherID: A-8585-2017 (Sevastopol, Russia)
- Mikhail V. Shokurov** – Head Scientist Researcher of FSBSI FRC MHI, Dr.Sci. (Phys.-Math.), ORCID ID: 0000-0003-1595-8281 (Sevastopol, Russia)
- Elena F. Vasechkina** – Deputy Director of FSBSI FRC MHI, Chief Research Associate of FSBSI FRC MHI, Dr.Sci. (Geogr.), ORCID ID: 0000-0001-7007-9496 (Sevastopol, Russia)
- Elizaveta V. Zabolotskikh** – Head Scientist Researcher of RSHU, Dr.Sci. (Phys.-Math.), Scopus Author ID: 6506482460 (Saint Petersburg, Russian)
- Vladimir B. Zalesny** – Head Scientific Researcher of INM of RAS, Dr.Sci. (Phys.-Math.), prof., ORCID ID: 0000-0003-3829-3374 (Moscow, Russia)
- Andrey G. Zatsepin** – Chief of Laboratory of FSBSI P.P. Shirshov IO of RAS, Chief Research Associate of FSBSI P.P. Shirshov IO of RAS, Dr.Sci. (Phys.-Math.), ORCID ID: 0000-0002-5527-5234 (Moscow, Russia)
- George Zodiatis** – Senior Researcher of Laboratory of Coastal and Marine Research of the Institute of Applied and Computational Mathematics, for Research and Technology Foundation – Hellas, Ph.D. (Oceanol.), ResearcherID: J-3032-2013 (Heraklion, Crete, Greece)

CONTENTS

Vol. 31, no. 5. 2024

September – October, 2024

THERMOHYDRODYNAMICS OF THE OCEAN AND THE ATMOSPHERE

- Basharin D. V., Shokurova I. G.** Steady winds over the Black Sea and atmospheric blocking events 593

ANALYSIS OF OBSERVATIONS AND METHODS OF CALCULATING HYDROPHYSICAL FIELDS IN THE OCEAN

- Lavrenteva A. I., Leonov I. I., Sokolikhina N. N.** Frequency of meteorological factors of vessel icing in the Barents Sea and ice accretion on its coast in a changing climate 609

EXPERIMENTAL AND FIELD RESEARCH

- Soloveva O. V., Tikhonova E. A., Gurov K. I.** Distribution and composition of hydrocarbons in the bottom sediments of Kamyshovaya Bay (Black Sea) 626
- Novotryasov V. V.** Excitation of internal waves in a shallow sea basin with an open inlet under conditions of parametric resonance 647

MATHEMATICAL MODELING OF MARINE SYSTEMS

- Mazova R. Kh., Martynenko A. A., Kurkin A. A.** Comparative numerical simulation of tsunami waves during the January 1, 2024 Noto Peninsula Earthquake, Japan..... 662
- Dymova O. A.** Estimates of available potential energy budget in the Black Sea using different schemes for calculating heat and salt advective transport 679
- Divinsky B. V.** Numerical study of hydrodynamic regime of the Taganrog Bay waters in the Sea of Azov 694
- Mizyuk A. I., Korotaev G. K.** Features of water exchange between the Black and Marmara Sea basins based on the results of numerical simulation with a simplified representation of the strait..... 707

SATELLITE HYDROPHYSICS

- Papkova A. S., Shybanov E. B., Kalinskaya D. V.** The effect of dust aerosol on satellite data from different color scanners 720
- Korolev Yu. P.** Express method for operational tsunami forecasting: Possibility of its application on the Pacific coast of Russia 736



All the materials of the journal are available under Creative Commons Attribution-NonCommercial 4.0 International (CC BY-NC 4.0)

Steady Winds over the Black Sea and Atmospheric Blocking Events

D. V. Basharin ✉, I. G. Shokurova

Marine Hydrophysical Institute of RAS, Sevastopol, Russian Federation

✉ dbasharin@rambler.ru

Abstract

Purpose. This paper aims at identifying and studying the cases of steady winds of one direction over the Black Sea and analyzing the accompanying conditions in the surface atmosphere and middle troposphere in winter (December–March).

Methods and Results. The situations with extremely steady winds of persistent direction, namely, when the prevailing wind over the sea does not change its direction for 5 days or more, are considered. The analysis is based on the 6-hour data on wind speed at the 10 m height, the 500 hPa geopotential height and the surface pressure from the ERA5 reanalysis of the European Centre for Medium-Range Weather Forecasts for 1979–2021. Within the analyzed period, 10 cases of steady, mostly north-eastern, winds were identified. At the same time there were 3 recorded cases of the eastern, northern and south-western winds. The empirical orthogonal function analysis performed for a set of steady wind cases shows that distribution of the first modes of the geopotential height and surface pressure fields has a spatial structure with a stable high-pressure area over the European territory. The contribution of these modes to the total variability is 65 and 47%, respectively. Analysis of the revealed situations with steady winds shows that in all the cases with northern and north-eastern winds, there was a blocking process in a form of a quasi-stationary anticyclone in the middle atmosphere located over the Northern Europe/Scandinavian Peninsula. In the case of northern wind, an extensive high-altitude anticyclone was located over the northern part of the European Russia. Values of the Tibaldi and Molteni blocking index confirm the fact that the considered cases of long-lasting north-eastern and northern winds correspond to the blocking conditions over the European region. A steady eastern wind was observed when the extensive anticyclone in the middle troposphere was actively moving from the north of the Scandinavian Peninsula to the south-east. In the case of a long-lasting south-western wind, a subtropical high-pressure ridge was presented in the middle troposphere as well as an intense transfer of cyclones took place over the European region that created a prevailing steady wind over the Black Sea.

Conclusions. The analysis results indicate that the considered cases with steady north-eastern and northern winds over the Black Sea are related to the blocking processes in the European region atmosphere.

Keywords: Black Sea, European region, steady winds, 500 hPa geopotential height, atmospheric blocking

Acknowledgements: The work was carried out within the framework of state assignment of FSBSI FRC MHI on theme FNNN-2024-0014 “Fundamental studies of interaction processes in the ocean-atmosphere system that form the physical state variability of marine environment at various spatial and temporal scales”.

For citation: Basharin, D.V. and Shokurova, I.G., 2024. Steady Winds over the Black Sea and Atmospheric Blocking Events. *Physical Oceanography*, 31(5), pp. 593-608.

© 2024, D. V. Basharin, I. G. Shokurova

© 2024, Physical Oceanography



Introduction

In recent years, there has been a trend towards an increase in the total number and intensity of regional hydrometeorological anomalies against the background of global climate change¹ [1, 2]. This is confirmed by relevant data and calculations of global and regional climate models capable of reconstructing observed climate change trends² [3], including those in the Black Sea region [4, 5].

It is known that long-term anomalous phenomena in the atmosphere surface layer are often associated with quasi-stationary situations in the mid-troposphere due to its blocking with a typical duration of 5 days or more [1, 3, 5, 6]. Blocking events observed in the atmosphere of the Northern Hemisphere mid-latitudes lead not only to intense regional anomalies in the hydrometeorological fields of the European region [5, 7–9]. Blocking is often accompanied by changes in air quality, for example, abnormally low ozone content, especially pronounced over Scandinavia and Alaska [10]. Extreme conditions and regional anomalies (including those due to atmospheric blocking) result in many negative consequences, in particular, mortality increase [10, 11]. That is why numerous works exceeding greatly the references given in this paper are focused on their study in the European–Black Sea region.

Currently, blocking is understood as a situation in the mid-latitude atmosphere when the jet stream crest becomes especially large and forms a separate anticyclone in the flow creating a large-scale stable weather regime (blocking) which prevents the propagation of Rossby waves [2, 12]. As a result of the quasi-stationary position of the blocking anticyclone, typical cyclone trajectories become redirected. In this case, the regionally stable westerly flow is often replaced locally by a meridional flow lasting from several days to several weeks³ [6, 13, 14]. Blockings can be different in their structure. In studies, the most frequently mentioned blockings are omega-type ones structured like the Greek letter Ω , when a large anticyclone located in the center is flowed around by cyclones [15, 16], and dipole blockings consisting of an anticyclone and a cyclone located southwards of the anticyclone [17].

According to [13, 17–19], typical region of the most active blocking is located in the 50–60°N band with its maximum amount in the west of the European region

¹ Masson-Delmotte, V., Zhai, P., Pirani, A., Connors, S. L., Péan, C., Berger, S., Caud, N., Chen, Y., Goldfarb, L. [et al.], 2021. Climate Change 2021: The Physical Science Basis. In: *Contribution of Working Group I to the Sixth Assessment Report of the Intergovernmental Panel on Climate Change*. Cambridge, United Kingdom: Cambridge University Press, 2339 p. <https://doi.org/10.1017/9781009157896>

² Pörtner, H.-O., Roberts, D.C., Tignor, M., Poloczanska, E.S., Mintenbeck, K., Alegría, A., Craig, M., Langsdorf, S., Löschke, S. [et al.], 2022. Climate Change 2022: Impacts, Adaptation and Vulnerability. In: *IPCC Sixth Assessment Report*. Netherlands: IPCC Publisher, 3675 p. <https://doi.org/10.1017/9781009325844>

³ Mokhov, I.I., Akperov, M.G., Lupo, A.R., Chernokulsky, A.V. and Timazhev, A.V., 2011. Regional Climate Extremes in Northern Eurasia Associated with Atmospheric Blockings: Interannual Variations and Tendencies of Change. *AGU Fall Meeting Abstracts*, 2011, pp. GC43F-06.

and Scandinavia. In this region, blocking is clearly manifested in extensive anomalies of the geopotential height of 500 hPa isobaric surface [20]. Consideration of such a pressure distribution was applied to create blocking indices [20] which make it possible to determine the presence of blocking at a specific longitude at a specific time based on gradients in the geopotential height field. The Tibaldi and Molteni blocking index is often used to verify calculations of blocking regimes in climate models, reanalyses and observational data ⁴ [9, 18–22].

Despite the large number of works analyzing the relationship between regional climatic anomalies in the European region of Russia and blocking processes in the atmosphere, there are few such studies for the Black Sea region, which are mainly focused on temperature anomalies or precipitation/droughts [3, 5, 23]. Studies of the causes of anomalous situations with steady winds and their relationship with blockings in the mid-troposphere have not been performed. At the same time, the wind regime is one of the important conditions for economic activity and human life. Knowledge of the wind regime and consideration of wind direction are important in the construction of hydraulic structures [24], forecasting wind waves, surge phenomena [25, 26], upwellings and storm conditions [27, 28] in the Black Sea region. In addition, the wind regime largely determines the nature of water circulation and changes in the thickness of the mixed layer [29, 30] and also affects regional weather conditions [31]. The cases where the wind direction is stable for a fairly long time are of particular interest. This determines the relevance of such studies. Therefore, the main purpose of the work is to identify situations with long winds over the Black Sea for the cold period of the year and to determine the relationship between the occurrence of such events and large-scale processes in the surface layer and mid-troposphere.

Materials and methods

In this work, we used the data from the ERA5 atmospheric reanalysis ($0.25^\circ \times 0.25^\circ$) [32] for 1979–2021:

- 6-h data on wind speed (m/s) at a height of 10 m above the Black Sea;
- 6-h data on surface pressure (hPa) and geopotential of the 500 hPa isobaric surface in the area bounded by coordinates 35–75°N, 10°W–100°E.

The direction of the wind prevailing over the Black Sea was determined for each 6-h period as the velocity vector direction, zonal and meridional components of which were obtained by averaging the wind speed components according to the data covering the sea area. The obtained direction was compared with one of eight main geographical directions: northern (N), north-eastern (NE), eastern (E), south-eastern (SE), southern (S), south-western (SW), western (W), north-western (NW).

⁴ Davini, P., 2013. *Atmospheric Blocking and Winter Mid-Latitude Climate Variability: Tesi di Dottorato*. Venezia: Universita Ca' Foscari, 141 p.

From the obtained time series, we identified cases with extremely steady winds, when the wind direction did not change for twenty 6-hour periods (i.e., 5 days) or more. For the identified situations, we calculated additionally the average wind direction by all grid nodes $\bar{\varphi}$ (°)

$$\bar{\varphi} = \frac{1}{NK} \sum_{i=1}^N \sum_{j=1}^K \varphi_{ij}$$

and its deviation φ^* (°) from the direction of geographic reference. Here, φ_{ij} is wind direction at each grid node; N is number of grid nodes over the sea area; K is number of 6-hour periods in a situation with steady wind.

To identify atmospheric conditions that lead to the occurrence of long-term situations with steady winds, the decomposition of 500 hPa geopotential height fields and surface pressure for a set of cases with these winds into empirical orthogonal functions (EOFs) was performed. The method consists of decomposing the initial field $F(x, t)$ into certain functions $X_n(x)$ with coefficients $T_n(t)$ ($n = 1 \dots N$, where N is number of periods with steady winds) ⁵ [33]. In this case, only one condition is applied as a basis for determining the unknown functions: the sum of squares of the decomposition errors over all points of a given set of fields must reach a minimum for any n .

To test the hypothesis that the situations with long-lasting winds possibly occur in the mid-troposphere due to blocking, the blocking index was calculated on the dates when the cases with such winds took place. The calculation was carried out according to the method proposed by Tibaldi and Molteni [20]. For each latitude, the northern *GHGN* (north geopotential height gradient) and southern *GHGS* (southern geopotential height gradient) gradients (in m/°) between the values of 500 hPa geopotential height were calculated:

$$GHGN = \left[\frac{Z(\phi_n) - Z(\phi_0)}{\phi_n - \phi_0} \right], \quad (1)$$

$$GHGS = \left[\frac{Z(\phi_0) - Z(\phi_s)}{\phi_0 - \phi_s} \right], \quad (2)$$

where $\phi_n = 80^\circ N + \delta$, $\phi_0 = 60^\circ N + \delta$, $\phi_s = 40^\circ N + \delta$, $\delta = -5^\circ, 0, +5^\circ$.

Blocking occurs when conditions $GHGS > 0$, $GHGN \leq -10$ are satisfied at least for one δ value. Southern gradient *GHGS* determines the measure of blocking intensity, while the northern gradient *GHGN* eliminates false blocking cases [20].

⁵ Björnsson, H. and Venegas, S.A., 1997. A Manual for EOF and SVD Analyses of Climatic Data. *CCGCR Report*, 97(1), pp.112-134.

Time series of 500 hPa geopotential height were previously smoothed by a 5-day moving average at each point of the spatial grid to ensure the search for prolonged blocking events.

Results and their discussion

Cases with long-lasting winds over the Black Sea. During the cold period of the year, 10 cases with extremely steady winds, when the prevailing wind direction over the sea did not change for 5 days or more (twenty or more 6-hour periods) (Table), were identified. In seven of all the identified cases, the north-eastern (NE) wind prevailed, in one case the northern (N) one, in one case the eastern (E) and in one case the steady south-western (SW) wind. Wind direction $\bar{\varphi}$ deviates from that of the geographic reference by an average of -6.6° (Table). The most frequent cases are the ones with steady north-eastern winds, they accounted for $\sim 62\%$ of all identified situations. Note that north-eastern winds also have the highest frequency per year – 18% according to long-term data [34, 35].

Characteristics of long-lasting wind cases over the Black Sea region

Case	Date	Wind direction	Duration, day	φ^* , °	Blocking index	max GHGS, m/°	V_{mean} , m/s	V_{max} , m/s
1	11–16.03.1986	NE	5.75	–8.2	+	7.0	7.0	11.6
2	01–07.01.1993	NE	6.50	4.3	+	5.0	9.7	16.6
3	07–14.12.1995	NE	8.75	–7.8	+	7.0	6.4	11.9
4	23–28.12.1995	SW	5.00	–4.9	–	<0	10.3	16.0
5	14–19.01.2001	NE	6.50	–7.3	+	5.0	7.7	13.6
6	28.11–03.12.2002	E	6.25	1.5	–	<0	6.3	16.7
7	07–12.02.2008	NE	5.75	–7.8	+	7.0	7.1	12.6
8	28.01–02.02.2012	N	5.25	–9.1	+	11.0	7.4	14.8
9	08–13.02.2017	NE	5.25	–10.2	+	8.0	6.5	16.9
10	22–27.03.2020	NE	5.25	–4.9	+	6.8	6.1	16.4

It is known that blocking events in the mid-troposphere are not rare. According to [16, 21, 36], the total number of days with atmospheric blocking in Europe during the winter season is 33 days and three independent blocking episodes on average. We identified only 10 cases with extremely steady winds lasting for 5 or more days. However, there can be more cases with steady winds of shorter duration (e.g., 3–4 days). At the same time, not all possible situations with a sufficiently stable wind

direction over the sea caused by blocking processes can be detected, since regional atmospheric processes can distort the wind direction at certain times.

It should be noted that, according to the results of calculations [21], a number of climate models presented in the sixth assessment report of the Intergovernmental Panel on Climate Change predict a slight decrease in the average number of atmospheric blockings in Europe in winter during the 21st century ¹.

Large-scale atmospheric conditions for a set of situations with steady winds

The EOF method made it possible to identify the leading spatial modes for cases with steady winds in the Black Sea. As a result of the analysis, we obtained the first-mode spatial structure of 500 hPa geopotential height containing 65% of the variability (Fig. 1, *a*). Distribution includes a large area of positive geopotential height anomalies covering the north of Europe and extending to the Ural Mountains/Caspian Sea. The anticyclone center is located in the Scandinavian Peninsula which is typical for the position of a blocking anticyclone (blocking).

The contribution of subsequent spatial modes of 500 hPa geopotential height from the second through the fifth is noticeably smaller; it was 9, 7, 6 and 4%, respectively.

Decomposition of the set of surface pressure fields into empirical orthogonal functions yields similar results. In the spatial structure of the first mode, a vast area of positive surface pressure anomalies is located over Central Europe and the European part of the Russian Federation in all seasons (Fig. 1, *b*); the first mode accounts for 47% of the surface pressure field variability at that. The contribution of subsequent modes, from the second to the fifth, of the surface pressure field for all cases of steady winds was 21, 9, 5, and 4%, respectively, in the cold season. Note that due to the greater spatiotemporal variability of surface fields, contribution of the leading first mode is less than that in the mid-troposphere.

The first mode distribution obtained for surface pressure generally corresponds to the typical pressure field characteristic of northern, north-eastern and eastern winds over the Black Sea [34, 37]. Winds of such directions arise on the periphery of a large-scale anticyclone located northwards and north-eastwards of the Black Sea.

It is known that the removal of cold/arctic air from high latitudes to the eastern/south-eastern periphery of anticyclone is typical for such atmospheric conditions in winter ⁴. The results [3] show that blocking anticyclones arising in the Central European region result in the emergence of negative air temperature anomalies near the Black Sea northern coast. At the same time, blocking events over the north-eastern part of Europe/Urals form areas of positive temperature anomalies covering the Black Sea region.

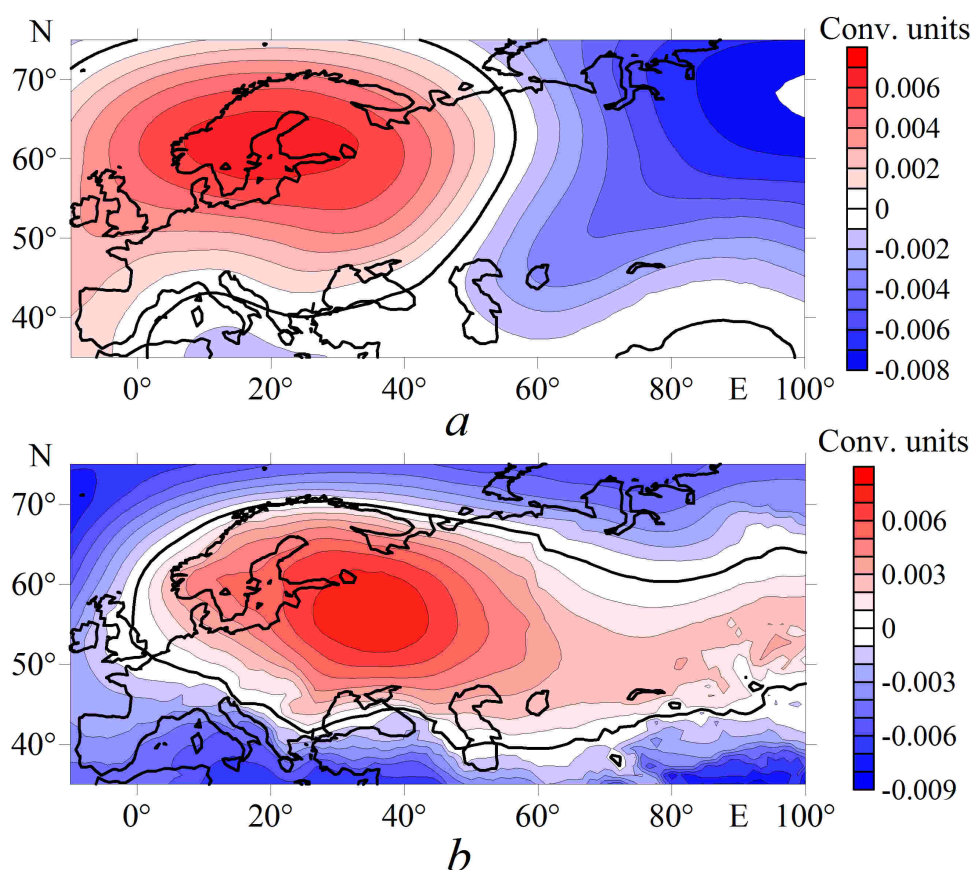


Fig. 1. Distribution of the first modes of the 500 hPa geopotential height anomalies (*a*) and the surface pressure field (*b*) for the cases of long-lasting northern, north-eastern and eastern winds in a cold season

North-eastern wind. Atmospheric conditions in the mid-troposphere for all cases with the long-lasting north-eastern wind over the Black Sea (cases 1–3, 5, 7, 9, 10, Table) satisfy the blocking conditions determined by the Tibaldi and Molteni index. This is the largest number of cases with long-lasting winds. The maximum southern gradient of 500 hPa geopotential height representing the measure of blocking intensity is 5–7 m/°. In these cases, a low-mobility blocking structure of omega shape or close to it is observed in the geopotential height distribution (Fig. 2).

The analysis of geopotential height fields revealed that the blocking anticyclone center was stably located over Eastern Europe in cases 1 (11–16.03.1986) and 2 (02–07.01.1993). The blocking cyclone dominated over the Scandinavian Peninsula in cases 3 (07–14.12.1995) and 9 (08–13.02.2017). The blocking anticyclone center was located over the north-western part of Europe in cases 5 (14–19.01.2001), 7 (07–12.02.2008) and 10 (22–27.03.2020). High-pressure area extended slowly eastwards, where the blocking conditions were also met (formulas (1) and (2)) in cases 2, 5, and 10. In the listed cases, a high-pressure area was present in the surface layer, and north/northeast winds prevailed on the south-eastern periphery [34, 37].

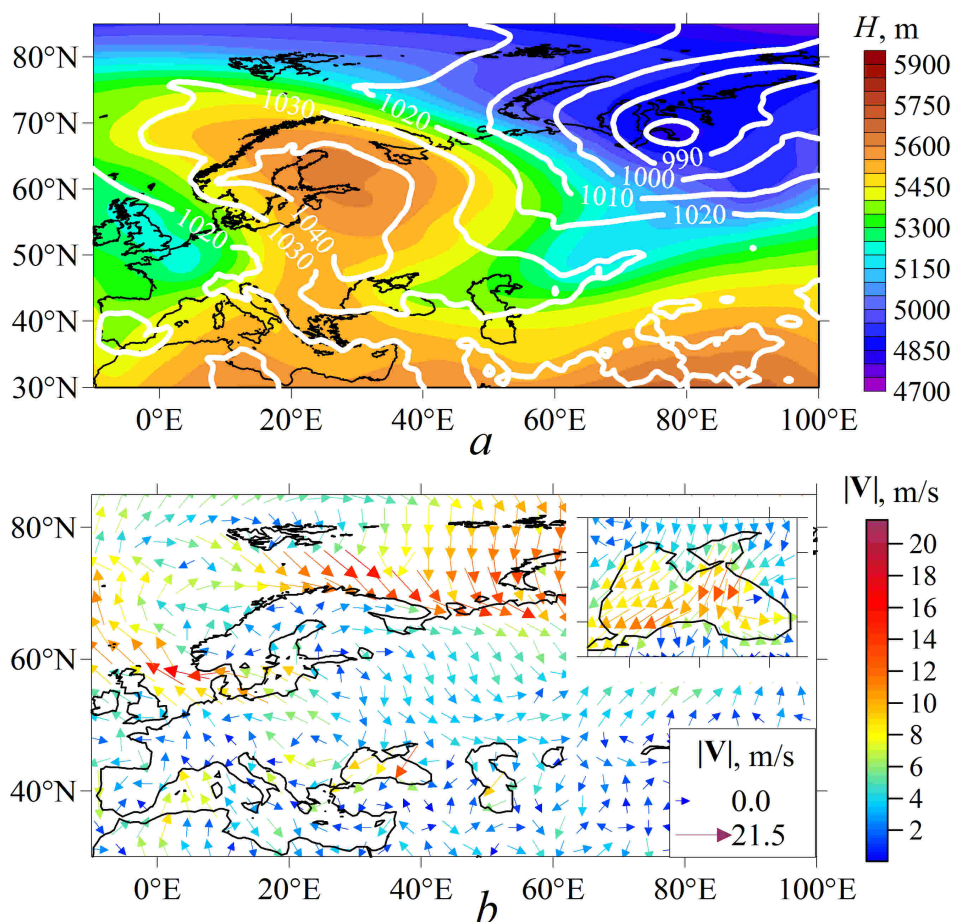


Fig. 2. Distribution of the 500 hPa geopotential height, sea level pressure (hPa, white isolines) (a) and wind field at the 10 m height (b) for 07.12.1995, 12:00 (a case of long-lasting north-eastern wind)

As an example illustrating cases with a steady north-eastern wind, Fig. 2 demonstrates the distribution of 500 hPa geopotential height anomalies (Fig. 2, a) and surface pressure distribution (Fig. 2, a) for case 3, 07–14.12.1995 (Table). The high-altitude blocking anticyclone was located over the northern part of the European territory of Russia and the Scandinavian Peninsula. The blocking structure in the mid-troposphere had a well-defined shape of the Greek letter Ω with low-pressure areas at the base on the eastern and western sides. At this time, a north-eastern wind with a maximum speed of 12 m/s blew over the Black Sea (Fig. 2, b, Table) and surface temperature anomalies reached minus 6–7 °C, according to the following websites: <https://psl.noaa.gov/cgi-bin/data>, https://www1.wetter3.de/archiv_gfs_dt.html.

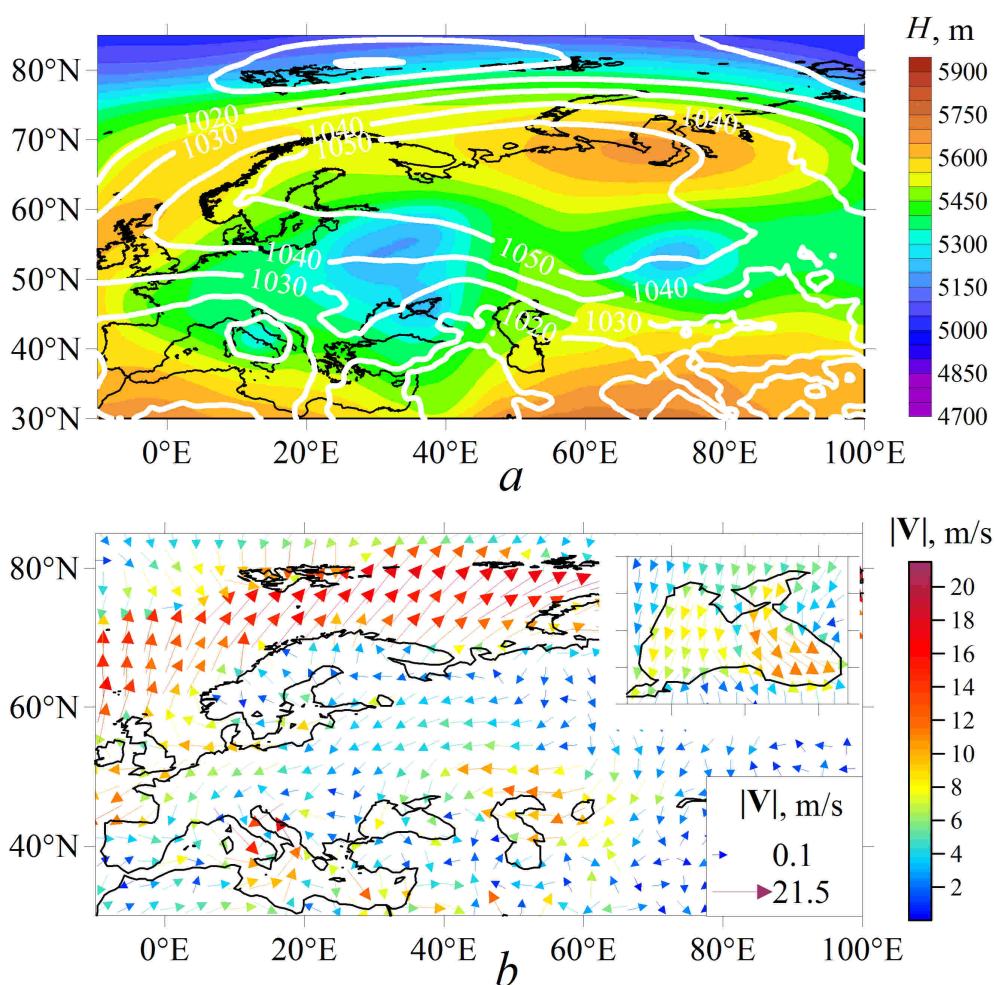


Fig. 3. The same as in Fig. 2, for 01.02.2012, 12:00 (a case of long-lasting northern wind)

Northern wind. A case with long-lasting northern wind (case 8 from the Table) was recorded for the period of 29 January – 2 February 2012. At this time, there was a steady blocking of the westerly transport in the mid-troposphere over the North Atlantic and Eurasia, characterized by the most intense, compared to all other cases, southern gradient (formula (2)) in the 500 hPa geopotential height (11 m/°). The blocking process which started in the third ten-day period of January and continued in February was accompanied by abnormal snowfalls and cold waves in Europe and the European part of Russia. These events are described in numerous publications ⁶ [7, 38–40].

⁶ Grazzini, F., 2013. Cold Spell Prediction beyond a Week: Extreme Snowfall Events in February 2012 in Italy. *ECMWF Newsletter*, (136), pp. 31-35.

Since mid-January, a typical westerly movement of Atlantic cyclones over Central Europe was disrupted due to the strengthening of the Siberian anticyclone ridge, stretching from the south of the Urals, its subsequent movement to the north-west and merging with the high-altitude ridge over the north-eastern Atlantic [39, 40]. An extreme increase in positive surface pressure anomalies took place in the lower layer of the troposphere [41]. By the end of January – early February, an extensive high-altitude blocking anticyclone was located in the north of the European part of Russia (Fig. 3, *a*). At the Black Sea coast, frosts were accompanied by strong winds (Fig. 3, *b*). During the period under review, from 29 January to 2 February 2012, a northerly wind blew over the Black Sea with a mean speed of 7.4 m/s and maximum values of up to 15 m/s.

The opposite situation developed in the Arctic region at that time. The realigning of large-scale circulation that took place during these months created favorable conditions for intensive advection of warm air from Western Europe and from the Atlantic Ocean to the central region of the Arctic Basin (Fig. 3, *b*). In the Arctic region, average monthly air temperature anomalies exceeded 15 °C [39]. At the same time, a polar air invasion from northern Siberia to the European part of Russia, central and southern Europe (Fig. 3, *b*) accompanied by severe frosts took place and a cold wave was also observed in eastern Asia [41].

Eastern wind. In the case of the long-lasting eastern wind (28.11–03.12.2002), the anticyclone center in the mid-troposphere shifted actively starting from 28 November for several days, from the north of the Scandinavian Peninsula in a south-easterly direction to the central part of the European territory of Russia. The spatial structure of the anticyclone changed significantly. For example, as of 1 December, it corresponded to the omega-type blocking (Fig. 4, *a*), but shifted quickly and was characterized by a less-than-zero southern gradient, which did not make it possible to identify it as a blocking anticyclone according to the Tibaldi and Molteni criterion [20]. By the end of the period, the anticyclone was located north/north-eastwards of the Black Sea and then gradually moved east. Easterly winds prevailed on its southern periphery over the Black Sea (Fig. 4, *b*). In general, the steady eastern wind with a mean speed of ~ 6.3 m/s and maximum values reaching 17 m/s prevailed over the sea area during the specified period according to ERA5 reanalysis data.

South-western wind. Case 4 with the steady south-western wind was recorded in the period from 23 December to 28 December 1995 (Fig. 5). It can be noted that this year appears twice in the cases with steady winds identified by us (Table). The winter of 1995–1996 is one of the longest in the 20th century second half with an increased number of extremes which is partly associated with blocking activity intensification³ [14]. During this period, from 23 December, the cold trough in the north-east of Eastern Europe was gradually filled while shifting to the east; an intense zonal transfer took place over the south of Europe bringing Atlantic warmth to the Black Sea region. This transfer was associated with a cyclone passage across

northern Europe. Later, from 27 December, we observed a cooling over the Black Sea region associated with the passage of a cold front of another fast moving cyclone which moved quickly eastwards across the region. In addition, a pronounced quasi-stationary subtropical high-pressure ridge took place (Fig. 5, *a*) and a relatively high stable temperature gradient was observed between the north and south of Europe throughout the period under consideration.

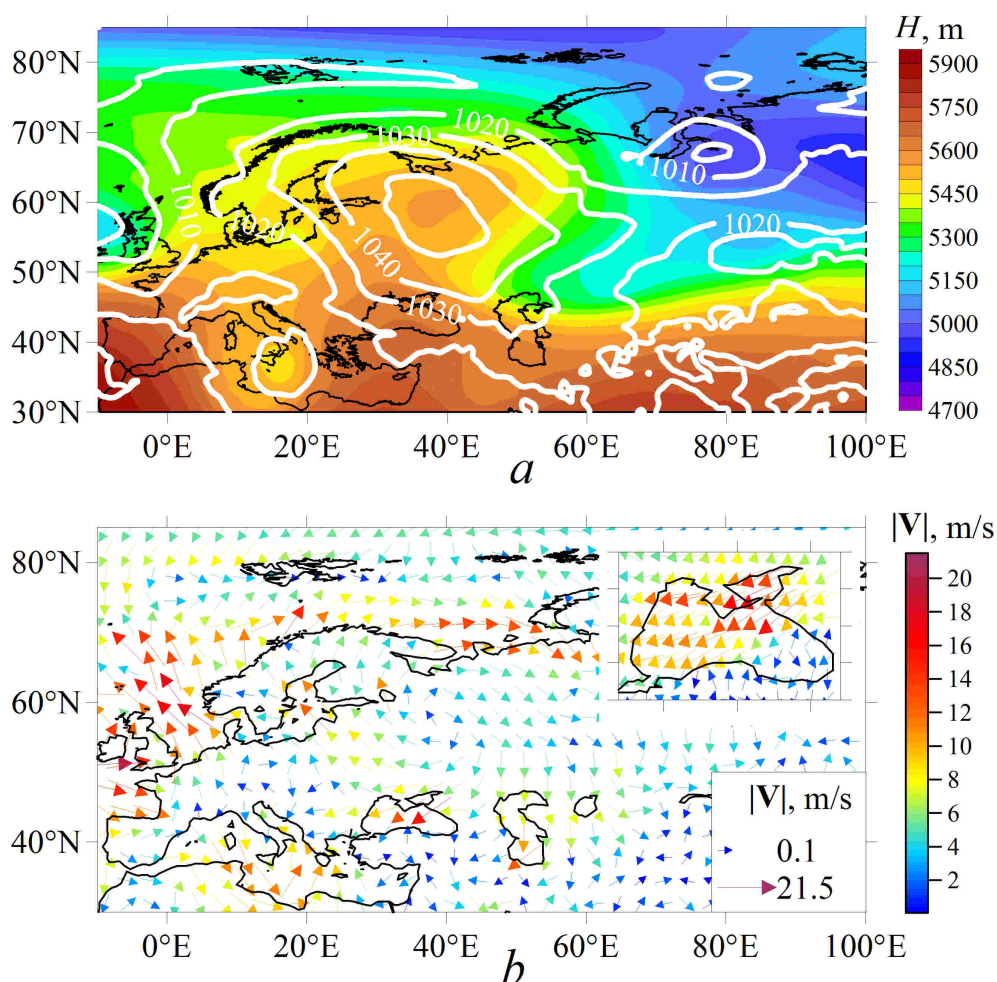


Fig. 4. The same as in Fig. 2, for 01.12.2002, 06:00 (a case of long-lasting eastern wind)

Thus, it can be concluded that the passage of cyclones one after another across the European region accompanied by an intense westerly transfer of air masses and a stable high-pressure ridge in the subtropical latitudes (Fig. 5, *a*) created conditions for the prevalence of the south-western wind over the Black Sea (Fig. 5, *b*). In general, the steady south-western wind with a mean speed of ~ 10.3 m/s with maximum values reaching 16 m/s prevailed over the sea.

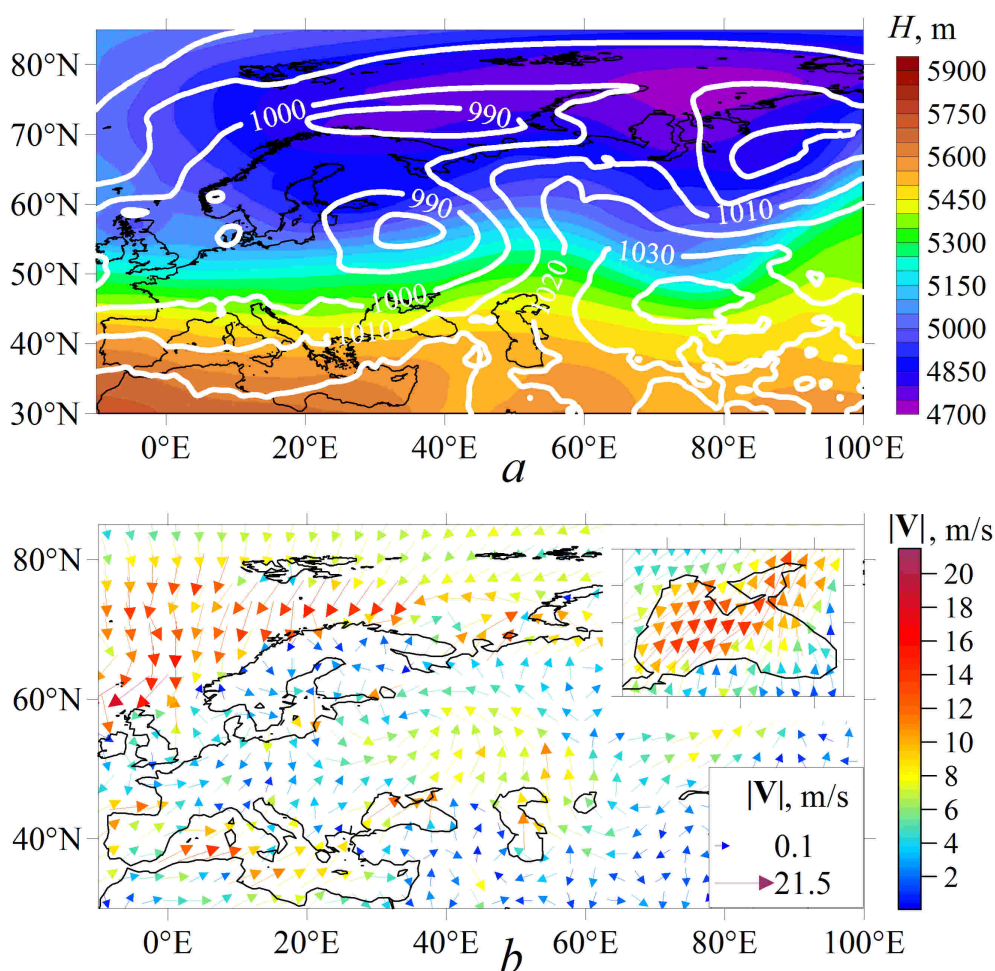


Fig. 5. The same as in Fig. 2, for 24.12.1995, 12:00 (a case of long-lasting south-western wind)

Conclusion

The paper identifies and examines cases of extremely steady winds over the Black Sea during the cold season (December to March). In total, 10 cases of winds lasting for 5 days or more were identified over 1979–2021. Atmospheric conditions in the surface layer and mid-troposphere were analyzed for all identified cases.

All cases with long-lasting north-eastern winds and the case with northern one were accompanied in the atmosphere by blocking events confirmed by the blocking index. Typically, a slow-moving high-altitude blocking anticyclone located over northern Europe/Scandinavia or over northern European Russia was present so that the Black Sea region was on its south-eastern periphery. In the surface layer, such an anticyclone position was accompanied by northern and north-eastern winds. Thus,

atmospheric blockings located predominantly over northern Europe can be accompanied by steady north-eastern and northern winds over the Black Sea.

The case with the south-western steady wind is characterized by distinctive atmospheric conditions compared to the previous listed cases. At this time, there was an intense westerly transfer with the passage of cyclones one after another across Europe. In the subtropical belt, a well-defined quasi-stationary high-pressure ridge was observed, and at the same time, a relatively high steady temperature gradient between the north and south of Europe occurred. Such a pressure distribution contributed to the presence of a steady south-western wind over the Black Sea.

In the future, it is of interest to identify and analyze events with long-lasting winds for the warm season. The results of this work can be used for studying currents and wind waves in the Black Sea during the periods of identified extremely steady winds via numerical modeling.

REFERENCES

1. Mokhov, I.I. and Semenov, V.A., 2016. Weather and Climate Anomalies in Russian Regions Related to Global Climate Change. *Russian Meteorology and Hydrology*, 41(2), pp. 84-92. <https://doi.org/10.3103/S1068373916020023>
2. Kautz, L.-A., Martius, O., Pfahl, S., Pinto, J.G., Ramos, A.M., Sousa, P.M. and Woollings, T., 2022. Atmospheric Blocking and Weather Extremes over the Euro-Atlantic Sector – A Review. *Weather and Climate Dynamics*, 3(1), pp. 305-336. <https://doi.org/10.5194/wcd-3-305-2022>
3. Stankūnavičius, G., Basharin, D., Skorupskas, R. and Vivaldo, G., 2017. Euro-Atlantic Blocking Events and Their Impact on Surface Air Temperature and Precipitation over the European Region in the 20th Century. *Climate Research*, 71(3), pp. 203-218. <https://doi.org/10.3354/cr01438>
4. Ginzburg, A.I., Kostianoy, A.G. and Sheremet, N.A., 2004. Seasonal and Interannual Variability of the Black Sea Surface Temperature as Revealed from Satellite Data (1982–2000). *Journal of Marine Systems*, 52(1-4), pp. 33-50. <https://doi.org/10.1016/j.jmarsys.2004.05.002>
5. Efe, B., Sezen, İ., Lupo, A.R. and Deniz, A., 2020. The Relationship between Atmospheric Blocking and Temperature Anomalies in Turkey between 1977 and 2016. *International Journal of Climatology*, 40(2), pp. 1022-1037. <https://doi.org/10.1002/joc.6253>
6. Barriopedro, D., García-Herrera, R. and Trigo, R.M., 2010. Application of Blocking Diagnosis Methods to General Circulation Models. Part I: A Novel Detection Scheme. *Climate Dynamics*, 35, pp. 1373-1391. <https://doi.org/10.1007/s00382-010-0767-5>
7. Luo, D., Yao, Y. and Feldstein, S.B., 2014. Regime Transition of the North Atlantic Oscillation and the Extreme Cold Event over Europe in January–February 2012. *Monthly Weather Review*, 142(12), pp. 4735-4757. <https://doi.org/10.1175/MWR-D-13-00234.1>
8. Schneidereit, A., Schubert, S., Vargin, P., Lunkeit, F., Zhu, X., Peters, D.H.W. and Fraedrich, K., 2012. Large-Scale Flow and the Long-Lasting Blocking High over Russia: Summer 2010. *Monthly Weather Review*, 140(9), pp. 2967-2981. <https://doi.org/10.1175/MWR-D-11-00249.1>
9. Mokhov, I.I., 2011. Specific Features of the 2010 Summer Heat Formation in the European Territory of Russia in the Context of General Climate Changes and Climate Anomalies. *Izvestiya, Atmospheric and Oceanic Physics*, 47, 653-660. <https://doi.org/10.1134/S0001433811060119>
10. Pope, R.J., Butt, E.W., Chipperfield, M.P., Doherty, R.M., Fenech, S., Schmidt, A., Arnold, S.R. and Savage, N.H., 2016. The Impact of Synoptic Weather on UK Surface Ozone and Implications for Premature Mortality. *Environmental Research Letters*, 11(12), 124004. <https://doi.org/10.1088/1748-9326/11/12/124004>

11. Wilby, R.L., 2007. A Review of Climate Change Impacts on the Built Environment. *Built Environment*, 33(1), pp. 31-45. <https://doi.org/10.2148/benv.33.1.31>
12. Stendel, M., Francis, J., White, R., Williams, P.D., and Woollings, T., 2021. The Jet Stream and Climate Change. In: T.M. Letcher, ed., 2021. *Climate Change*. Elsevier, pp. 327-357. <https://doi.org/10.1016/B978-0-12-821575-3.00015-3>
13. Khokhlov, V.N. and Romanova, A.V., 2005. [The Repeatability of Blocking Situations over Europe at the Beginning of the 21st Century]. *Meteorology, Climatology and Hydrology*, 49, pp. 82-88 (in Russian).
14. Li, C., Zhang, Q., Ji, L. and Peng, J., 2012. Interannual Variations of the Blocking High over the Ural Mountains and Its Association with the AO/NAO in Boreal Winter. *Acta Meteorologica Sinica*, 26(2), pp.163-175. <https://doi.org/10.1007/s13351-012-0203-3>
15. Barriopedro, D., García-Herrera, R., Lupo, A.R. and Hernández, E., 2006. A Climatology of Northern Hemisphere Blocking. *Journal of Climate*, 19(6), 1042-1063. doi:10.1175/JCLI3678.1
16. Sousa, P.M., Trigo, R.M., Barriopedro, D., Soares, P.M.M. and Santos, J.A., 2018. European Temperature Responses to Blocking and Ridge Regional Patterns. *Climate Dynamics*, 50, 457-477. <https://doi.org/10.1007/s00382-017-3620-2>
17. Rex, D.F., 1950. Blocking Action in the Middle Troposphere and Its Effect upon Regional Climate: Part I. *Tellus*, 2(4), pp.275-301. doi:10.3402/tellusa.v2i4.8603
18. Wiedenmann, J.M., Lupo, A.R., Mokhov, I. and Tikhonova, E.A., 2002. The Climatology of Blocking Anticyclones for the Northern and Southern Hemispheres: Block Intensity as a Diagnostic. *Journal of Climate*, 15(23), pp. 3459-3473. [https://doi.org/10.1175/1520-0442\(2002\)015<3459:TCOBAF>2.0.CO;2](https://doi.org/10.1175/1520-0442(2002)015<3459:TCOBAF>2.0.CO;2)
19. Pelly, J.L. and Hoskins, B.J., 2003. A New Perspective on Blocking. *Journal of the Atmospheric Sciences*, 60(5), pp. 743-755. [https://doi.org/10.1175/1520-0469\(2003\)060<0743:ANPOB>2.0.CO;2](https://doi.org/10.1175/1520-0469(2003)060<0743:ANPOB>2.0.CO;2)
20. Tibaldi, S. and Molteni, F., 1990. On the Operational Predictability of Blocking. *Tellus A*, 42(3), pp. 343-365. <https://doi.org/10.1034/j.1600-0870.1990.t01-2-00003.x>
21. Bacer, S., Jomaa, F., Beaumet, J., Gallée, H., Le Bouëdec, E., Ménégoz, M. and Staquet, C., 2022. Impact of Climate Change on Wintertime European Atmospheric Blocking. *Weather and Climate Dynamics*, 3(1), pp. 377-389. <https://doi.org/10.5194/wcd-3-377-2022>
22. Mokhov, I.I., Akperov, M.G., Prokofyeva, M.A., Timazhev, A.V., Lupo, A.R. and Le Treut, H., 2013. Blockings in the Northern Hemisphere and Euro-Atlantic Region: Estimates of Changes from Reanalysis Data and Model Simulations. *Doklady Earth Sciences*, 449(2), pp. 430-433. <https://doi.org/10.1134/S1028334X13040144>
23. Polonskii, A.B. and Kibal'chich, I.A., 2015. Circulation Indices and Thermal Regime of Eastern Europe in Winter. *Russian Meteorology and Hydrology*, 40, pp. 1-9. <https://doi.org/10.3103/S106837391501001X>
24. Dovgaya, S.V., Dymova, O.A., Markova, N.V., Demyshev, S.G. and Cherkasov, L.V., 2014. Assessment of the State of the Marine Environment under Extreme Storm Conditions in some Areas of Oil, Gas and Gas Condensate Fields off the Black Sea Coast of Crimea. In: *Ecological Safety of Coastal and Shelf Zones and Comprehensive Use of Shelf Resources*. Sevastopol: MHI. No. 28, pp. 276-286 (in Russian).
25. Myslenkov, S., Zelenko, A., Resnyanskii, Y., Arkhipkin, V. and Silvestrova, K., 2021. Quality of the Wind Wave Forecast in the Black Sea Including Storm Wave Analysis. *Sustainability*, 13(23), 13099. <https://doi.org/10.3390/su132313099>
26. Kharitonova, L.V., Ivancha, E.V. and Alekseev, D.V., 2015. Effect of Storm Surges and Wind Waves on Morphodynamic Processes in the Bakalskaya Spit Region. *Physical Oceanography*, (1), pp. 73-84. <https://doi.org/10.22449/1573-160X-2015-1-73-84>

27. Surkova, G.V., Koltermann, K.P. and Kislov, A.V., 2012. Method of Forecasting Storm Conditions for the Black Sea under Climate Changes. *Vestnik Moskovskogo Universiteta. Seriya 5, Geografiya*, (6), pp. 25-31 (in Russian).
28. Surkova, G., Arkhipkin, V. and Kislov, A., 2013. Atmospheric Circulation and Storm Events in the Black Sea and Caspian Sea. *Open Geosciences*, 5(4), pp. 548-559. <https://doi.org/10.2478/s13533-012-0150-7>
29. Stanev, E.V., 2005. Understanding Black Sea Dynamics: Overview of Recent Numerical Modeling. *Oceanography*, 18(2), pp. 56-75. <https://doi.org/10.5670/oceanog.2005.42>
30. Kubryakov, A.A., Belokopytov, V.N., Zatsepin, A.G., Stanichny, S.V. and Piotukh, V.B., 2019. The Black Sea Mixed Layer Depth Variability and Its Relation to the Basin Dynamics and Atmospheric Forcing. *Physical Oceanography*, 26(5), pp. 397-413. <https://doi.org/10.22449/1573-160X-2019-5-397-413>
31. Shokurova, I.G., Garmashov, A.V., Toloknov, Yu.N. and Korovushkin, A.I., 2016. Analysis of the Meteorological Regime in the North-Western Part of the Black Sea from Observational Data on Fixed Offshore Platform. In: *Ecological Safety of Coastal and Shelf Zones of Sea*. Sevastopol: MHI. No. 2, pp. 41-51 (in Russian).
32. Hersbach, H., Bell, B., Berrisford, P., Hirahara, S., Horányi, A., Muñoz-Sabater, J., Nicolas, J., Peubey, C., Radu, R., [et al.], 2020. The ERA5 Global Reanalysis. *Quarterly Journal of the Royal Meteorological Society*, 146(730), pp. 1999-2049. <https://doi.org/10.1002/qj.3803>
33. Bagrov, N.A., 1959. [Analytical Representation of Meteorological Field Series by Natural Orthogonal Components]. *Trudy TsIP* [Transactions of the Central Institute of Forecasts], (74), pp. 3-24 (in Russian).
34. Ivanov, V.A. and Belokopytov, V.N., 2013. *Oceanography of the Black Sea*. Sevastopol: ECOSI-Gidrofizika, 210 p.
35. Shokurov, M.V. and Shokurova, I.G., 2017. Wind Stress Curl over the Black Sea under Different Wind Regimes. *Physical Oceanography*, (6), pp. 12-23. <https://doi.org/10.22449/1573-160X-2017-6-12-23>
36. Voskresenskaya, E.N. and Kovalenko, O.Yu., 2016. Blocking Anticyclones in the European Region and Their Variability Associated with El Nino Events. *Izvestiya Rossiiskoi Akademii Nauk. Seriya Geograficheskaya*, (1), pp. 49-57. <https://doi.org/10.15356/0373-2444-2016-1-49-57> (in Russian).
37. Shokurova, I.G., Kubryakov, A.A. and Shokurov, M.V., 2021. Influence of Long-Term Changes in the Large-Scale Sea Level Pressure Field on the Wind Regime and the Wind Stress Curl in the Black Sea. *Physical Oceanography*, 28(2), pp. 165-179. <https://doi.org/10.22449/1573-160X-2021-2-165-179>
38. Demirtaş, M., 2017. The Large-Scale Environment of the European 2012 High-Impact Cold Wave: Prolonged Upstream and Downstream Atmospheric Blocking. *Weather*, 72(10), pp. 297-301. <https://doi.org/10.1002/wea.3020>
39. Golubev, A.D., Kabak, A.M., Nikolskaya, N.A., Butova, G.I. and Berezhnaya, T.V., 2013. Blocking of the Western Transfer over Eurasia in the Winter of 2012 and Related Weather Anomalies. *Proceedings of the Hydrometeorological Research Center of the Russian Federation*, (349), pp. 188-213 (in Russian).
40. Semenov, E.K., Sokolikhina, N.N., Tudrii, K.O. and Shchenin, M.V., 2015. Synoptic Mechanisms of Winter Warming in the Arctic. *Russian Meteorology and Hydrology*, 40(9), pp. 576-583. <https://doi.org/10.3103/S1068373915090022>
41. Wu, B., Yang, K. and Francis, J.A., 2017. A Cold Event in Asia during January–February 2012 and Its Possible Association with Arctic Sea Ice Loss. *Journal of Climate*, 30(19), pp. 7971-7990. <https://doi.org/10.1175/JCLI-D-16-01115.1>

About the authors:

Dmitry V. Basharin, Senior Research Associate, Marine Hydrophysical Institute of RAS (2 Kapitanskaya Str., Sevastopol, 299011, Russian Federation), CSc. (Geogr.), **ResearcherID: J-9539-2018**, **Scopus Author ID: 6507420563**, **ORCID ID: 0000-0002-6389-8407**, dbasharin@rambler.ru

Irina G. Shokurova, Senior Research Associate, Marine Hydrophysical Institute of RAS (2 Kapitanskaya Str., Sevastopol, 299011, Russian Federation), CSc. (Geogr.), **ResearcherID: C-8223-2016**, **Scopus Author ID: 25822860800**, **ORCID ID: 0000-0002-3150-8603**, igshokurova@mail.ru

Contribution of the co-authors:

Dmitry V. Basharin – methodology for identifying blockings, calculations of empirical orthogonal functions, writing – original draft, review and editing, analysis of results

Irina G. Shokurova – problem statement, calculations of steady winds and blocking indices, visualization, writing – original draft, review and editing, analysis of results

The authors have read and approved the final manuscript.

The authors declare that they have no conflict of interest.

Frequency of Meteorological Factors of Vessel Icing in the Barents Sea and Ice Accretion on its Coast in a Changing Climate

A. I. Lavrenteva ¹, ✉, I. I. Leonov ², N. N. Sokolikhina ¹

¹ Lomonosov Moscow State University, Moscow, Russian Federation

² Rosseti R&D Center, Moscow, Russian Federation

✉ lavrentevaai@my.msu.ru

Abstract

Purpose. The work is purposed at analyzing the regional characteristics of ice accretion frequency and meteorological conditions of vessel icing in the Barents Sea region as well as long-term trends of these characteristics observed in the context of modern climate change.

Methods and Results. The results of studying the frequency of ice accretions are obtained by statistical processing of standard observations at a network of weather stations located near the coast and on the islands of the Barents Sea for the period of 1966–2022. The frequency of vessel icing is estimated using the D. Overland method which is based on calculating the spray icing intensity involving the data on wind speed, air temperature, sea water temperature and its freezing point. The ERA5 reanalysis for 1979–2022 is used as the input data for the D. Overland method. The average annual number of days with the atmospheric phenomena during which dangerous ice accretions of different types can be formed, is obtained based on the observation data. The time trends in the average annual number of days with such phenomena are quantitatively evaluated. The reanalysis data processing has permitted to obtain the average annual number of days with vessel icing for the Barents Sea area. The regions of the highest frequency of extreme vessel icing are identified. The time trends in frequency of the changes in a number of days with vessel icing of different intensity are considered for the period of 1979–2022.

Conclusions. On the Barents Sea coast, about three days with dangerous ice accretions of different types are observed on average annually. From 1966 to 2022, the number of such phenomena decreased on average by 0.58 days every 10 years. The highest frequency of marine icing is revealed in the eastern part of the Barents Sea and near the western coast of Novaya Zemlya where the average number of days with extreme icing exceeds 30 days per year. In course of the period of 1979–2022, both a decrease in the average annual number of days with icing up to three ones per year (south of 75°N and west of 50°E) and their increase up to three days per year (in the northern and eastern parts of the Barents Sea) were observed.

Keywords: Arctic, Barents Sea, climate changes, climate risks, hazardous hydrometeorological phenomena, icing, ice accretion, glaze ice, reanalysis, ERA5

Acknowledgements: The research was carried out at Lomonosov Moscow State University with the support of Russian Science Foundation (project No. 24-27-00047).

For citation: Lavrenteva, A.I., Leonov, I.I. and Sokolikhina, N.N., 2024. Frequency of Meteorological Factors of Vessel Icing in the Barents Sea and Ice Accretion on its Coast in a Changing Climate. *Physical Oceanography*, 31(5), pp. 609-625.

© 2024, A. I. Lavrenteva, I. I. Leonov, N. N. Sokolikhina

© 2024, Physical Oceanography



*The paper is dedicated to the memory of
Galina V. Surkova, eminent scientist in
the field of climatology, a brilliant
lecturer and mentor*

Introduction

Interest in the Arctic region climate changes has been steadily increasing in recent decades. This is mainly due to the fact that the average annual air temperatures in high latitudes rise much faster than in the world as a whole. The frequency of certain dangerous hydrometeorological phenomena is also increasing ¹ [1].

Hydrometeorological conditions of vessel icing in the Barents Sea and ice accretion on its coast are the subject of study in this work. Phenomena of this type have a significant impact on the development of human economic activity [2]. Atmospheric and marine icing complicates significantly the process of gas and oil exploration and production as well as their transportation [3, 4]. Under conditions of intense icing, sea vessels can lose stability and capsize. The loss of vessels due to icing, much less a threat of their loss, is not such a rare phenomenon in some areas of the World Ocean ². It is assumed that marine activities will strongly develop in the polar and subarctic regions as a part of overall economic development including transport, fisheries and tourism [5]. In this regard, the study and understanding of risks associated with icing phenomena in the Arctic are an urgent task.

On land, icing is associated with atmospheric processes. The first process is associated with precipitation icing which causes the formation of ice and wet snow accretion. The second is in-cloud icing which leads to the formation of hard and soft rime. The greatest hazard is posed by ice, hard rime and wet snow accretion [6].

In the sea basins, the most significant type of marine icing is that in the flow of sea spray, formed when waves hit the hull of a vessel. This icing is called spray icing. Mixed icing is formed on vessels under the combined impact of spray and atmospheric icing ³. According to statistical calculations, ice accretion takes place on the surface of a vessel as a result of spray icing in 90% of cases [7].

Icing intensity depends on various hydrometeorological conditions which, in turn, are subject to atmospheric processes. Ice accumulation increases with

¹ Kattsov, V.M., 2022. *The Third Assessment Report on Climate Change and Its Consequences on the Territory of the Russian Federation*. Saint Petersburg: Science-Intensive Technologies, 676 p. (in Russian).

² Aksyutin, L.R., 1979. [*Icing of Ships*]. Leningrad: Shipbuilding, 128 p. (in Russian).

³ Kachurin, L.G., Smirnov, I.A. and Gashin, L.I., 1980. [*Icing of Ships*]. Leningrad: LPI, 56 p. (in Russian).

the growth of waves caused by strong winds. High wind speeds can be associated with mesoscale cyclones with a short lifespan [8].

Previously performed studies have shown that both a trend towards the icing frequency decrease in some areas and a trend towards its increase in others have been observed on the Barents Sea coasts and waters over the past decades [9]. Climate warming cannot mean an unambiguous decrease in the number of cases of vessel icing. It is necessary to analyze the combination of factors that lead to ice accretion [10, 11].

The work is purposed at analyzing the regional features of ice accretion frequency and meteorological conditions of marine icing in the Barents Sea area as well as long-term trends in these characteristics observed under modern climate change conditions. As a result of this work, we obtained spatial and temporal distribution of ice accretion on the Barents Sea coast over a long-term period using observation data from weather stations. Spatial distribution of marine icing characteristics over a long-term period using ERA5 reanalysis data was obtained and time trends in the number of days with conditions for spray icing of vessels in the Barents Sea for the modern climate were estimated.

Research materials and methods

This paper examines various types of hydrometeorological phenomena that lead to icing of sea vessels as well as offshore structures on the coast and in the sea basins. In this regard, various approaches to the analysis of these phenomena were chosen.

The analysis of ice accretion distribution on the Barents Sea coast was based on urgent observation data from weather stations. The main meteorological parameters were obtained from the FSBI “RIHMI-WDC” open data archive ⁴.

This archive contains urgent observation data from 521 stations for the observation period from 1966 till the present. The list of stations is based on that of Roshydromet stations included in the Global Climate Observing Network. During the study, weather stations located on the coast of the Barents Sea and on the islands in its waters were selected. In addition, several weather stations located on the coasts of the White, Greenland and Kara Seas were selected.

To assess the frequency, spatial distribution and temporal changes, the average annual number of days with atmospheric phenomena potentially leading to severe ice accretion was obtained for each weather station. Days with such phenomena were considered to be the ones when at least one meteorological period corresponds to a certain weather code.

⁴ Bulygina, O.N., Veselov, V.M., Razuvaev, V.N. and Aleksandrova, T.M., 2014. *Description of the Dataset of Observational Data on Major Meteorological Parameters from Russian Weather Stations*. Database State Registration Certificate No. 2014620549 (in Russian).

Time periods during which the observer recorded freezing precipitation were taken as glaze ice cases. Glaze ice accretions have high density and strength, therefore, all periods during which we observed freezing precipitation were considered potentially dangerous.

The KN-01 code does not differentiate between hard and soft rime. Therefore, the analysis was carried out on days corresponding to fog with rime accretion. In order to filter out soft rime accretion, we selected only those rime cases that were observed in the air temperature range from -10.3 to -0.7 °C and at a wind speed of 2 m/s or more. Previously, based on the processing of instrumental observation data, it was indicated that 90% of hazardous (more than 50 mm in diameter) hard rime accretions in Russia were formed precisely within this temperature and wind range [12]. Such data filtering makes it possible to remove the majority of soft rime accretions from the sample as it does not pose a serious hazard and is formed under light winds and air temperatures below -10 °C.

Filtering of samples was also performed for identifying days with wet snow, for which the KN-01 code does not provide a separate code. To identify wet snow, we selected days on which precipitation was observed in the form of moderate continuous or heavy snow, falling at an air temperature from 0 to 0.6 °C and a wind speed under 1 m/s. This range was previously substantiated by the authors of the work as the most favorable one for the formation of dangerous wet snow accretions [12].

As a result, the average annual number of days with atmospheric phenomena potentially leading to the formation of ice, hard rime and wet snow was obtained for each weather station for the period of 1966–2022. Only years without gaps in observations during the cold period were considered. Linear time trends were obtained for each type of accretions; these trends were tested for reliability using the Mann–Kendall criterion [13, 14]. This criterion was previously used by other authors to assess trends in the ice accretion characteristics [15].

Next, spray icing was considered. This type of icing is the most intense and poses the greatest hazard to seagoing vessels. Icing probability and factors contributing to spray icing can be determined by various statistical methods [16]. Most of the methods are based on determining the sea icing probability as a set of specified intervals of values of meteorological parameters: wind speed, water and air temperature. For example, the methodological guidelines for preventing the threat of vessel icing developed at AARI to determine the icing probability and intensity include a combination of wind speed and air temperature ⁵. Similar methods are also applied in the fishing industry ⁶.

⁵ Borisenkov, E.P. and Pchelko, I.G., eds., 1972. [*Methodological Guidelines for Preventing the Threat of Icing on Ships*]. Leningrad: AANII, 81 p. (in Russian).

⁶ Giprorybflot, 1983. [*Instruction on Prevention of Accidents and Struggle for Survivability of Vessels of the USSR Fishing Industry Fleet*]. Leningrad: Transport, 120 p. (in Russian).

In this paper, the method proposed by D. Overland was applied for calculating the intensity of marine spray icing. This method provides the determination of icing rate of sea vessels using the icing index [17]. In addition to wind speed and air temperature, this icing index also considers the values of sea water temperature as well as its freezing temperature.

The formula for calculating icing index *PPR* has the following form:

$$PPR = \frac{V_a(T_f - T_a)}{1 + 0.4(T_w - T_f)},$$

where *PPR* is icing index proportional to its intensity; V_a is wind speed, m/s; T_f is sea water freezing point; T_a is air temperature and T_w is water temperature, °C.

The obtained values of icing index *PPR* correspond to different intensities of icing rate (Table 1).

Table 1

Ratio between icing index *PPR* and icing rate *IR*

Parameter	Icing class				
	Light	Moderate	Heavy	Extreme	Particularly extreme
<i>PPR</i> , (m·°C)/s	> 0	> 20.6	> 45.2	> 70.0	> 83.0
Icing rate <i>IR</i> , cm/h	> 0	> 0.7	> 2.0	> 4.0	> 5.3

The following empirical formula exists for converting icing index into icing rate *IR* (cm/h):

$$IR = A(PPR) + B(PPR)^2 + C(PPR)^3,$$

where A , B , C are empirical constants ($A = 2.73 \cdot 10^{-2}$, $B = 2.91 \cdot 10^{-4}$, $C = 1.84 \cdot 10^{-6}$).

The meteorological data applied for constructing the icing rate fields by the D. Overland method were the ERA5 reanalysis data available on regular latitude and longitude grids with a resolution of $0.25^\circ \times 0.25^\circ$ [18]. The calculations for the Barents Sea area from 1979 to 2022 were carried out with one-hour frequency.

The *PPR* index was calculated for each period from 1979 to 2022. The index was calculated only for grid cells that contained sea surface temperature data (corresponding to “sea” cells) as well as for cells in which sea ice occupied less than 50% of the cell area. If the proportion of sea ice in a cell was more than 50%, then we assumed that spray icing was absent.

Next, the average monthly and average annual values of number of days with sea vessels icing of varying intensity (all cases of icing and extreme icing) were calculated. Any day during which icing of a given intensity was observed at least in one of 24 periods of hourly reanalysis data was considered to be an icing day. To

identify all days with icing, the intensity $PPR > 0$ was set as well as $PPR > 83$ for days with extreme icing.

After estimating average values using the least squares method, long-term linear trends in the number of days with sea icing were obtained. The resulting trends were tested for reliability using the Mann–Kendall criterion [13, 14].

Results and discussion

Table 2 presents the obtained data on the average annual number of days with atmospheric phenomena that can lead to the formation of hazardous ice accretion on the Barents Sea coast and in its waters.

Based on these data, a schematic map of the frequency of days with dangerous phenomena of each type was constructed. The map-scheme for each weather station represents a circular diagram indicating the share of average annual number of cases of atmospheric phenomena that cause the formation of various-type ice accretions. The obtained data indicate that it is impossible to single out the predominance of any atmospheric phenomenon in the region under consideration (Fig. 1).

The highest frequency of fogs with rime accretion formed at sufficient wind speed and a temperature range favorable for hard rime formation is observed in the southeastern part of the Barents Sea. A fog with rime accretion is also often observed at several weather stations located far from the coast – Murmansk and Polyarny.

The spatial distribution pattern of the number of days with freezing precipitation is extremely heterogeneous. However, we can make some assumptions regarding this distribution. Glaze ice is least common at Konstantinovskiy Cape and Fedorov station. These are weather stations located in the southeast of the Barents Sea and in the Kara Strait on the Kara Sea side, respectively. In this location, there is a low frequency of warm fronts with thermal stratification of the “warm nose” type with a characteristic raised layer of warm air, leading to the formation of freezing precipitation. Low frequency of freezing precipitation in the Murmansk area can be due to the immediate proximity of the Murmansk Coastal Warm Current which promotes the existence of a warm lower layer of the atmosphere preventing the formation of freezing precipitation.

Spatial features of wet snow frequency are traced more clearly. It is known that wet snow accretion is most often formed at air temperatures from -0.1 to 0.3 °C and at low wind speeds (from 1 to 4 m/s) or in calm weather [12]. This is due to the physical properties of snow: snowflakes are large in size, with high windage, easily blown away by strong winds from objects on which icing occurs. Therefore, the wind should not be too strong throughout the icing phase for the formation of hazardous wet snow accretion. This is associated with the fact that the highest frequency of hazardous wet snow accretion is observed in the White Sea area as well

as at some weather stations with a high frequency of near-zero air temperatures and low wind speeds due to their location in orographically protected relief forms. For example, Barenburg is located on the Isfjord coast and Vaida Bay weather station is located in the bay of the corresponding name. Murmansk and Polyarny are also located in the Kola Bay.

Table 2

Average annual number of days with potentially hazardous weather events (AN) and linear trend values (days/10 years) for the period of 1966–2022

Weather station	Rime fog		Freezing precipitation		Wet snow		All events	
	AN	trend	AN	trend	AN	trend	AN	trend
Krenkel	0.72	-0.28	2.72	-0.97	0.35	-0.01	3.79	-1.26
Barenburg	0.33	0.08	0.71	0.14	2.50	0.18	3.54	0.40
Malye Karmakuly	0.37	-0.20	1.19	-0.65	0.23	-0.03	1.79	-0.88
Fedorov	2.93	-0.33	0.23	-0.08	0.09	-0.04	3.25	-0.45
Vaida Guba	0.38	0.11	0	0	0.43	-0.05	0.81	0.06
Polyarny	1.47	-0.01	0	0	0.84	0.01	2.31	0
Teriberka	0.12	-0.03	0	0	0.55	-0.08	0.67	-0.11
Kolguyev Severny	2.06	-0.27	0.81	-0.27	0.31	-0.06	3.18	-0.60
Murmansk	1.71	-0.19	0.08	0	1.51	-0.04	3.30	-0.24
Svyatoy Nos	0.25	-0.17	0.19	-0.06	0.31	-0.01	0.75	-0.24
Kanin Nos	4.06	-0.17	0.32	0.11	0.28	0.06	4.66	0
Kandalaksa	0.16	-0.02	0.63	0.1	2.33	0.38	3.12	0.46
Sojna	5.52	0.18	1.73	-0.16	0.2	-0.03	7.45	-0.02
Indiga	1.33	-0.61	0.63	0	0.27	-0.07	2.23	-0.67
Umba	0.81	-0.04	0.56	-0.33	1.17	0.31	2.54	-0.06
Sosnovets Island	1.24	-0.41	0.59	-0.24	0.37	-0.12	2.2	-0.77
Gridino	0.43	-0.26	1.11	-0.61	0.54	-0.08	2.08	-0.95
Zizgin	1.38	-0.37	0.4	-0.18	0.32	-0.11	2.10	-0.65
Kem port	0.95	0.09	0.27	-0.02	0.82	0.12	2.04	0.18
Arhangelsk	0.57	-0.17	1.12	-0.01	1.12	0.23	2.81	0.06
Onega	0.21	-0.07	1.68	0.37	1.88	-0.02	3.77	0.28
Konstantinovsky Cape	3.60	-0.28	0.50	-0.09	0.17	-0.03	4.27	0.33

Note. Significant trends are in bold.

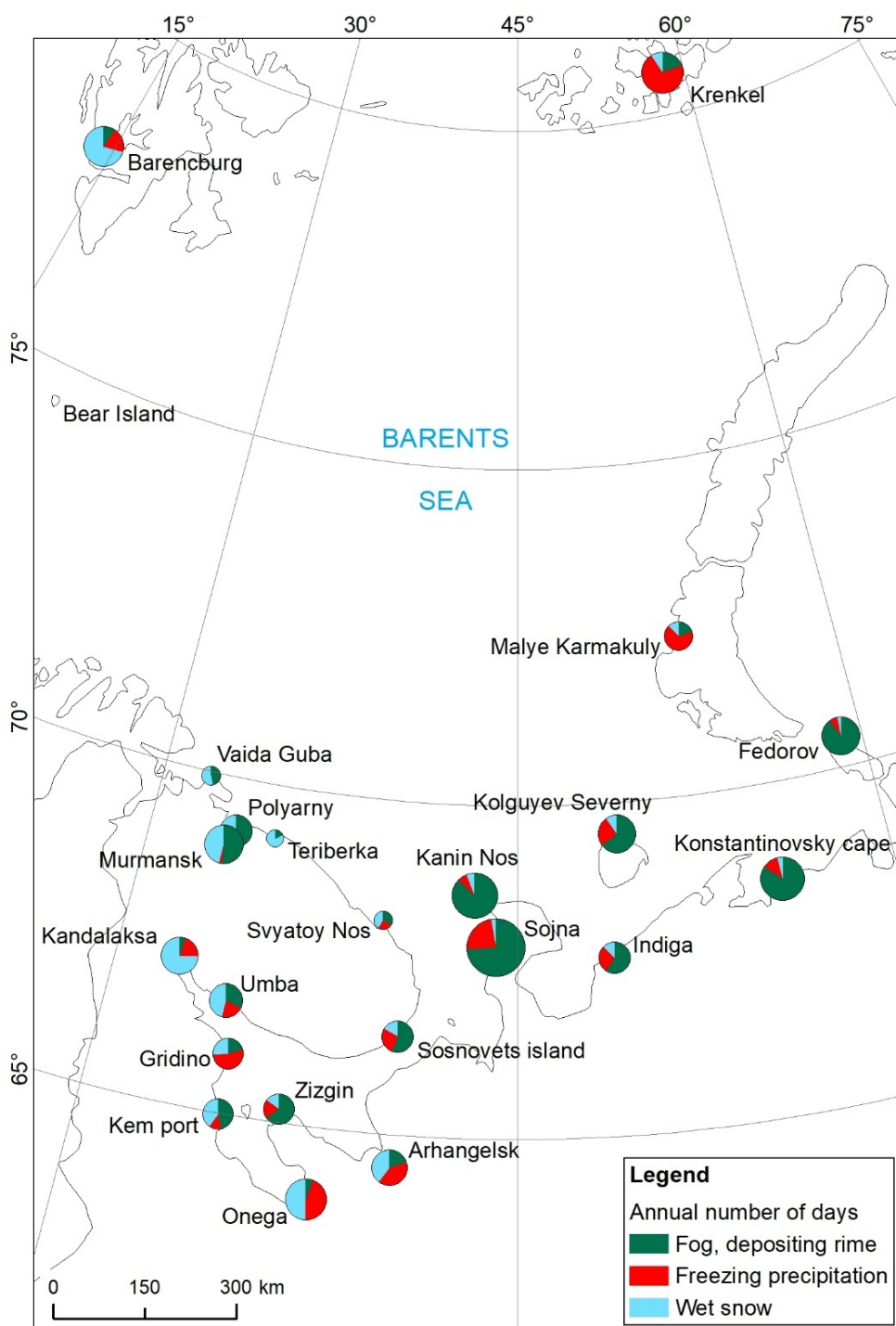


Fig. 1. Map of the average annual number of days with hazardous atmospheric phenomena for the period of 1966–2021 based on visual observations

This work is mainly focused on the phenomena that can result in the formation of hazardous ice accretion. As already noted in Research Materials and Methods, the work involved filtering the data of the main observations with regard to previously obtained ranges of air temperature and wind speed characteristic of hazardous ice accretion of each type.

The process of data filtering can be approached in different ways. The use of stricter criteria leads to a significant reduction in the selected events. For example, when selecting the wet snow events, it was assumed that wet snow accretion can be formed at a speed of up to 1 m/s, inclusively. If it were assumed that dangerous wet snow accretion could only form in calm weather, the number of selected wet snow events would be reduced threefold. On the contrary, if potentially hazardous snowfalls were considered to be the snowfall events at air temperatures from -2 to 2°C at any wind speed, then the average number of days with wet snow in the Barents Sea region would increase by 45 times – from 0.75 to 33 days per year.

The same applies to fogs with rime formation. To tighten the selection criteria, we can rise the wind speed, increasing the density of the flow of supercooled fog droplets and thereby leaving the cases of the most intense hard rime deposits and excluding an increasing part of the cases of soft rime.

Table 2 presents the estimates of linear trends for the number of days with atmospheric phenomena leading to the formation of hazardous ice accretion for the 1966–2022 period. Estimates for fogs with rime accretion, freezing precipitation and wet snow are given separately. Estimates of the trend for the number of days with all phenomena are also presented. The Mann–Kendall test [13, 14] revealed that some of the obtained trends were reliable for the 5% significance level.

It is shown that significant trends in the number of days with rime have negative values from -0.61 to -0.07 days per decade. The number of days with freezing precipitation also tends to decrease. Linear trends in the number of days with wet snow are significant only at 4 stations out of 22. In general, the trends in the number of days with wet snow can be assessed as near-zero, weakly significant, with individual remarkable positive changes at Kandalaksha, Umba and Onega weather stations.

Since in this paper the trends in the number of days with atmospheric phenomena causing the formation of ice accretion were considered in the context of climate risks in the Arctic, it is appropriate to estimate the trend in the total number of such phenomena.

Fig. 2 represents a schematic map showing the linear trend value of the total number of days with observation of all potentially hazardous atmospheric phenomena for each weather station over the 1966–2022 period. The trend of the number of days for 10 years is shown for convenience.

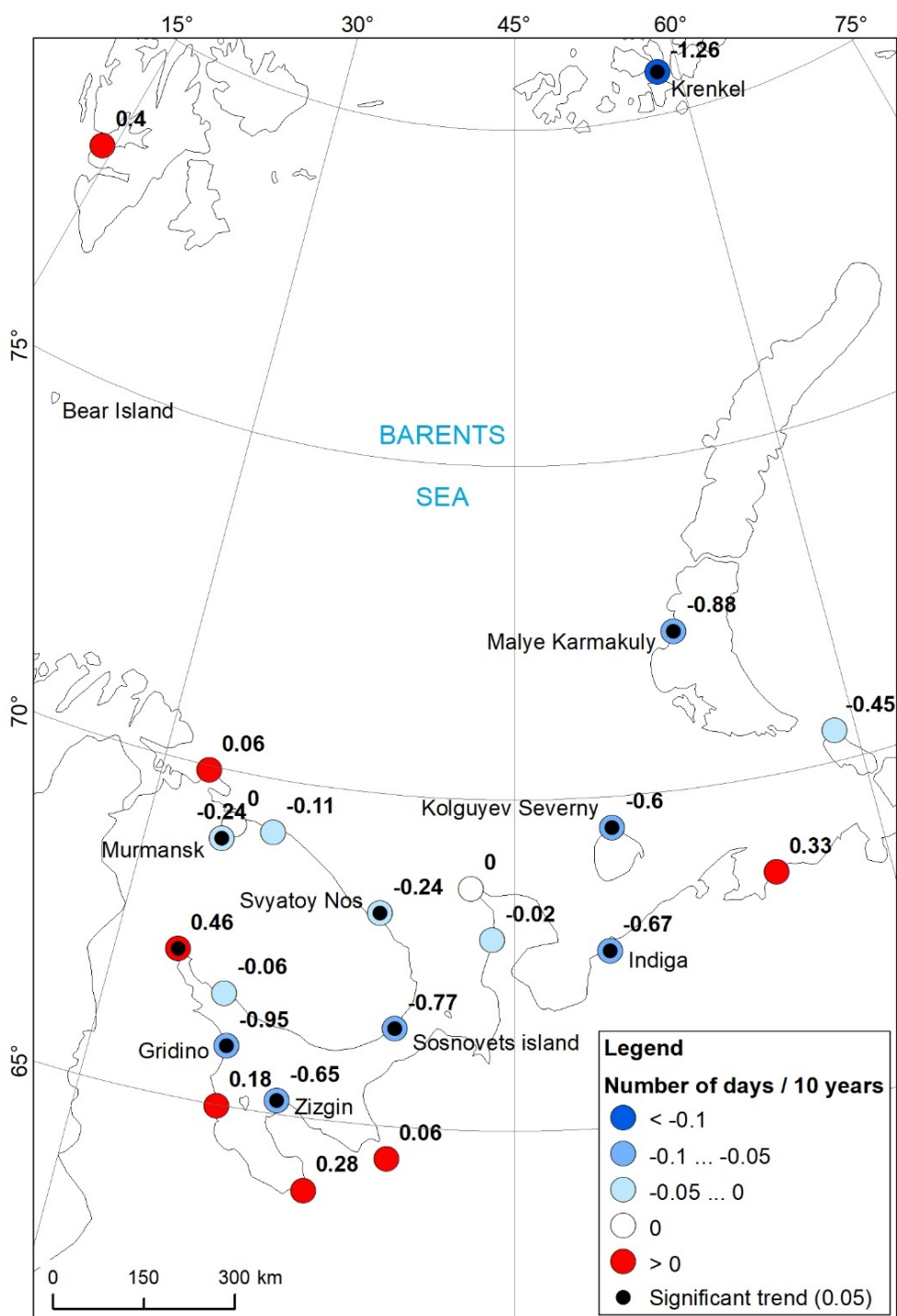


Fig. 2. Map of time trends (number of days / 10 years) of the hazardous atmospheric phenomena frequency for the period of 1966–2021

It follows from the map that negative trends are observed mainly in the territories facing the coasts of the White and Barents Seas. Positive trends are usually observed at weather stations with a more continental location. Almost all significant trends have a negative sign. The exception is Kandalaksha weather station where the wet snow have contributed to the positive trend the most.

Previously published works estimated the trends in the average annual number of days with ice on the territory of Russia [19]. In general, a weak negative trend (-0.2 days/year) in the number of days with freezing rain was obtained for the Atlantic Arctic. The negative trend in the number of days with hazardous ice phenomena obtained in this work is in good agreement with the previously presented estimates.

Despite the fact that this study provides average estimate only for significant trends, it is impossible to make an unambiguous and reliable conclusion about long-term changes in the frequency of potentially hazardous atmospheric icing phenomena in the region under consideration. This is due to the fact that the obtained values of linear trends are characterized by a large scatter, and the initial data of ice accretion visual observations are highly heterogeneous.

According to the report on the climate features on the Russian Federation territory, trends in modern changes in the ice accretion characteristics in Russia obtained by instrumental observations reveal that there is an insignificant positive trend in the number of days with glaze ice and a significant trend in the number of days with wet snow accretion for the quasi-homogeneous climatic region of the Atlantic Arctic ⁷.

Thus, it is possible to expect about three days per year when atmospheric phenomena leading to the formation of heavy ice accretion will be observed in the Barents Sea region. A number of days with atmospheric icing will probably decrease by an average of 0.2 days per decade. The reduction in the number of days with icing and the decrease of its impact on vessels and seaport infrastructure can be considered to be a positive effect of climate change in the Arctic. However, despite the substantial proportion of significant trends, such estimates should be treated with caution, considering the complexity of atmospheric observations which affects the processed data quality as well as the climate variability of this region.

The approach based on the data of the main urgent observations can be applied to the assessment of changes in the frequency of ice accretion of different intensity, primarily for those regions where no instrumental observation data are available. However, it should be noted that this method requires testing in territories located in other climatic regions of Russia.

⁷ Roshydromet, 2022. *A Report on Climate Features on the Territory of the Russian Federation in 2021*. Moscow: Roshydromet, 110 p. (in Russian).

Climatology of spray icing in the Barents Sea is further examined in the paper. In this case, icing is a set of meteorological factors that contribute to the icing formation according to the D. Overland method. The frequency of vessel icing in the Barents Sea was obtained for the 1979–2022 period. The highest values of the average number of days with icing are recorded westwards of Svalbard and Novaya Zemlya as well as on the Kola Peninsula northern coast (Fig. 3, *a*). Thus, on average, more than 150 days with icing are observed in these areas per year. Along the mainland coast, the average annual number of days with icing has a non-uniform distribution. Along the coastline of Arkhangelsk Oblast and the Nenets Autonomous Okrug, vessel icing is observed less frequently than along the Murmansk Oblast coastline. Absolute heights above sea level on the Kola Peninsula are higher; this can lead to strong katabatic winds and an increase in the number of icing events. Under effect of the warm Norwegian Current, the probability of vessel icing is significantly reduced, its contribution can be traced to 40°E. In this case, on average, no more than 120 days with ice accretion on the vessel surface as a result of spray icing are observed during the year. The highest values of the average number of days with extreme icing have similar distribution (Fig. 3, *b*). Thus, extreme icing is most often encountered westwards of Svalbard and Novaya Zemlya. In these areas, the number of days with conditions for extreme icing is approximately six times less than the average number of days with icing in general and ranges from 21 to 30 days per year. Northwards of the islands, the icing frequency is relatively low due to the formation of a long-term ice cover; on average, less than 10 days with icing of vessels are observed per year. Southwards of Svalbard, higher temperatures are observed due to the warm Norwegian Current; this also leads to a lower frequency of icing.

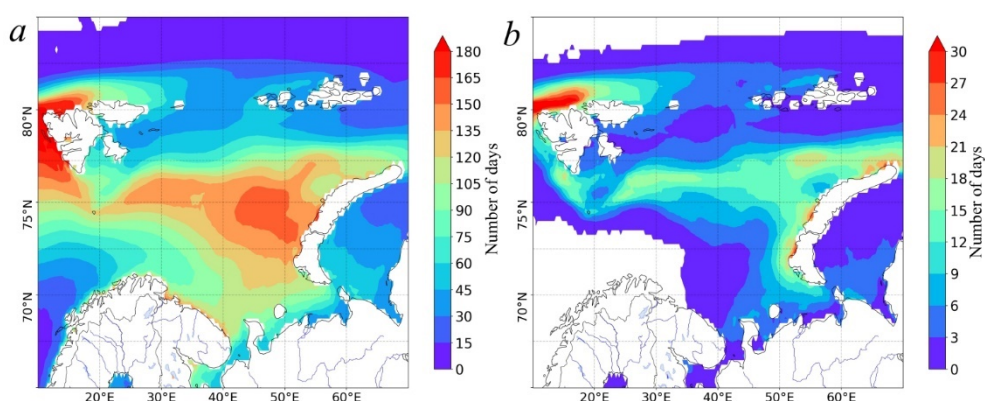


Fig. 3. Average annual number of days with vessel icing (*a*) and extreme icing ($PPR > 83$) (*b*) in the Barents Sea for the period of 1979–2022

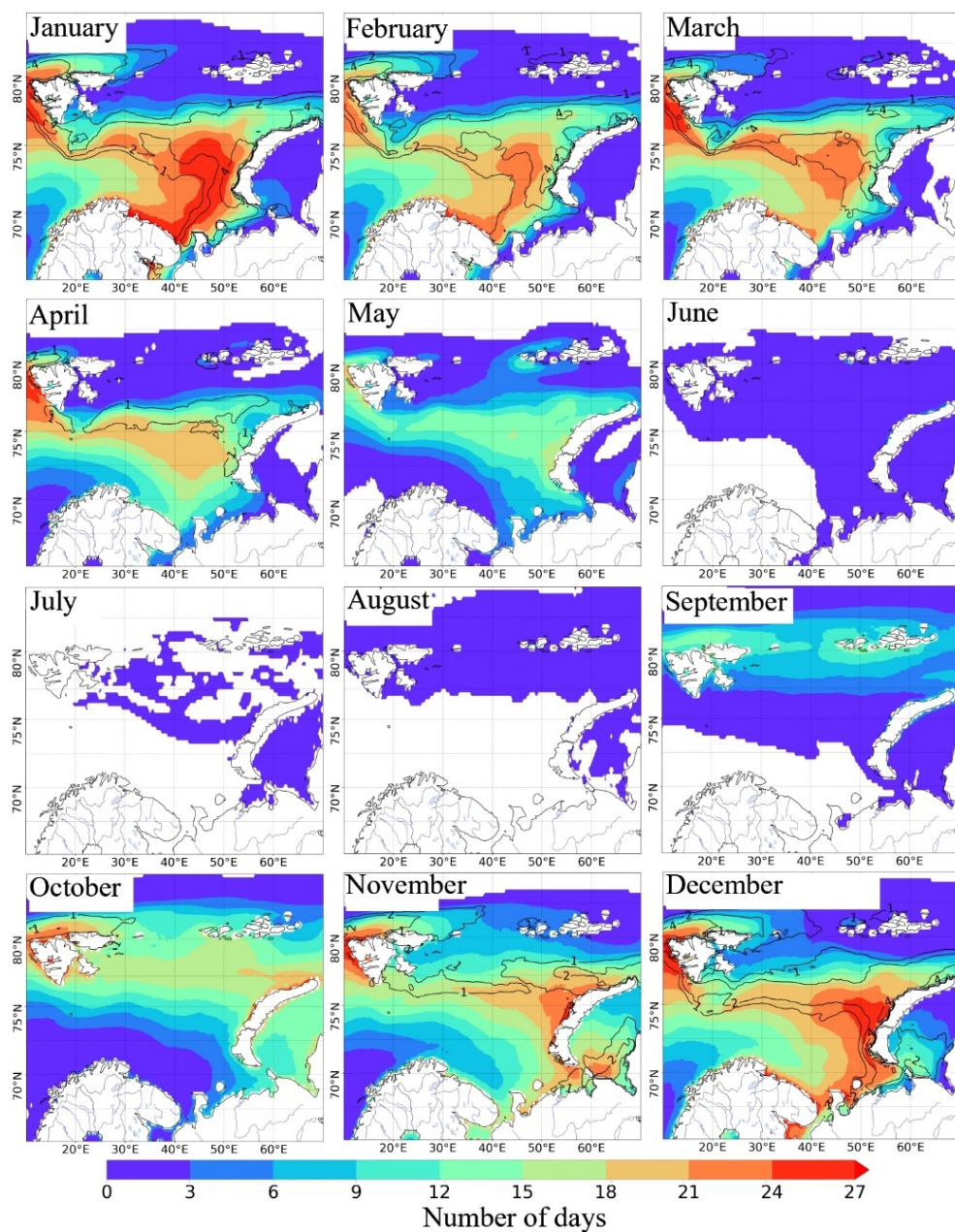


Fig. 4. Average number of days with vessel icing in the Barents Sea for each month during the period of 1979–2022. Black isolines show the number of days with extreme icing ($PPR > 83$) per month

Further, we will consider annual course of number of days with spray icing in the Barents Sea (Fig. 4). Maps of the number of days with sea icing were plotted for each month of the year. The results revealed that the greatest number of days with icing were observed from October to April. In the areas most favorable for icing, this

phenomenon is observed, on average, almost every day (more than 27 days per month). The smallest number of days with icing is observed in July.

Fig. 4 also shows the average long-term number of days with extreme vessel icing. During the year, extreme icing is observed most frequently in January (up to five days per month). During the warm period of the year from May to September, the average number of days with extreme spray icing is less than one per month.

Let us consider the obtained time changes in the frequency of the total number of days with icing per year and the number of days with extreme icing during the year (Fig. 5). The distribution fields of these two indicators are similar.

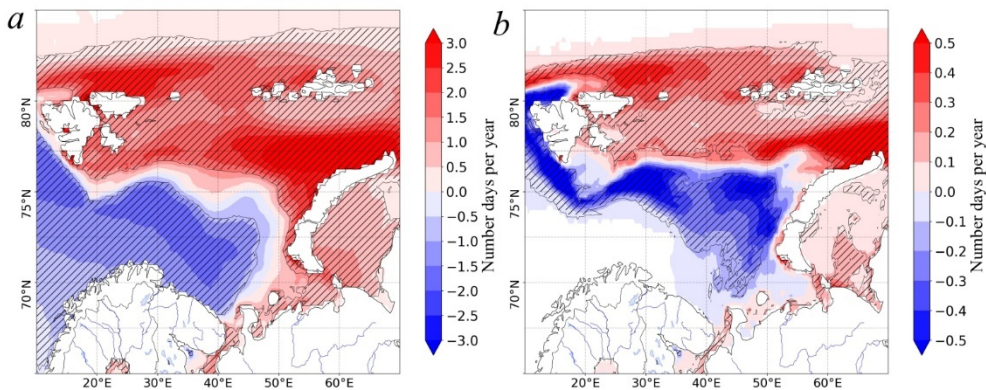


Fig. 5. Temporal change in the frequency of vessel icing in the Barents Sea for the total number of days with icing (*a*) and for the number of days with extreme icing (*b*) in 1979–2022. Shading shows the areas in which the obtained trends are reliable at the 1% significance level

Due to the average annual increase in air temperature, the sea ice area decreases. The areas previously covered by sea ice are water surfaces that are a source of sea spray which contributes to the spray icing formation. In this regard, there is an increase in the frequency of vessel icing in the Barents Sea area located between Svalbard, Franz Josef Land and Novaya Zemlya. In some areas, the icing frequency can increase by three days per year and more.

In the south of the Barents Sea below 75°N and west of 50°E, the influence of the warm Norwegian Current is observed. Due to the most intense climate warming in the Arctic, the average air temperature in this area, not covered by sea ice, increases, which leads to a decrease in the frequency of sea icing. In this case, the frequency of icing changes by approximately three days per year, now in the direction of decreasing cases with ice buildup on the vessel surface.

For the period from October to April, 53 synoptic events were analyzed and conditions for extreme icing during them were diagnosed. It was found that such conditions were recorded most often in January (14 cases out of 53), February and

December (11 and 10 cases, respectively). In the overwhelming majority of cases, conditions for extreme icing were created in the rear parts of cyclones characterized by high wind speed and powerful advection of cold air. Both high wind speeds and low air temperatures contribute to ice formation and accretion on the vessel surface as a result of spray icing. In addition, extreme values were noted in the prefrontal region in some cases. Icing was traced in a narrow strip ahead of the warm front. The prefrontal region is characterized by wind gustiness decrease and simultaneous increase in wind speed. It can be assumed that extreme values of vessel icing in the prefrontal region are associated with a wind speed increase.

Conclusion

The work has studied the spatial and temporal changes in sea vessel icing in the Barents Sea and ice accretion on its coast under modern climate conditions.

It was demonstrated that in this region, on average, there are about three days a year with atmospheric phenomena during which hazardous ice accretion can be formed on the coast. From 1966 to 2022, a trend towards decrease in the average annual number of days with such phenomena was traced. Statistically significant linear trend was, on average, about -0.58 days over 10 years. A significant positive trend was observed only at Kandalaksha weather station, with other positive trends being statistically insignificant. In general, the trends have a large scatter which results in the ambiguous conclusion about long-term changes in the frequency of atmospheric icing phenomena.

Frequency of meteorological conditions for seagoing vessel icing is obtained using ERA5 reanalysis data for 1979–2022 period. The areas with maximum and minimum frequency of the average annual number of days with icing of varying intensity are identified. It is revealed that the average number of days with extreme icing is more than 30 days per year in some areas of the Barents Sea. The highest marine icing frequency is observed in the eastern part of the Barents Sea including the area near the Novaya Zemlya western coast.

It is shown that significant changes in the frequency of vessel icing in the Barents Sea have occurred over the past decades. Both a decrease in the average annual number of days with icing to three days per year (southwards of 75°N and westwards of 50°E) and an increase to three days per year (in the northern and eastern parts of the Barents Sea) were observed.

REFERENCES

1. Zhilina, I.Yu., 2021. Warming in the Arctic: Opportunities and Risks. *Economic and Social Problems of Russia*, 1(45), pp. 66-87. <https://doi.org/10.31249/espr/2021.01.04> (in Russian).
2. Sukhanov, S.I., Lavrenov, I.V. and Yakovleva, N.P., 2006. Icing of Ships on the Black Sea. *Meteorologiya i Gidrologiya*, 12, pp. 75-86 (in Russian).

3. Gautier, D.L., Bird, K.J., Charpentier, R.R., Grantz, A., Houseknecht, D.W., Klett, T.R., Moore, T.E., Pitman, J.K., Schenk, C.J. [et al.], 2009. Assessment of Undiscovered Oil and Gas in the Arctic. *Science*, 324(5931), pp. 1175-1179. <https://doi.org/10.1126/science.1169467>
4. Dehghani-Sani, A.R., Dehghani, S.R., Naterer, G.F. and Muzychka, Y.S., 2017. Marine Icing Phenomena on Vessels and Offshore Structures: Prediction and Analysis. *Ocean Engineering*, 143, pp. 1-23. <https://doi.org/10.1016/j.oceaneng.2017.07.049>
5. Mintu, S. and Molyneux, D., 2022. Ice Accretion for Ships and Offshore Structures. Part 1- State of the Art Review. *Ocean Engineering*, 258, 111501. <https://doi.org/10.1016/j.oceaneng.2022.111501>
6. Shakina, N.P., Khomenko, I.A., Ivanova, A.R. and Skriptunova, Ye.N., 2012. Origination and Forecasting of Freezing Precipitation: Review and Some New Results. *Proceedings of the Hydrometcenter of Russia*, 348, pp. 130-161 (in Russian).
7. Zhou, L., Liu, R. and Yi, X., 2022. Research and Development of Anti-Icing/Deicing Techniques for Vessels: Review. *Ocean Engineering*, 260, 112008. <https://doi.org/10.1016/j.oceaneng.2022.112008>
8. Petrov, A.G., 1998. Synoptic Conditions of Ship Icing in the Far Eastern Seas. In: I. E. Kochergin, ed., 1998. *Hydrometeorological Processes on the Shelf: Assessment of the Impact on the Marine Environment*. Vladivostok: Dalnauka, pp. 38-45 (in Russian).
9. Surkova, G.V., Lavrenteva, A.I. and Tkacheva, E.S., 2024. Regional Features of Glaze Ice Events Frequency in the North of the European Territory of Russia in the Current Changing Climate. *Arctic and Antarctic Research*, 70(1), pp. 21-32. <https://doi.org/10.30758/0555-2648-2024-70-1-21-32> (in Russian).
10. Naseri, M. and Samuelsen, E.M., 2019. Unprecedented Vessel-Icing Climatology Based on Spray-Icing Modelling and Reanalysis Data: A Risk-Based Decision-Making Input for Arctic Offshore Industries. *Atmosphere*, 10(4), 197. <https://doi.org/10.3390/atmos10040197>
11. Samuelsen, E.M. and Graversen, R.G., 2019. Weather Situation during Observed Ship-Icing Events off the Coast of Northern Norway and the Svalbard Archipelago. *Weather and Climate Extremes*, 24, 100200. <https://doi.org/10.1016/j.wace.2019.100200>
12. Leonov, I.I. and Arzhanova, N.M., 2023. Meteorological Conditions for the Formation of Ice Accretions in Russia. *Fundamental and Applied Climatology*, 9(1), pp. 107-126. <https://doi.org/10.21513/2410-8758-2023-1-107-126> (in Russian).
13. Kendall, M., 1970. *Rank Correlation Methods*. London: Griffin, 202 p.
14. Mann, H., 1945. Nonparametric Tests against Trend. *Econometrica*, 13(3), pp. 245-259. <https://doi.org/10.2307/1907187>
15. Arzhanova, N.M. and Korshunova, N.N., 2019. Characteristics of Glaze-Ice and Rime Phenomena over the Russian Territory under Current Climate Change. *Trudy VNIIGMI-MCD*, 184, pp. 33-44 (in Russian).
16. Mastryukov, S.I., 2011. Evaluation of the Domestic and Foreign Methods Used to Calculate the Ice Formation on Vessels due to Spraying. *Navigation and Hydrography*, (31), pp. 81-86 (in Russian).
17. Overland, J.E., Pease, C.H., Preisendorfer, R.W. and Comiskey, A.L., 1986. Prediction of Vessel Icing. *Journal of Applied Meteorology and Climatology*, 25(12), pp. 1793-1806. [https://doi.org/10.1175/1520-0450\(1986\)025%3C1793:POVI%3E2.0.CO;2](https://doi.org/10.1175/1520-0450(1986)025%3C1793:POVI%3E2.0.CO;2)
18. Hersbach, H., Bell, B., Berrisford, P., Hirahara, S., Horányi, A., Muñoz-Sabater, J., Nicolas, J., Peubey, C., Radu, R. [et al.], 2020. The ERA5 Global Reanalysis. *Quarterly Journal of the Royal Meteorological Society*, 146(730), pp. 1999-2049. <https://doi.org/10.1002/qj.3803>

19. Groisman, P., Bulygina, O., Yin, X., Vose, R., Gulev, S., Hanssen-Bauer, I. and Førland, E., 2016. Recent Changes in the Frequency of Freezing Precipitation in North America and Northern Eurasia. *Environmental Research Letters*, 11(4), 045007. <https://doi.org/10.1088/1748-9326/11/4/045007>

Submitted 16.04.2024; approved after review 17.06.2024;
accepted for publication 17.07.2024.

About the authors:

Anastasia I. Lavrenteva, Student, Lomonosov Moscow State University (1 Leninskie Gory, Moscow, 119991, Russian Federation), **ORCID ID: 0000-0002-2985-0063**, lavrentevaai@my.msu.ru

Igor I. Leonov, Chief Specialist, Rosseti R&D Center (22, Building 3, Kashirskoe Shosse, Moscow, 115201, Russian Federation), CSc. (Geogr.), **ORCID ID: 0009-0000-6747-8170**, **SPIN-code: 5038-0828**, ebornlev@gmail.com

Natalia N. Sokolikhina, Assistant Professor, Lomonosov Moscow State University (1 Leninskie Gory, Moscow, 119991, Russian Federation), CSc. (Geogr.), Associate Professor, **ORCID ID: 0000-0001-9373-609X**; **WOS Research ID: L-6159-2015**; **Scopus Author ID: 6507391878**, natalia.sokolikhina@gmail.com

Contribution of the co-authors:

Anastasia I. Lavrenteva – literature review on the research problem; meteorological data collection; construction of tables, graphs, diagrams; analysis of research results; preparation of paper text

Igor I. Leonov – formulation of the study goals and objectives; development of research method; performing calculations; analysis and synthesis of research results; construction of tables, graphs, diagrams; preparation of paper text

Natalia N. Sokolikhina – research initiation; statistical data analysis; formulation of conclusions; discussion of paper materials; revision of paper text

*The authors have read and approved the final manuscript.
The authors declare that they have no conflict of interest.*

Distribution and Composition of Hydrocarbons in the Bottom Sediments of Kamyshovaya Bay (Black Sea)

O. V. Soloveva ¹, E. A. Tikhonova ¹, K. I. Gurov ², ✉

¹ A. O. Kovalevsky Institute of Biology of the Southern Seas of RAS,
Sevastopol, Russian Federation

² Marine Hydrophysical Institute of RAS, Sevastopol, Russian Federation
✉ gurovki@gmail.com

Abstract

Purpose. The purpose of the study is to identify the features of spatial and vertical distribution of hydrocarbons in bottom sediments of the coastal area under constant anthropogenic load, and to assess the likely sources of their inlet into the marine environment (using Kamyshovaya Bay as an example).

Methods and Results. The surface layer of bottom sediments (nine stations) and the sediment column were sampled in July 2021 as a part of long-term monitoring of the Sevastopol bays jointly performed by FRC IBSS and FRC MHI. The features of spatial distribution of hydrocarbons, alkanes and some geochemical markers in the surface layer (0–5 cm) and the vertical profile of bottom sediments are studied. The 30-year accumulation history of the considered substances in the bay bottom sediments is analyzed. The concentration of hydrocarbons in the bottom sediments ranges from 27.6 to 98.5 mg/kg that allows us to classify these sediments as low-polluted. A layer-by-layer study of the hydrocarbon composition in the bay bottom sediments shows that in the course of 30 years the bottom sediments were not significantly polluted with hydrocarbons. The results of analyzing the alkane composition and the geochemical marker values make it possible to establish that, as well as in the surface layer, the predominant source of hydrocarbon inlet was allochthonous and autochthonous organic matter. The increased values of geochemical markers identifying oil pollution indicate the fact that the inlet of oil and oil products can be considered a secondary source of hydrocarbons.

Conclusions. Hydrocarbons in the bottom sediments are distributed unevenly over the Kamyshovaya Bay water area, namely in the central part of the bay, a zone of the increased pollution is formed. It can be a consequence of the processes taking place in the semi-enclosed bay, as well as conditioned by the type of bottom sediments. The results of studying the hydrocarbon composition of bottom sediments show that in the course of the past 30 years and up to the present, Kamyshovaya Bay has been under the anthropogenic load which fluctuated insignificantly due to the degree of economic activity of the port. At the same time, the level of pollution in the bay remains low.

Keywords: bottom sediments, hydrocarbons, n-alkanes, markers, Kamyshovaya Bay, Black Sea

Acknowledgements: The work was carried out within the framework of state assignments of IBSS on theme “Study of biogeochemical patterns of radioecological and chemoecological processes in the ecosystems of water bodies of the Sea of Azov–Black Sea Basin in comparison with other areas of the World Ocean and individual aquatic ecosystems of their drainage basins to ensure sustainable development in the southern seas of Russia” (No. 124030100127-7), and FSBSI FRC MHI on themes “Fundamental studies of the processes that determine fluxes of matter and energy in the marine environment and at its boundaries, the state and evolution of the physical and biogeochemical structure of marine systems in modern conditions” (FNNN-2024-0001) and “Monitoring of the carbonate system, CO₂ content and fluxes in the marine environment of the Black Sea and the Sea of Azov” (FNNN-2022-0002).

For citation: Soloveva, O.V., Tikhonova, E.A. and Gurov, K.I., 2024. Distribution and Composition of Hydrocarbons in the Bottom Sediments of Kamyshovaya Bay (Black Sea). *Physical Oceanography*, 31(5), pp. 626-646.

© 2024, O. V. Soloveva, E. A. Tikhonova, K. I. Gurov

© 2024, Physical Oceanography

626

ISSN 1573-160X PHYSICAL OCEANOGRAPHY VOL. 31 ISS. 5 (2024)



The content is available under Creative Commons Attribution-NonCommercial 4.0 International (CC BY-NC 4.0) License

Introduction

The Sevastopol region is home to over 30 bays, some of which have been developed into ports. Such port water areas are subject to constant anthropogenic impact. Kamyshovaya Bay is no exception [1]. The anthropogenic load on the Kamyshovaya Bay waters is attributable to a number of factors, including the port's operational status, the location of the *Yugtorsk* oil loading enterprise on the bay shores, the presence of treatment facilities, a cement plant and the most powerful boiler house in Crimea (255 MW) [1].

Organic substances of petroleum origin enter seawater not only during the course of marine transport operations, but also with storm and sewage waters, including as a result of the construction of capital construction projects [2, 3]. Additionally, according to previously conducted field observations (June 2012), the bay waters were slightly polluted with oil and petroleum products compared to other port water areas (Sevastopol Bay, Balaklavskaya Bay). The presence of petroleum hydrocarbons was observed at concentrations below the limit of quantitative determination via IR spectrometry in the water [1].

As proposed by the authors [4], the water purification process in Kamyshovaya Bay occurs as a result of the adsorption of organic substances by fine-grained material of bottom sediments. The previously obtained data indicate a slight decrease in the content of chloroform-extractable substances in bottom sediments since 2009. Furthermore, the concentration of petroleum hydrocarbons in the bottom sediments did not exceed 100 mg / 100 g until 2015, which corresponds to the natural content level of this class of substances [5].

However, in later works [6], the results presented by the authors indicate an increase in the organic matter content and the absence of significant permanent sources of its inflow. It is noted that the increase in the organic matter content against the background of decreasing anthropogenic load is explained by the influence of natural factors. The maintenance of such trends may lead to the replacement of suboxic conditions in the bottom sediments by anaerobic ones, with negative consequences for the entire bay area. The natural factors that influence the redistribution of organic matter, including hydrocarbons, in the water area include the following characteristics of the bay: its semi-enclosed nature, the indented coastline, the large number of piers and ship moorings, the uneven anthropogenic load, the presence of a protective jetty that prevents water exchange between the bay and the open sea, etc. In connection with the above, a constant monitoring of the bay water area state is required. Bottom sediments as a “depot” for pollutants are the most informative and indicative in terms of time.

The aim of the study is to identify the characteristics of spatial and vertical distribution of hydrocarbons in bottom sediments of coastal water area under

constant anthropogenic load and to assess the probable sources of their input into the marine environment (using Kamyshovaya Bay as an example).

Characteristics of the study area

Kamyshovaya Bay is located in the north of the Heracleian Peninsula. Like Streletsкая Bay, it extends deep into the land (Fig. 1). The length of the bay is 2.75 km, the width at the mouth is 1 km, the depth is 11–18 m; the width in the central part is 300–350 m, the depth is 7–12 m, the width at the top of the bay is 100–130 m, the depth is 6–7 m [7].

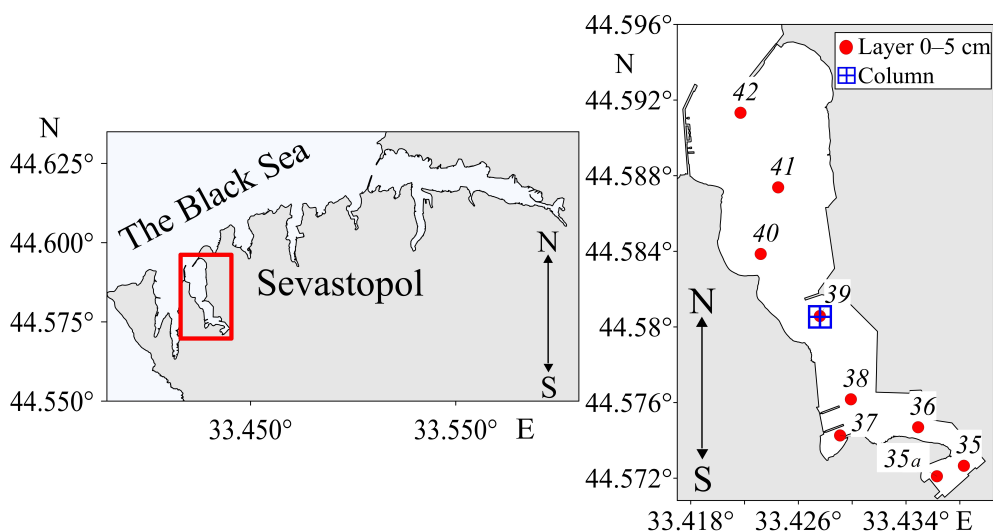


Fig. 1. Study area (left) and scheme of bottom sediment sampling stations in Kamyshovaya Bay, summer 2021 (right)

At the apex of the bay there is *Put' Ilyicha* (a fishery collective farm), *Atla* LLC (works on repair, modernisation and adjustment of technological equipment for processing of fish and krill raw materials on fishing vessels and food industry enterprises of the Azov–Black Sea basin) and a reloading port complex for construction aggregates, designed for unloading metal from ships for further processing in the plant. On the eastern side of the bay there is a fishing port, a factory for the production of mosquito nets, *Victoria* (a factory for the production of plastic windows), and on the western side – *Industriya Penoplasta* (a factory for the production of polymer materials), workshops for the repair of marine engines, *Porto Franco* (a residential complex).

According to [8], untreated wastewater from two permanent and one emergency outfall, as well as stormwater runoff, flows into Kamyshovaya Bay.

Material and research methods

Bottom sediment samples were collected in the summer of 2021 using a 0.038 m² Peterson grab sampler, then placed in sealed bags, labelled and delivered to the laboratory in refrigerated equipment.

To study the vertical distribution of hydrocarbons, bottom sediments were collected using a hand sampler with a plexiglass tube and a vacuum seal. In the laboratory, the soil column was divided into 2 cm layers, dried, ground in a mortar and a portion of the sample was sieved through 0.25 mm cell diameter sieves.

The data on the granulometric composition of the bottom sediments of Kamyshovaya Bay were taken from [4, 6].

Concentrations of hydrocarbons and n-alkanes were determined at the FRS IBSS Spectrometry and Chromatography Collective Use Centre. A detailed methodology for the determination of hydrocarbons and n-alkanes is presented in [9]. A Kristal 5000.2 gas chromatograph with a flame ionisation detector (FID) was used to analyse the alkanes from the hydrocarbon fraction. Hydrocarbons were separated on a TR-1MS capillary column of 30 m length, 0.32 mm diameter and a stationary phase thickness (100% dimethylpolysiloxane) of 0.25 µm (Thermo Scientific). For absolute calibration of the instrument, the standard ASTM D2887 Reference Gas Oil (*Supelco*, USA) was used as a hydrocarbon mixture. Chromatec Analysis 3.0 software, absolute calibration and percentage normalisation methods were used to process the results.

Nevertheless, it is not feasible to assess all hydrocarbons present in the bottom sediments via gas chromatography due to the transformation of organic matter and formation of more complex compounds. One illustrative example is that of cycloalkanes (naphthenes). A mixture of such organic substances is referred to as an unresolved complex mixture (*UCM*), a chromatographically inseparable background (i/b) or a ‘hump’. The calculation of *UCM* is achieved by subtracting the peak areas of chromatographically separated hydrocarbons from the total area of the chromatogram [9].

To identify the probable genesis of hydrocarbons, a number of diagnostic indices (markers) are employed. To differentiate between compounds of allochthonous and autochthonous origin, the ratio of terrigenous and autochthonous compounds (*TAR*, *TMD*, C_{31}/C_{19}), hydrocarbon average chain length (*ACL*), and the ratio of low-molecular and high-molecular homologues (*LWH/HWH*) are used. The application of individual markers enables the clarification of the biogenic nature of compounds, particularly the assessment of the contribution of herbaceous and woody vegetation to the formation of the allochthonous component of hydrocarbons entering bottom sediments. This is achieved through the use of ratios such as: C_{31}/C_{29} , P_{aq} . In order to differentiate between petroleum or biogenic hydrocarbons,

a number of ratios are employed, including the carbon preference index (*CPI*), in particular *CPI*₂ calculated for the high-molecular weight part, the ratio of the unresolved background to the total content of n-alkanes (*UCM/n-alkanes*), *ACL*, and *LWH/HWH* [10–15]. To identify petroleum origin of hydrocarbons, the isoprenoid coefficient ($Ki = (Pr + Ph)/(n-C_{17} + C_{18})$) and the ratio of isoprenoid alkanes pristane and phytane (*Pr/Ph*) are also frequently applied [16, 17].

In this study we assessed the probable origin of hydrocarbons by analysing the values of the following markers: *Pr/Ph*, *Ki*, *UCM/n-alkanes*, *LWH/HWH*, *P_{aq}*, *TAR*, *ACL*, *TMD*, *C₃₁/C₁₉*, *CPI*₂, *C₃₁/C₂₉* [10–17]. These indices were calculated using the formulas [10–17], as presented in Table 1.

Table 1

Diagnostic molecular ratios and their typical values

Diagnostic index (calculation formula) [10–17]	Value	Decoding the result
1	2	3
<i>UCM/n-alkanes</i>	> 10 < 10	Chronic pollution of bottom sediments Fresh inflow of oil
$LWH/HWH = \sum(C_{11}-C_{21})/\sum(C_{22}-C_{35})$	> 1 < 1	Oil origin Terrigenous origin, higher vegetation
$CPI_2 = (1/2) \{ (C_{25}+C_{27}+C_{29}+C_{31}+C_{33}+C_{35}) / (C_{24}+C_{26}+C_{28}+C_{30}+C_{32}+C_{34}) + (C_{25}+C_{27}+C_{29}+C_{31}+C_{33}+C_{35}) / (C_{26}+C_{28}+C_{30}+C_{32}+C_{34}) \}$	~ 1 < 1 > 1	Large share of hydrocarbons of oil origin Predominantly biogenic origin Biogenic influence on hydrocarbon composition of terrigenous organic matter
$Ki = (Pr + Ph)/(n-C_{17} + C_{18})$	$0.8 \leq Ki \leq 1.5$ $0.3 \leq Ki \leq 0.8$ $Ki \leq 0.3$	Presence of medium degraded oil Presence of slightly degraded oil Presence of fresh oil
<i>Pr / Ph</i>	< 1 0.1	Presence of oil in bottom sediments Traces of terrigenous degraded vegetation
$P_{aq} = (C_{23}+C_{25})/(C_{23}+C_{25}+C_{29}+C_{31})$	$0.1 < P_{aq} < 0.4$ $0.4 < P_{aq} < 1$	Fresh macrophytes Aquatic macrophytes
$TAR = (C_{27}+C_{29}+C_{31})/(C_{15}+C_{17}+C_{19})$	High TAR	Predominance of terrigenous material
$ACL = [25C_{25}+27C_{27}+29C_{29}+31C_{31}+33C_{33}] / [C_{25}+C_{27}+C_{29}+C_{31}+C_{33}]$	Low ACL	Oil emissions
$TMD = (C_{25}+C_{27}+C_{29}+C_{31}+C_{33}) / (C_{15}+C_{17}+C_{19}+C_{21}+C_{23})$	< 0.5 $0.5 < TMD < 1$ > 1	Autochthonous origin Mixed origin Terrestrial vegetation
<i>C₃₁/C₁₉</i>	< 0.4 > 0.4	Autochthonous matter Allochthonous matter
<i>C₃₁/C₂₉</i>	< 0.4 > 0.4	Predominance of woody vegetation Predominance of herbaceous vegetation

The Statistica 12 software package was employed for the processing of statistical data. A cluster analysis of the bottom sediment layers collected in Kamyshovaya Bay (station 39) was conducted using a combination method based on data on the total hydrocarbon content, *UCM* value, and the composition features of n-alkanes.

Results and discussion

Content, composition and genesis of hydrocarbons in the surface layer of the Kamyshovaya Bay bottom sediments

The granulometric composition of the collected bottom sediments in Kamyshovaya Bay is heterogeneous [6]. In the apex (stations 35a, 35, 36) and central (stations 37, 38, 39) parts, the sediments were grey silts. At station 40, the sediments were shell rock with an admixture of sand. At the bay exit (stations 41, 42), the sediments were sand with shells and shell detritus. It was observed that the mean particle size of the sediments (1.5 mm) is approximately one order of magnitude larger than that observed in other bays of Sevastopol [6].

As a consequence, the spatial distribution of organic carbon content (C_{org}) in the surface layer of bottom sediments was also not uniform, with figures of 0.3–0.4% in gravel and sand deposits in the bay upper part, 2–2.2% in silt deposits in the central part of the bay, and 1.2–1.8% in the apex parts of the bay [6]. These figures were markedly lower than those observed in the nearby Streletsкая Bay, where the C_{org} content exhibited fluctuations within the range of 4.28 to 6.3% [9], as well as in other bays of Sevastopol [6]. The noted physico-chemical characteristics of the bottom sediments largely determined their sorption capacity in general and the features of hydrocarbon accumulation in them in particular.

The distribution of hydrocarbon content in the bottom sediments of Kamyshovaya Bay exhibits considerable variation across all sampling stations, with a notable unevenness in the distribution across the water area (Fig. 2). The highest values were recorded in the central region of the bay (station 38, 98.5 mg/kg), followed by the apex (station 35a, 64.5 mg/kg) and the lowest in the area closest to the bay exit (station 42, 27.6 mg/kg).

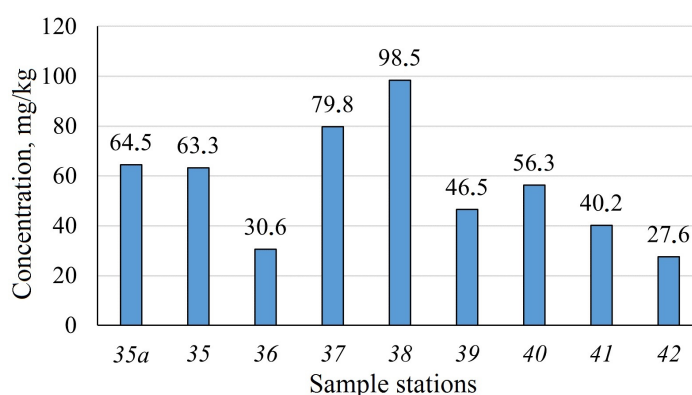


Fig. 2. Concentrations of hydrocarbons in the bottom sediments of Kamyshovaya Bay

The concentrations of hydrocarbons identified in the various lithological types of bottom sediments were found to exceed background levels. At stations with silty bottom sediments, the concentrations of hydrocarbons were found to be 50 mg/kg, which is above the value typically observed in clean zones [18]. In the bay areas with a predominance of sand and shells, the concentrations of hydrocarbons (10 mg/kg) were also found to be higher than background levels [19]. Nevertheless, it can be assumed that such levels have an insignificant effect on the biota state. As indicated in the data presented in [19, 20], concentrations of up to 50 mg/kg do not result in a notable transformation of the benthic community.

The mean hydrocarbon concentration in the entire water area of Kamyshovaya Bay (nine stations) is 56.4 ± 23.2 mg/kg. For comparison, the hydrocarbon content in the nearby Streletskaya Bay fluctuated within the range of 328 to 2175 mg/kg, with an average value of 1159.8 ± 35.3 mg/kg [9].

The bay water area can be subdivided into three sections: the apex (stations 35a, 36), the central region (stations 37–39), and the bay exit (stations 40–42). The mean concentration of hydrocarbons in the apex section was found to be 53.3 mg/kg, which is comparable to the overall hydrocarbon concentration observed in the bay. The mean concentration of hydrocarbons in the central region was 74.9 mg/kg, while the concentration at the bay exit was 41.4 mg/kg. Therefore, the silt deposits of the central part of the bay exhibit the highest concentrations of hydrocarbons and C_{org} (Fig. 3, a).

The observation of the maximum concentrations of hydrocarbons in the central part of the bay, in conjunction with the granulometric composition of the bottom sediments, may be attributed to the geomorphological features of the water area and the circulating currents, which result in the accumulation of substances entering the marine environment in this particular part of the bay.

It should be noted that the presence of chromatographically unresolved background, indicative of the burial of transformed organic matter, was not observed in all chromatograms. The mean concentration of the unresolved mixture in areas where it was indicated was found to be (91.2 ± 36.4) mg/kg. The maximum value was observed at station 39, with a concentration of 172.3 mg/kg (Fig. 3, b). The absence of the ‘hump’ in the chromatograms from three stations at the bay exit (stations 40, 41, 42) is primarily attributable to the type of bottom sediments (shell rock and sand), which do not contribute to the accumulation of substances [6]. The relationship between the ‘hump’ value and the granulometric composition of the bottom sediments (the presence of finely dispersed fractions) is confirmed by the maximum linear positive correlation (0.86) between the *UCM* value and the proportion of the pelitic fraction.

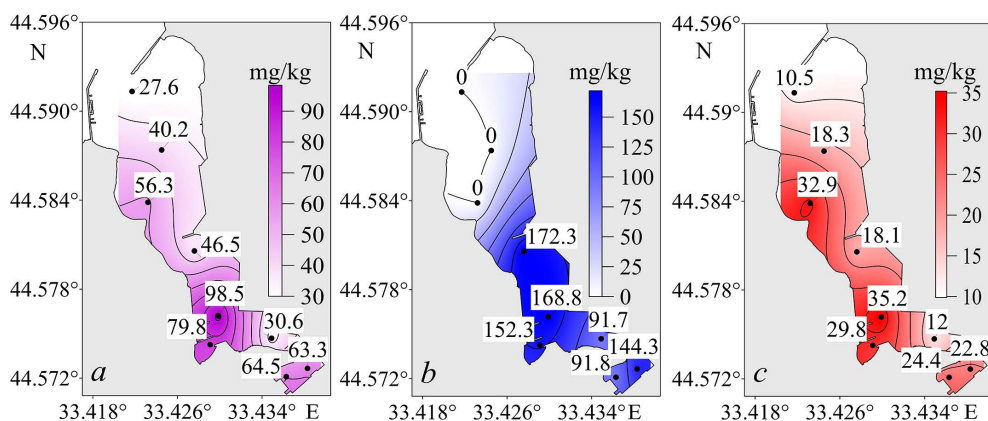


Fig. 3. Spatial distribution of hydrocarbons (a), UCM (b), and n-alkanes (c) in the bottom sediments surface layer of Kamyshevaya Bay

The background in the chromatograms from various recording stations exhibited differences in their outlines. At stations 35, 36, 37 and 38, the ‘hump’ had bimodal characteristics, with maxima observed in the low-molecular region, indicative of the burial of autochthonous material, and in the high-molecular region, which is typically associated with the burial of oil products [21]. At stations 35a and 39, the ‘hump’ was observed in the high-temperature region, which may indicate the predominant deposition of oil components and oil products (Fig. 4).

The mean concentration of n-alkanes was established at (22.7 ± 8.8) mg/kg. The lowest concentration (10.5 mg/kg) was observed at the point of exit from the bay (station 42) (Fig. 3, c). The spatial distribution of n-alkane concentrations exhibited a similar character to that observed in the distribution of hydrocarbons (Fig. 3, a).

The range of C_{15} – C_{34} n-alkanes was identified in all samples obtained from the bottom sediments of the bay (Fig. 5). Isoprenoid alkanes, pristane and phytane, were identified in all samples. The distributions of n-alkanes at stations in the apex, central parts and in the bay exit (Fig. 5) were found to have a similar character.

The principal characteristics of the data set were bimodality (Figs. 4, 5), which suggests two distinct hydrocarbon sources. The presence of odd phytoplankton peaks was observed to reach its highest concentration within the range of C_{17} – C_{21} [21]. The second group of peaks refers to compounds in the range of C_{27} , C_{29} and C_{31} . The odd homologues in this range are genetically related to allochthonous organic matter [22] and are typical for coastal areas [10].

The distribution of n-alkanes at the stations situated in the outer part of the bay had distinctive characteristics. In the low-molecular weight region, the predominant peaks were not of a phytoplanktonic nature, but bacterial in origin (C_{20} , C_{22}) [11]. The bottom sediments at station 40 exhibited a notably elevated concentration of these homologues (57%).

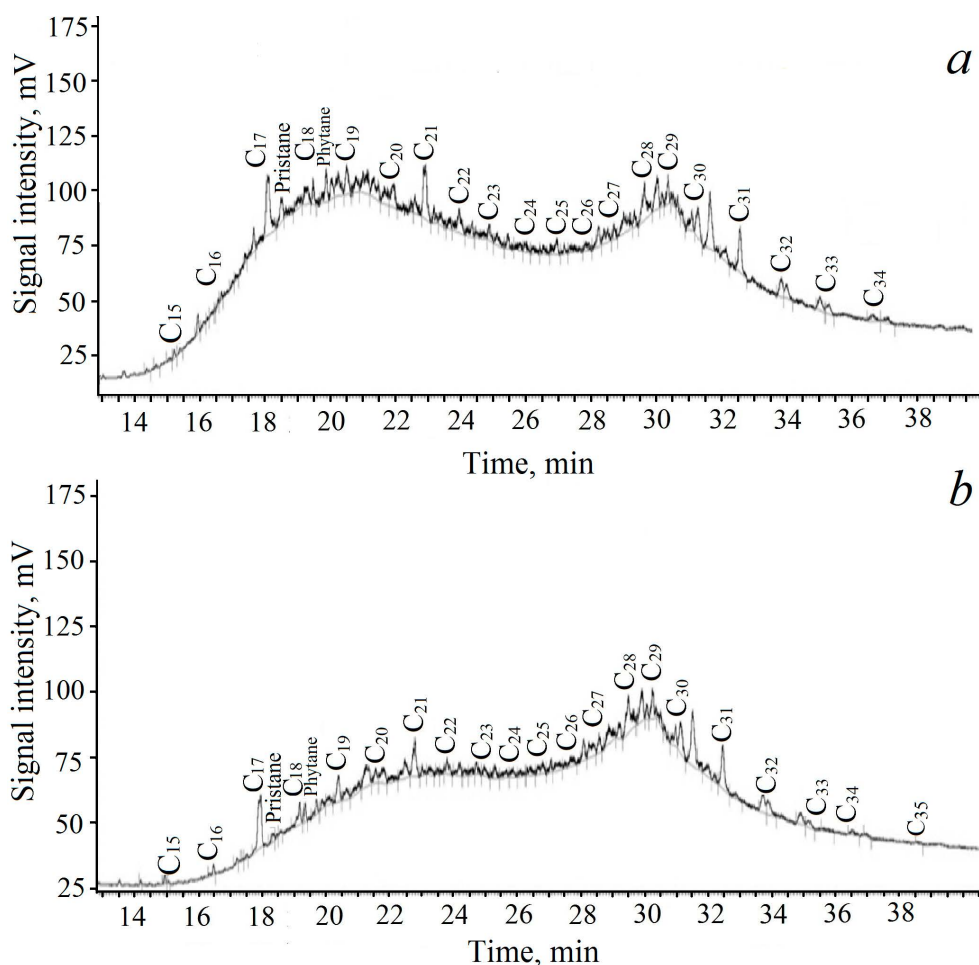


Fig. 4. Typical chromatograms of bottom sediments in Kamyshevaya Bay: *a* – station 38 (distribution due to a few sources); *b* – station 35a

It can therefore be concluded that the intensive development of phytoplankton in the inner part of the water area is reflected in the composition of the bottom sediments. Furthermore, this process has a much lower significance for the formation of the hydrocarbon composition of the bottom sediments in the outer part of the bay, where intensive bacterial transformation of organic matter is noted.

In order to establish the source of hydrocarbons in surface bottom sediments, diagnostic indices were calculated and their values at the sampling stations are presented in Table 2.

CPI_2 values at stations 35, 37, 38, 39 were close to 1, which may be an indication of relatively fresh oil pollution [12]. At the remaining stations 35a, 36, 40, 41, 42, the marker values were higher than 1, which may be an indicator of the prevalence of biogenic matter (Table 2).

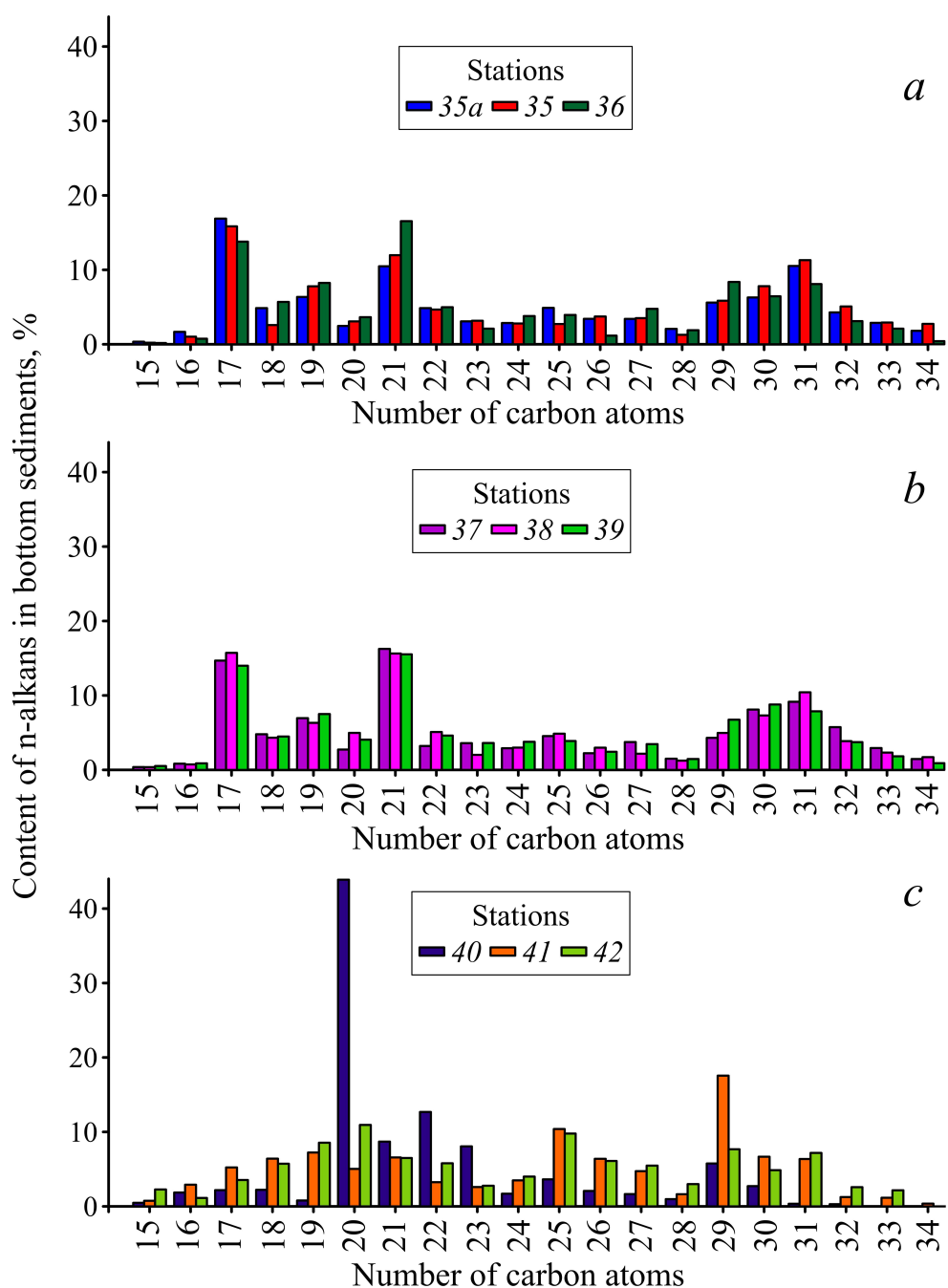


Fig. 5. Composition of n-alkanes in the surface layer of bottom sediments in Kamyshovaya Bay by stations: a – 35a, 35, 36; b – 37, 38, 39; c – 40, 41, 42

The ratio of pristane to phytane, which is a marker of oil presence, indicated the probable presence of oil pollution ($Pr/Ph < 1$) in almost all the samples collected.

Table 2

Index values in the surface layer of bottom sediments

Indices	Stations								
	35a	35	36	37	38	39	40	41	42
<i>Pr/Ph</i>	0.71	0.92	0.47	0.08	0.69	0.22	0.33	0.41	0.21
<i>Ki</i>	0.24	0.37	0.30	0.19	0.30	0.22	0.80	0.52	0.71
<i>UCM/n-alkane</i>	3.77	6.32	7.62	5.11	4.79	9.52	0.00	0.00	0.00
<i>LWH/HWH</i>	0.91	0.89	1.16	0.99	1.13	1.06	2.68	0.60	0.80
<i>P_{aq}</i>	0.33	0.26	0.27	0.38	0.31	0.34	0.66	0.35	0.46
<i>TAR</i>	0.83	0.87	0.96	0.78	0.78	0.82	2.25	2.17	1.41
<i>ACL</i>	29.35	29.52	29.09	29.18	29.43	29.36	27.5	28.16	28.35
<i>TMD</i>	0.73	0.67	0.67	0.59	0.62	0.58	0.56	1.80	1.36
<i>C₃₁/C₁₉</i>	1.66	1.45	0.98	1.32	1.65	1.05	0.44	0.88	0.84
<i>CPI₂</i>	1.49	1.20	1.86	1.21	1.34	1.25	1.68	2.25	1.76
<i>C₃₁/C₂₉</i>	1.88	1.93	0.97	2.13	2.10	1.17	0.06	0.36	0.94

The isoprenoid coefficient, which enables the estimation of the extent of oil biodegradation [17], fluctuated within the range typical of fresh and slightly degraded oil pollution. The highest values of this index, which is characteristic of slightly degraded oil (0.52–0.8), were recorded at stations 40–42 (Table 2).

The *UCM/n-alkanes* ratio did not exceed 9.52, which is a value that indicates modern influx of oil products [23]. The analysis of this marker is in accordance with the results obtained from the isoprenoid coefficient.

A study of oil pollution markers allows us to conclude that the current influx of oil and oil products into the bottom sediments, as well as their biotransformation there, is a plausible assumption.

The *LWH/HWH* index at all stations, with the exception of station 40 (situated in the central region of the bay), demonstrates a relatively equal ratio of light and heavy homologues, indicating an equal contribution of autochthonous and allochthonous hydrocarbon sources [24], which is typical for coastal water areas.

The *P_{aq}* index at all stations, with the exception of stations 40 and 42, demonstrated a range of 0.26 to 0.38, which suggests that the organic matter present in the bay bottom sediments has a predominantly terrigenous origin [25]. It is possible that aquatic vegetation makes a significant contribution at stations 40 and 42.

The *TAR* index at stations 35a–39 is less than one, indicating the input of autochthonous material into the bottom sediments. In contrast, at the other stations the terrigenous material input is dominant. The calculated *ACL* index indicates a combination of herbaceous and woody vegetation contributions. The *TMD* index

at stations 35a–40 exhibited a range of 0.56 to 0.73, indicative of a mixed contribution from terrestrial and marine sources. At stations 41 and 42, the contribution of terrestrial vegetation is dominant, indicating a lower content of odd phytoplanktonic n-alkanes in the bottom sediments of these stations. The C_{31}/C_{19} ratio at all stations except station 40 has a high value (0.84–1.66), which reflects the predominant contribution of terrestrial vegetation.

The C_{31}/C_{29} ratio at stations 35a–39, 42 indicates that herbaceous vegetation is the dominant component, whereas at stations 40, 41, woody vegetation plays a more significant role.

The distribution of the principal markers at the sampling stations is illustrated in Fig. 6. The indices at stations 35a, 35 and 36 are similar in value, which may indicate uniform conditions for the accumulation and transformation of hydrocarbons in the bottom sediments of the specified stations. Furthermore, the indices at stations 37, 38 and 39 are also comparable on the graph. The indices at station 40 differ from those at the other stations, which is most likely due to the composition of the bottom sediments (the sampling station is located on the limestone slope of the bay). The distribution of markers at stations 41 and 42 is distinctive due to their distance from the bay upper part and a more intense water exchange observed in this area.

The results of the studies indicated that the concentration of hydrocarbons in the bay bottom sediments demonstrated fluctuations within the range of 27.6–98.5 mg/kg. In regard to the types of bottom sediments (silts, sands, shell rock) with varying degrees of pollution, these indicators align with those observed in relatively healthy water areas experiencing anthropogenic load. The analysis of alkane chromatograms with predominant peaks corresponding to natural sources of hydrocarbons and individual geochemical markers, the values of which correspond to the predominance of biogenic organic matter, allows us to conclude that the main sources of these hydrocarbons in the bottom sediments are natural processes. At the same time, the evidence (CPI_2 values at specific stations are close to 1, $Pr/Ph < 1$, elevated Ki values, UCM/n -alkanes < 10) indicated a recent flow of oil and oil products.

Long-term changes in the content, composition and genesis of hydrocarbons in the Kamyshovaya Bay bottom sediments

In order to analyse the characteristics of hydrocarbon accumulation by bottom sediments and the temporal variability of their input into the bay water area, a column of bottom sediments was sampled and divided into 2 cm layers. The studies were conducted at one of the stations (station 39) situated in the central region of the bay. The sampled column had a height of 14 cm.

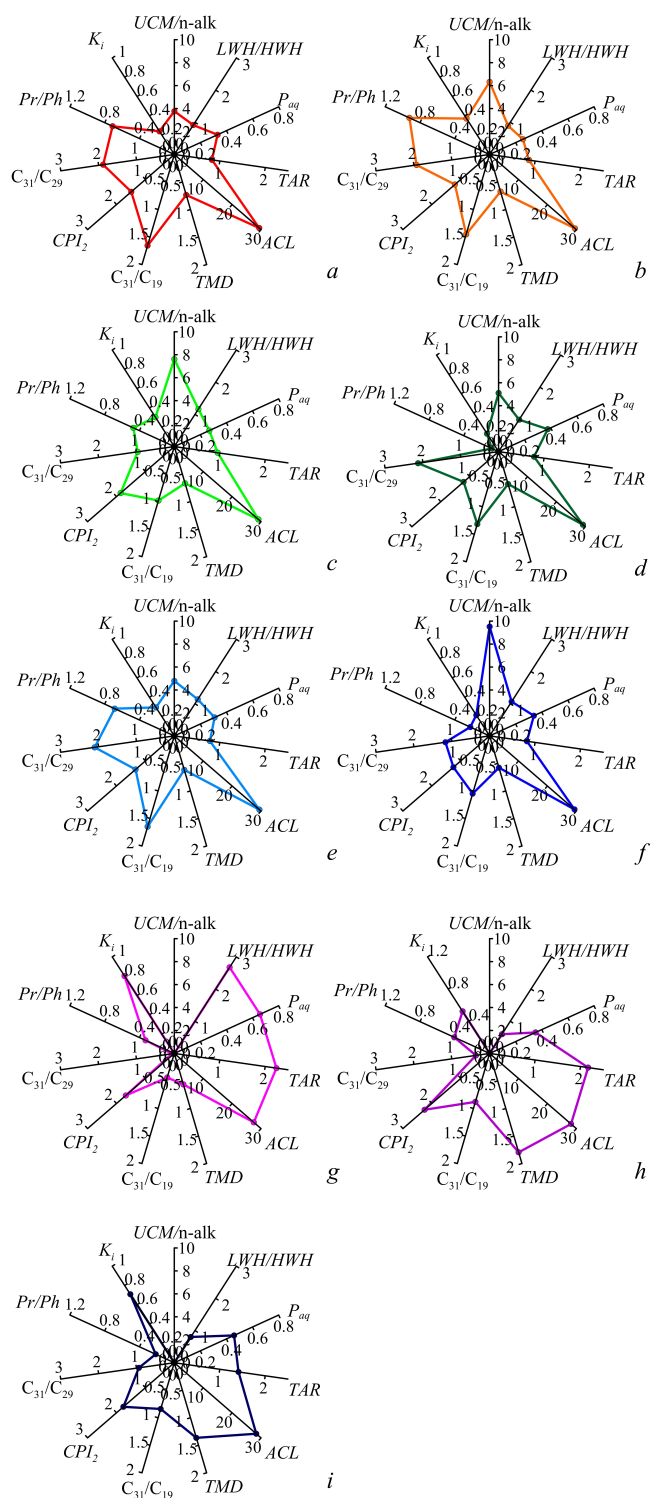


Fig. 6. Ratio of the main markers in bottom sediments of Kamyshevaya Bay by station: a – 35a; b – 35; c – 36; d – 37; e – 38; f – 39; g – 40; h – 41; i – 42

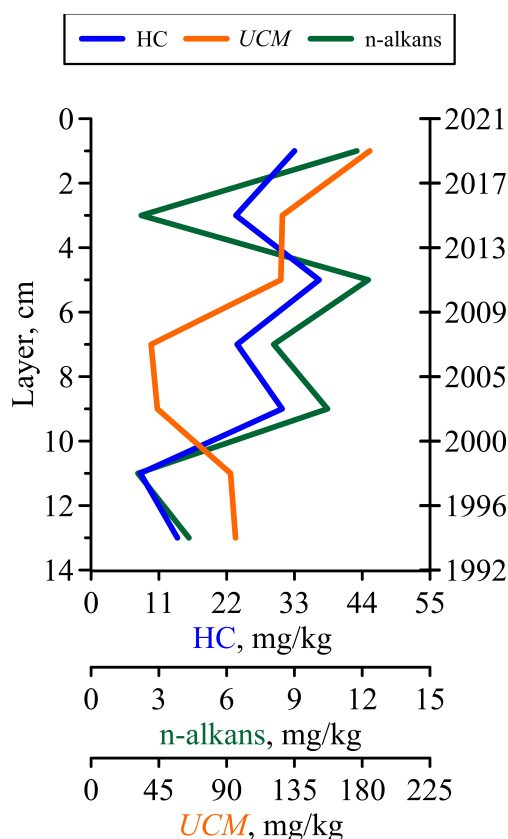


Fig. 7. Distribution of hydrocarbons, *UCM* and *n*-alkanes in the bottom sediments column of Kamyshovaya Bay (station 39)

A relatively uniform distribution of the studied substances was observed across the horizons within the depth range of 0 to 10 cm, with the hydrocarbon content exhibiting fluctuations between 24.5 and 33.0 mg/kg (Fig. 7). In the deeper layers (10–12 and 12–14 cm), a decrease in the hydrocarbon concentration was observed, reaching 8.0–14.0 mg/kg. The concentration of *n*-alkanes in the columnar layers had a range of 2.5–11.4 mg/kg. The proportion of *n*-alkanes from hydrocarbons remained relatively consistent, with an average value of 31% and a range of 29 to 36%.

A chromatographically unresolved background was identified in all the layers under investigation. A gradual decline in the ‘hump’ was observed from the 0–2 cm layer (185 mg/kg) to the 6–8 cm layer (39.9 mg/kg), followed

by an increase in the *UCM* concentration towards the 12–14 cm layer (95.9 mg/kg). The change in hydrocarbon, n-alkane and *UCM* content with depth was found to be uneven. The maximum concentration of hydrocarbons (37 mg/kg) was observed in the 4–6 cm layer, while the highest *UCM* values were in the 0–6 cm layer (125–185 mg/kg). This may be a consequence of changes in the intensity and nature of pollution, with the accumulation of an unresolved mixture in the bottom sediments serving as an indicator.

The bottom sediments in the vertical section of the bay are slightly polluted and correspond to the first pollution class [20]. Taking into account the silty nature of the bottom sediments, they can be considered conditionally clean (up to 50 mg/kg). The literature also indicates that during studies of the bottom sediments of Kamyshovaya Bay in the 20th century, slightly elevated levels of petroleum hydrocarbons were recorded, which characterises the water body as slightly polluted [13]. For comparison, in the column of bottom sediments collected in Streletskaya Bay (Sevastopol coast), the concentrations of hydrocarbons were two orders of magnitude higher (1488–4558 mg/kg) [9].

According to the results of [4], the sedimentation rate in the bay, derived from the $^{210}\text{Pb}_{\text{exc}}$ vertical distribution data, was 0.47 cm/year. At this rate, the 14 cm layer sampled represents 30 years, each 2 cm layer approximately 4.25 years, which allows us to estimate the history of hydrocarbon accumulation.

The maximum concentration of hydrocarbons in the bottom sediments (in terms of sedimentation rate) was observed in 2017–2021 (0–2 cm horizon) and in 2009–2013 (4–6 cm horizon). In 2013–2017 (2–4 cm horizon) the concentration of hydrocarbons was lower compared to 2017–2021 and 2009–2013. The minimum concentrations of hydrocarbons in the periods 1992–2000 may be associated with the economic downturn in Sevastopol and, as a result, a decrease in the turnover of the port: in 1993 it decreased to 349 thousand tons/year. A similar trend was observed in the water area of Streletskaya Bay [9], indicating a reduced anthropogenic load on the coast during this period.

The increase in hydrocarbon concentrations after 2000 may be due to the increased impact on the water surface caused by the construction of new housing estates and the use of the bay as an oil and fishing port. At the same time, given the low levels of hydrocarbons, the observed variations may be largely natural.

In the vertical section, n-alkanes in the range C_{16} – C_{34} were identified (Fig. 8), compounds C_{17} – C_{33} were present in all layers studied. Isoprenoid alkanes, pristane and phytane, were identified in 100% of the samples. The distribution of n-alkanes was bimodal in all the horizons studied. Autochthonous C_{19} (2–11%) and C_{21} (5–20%) predominated. C_{17} (up to 2%), which is probably more bioavailable and transformed, played a minor role. The bacterial peak C_{22} (8–11%) was also present in significant amounts. The most pronounced allochthonous peak was C_{31} (12–16%), which links the hydrocarbons in the bottom sediments to the herbaceous vegetation corresponding to the steppe coast of this region.

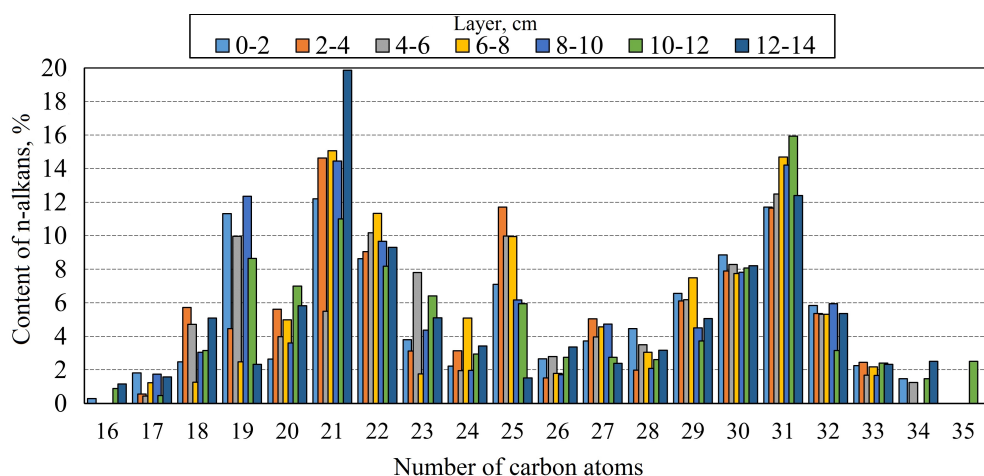


Fig. 8. Content of n-alkanes in the bottom sediments column of Kamyshovaya Bay (station 39)

To determine the genesis of hydrocarbons in bottom sediments, diagnostic indices were calculated (Table 3).

Table 3

Values of n-alkane genesis markers in the vertical profile of bottom sediments in Kamyshovaya Bay (station 39)

Markers	Layer, cm						
	0–2	2–4	4–6	6–8	8–10	10–12	12–14
<i>Pr/Ph</i>	1.40	0.16	0.28	0.25	1.01	2.37	1.19
<i>Ki</i>	1.50	0.70	1.20	1.30	1.60	1.60	1.20
<i>CPI₂</i>	1.29	2.03	1.55	1.93	1.69	1.71	0.98
<i>UCM/n-alkane</i>	18.03	15.04	11.02	5.49	4.54	37.22	23.54
<i>LWH/HWH</i>	0.80	0.83	0.66	0.74	1.09	0.88	1.06
<i>P_{aq}</i>	0.37	0.45	0.49	0.35	0.36	0.39	0.28
<i>TAR</i>	1.67	4.54	2.17	7.21	1.66	2.46	5.07
<i>ACL</i>	30.00	29.90	30.0	30.0	30.00	30.90	30.30
<i>TMD</i>	1.10	1.60	1.40	1.90	1.00	1.30	0.80
<i>C₃₁/C₁₉</i>	1.00	2.60	1.30	5.90	1.20	1.80	5.30
<i>C₃₁/C₂₉</i>	1.30	1.90	2.00	2.00	3.20	4.30	2.40

In the thickness of the bottom sediments, except for layers 2–4, 4–6, 6–8 cm, a predominance of pristane (mainly biogenic) over phytane was observed. In other layers this ratio indicates the presence of oil pollution. The isoprenoid coefficient Ki in the 2–4 cm layer corresponded to the presence of slightly degraded oil products, in the other layers its values indicated presence of oil and oil products of medium degradation [17]. Thus, the isoprenoid n-alkane composition in the vertical section of the bay bottom sediments corresponds to the periodic uptake and further degradation of petroleum hydrocarbons.

CPI_2 values, which ranged from 0.98 to 2.03 in the high molecular weight range (average 1.60), may indicate both transformed oil contamination and the biogenic nature of OM [14, 26, 27].

The ratio UCM/n -alkanes varied from 4.54 to 37.22. The minimum ratios were noted at the 6–8 and 8–10 cm layers from 2001 to 2009. The maximum value of this ratio (37.22) was observed at the 10–12 cm layer corresponding to the period 1996–2000. The LWH/HWH index values were 0.66–1.09 with an average of 0.87 indicating the influx of terrigenous material [24].

The P_{aq} index varied from 0.28 to 0.49, which corresponds to the predominant accumulation of allochthonous compounds. The obtained TAR index values varied from 1.66 to 7.21, also indicating the accumulation of allochthonous matter in the bottom sediments [25].

The average hydrocarbon chain length (ACL) varied within a small range of 29.90–30.90, which characterises the stability of the organic matter accumulation and transformation processes in the water basin.

The TMD index with values of 1.00–1.90 and the C_{31}/C_{19} n-alkane ratio indicate the predominant burial of high molecular weight hydrocarbons in the bottom sediments.

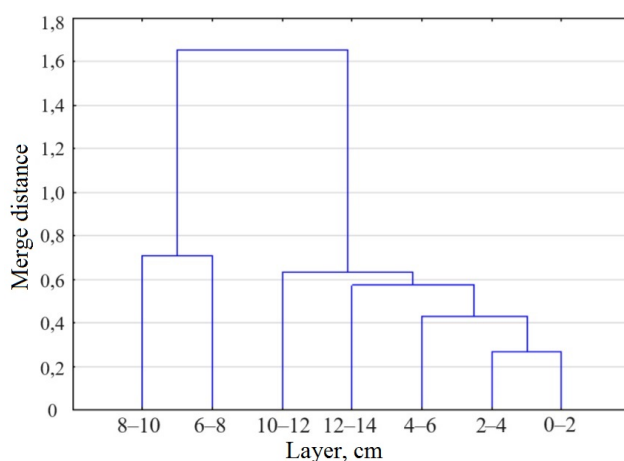


Fig. 9. Results of cluster analysis of the bottom sediments layers sampled in Kamyshevaya Bay (station 39)

In order to identify periods with different characteristics of hydrocarbon background of the bottom sediments of Kamyshevaya Bay, clustering of the bottom

sediment layers (Fig. 9) was performed according to the total hydrocarbon content, *UCM* value and n-alkane concentration.

Over the 30-year period studied, layers corresponding to the period 2000–2009 were identified (6–8 and 8–10 cm), when the *UCM*/n-alkane ratio was lower. It can be assumed that during this period conditions for the inflow and accumulation of hydrocarbons changed. At the same time, the quality of the bottom sediments characterised the state of the bay as favourable in all periods studied.

It can be concluded that the hydrocarbon content in the bottom sediment layers of different depths fluctuated slightly and was within the range of 8.0–37.0 mg/kg, which corresponds to the indicators for clean water areas. At the same time, a chromatographically unresolved background was detected, indicating the burial of transformed organic compounds. Based on the analysis of alkane chromatograms and individual geochemical markers, the predominant source of hydrocarbons in the bottom sediments over the last 30 years has been the natural flux of organic matter. Traces of transformed oil are also present.

Conclusion

Despite its small size, Kamyshevaya Bay has a clear zoning, which, as shown in the literature, is associated with different conditions of organic matter accumulation in bottom sediments. As a consequence, hydrocarbons in the bottom sediments of Kamyshevaya Bay are distributed unevenly throughout the water area, and a zone of increased pollution is formed in the central part of the bay. The recorded distribution of hydrocarbon content in the bottom sediments of the bay is a consequence of the processes occurring in the semi-enclosed bay and is also determined by the heterogeneity of the granulometric composition of bottom sediments, which contributes to the accumulation of substances of different nature to a different extent. The concentration of hydrocarbons in bottom sediments ranged from 27.6 to 98.5 mg/kg, which allows us to classify them as slightly contaminated. Judging by the character of chromatograms with predominant peaks corresponding to natural sources of hydrocarbons and some geochemical markers (*LWH/HWH*, *P_{aq}*, *TAR*, *ACL*, *TMD*, *C₃₁/C₁₉*, *C₃₁/C₂₉*), the values of which correspond to the predominance of biogenic organic matter, the main source of hydrocarbons in bottom sediments is the input of autochthonous and allochthonous compounds. Markers (*CPI₂* values at some stations are close to 1, *Pr/Ph* < 1, increased *Ki* values, *UCM*/n-alkanes < 10) of recent oil and oil product input were recorded.

A layer-by-layer study of the hydrocarbon composition of the bay bottom sediments revealed that they had not been significantly contaminated by hydrocarbons over the past 30 years. The predominant source of hydrocarbons, based on analysis of alkane composition and geochemical marker values, and in the surface layer, was allochthonous and autochthonous organic matter. Judging

from the values of geochemical markers diagnosing oil contamination, the influx of oil and oil products can be considered as a secondary source of hydrocarbons.

Thus, both over the past 30 years and at present, Kamyshovaya Bay has been subject to anthropogenic pollution, with minor fluctuations due to the level of economic activity in the port, while the level of pollution in the bay has remained low.

REFERENCES

1. Mezenceva, I.V. and Malchenko, Y.A., 2015. Integrated Approach in the Organization of Marine Pollution Monitoring in Coastal Water Areas of Sevastopol. *Proceedings of N.N. Zubov State Oceanographic Institute*. Moscow: GOIN, pp. 326-339 (in Russian).
2. Kuftarkova, E.A., Rodionova, N.Yu., Gubanov, V.I. and Bobko, N.I., 2008. Hydrochemical Characteristics of Several Bays of Sevastopol Coast. In: YugNIRO, 2008. *YugNIRO Proceedings*. Kerch: YugNIRO. Vol. 46, pp. 110-117 (in Russian).
3. Mironov, O.G. and Alyomov, S.V., eds., 2018. *Sanitary and Biological Studies of the South-Western Crimea Coastal Waters at the Beginning of XXI Century*. Simferopol: PP "ARIAL", 276 p. <https://doi.org/10.21072/978-5-907118-89-8> (in Russian).
4. Kremenchutskii, D.A. and Gurova, Yu.S., 2023. Factors Forming the Spatial Distribution of Natural and Man-Made Radionuclides in the Bottom Sediments of the Kamyshovaya Bay, Sevastopol. *Physical Oceanography*, 30(5), pp. 652-665.
5. Soloveva, O.V. and Tikhonova, E.A., 2018. The Organic Matter Content Dynamics in the Sea Bottom Sediments of the Sevastopol Harbor Water Area. *Scientific Notes of V.I. Vernadsky Crimean Federal University. Biology. Chemistry*, 4(70), pp. 196-206 (in Russian).
6. Kurinnaya, Yu.S., Gurov, K.I., Zabegaev, I.A. and Orekhova, N.A., 2022. Redox Conditions and Characteristics of Bottom Sediments in the Bays of the Sevastopol Region. *Ecological Safety of Coastal and Shelf Zones of Sea*, (1), pp. 42-54. <https://doi.org/10.22449/2413-5577-2022-1-42-54>
7. Petrenko, O.A., ed., 2008. *Main Results of Complex Research in the Azov-Black Sea Basin and the World Ocean*. Kerch: YugNIRO, 195 p. (in Russian).
8. Ovsyany, E.J., Romanov, A.S., Min'kovskaya, R.Ya., Krasnovid, I.I., Ozyumenko, B.A. and Zymbal, I.M., 2001. Basic Polluting Sources of Sea near Sevastopol. In: MHI, 2001. *Ecological Safety of Coastal and Shelf Zones and Comprehensive Use of Shelf Resources*. Sevastopol: ECOSI-Gidrofizika. Iss. 2, pp. 138-152 (in Russian).
9. Tikhonova, E.A., Gurov, K.I. and Soloveva, O.V., 2023. Features of Distribution of Hydrocarbons in Bottom Sediments of the Streletskaya Bay (Black Sea). *Physical Oceanography*, 30(5), pp. 632-651.
10. Osadchaya, T.S., 2013. Oil Hydrocarbons in Bottom Sediments of Sevastopol Coastal Areas (The Black Sea). *Scientific World*, 43(3), pp. 30-36 (in Russian).
11. Venkatesan, M.I. and Kaplan, I.R., 1982. Distribution and Transport of Hydrocarbons in Surface Sediments of the Alaskan Outer Continental Shelf. *Geochimica et Cosmochimica Acta*, 46(11), pp. 2135-2149. [https://doi.org/10.1016/0016-7037\(82\)90190-9](https://doi.org/10.1016/0016-7037(82)90190-9)
12. Glyaznetsova, Yu.S. and Nemirovskaya, I.A., 2020. Features of Bitumoid Distribution in Bottom Sediments of the Barents Sea. *Oceanology*, 60(6), pp. 831-839. <https://doi.org/10.1134/S0001437020050057>
13. Mironov, O.G., Kirjukhina, L.N. and Alyomov, S.V., 2003. *Sanitary-Biological Aspects of the Sevastopol Bays Ecology in XX Century*. Sevastopol: ECOSI-Gidrofizika, 185 p. (in Russian).

14. Kashirtsev, V.A., 2003. *Organic Geochemistry of Naphthides of the Eastern Siberian Platform*. Yakutsk: YAF SO RAN, 160 p. (in Russian).
15. Soloveva, O.V., Tikhonova, E.A., Mironov, O.A. and Alyomova, T.E., 2021. Origin of Hydrocarbons in the Water of the River–Sea Mixing Zone: A Case Study from the Chernaya River – The Sevastopol Bay, Black Sea. *Regional Studies in Marine Science*, 45, 101870. <https://doi.org/10.1016/j.rsma.2021.101870>
16. Peters, K.E. and Moldowan, J.M., 1993. *The Biomarker Guide: Interpreting Molecular Fossils in Petroleum and Ancient Sediments*. New Jersey: Prentice Hall, 363 p.
17. Peters, K.E., Walters, C.C. and Moldowan, J.M., 2005. *The Biomarker Guide. Volume 1: Biomarkers and Isotopes in the Environment and Human History*. Cambridge, New York, Melbourne: Cambridge University Press, 1132 p. <https://doi.org/10.1017/CBO9780511524868>
18. Bouloubassi, I. and Saliot, A., 1993. Investigation of Anthropogenic and Natural Organic Inputs in Estuarine Sediments Using Hydrocarbon Markers (NAH, LAB, PAH). *Oceanologica Acta*, 16(2), pp. 145-161.
19. Tolosa, I., Mora, S., Sheikholeslami, M.R., Villeneuve, J.P., Bartocci, J. and Cattini, C., 2004. Aliphatic and Aromatic Hydrocarbons in Coastal Caspian Sea Sediments. *Marine Pollution Bulletin*, 48(1-2), pp. 44-60. [https://doi.org/10.1016/S0025-326X\(03\)00255-8](https://doi.org/10.1016/S0025-326X(03)00255-8)
20. Mironov, O.G., Milovidova, N.Yu. and Kiryukhina, L.N., 1986. On Maximum Permissible Concentrations of Petroleum Products in Bottom Sediments of the Black Sea Littoral. *Gidrobiologicheskii Zhurnal*, 22(6), pp. 76-78 (in Russian).
21. Nemirovskaya, I.A., 2013. *Oil in the Ocean (Pollution and Natural Flow)*. Moscow: Scientific World, 432 p. (in Russian).
22. Cranwell, P.A., 1973. Chain-Length Distribution of *n*-Alkanes from Lake Sediments in Relation to Post-Glacial Environmental Change. *Freshwater Biology*, 3(3), pp. 259-265. <https://doi.org/10.1111/j.1365-2427.1973.tb00921.x>
23. Gao, Y., Han, Y., Xia, J., Tan, J., Wang, Y.-P. and Wang, S., 2021. Composition and Distribution of Aliphatic Hydrocarbon Compounds and Biomarkers in Seafloor Sediments from Offshore of the Leizhou Peninsula (South China). *ACS Omega*, 6(50), pp. 34286-34293. <https://doi.org/10.1021/acsomega.1c03529>
24. Wang, X.-C., Sun, S., Ma, H.-Q. and Liu, Y., 2006. Sources and Distribution of Aliphatic and Polyaromatic Hydrocarbons in Sediments of Jiaozhou Bay, Qingdao (China). *Marine Pollution Bulletin*, 52(2), pp. 129-138. <https://doi.org/10.1016/j.marpolbul.2005.08.010>
25. Ficken, K.J., Li, B., Swain, D.L. and Eglinton, G., 2000. An *n*-Alkane Proxy for the Sedimentary Input of Submerged/Floating Freshwater Aquatic Macrophytes. *Organic Geochemistry*, 31(7-8), pp. 745-749. [https://doi.org/10.1016/S0146-6380\(00\)00081-4](https://doi.org/10.1016/S0146-6380(00)00081-4)
26. Nemirovskaya, I.A., 2020. Hydrocarbons in the Water and Bottom Sediments of the Barents Sea during Ice Cover Variability. *Geochemistry International*, 58(7), pp. 822-834. <https://doi.org/10.1134/S0016702920070071>
27. Yunker, M.B., Macdonald, R.W., Ross, P.S., Johannessen, S.C. and Dangerfield, N., 2015. Alkane and PAH Provenance and Potential Bioavailability in Coastal Marine Sediments Subject to a Gradient of Anthropogenic Sources in British Columbia, Canada. *Organic Geochemistry*, 89-90, pp. 80-116. <https://doi.org/10.1016/j.orggeochem.2015.10.002>

Submitted 01.04.2024; approved after review 15.04.2024;
accepted for publication 17.07.2024.

About the authors:

Olga V. Soloveva, Leading Research Associate, A. O. Kovalevsky Institute of Biology of the Southern Seas of RAS (2 Nakhimova Ave., Sevastopol, 299011, Russian Federation), CSc. (Biology), **ORCID ID: 0000-0002-1283-4593**, **Scopus Author ID: 57416802600**, **ResearcherID: X-4793-2019**, kozl_ya_oly@mail.ru

Elena A. Tikhonova, Leading Research Associate, A. O. Kovalevsky Institute of Biology of the Southern Seas of RAS (2 Nakhimova Ave., Sevastopol, 299011, Russian Federation), CSc. (Biology), **ORCID ID: 0000-0002-9137-087X**, **Scopus Author ID: 57208495804**, **ResearcherID: X-8524-2019**, tihonova@mail.ru

Konstantin I. Gurov, Research Associate, Marine Hydrophysical Institute of RAS (2 Kapitanskaya Str., Sevastopol, 299011, Russian Federation), CSc. (Geogr.), **ORCID ID: 0000-0003-3460-9650**, **ResearcherID: L-7895-2017**, gurovki@gmail.com

Contribution of the co-authors:

Olga V. Soloveva – general scientific supervision of the research; data preparation; analysis and synthesis of research result; interpretation of the results; processing and description of the study results; analysis and preparation of initial conclusions

Elena A. Tikhonova – analysis of literature data; participation in the discussion of the paper materials; editing and supplementing the text of the paper; paper correction; advisory assistance.

Konstantin I. Gurov – formulation of goals and objectives of the study; presentation of data in the text and their analysis; paper correction; discussion of the study results; preparation of graphic and text materials; formulation of the conclusions.

The authors have read and approved the final manuscript.

The authors declare that they have no conflict of interest.

Excitation of Internal Waves in a Shallow Sea Basin with an Open Inlet under Conditions of Parametric Resonance

V. V. Novotryasov

*V. I. Il'ichev Pacific Oceanological Institute, Far Eastern Branch of RAS, Vladivostok,
Russian Federation*

✉ vadimnov@poi.dvo.ru

Abstract

Purpose. The purpose of the study is to show (using the *in situ* measurement data) that in autumn under parametric resonance conditions, internal waves (IW) are excited in Posyet Bay under the influence of seiche vibrations of its level.

Methods and Results. The spectral analysis methods have revealed a number of IW frequencies close to those of the most intensive seiche vibrations of the bay. The Mathieu equation was obtained and analyzed for the horizontal component of IW orbital velocity. For the conditions for observing IW, the necessary and sufficient conditions for implementing the parametric resonance in the model basin approximating Posyet Bay, were formulated. Verification of these conditions has shown that in autumn both necessary and sufficient conditions of the parametric resonance between the IW and sea level seiche vibrations are fulfilled in the bay.

Conclusions. The experimental data indicate that in the autumn season a number of IW frequencies are close to those of free oscillations of the sea level in Posyet Bay. It is shown that the barotropic currents induced by seiche vibrations can excite internal waves by means of parametric resonance.

Keywords: seiches, barotropic wave current, Posyet Bay, internal waves, parametric instability, parametric resonance

Acknowledgements: The work was carried out within the framework of state assignment of POI FEB RAS (theme No. 1240-2210-0072-5).

For citation: Novotryasov, V.V., 2024. Excitation of Internal Waves in a Shallow Sea Basin with an Open Inlet under Conditions of Parametric Resonance. *Physical Oceanography*, 31(5), pp. 647-661.

© 2024, V. V. Novotryasov

© 2024, Physical Oceanography

Introduction

Internal waves (IW) play a significant role in the mixing processes occurring in the surface and bottom boundary layers, participating in their formation [1, 2]. Along with winter convection, these waves play an essential role in the processes of heat and mass transfer in the surface layer of ice-covered basins [3].

As is known ¹ [4], excitation of IW with frequencies of $\sim 0.7 N_{\max}$, where N_{\max} is the maximum value of buoyancy frequency in the basin, occurs due to pressure pulsations or tangential wind stress. This paper presents an alternative mechanism for the excitation of such waves. It is based on the phenomenon of IW parametric

¹ Miropol'sky, Yu.Z., 1981. *Dynamics of Internal Gravity Waves in the Ocean*. Leningrad: Gidrometeoizdat, 302 p. (in Russian).



instability, which can be caused by external effects such as seiche vibrations of the basin free surface. This mechanism is particularly effective under conditions of parametric resonance, which is a special type of parametrically excited oscillations.

The study of IW parametric instability in a stratified fluid is a relatively recent development, having only commenced in the last few decades [5]. The cited work presents a number of considerations regarding the potential for high-frequency disturbances to increase in the presence of a low-frequency internal wave. A theoretical study of the parametric instability of a weakly nonlinear internal wave is presented in [6]. The present study demonstrates that an internal wave of finite amplitude can be unstable. In the studies [7, 8], the use of *in situ* data enabled the determination that the steepening of the leading edge of a semidiurnal internal wave in Posyet Bay coastal zone results in the effective generation of its harmonics with periods $T_n = 12.4 / n$ (h), $n = 2, 3, 4, \dots$.

In the present work, the necessary and sufficient conditions for IW excitation by means of parametric resonance are obtained analytically for the case of long internal and surface waves in a sea basin with a semi-open boundary. It is demonstrated that the physical nature of this excitation mechanism is constituted by the parametric amplification of the IW amplitude due to modulation of its horizontal orbital velocity component, which is caused by the barotropic current induced by seiche vibrations. This method of wave generation in a stably stratified fluid differs significantly from the widely known ones [9, 10] and is implemented without introducing additional anisotropy into the system. This ensures, in particular, the absence of spatial dissipation of energy transferred by the IW. *In situ* data are employed to analyse the feasibility of implementing the necessary and sufficient conditions for parametric resonance between the field of internal waves and the barotropic wave current generated by the Helmholtz mode and subsequent modes of seiche vibrations in Posyet Bay.

The objective of this study is to examine the process of internal wave parametric excitation in a shallow sea basin, specifically the role of seiche vibrations in hydrodynamic systems under conditions of parametric resonance. The study draws upon theoretical concepts of parametric resonance and field observations carried out in Posyet Bay over several years.

Study area and measurement data

The frequency content of seiche vibrations was analyzed using the data obtained from a tide gauge. The measurement error was 0.5 cm and the sampling interval was 7.5 min in October 2001 and 1 min in August 2003. The tide gauge was installed in the coastal zone of the Gamov Peninsula, within the Posyet Bay area. Its position is indicated by a diamond-shaped symbol on the map of the bay (Fig. 1). The map also provides the bathymetry of the bay obtained from navigational charts of the bay and its adjacent areas ². The area of water adjacent to the bay is limited by a semicircle

² Russian Emergencies Ministry, 2009. [*Atlas of the Peter the Great Gulf and Northwestern Coast of the Sea of Japan to the Sokolovskaya Bay (for Small-Size Vessels)*]. Vladivostok: GIROSKOP, 61 p. (in Russian).

with a radius of $L \sim 13.5$ km. As indicated on the navigational chart, the depth of the bay at its entrance is ~ 45 – 50 m.

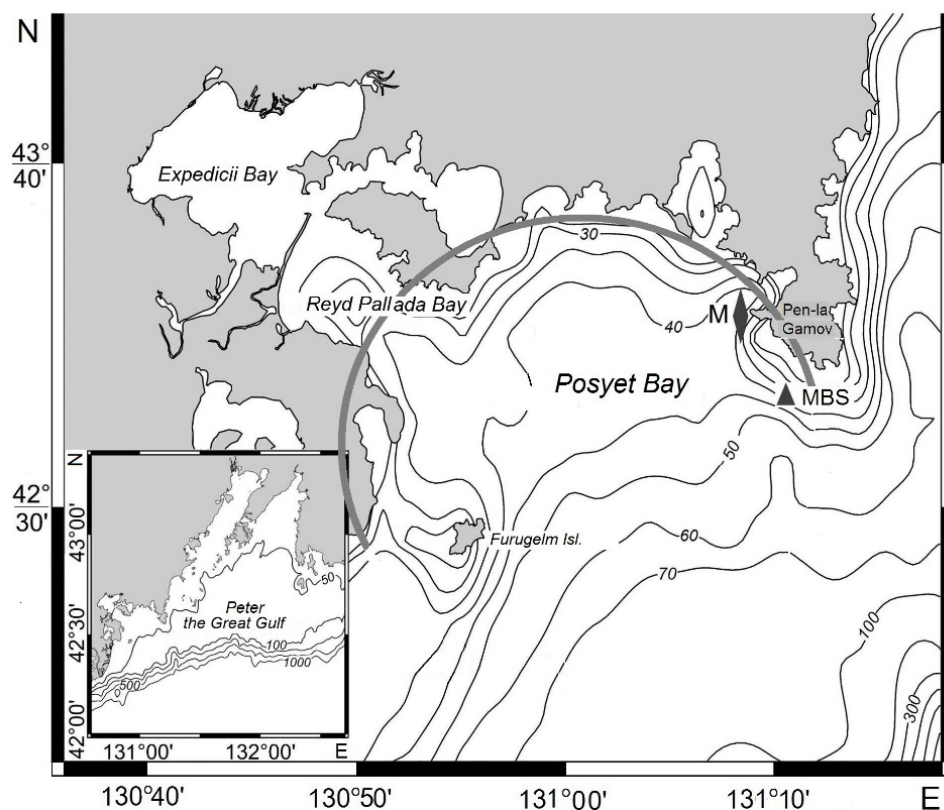


Fig. 1. Map-diagram of Posyet Bay. The inset shows Peter the Great Gulf

The study of internal waves was performed according to the measured data of the vertical section of the temperature field using a moored buoy station (MBS) deployed on the 40 m isobath on 14 September 2013. The geographical location of the MBS is indicated by a black triangle in Fig. 1. It was equipped with nine HOBO thermographs spaced 4 m apart from the surface. The HOBO autonomous digital thermograph, manufactured by *Onset*, has an accuracy of 0.21°C in the range 0 – 50°C and a resolution of 0.02°C at 25°C , as well as 64 kB of memory ($\sim 42,000$ 12-bit temperature measurements). Temperature recording at the stations was carried out with a resolution of 1 min. Duration of the measurements was just over 10 days.

Fig. 2 shows a 5-day temperature realization at $z = -24$ m horizon, recorded by the MBS thermograph, and its low-frequency trend. The realization of high-frequency temperature variations is also shown.

In the area of the buoy stations, 8 hydrological probings with a discreteness of 3 h were performed on 13 September 2013. The probings were performed with a Canadian RBR XRX-620 probe.

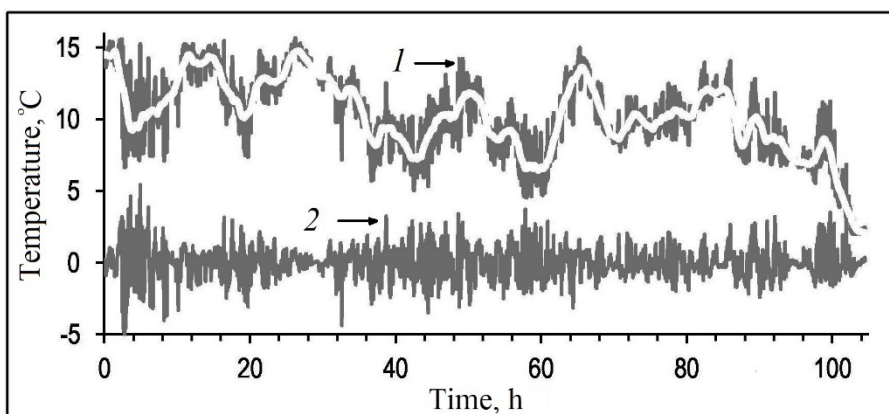


Fig. 2. Temperature near the moored buoy station (1), its low-frequency trend (white color graph) and high-frequency pulsations (2)

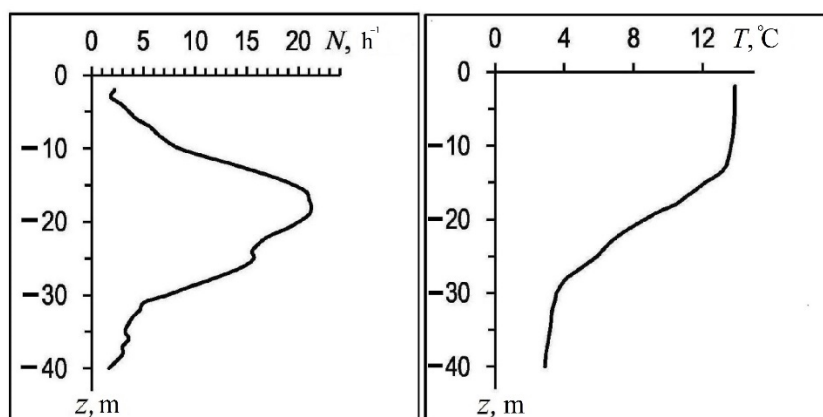


Fig. 3. Mean daily profiles of buoyancy frequency N (left) and temperature (T) (right) in the vicinity of buoy station

Fig. 3 (left) shows the typical buoyancy frequency profile for the autumn season in Posyet Bay. The presented profile $N(z)$ was used to calculate the phase velocity of the lowest IW mode with the frequencies of the bay seiche oscillations. The analysis of the daily mean temperature profile (Fig. 3, right) showed that the background conditions at the horizon $z_1 = -24$ m during the experiment near the MBS were characterised by a quasi-linear temperature dependence with depth.

Methodology of spectral data processing and its results

The characteristic time scales of sea level seiche oscillations (ζ) and temperature pulsations (T , °C) in the bay caused by internal waves were determined using standard spectral analysis methods³ [11]. The ζ and T fluctuations were separated

³ Dragan, Ya.P., Rozhkov, V.A. and Yavorskiy, I.M., 1987. *Methods of Probabilistic Analysis of Oceanological Process Rhythms*. Leningrad: Gidrometeoizdat, 319 p. (in Russian).

into a high-frequency component and a low-frequency trend by a Hamming filter with a window of 256 min duration. The low-frequency trend realizations obtained after filtering served as the background for determining the frequencies of internal waves and seiche oscillations with periods of 8–256 min. The realizations with the frequencies of the seiche oscillations were calculated as the difference between the initial level and temperature realizations and those of the low-frequency trend ζ and T . The resulting time series of the ζ and T fluctuations were used to calculate the spectral densities (hereafter referred to as spectra) of the level fluctuations ($Sp_{\zeta\zeta}$) and temperature pulsations ($Sp_{\eta\eta}$).

The spectra of the bay level fluctuations are normalized to the maximum value falling on the period of ~ 47 min (Fig. 4, *a, b*) and ~ 22 min (Fig. 4, *c*). The spectrum with the maximum at period $T_0 \sim 47$ min and the spectrum with a less pronounced broadband maximum at period $T_1 \sim 96$ min are shown in blue. The spectrum with the dominant maximum located at period $T_7 \sim 96$ min (Fig. 4, *b*) and the dominant maximum at period $T_1 \sim 22$ min (Fig. 4, *c*) are highlighted in green. The spectrum in Fig. 4, *a* is calculated from a two-week realization, in Fig. 4, *b, c* – from two consecutive weekly realizations obtained in October 2001.

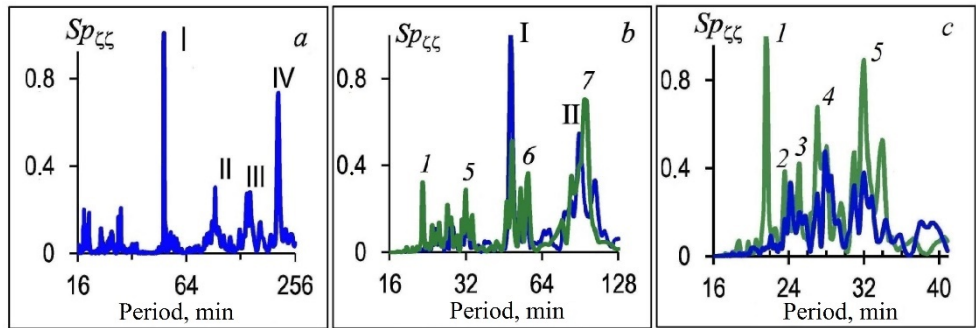


Fig. 4. Normalized spectra of the Posyet Bay level fluctuations in August 2003 (*a*) and October 2001 (*b, c*)

The spectrum in Fig. 4, *a* is characterized by a delta-shaped maximum at the period $T_0 \sim 47$ min, marked with the Roman numeral I, and a less intense broadband maximum at the period $T_1 \sim 96$ min marked with the Roman numeral II. We recorded two maxima in the range of periods exceeding 100 min; they are marked with the Roman numerals III and IV.

Let us now consider the spectra shown in Fig. 4, *b, c*, obtained in 2001 for two consecutive 7-day realizations. In the range of 16–28 min periods, the corresponding maxima are numbered 1, 2, ..., 7. Here we give the values of the periods in which these maxima are located:

Spectrum maxima	<i>I</i>	<i>2</i>	<i>3</i>	<i>4</i>	<i>5</i>	<i>6</i>	<i>7</i>
T_m , min	22	24	25	27	32	47	96

Thus, as a result of the spectral analysis, intense manifestations of water level fluctuations in the bay were identified at frequencies $\nu_0 \sim 47 \text{ min}^{-1}$ and

$\nu_0^+ \sim 1/96 \text{ min}^{-1}$, as well as less intense manifestation at frequencies $\nu_1 \sim 1/32 \text{ min}^{-1}$, $\nu_2 \sim 1/27 \text{ min}^{-1}$ and $\nu_3 \sim 1/25 \text{ min}^{-1}$.

We will consider the spectral composition of temperature pulsations in the bay. We will present the results of calculating the energy spectrum of these pulsations in the ranges of 10–40 and 32–128 min^{-1} , i.e. in the same ranges as the fluctuations of their level. The spectral analysis was carried out according to the implementation of high-frequency temperature pulsations recorded by the MBS thermograph at the horizon $z_1 = -20 \text{ m}$ (Fig. 2).

Fig. 5 shows the spectrum normalized to the maximum value of the temperature pulsations recorded by the MBS at the $z = -24 \text{ m}$ horizon. The numbers 1–12 indicate the numbers of the corresponding spectral maxima on a low-frequency background, showing the modulation of these pulsations by the low-frequency component.

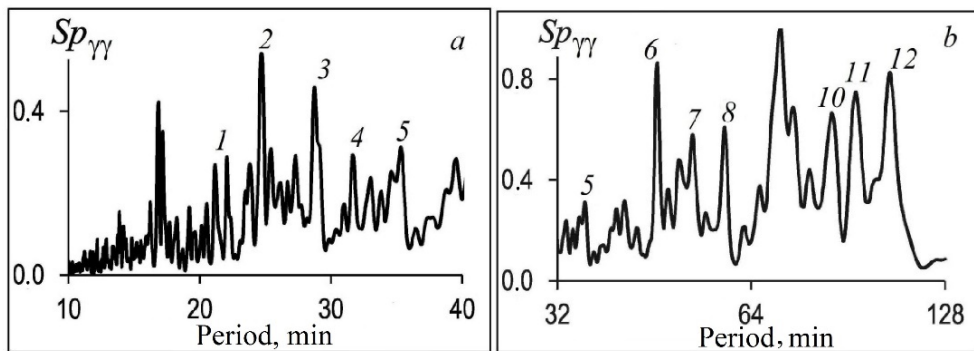


Fig. 5. Temperature pulsation normalized spectrum in the ranges 10–40 min (a) and 32–128 min (b)

Here are the values of T_m (min) periods of $Sp_{\gamma\gamma}$ spectral maxima shown in Fig. 5:

Spectral maxima	1	2	3	4	5	6	7	8	9	10	11	12
T_m , min	22	25	28	32	35	46	52	58	71	85	93	105

In the spectra, the most noticeable feature is the narrow-band maximum at the frequency $\nu_0 \sim 1/46 \text{ min}^{-1}$ with $m = 6$. It should also be noted that the maxima at the frequencies $\nu_1 \sim 1/25 \text{ min}^{-1}$ and $\nu_2 \sim 1/28 \text{ min}^{-1}$ are close to those at the frequencies of the bay seiche oscillations $\sim 1/25 \text{ min}^{-1}$ and $\sim 1/27 \text{ min}^{-1}$.

If we analyze the temperature pulsation spectrum shown in Fig. 3, a, we notice that the differences between the frequencies $\nu_1 - \nu_0$ and $\nu_2 - \nu_0$ are close to the maximum frequencies in the spectrum at 52 and 71 min^{-1} periods. In other words, for the frequencies corresponding to these periods the following approximate relationships are fulfilled: $\nu_1 - \nu_0 \sim 1/55 \text{ min}^{-1}$ and $\nu_2 - \nu_0 \sim 1/72 \text{ min}^{-1}$. It should also be noted that the frequencies $\nu_0 \sim 1/46 \text{ min}^{-1}$, $\nu_1^- \sim 1/105 \text{ min}^{-1}$, $\nu_2^- \sim 1/180 \text{ min}^{-1}$, around which the spectral maxima are located, satisfy the approximate expressions $\nu_n \sim \nu_0 + \nu_n^-$ where n is equal to 1 and 2, $\nu_1 \sim 1/32 \text{ min}^{-1}$ and $\nu_2 \sim 1/37 \text{ min}^{-1}$.

The observed features of the spectra in the area of the buoy station deployment may be an indirect indication of the IW parametric instability, caused, among other things, by seiche oscillations.

Parametric excitation of internal waves in a shallow sea basin by seiche oscillations of its free surface

We introduce a rectangular coordinate system with z -axis directed vertically upwards; x -axis is compatible with the velocity direction of the barotropic one-dimensional current of stratified fluid. The system of hydrodynamic equations for sufficiently long linear IWs in the Boussinesq approximation in the specified flow has the following form [4, 10]:

$$D_0 u = \frac{1}{\rho_0} \frac{\partial p}{\partial x}, \quad \frac{1}{\rho_0} \frac{\partial p}{\partial z} - b = 0, \quad (1)$$

$$D_0 \rho = w \frac{d\rho_0}{dz}, \quad \frac{\partial u}{\partial x} + \frac{\partial w}{\partial z} = 0. \quad (2)$$

Here $D_0 = \partial/\partial t + U \partial/\partial x$, U is barotropic current velocity; u and w are horizontal and vertical components of IW orbital velocity; p and ρ are wave disturbances of pressure and density; $\rho_0(z)$ is average density of liquid layer; $b = \rho g/\rho_0$ is wave fluctuations of buoyancy per unit volume. We transform the system of equations (1), (2) into a single equation for u of the following form:

$$D_0^2 \left(\frac{\partial^2 u}{\partial z^2} - \frac{2}{N} \frac{dN}{dz} \frac{\partial u}{\partial z} \right) + N^2 \frac{\partial^2 u}{\partial x^2} = 0, \quad (3)$$

where $N(z) = (g d \ln \rho_0 / dz)^{1/2}$ is buoyancy frequency.

Since the system of equations (1), (2) is horizontally homogeneous, the solution of equation (3) is described by a superposition of IW modes of arbitrary shape $u_m \sim \psi(c_m t) \varphi_m(z) \exp(ikx)$. In this expression $\psi_m(t)$ is the amplitude function of the wave mode with the number m ; $\varphi_m(z)$ and c_m are the eigenfunction and eigenvalue of the boundary value problem

$$\frac{d^2 \varphi_m}{dz^2} - \frac{2}{N} \frac{dN}{dz} \frac{d\varphi_m}{dz} + \frac{N^2}{c_m^2} \varphi_m = 0, \quad \varphi_m(0) = \varphi_m(-H) = 0. \quad (4)$$

Here it is assumed that the bottom ($z = -H$) and the free surface ($z = 0$) are rigid walls.

For the function $\psi_m(t)$ (hereinafter we omit the index m , assuming $m = 1$), taking into account the orthogonality of the set of functions $\varphi_m(z)$, after a series of transformations we obtain the equation

$$\frac{d^2 \psi}{dt^2} + 2i(kU) \frac{d\psi}{dt} + \left[(kU)^2 + (kc_{ph})^2 \right] \psi = 0, \quad (5)$$

which we reduce to normal form using the transformation $\psi(t) = \zeta(t) \exp\left(i \int k U dt\right)$. As a result, we obtain the following equation for the function $\zeta(t)$:

$$d^2 \zeta / dt^2 + \left[(kc_{ph})^2 - i(k dU/dt)^2 \right] \zeta = 0. \quad (6)$$

Next, we define the velocity of a barotropic current pulsating with a frequency ω as follows: $U = u_0 \exp(i\omega t)$. Then the imaginary term in the square brackets of equation (6) is equal to $\omega k U$. We represent the equation (6) solution as the sum of real and imaginary parts. In this case, the real part of the solution (denoted as $\eta = \text{Re}(\zeta)$) satisfies the equation

$$d^2 \eta / dt^2 + \Omega_0^2 (1 + \mu \sin(\Omega t)) \eta = 0, \quad (7)$$

where $\mu = (u_0/c_{ph})(\Omega/\Omega_0)$, and dimensional quantities (indicated by dashes) have the form $\eta = \eta'/H$, $t = t'/N_{\max}$, $\Omega = \omega/N_{\max}$, $\Omega_0 = \omega_0/N_{\max}$, $\omega_0 = kc_{ph}$ is internal wave frequency.

Thus, when an internal wave of a fixed (lowest) mode propagates in a barotropic current pulsating with a frequency ω , the real part of its amplitude function evolves according to equation (7).

Equation (7) is the well-known Mathieu equation. Its general solution has the following form⁴

$$\eta(t) = C_1 \exp(-i\sigma t) \Phi(t) + C_2 \exp(-i\sigma t) \Phi(-t), \quad (8)$$

where C_1, C_2 are constants; $\Phi(t)$ and $\Phi(-t)$ are periodic functions. The value σ characterizes the growth rate of the solution (8) and is a complex function of ω_0 and μ parameters. In this case, the solution (8) grows exponentially with time. The phenomenon consisting in the increase in oscillations of hydrodynamic system parameters is called parametric resonance.

Next, we show that in a sea basin affected by weak periodic fluctuations in the velocity of barotropic current $U = u_0 \sin(\omega t)$ induced by seiche level vibrations, the IW parametric generation with c_{ph} phase velocity is possible under condition $u_0^2 \ll c_{ph}^2$. During the generation process, the wave amplitude, specified by the function $\eta(t)$, is described by equation (7). We will seek a solution to this equation in the region of the main demultiplication resonance, i.e. when condition $|\Omega_0 - \Omega/2| \leq \mu$ is satisfied in the following form

$$\eta(t) = A(t) \sin[\Omega t/2 - \theta(t)]. \quad (9)$$

Using the Krylov – Bogolyubov averaging method⁵, for the amplitude A and phase θ we obtain a system of equations

⁴ Yakubovich, V.A. and Starzhinskii, V.M., 1987. [*Parametric Resonance in Linear Systems*]. Moscow: Nauka, 328 p. (in Russian).

⁵ Krylov, N.M. and Bogolyubov, N.N., 1937. *Introduction to Non-Linear Mechanics*. Kyiv: Publishing House of the Academy of Sciences of the Ukrainian SSR, 363 p. (in Russian).

$$dA/dt = \varepsilon A \cos(2\theta), \quad d\theta/dt = \delta - \varepsilon \cos(2\theta), \quad (10)$$

where $\varepsilon = -\mu\Omega_0/4$; $\delta = \Omega_0 - \Omega/2$. System (8) has the following invariant

$$I = A^2(d\theta/dt) = \text{const}, \quad (11)$$

which allows it to be easily integrated. It turns out that when the condition $\varepsilon^2 > \delta^2$ is satisfied, a solution of the form $A \sim \exp\left(t\sqrt{\varepsilon^2 - \delta^2}\right)$ exists. This can be verified by simply substituting the indicated solution into equation (7). Thus, the amplitude of the IW fixed mode is proportional to $\exp\left(t\sqrt{\varepsilon^2 - \delta^2}\right)$, and the condition for its small-amplitude exponential growth of horizontal velocity of wave currents is the condition $|\delta| < \varepsilon$, which corresponds to the parametric instability criterion of a pendulum oscillations with a vibrating suspension point in the absence of friction ⁶. In addition, the smallness condition of parameter $\mu \ll 1$ and parametric resonance of frequencies $|\delta| < \min\{\mu, \varepsilon\}$ must be met. Hence, taking into account the inequality $\mu \ll 1$, the condition of IW amplitudes “swinging” by a depth-uniform pulsating flow with a frequency Ω and a maximum value of its velocity u_0 takes the form

$$|\Omega_0 - \Omega/2| = \Omega u_0 / 4c_{ph}. \quad (12)$$

We can easily see that parametric resonance should take place at any $\omega = n\omega_0/2$ (where n is an integer), including $n = 2$. In this case, the boundaries of the parametric generation second zone are determined by the inequalities from the work ⁷:

$$-5\mu^2 \omega / 24 < \omega_0 - \omega < \mu^2 \omega / 4, \quad (13)$$

where ω is a frequency of pulsating barotropic current.

In conclusion, we formulate the necessary and sufficient conditions under which IW parametric generation is realized in a shallow basin being affected by the modulation of its horizontal component of the orbital motion velocity caused by the seiche vibrations (SV) barotropic current of the basin free surface.

Parametric generation of fixed-mode IWs with phase velocity c_{ph} and wave number k in a sea basin of depth H by a field of standing surface waves with frequency ω is possible if the following conditions are met:

⁶ Landau, L.D. and Lifshitz, E.M., 1969. *Mechanics*. Oxford, London, Edinburgh, New York: Pergamon Press, 165 p.

⁷ Rabinovich, M. I. and Trubetskov, D.I., 1984. *Introduction to the Theory of Oscillations and Waves*. Moscow: Nauka, 432 p. (in Russian).

- the lengths of internal (λ_{int}) and surface (λ_{sur}) waves significantly exceed the basin depth H , i.e. $H \ll \lambda_{int} \ll \lambda_{sur}$, and the IWs frequency range is limited by the frequency $\omega_*/2$, where ω_* is the lowest frequency of basin seiche oscillations;
- the IW phase velocity (c_{ph}) significantly exceeds the maximum value of barotropic current velocity (u_0), i.e. their ratio $\mu = (u_0/c_{ph}) \ll 1$. The mismatch between the IW frequency $\omega_0 = kc_{ph}$ and that of seiche oscillations ω should not exceed the product $\mu\omega$, i.e. $|\omega_0 - \omega| < \mu\omega$.

Using *in situ* data, we will demonstrate the formation of necessary and sufficient conditions for the IW excitation under effect of parametric resonance caused by the fundamental zero mode (Helmholtz mode) (as well as the first, second and subsequent SV modes of the bay water mass) in a model basin with a semicircular water area approximating Posyet Bay in autumn.

Discussion

Spectral analysis of temperature pulsations caused by the IW field in the bay showed that a number of frequencies of these pulsations are close to those of seiche level oscillations. Consequently, the necessary condition for IW parametric excitation by seiche oscillations is fulfilled.

In the autumn period, which is characterized by intense seiche oscillations, a sufficient condition for parametric resonance implementation between wave movements is fulfilled. Consequently, the IWs are excited in Posyet Bay in this period under SV effect.

Let us turn now to the data of *in situ* level measurements in the bay. Fig. 4 shows the spectrum of free surface fluctuations of the bay in the 1/16–1/256 min⁻¹ frequency range, which is typical for October. Two dominant maxima at periods of 47 and 92 min and three less pronounced maxima at periods of ~ 33 , ~ 28 and ~ 25 min, respectively, stand out in the spectrum. It should be noted that the ratio of these periods to $T_0 \sim 47$ min period is ~ 0.7 , ~ 0.6 and ~ 0.5 .

A number of experimental studies [12–15] revealed that the Helmholtz mode, a longitudinal fluctuation of barotropic current level and velocity with T_0 period, directed along the normal to the open boundary, has the greatest intensity in a basin with a semi-enclosed water area. For the basins of the simplest form, the periods of the first and subsequent modes are calculated using the formula from [16, 17]

$$T_m = \alpha_m T_0 / (2m + 1), \quad (14)$$

where T_0 is the Helmholtz mode period; α_m is parameter characterizing the basin form; m is mode number.

In [18], Table 2.1 with the periods of longitudinal modes of free oscillations in the basins of the simplest form is given. According to this table, in a semicircular-shaped basin with a depth profile specified by the dependence $h(x) = h_1(1-x^2/L^2)$, the ratio $\alpha_m/(2m+1)$ is equal to ~ 0.7 , ~ 0.6 and ~ 0.5 for m equal to 1, 2 and 3, respectively. The Helmholtz mode period for such a basin is calculated by the formula

$$T_0 = 2,2 \cdot 2L / \sqrt{gh_1}, \quad (15)$$

where h_1 is depth at the basin inlet; L is its length equal to the basin water area radius.

We assume that the maximum in the spectrum of level fluctuations belongs to the Helmholtz mode, in this case $T_0 = 47$ min. Then the periods of the first, second and subsequent modes are 33, 28 and 24 min. Having determined the period of the most intense fluctuations (T_0) of free surface and knowing the basin depth at the inlet (h_1), it is easy to determine its length. Using relation (15), we obtain the expression $L = (gh_1)^{1/2} (T_0/4.44)$. Hence, the length of the basin L with a depth at its inlet $h_1 \sim 45$ m and the Helmholtz mode period $T_0 = 47$ min will be ~ 13.5 km.

The map-diagram of Posyet Bay (Fig. 1) demonstrates a semicircular water area with a diameter and depth at the inlet of ~ 28 km and ~ 45 m, respectively. According to Fig. 1, geometric dimensions of the model basin, as well as its shape and bottom profile, are in satisfactory agreement with the dimensions and shape of Posyet Bay in the first approximation.

In shallow bays and harbors, along with longitudinal fluctuations, there are also transverse seiche vibrations [19]. In what follows, we will need the periods of the first and subsequent modes of this type of oscillations. For the basin under consideration, the first mode period is calculated using the formula $\tau_1 = \tau_{\max}/\sqrt{2}$. In this expression, $\tau_{\max} = 8.88L/\sqrt{gh_1}$. Consequently, for the specified parameters of the basin, the period of the first transverse seiche τ_1 will be 70 min.

Thus, in the model of a semicircular sea basin with a quadratic bottom profile, the Helmholtz mode, the first and subsequent modes have periods of 47, 34, 29 and 24 min. In the same basin, the first and subsequent modes of transverse seiches have periods close to $\tau_1 = 70$ min, $\tau_2 = 44$ min, $\tau_3 = 31$ min, $\tau_4 = 24$ min.

We turn now to the analysis of the IWs frequency composition in area under study. Fig. 5 represents the spectrum of temperature pulsations caused by these waves. The spectrum is calculated within the 10–128 min range of periods, common with that of seiche vibrations. The numbers in the spectrum highlight its maxima, the periods of which are close to the ones of the maxima in the spectrum of free surface fluctuations of the bay, i.e. its seiche oscillations.

The calculations performed using the buoyancy frequency profile (Fig. 3) revealed that the phase velocity of the first-mode IW ranges within $0.15\text{--}0.3 \text{ m} \cdot \text{s}^{-1}$, and the wavelength λ_{in} with a period $T_{in} \sim 15$ min is ~ 300 m. Therefore, the bay is a shallow sea basin for IWs with the periods exceeding 15 min.

Next, we show that a sea basin with a depth of 45 m at the inlet is shallow for a surface wave with $T_{sr} \sim 15$ min period. The length of surface waves λ_{sr} (equal to $(gh_1)^{1/2} T_{sr}$) with this period is ~ 19 km, which significantly exceeds λ_{in} . Therefore, the bay is a sea basin in which the inequality $\lambda_{sr} \gg \lambda_{in} \gg H$ is satisfied, i.e. it is a shallow basin for both surface and internal waves with frequencies from the frequency range of seiche oscillations.

A sufficient condition for the “swinging” of the IW amplitudes with T_{int} period by seiche oscillations with T_{sr} period, taking into account (12), will take the following form:

$$|1 - 2T_{sur}/T_{int}| \leq \mu / 2, \quad (16)$$

where $\mu = (u_0/c_{ph})$.

We are to show that IW amplitude with a phase velocity $c_{ph} \sim 0.2 \text{ m} \cdot \text{s}^{-1}$ and a period $T_{int} \sim 93 \text{ min}$ is parametrically “swinging” by the Helmholtz mode with an amplitude $\zeta_0 \sim 0.1 \text{ m}$ and a period $T_{sur} \sim 47 \text{ min}$ in the main resonance zone. For this purpose, we will check the sufficient condition for the implementation of this process. Condition (12) will be represented in the following form

$$\delta T/T_{int} \leq (u_0/c_{ph})(T_{int}/T_{sur})/2, \quad (17)$$

where $\delta T = (T_{int} - 2T_{sur})$ is a period mismatch; $u_0 = \zeta_0 \sqrt{g/H}$ is the maximum velocity of barotropic current induced by the Helmholtz mode. Using the given values, we obtain $\delta T/T_{int} \sim 10^{-2}$, $u_0/c_{ph} \sim 2.5 \cdot 10^{-1}$. Thus, the right-hand side of relation (17) will be ~ 0.2 , which is an order of magnitude greater than the left-hand side value of this relation. Consequently, the sufficient condition for the exponential growth of the wave amplitude with 93 min period and a phase velocity of $\sim 0.2 \text{ m} \cdot \text{s}^{-1}$ is satisfied.

Now we check the sufficient condition under which the IW excitation with the frequencies of seiche oscillations of the bay is possible, i.e. parametric excitation of waves in the first zone of parametric resonance. We represent this condition in accordance with (13) in the following form

$$\delta T \leq (u_0/c_{ph})^2 T_{int} / 2.$$

According to the works [16, 17], $u_0 = \eta_0 \sqrt{g/H}$, then $u_0 \sim 0.047 \text{ m} \cdot \text{s}^{-1}$. Considering that $c_{ph} \sim 0.25 \text{ m} \cdot \text{s}^{-1}$, we obtain $(u_0/c_{ph})^2 \sim 0.035$. Hence, the detuning of internal wave period with $T_{int} = 47 \text{ min}$ should not exceed 0.5 min.

It is obvious that verification of the sufficient condition (13) using the data of a natural experiment is a very complex task in terms of method. The relative stability of the excitation frequency of an internal wave with a period of 47 min, corresponding to the ratio $\delta T/T_{int}$, is $\sim 1\%$, which is unlikely in marine conditions for the excitation interval, the upper limit of which is $\sim 8 \text{ h}$.

At the same time, the excitation of internal waves in the first zone of parametric resonance is possible within the framework of the following scheme. Note that the periods of the most significant spectral maxima T_1 , T_2 , T_3 and T_4 are 17, 25, 29 and 47 min, respectively. The same periods correspond to 16, 26, 30 and 44 min of

the semidiurnal tidal harmonics with a period of 12.4 h, which are close to the previous periods.

In [18], it was found that in Posyet Bay the tidal IW with a semidiurnal period changes its shape during propagation, i.e. the velocity of the liquid particles at the top exceeds the velocity of the particles at the bottom. In the spectral description of the wave motion this means that the maxima in the spectrum occur at $T_n = 12.4/n$ (h) periods, where $n = 1, 2, 3, \dots$, is the harmonic number. Consequently, when standing surface waves with seiche oscillation frequencies propagate in a wave field, parametric resonance is possible between this field and the corresponding harmonics of the internal tidal wave with a frequency of $1/12.4 \text{ h}^{-1}$.

In other words, the semidiurnal tidal IW, propagating in the shallow water zone of the bay covered by seiche oscillations, transforms under the effect of quadratic nonlinearity from a harmonic wave with frequency $\nu = 1/12.4 \text{ h}^{-1}$ to a polyharmonic wave with harmonic frequencies $\nu_n = n\nu$. At close values ν between the frequencies of the seiche oscillations and those of the tidal IW harmonics, a parametric resonance occurs, i.e. an exponential increase in the amplitudes of the corresponding harmonics of the tidal IW.

Thus, in the presence of sufficiently intense seiche oscillations of the level and a weakly nonlinear IW with a frequency of $\nu = 1/12.4 \text{ h}^{-1}$, a sufficient condition for the parametric generation of IW with the seiche oscillation frequencies in the first zone of parametric resonance is realized in the bay.

Conclusion

This paper examines the results of field studies of standing surface and free internal waves in Posyet Bay in the frequency range $1/16\text{--}1/256 \text{ min}^{-1}$. Using Fourier analysis, we identified the frequencies at which the most significant maxima in the spectra of both surface and internal waves are located in the specified frequency range. We have shown the proximity of a number of frequencies at which these maxima are located in the spectra of the specified wave processes.

Using a model basin approximating Posyet Bay, the period estimates of the Helmholtz mode and subsequent ones in such a basin were obtained. By analyzing the spectrum of the free surface fluctuations of the bay, we found that its maxima fall on the above periods, which are those of the level or seiche free fluctuations in the bay. Thus, the necessary conditions for the IW parametric instability caused by seiche level oscillations in the bay are formed in the autumn period.

Within the framework of the parametric resonance theory, it was found that under the influence of the barotropic current caused by seiche oscillations, the modulation of horizontal component of the IW orbital motion velocity takes place. With the corresponding ratio $u_0/c_{ph} \ll 1$, a sufficient condition for the parametric excitation of IWs in the zero zone of parametric resonance in the bay is realized.

Within the same theory, it has been shown that in the bays and coves of marginal seas, internal waves can be excited in the first zone of parametric resonance with frequencies of IW harmonics of $\nu_{td} = 1/12.4 \text{ h}^{-1}$ frequency. The condition for this resonance is that the frequencies of the Helmholtz mode and subsequent basin modes are close to those of the internal tide harmonics.

REFERENCES

1. Sheen, K.L., Brearley, J.A., Naveira Garabato, A.C., Smeed, D.A., Waterman, S., Ledwell, J.R., Meredith, M.P., Laurent, L.St., Thurnherr, A.M. [et al.], 2013. Rates and Mechanisms of Turbulent Dissipation and Mixing in the Southern Ocean: Results from the Diapycnal and Isopycnal Mixing Experiment in the Southern Ocean (DIMES). *Journal of Geophysical Research: Oceans*, 118(6), pp. 2774-2792. <https://doi.org/10.1002/jgrc.20217>
2. MacIntyre, S., 1993. Vertical Mixing in a Shallow, Eutrophic Lake: Possible Consequences for the Light Climate of Phytoplankton. *Limnology and Oceanography*, 38(4), pp. 798-817. <https://doi.org/10.4319/lo.1993.38.4.0798>
3. Volkov, S.Yu., Bogdanov, S.R., Zdorovenov, R.E., Palshin, N.I., Zdorovenova, G.E., Efremova, T.V., Gavrilenko, G.G. and Terzhevik, A.Yu., 2020. Resonance Generation of Short Internal Waves by the Barotropic Seiches in an Ice-Covered Shallow Lake. *Physical Oceanography*, 27(4), pp. 374-389. <https://doi.org/10.22449/1573-160X-2020-4-374-389>
4. LeBlond, P.H. and Mysak, L.A., 1978. *Waves in the Ocean*. Amsterdam, Oxford, New York: Elsevier Scientific Publishing Company, 602 p.
5. McEwan, A.D. and Robinson, R.M., 1975. Parametric Instability of Internal Gravity Waves. *Journal of Fluid Mechanics*, 67(4), pp. 667-687. <https://doi.org/10.1017/S0022112075000547>
6. Stepanov, D.V. and Novotryasov, V.V., 2013. Sub-Inertial Modulation of Nonlinear Kelvin Waves in the Coastal Zone. *Nonlinear Processes Geophysics*, 20(3), pp. 357-364. <https://doi.org/10.5194/npg-20-357-2013>
7. Novotryasov, V.V., Filonov, A. and Lavin, M.F., 2011. Nonlinear Internal Tidal Waves in a Semi-Enclosed Sea (Gulf of California). *Geophysical Researcher Letters*, 38(24), L24611. <https://doi.org/10.1029/2011GL049886>
8. Novotryasov, V.V. and Pavlova, E.P., 2011. Determination of Parameters of Low-Frequency Internal Waves in the Coastal Zone of a Fringing Sea Using Field Measurements and Basing on the Nonlinear Theory. *Russian Meteorology and Hydrology*, 36(4), pp. 269-272. <https://doi.org/10.3103/S106837391104008X>
9. Lighthill, J., 1978. *Waves in Fluids*. Cambridge: Cambridge University Press, 504 p.
10. Miropol'sky, Yu.Z., 2001. *Dynamics of Internal Gravity Waves in the Ocean*. Dordrecht: Springer, 406 p.
11. Thomson, R.E. and Emery, W.J., 2001. *Data Analysis Methods in Physical Oceanography*. Amsterdam, Netherlands: Elsevier Science, 654 p.
12. Rabinovich, A.B., 2009. Seiches and Harbor Oscillations. In: Y. C. Kim, ed., 2009. *Handbook of Coastal and Ocean Engineering*. Singapore: World Scientific Publishers, pp. 193-236. https://doi.org/10.1142/9789812819307_0009
13. Chupin, V., Dolgikh, G., Dolgikh, S. and Smirnov, S., 2022. Study of Free Oscillations of Bays in the Northwestern Part of Posyet Bay. *Journal of Marine Science and Engineering*, 10(8), 1005. <https://doi.org/10.3390/jmse10081005>
14. Smirnov, S.V., Yaroshchuk, I.O., Leontyev, A.P., Shvyrev, A.N., Pivovarov, A.A. and Samchenko, A.N., 2018. Studying Resonance Oscillations in the Eastern Part of the Posyet Bay. *Russian Meteorology and Hydrology*, 43(2), pp. 88-94. <https://doi.org/10.3103/S1068373918020048>
15. Dolgikh, G.I., Budrin, S.S., Dolgikh, S.G., Plotnikov, A.A., Chupin, V.A., Shvets, V.A. and Yakovenko, S.V., 2016. Free Oscillations of Water Level in the Posyet Gulf Bays (the Sea of

- Japan). *Russian Meteorology and Hydrology*, 41, pp. 559-563. <https://doi.org/10.3103/S1068373916080057>
16. Manilyuk, Yu.V. and Cherkosov, L.V., 2017. Investigation of Seiche Oscillations in a Free Entrance Bay. *Physical Oceanography*, (4), pp. 16-25. <https://doi.org/10.22449/1573-160X-2017-4-16-25>
 17. Ivanov, V.A., Manilyuk, Y.V. and Sannikov, V.F., 2018. Seiches in a Basin with an Open Entrance. *Journal of Applied Mechanics and Technical Physics*, 59, pp. 594-600. <https://doi.org/10.1134/S0021894418040041>
 18. Rabinovich, A.B., 1993. *Long Gravitational Waves in the Ocean: Capture, Resonance, and Radiation*. Saint Petersburg: Gidrometeoizdat, 326 p. (in Russian).
 19. Wilson, B.W., 1972. Seiches. In: Ven Te Chow, ed., 1972. *Advances in Hydrosiences*. New York: Academic Press. Vol. 8, pp. 1-94. <https://doi.org/10.1016/B978-0-12-021808-0.50006-1>

Submitted 28.03.2024; approved after review 05.07.2024;
accepted for publication 13.07.2024.

About the author:

Vadim V. Novotryasov, Leading Research Associate, Ocean Physics and Atmosphere Department, V. I. Il'ichev Pacific Oceanological Institute, Far Eastern Branch of RAS (43 Baltiyskaya Str., Vladivostok, 690041, Russian Federation), DSc. (Phys.-Math.), Associate Professor, **ORCID ID: 0000-0003-2607-9290**, vadimnov@poi.dvo.ru

The author has read and approved the final manuscript.

The author declares that he has no conflict of interest.

Comparative Numerical Simulation of Tsunami Waves during the January 1, 2024 Noto Peninsula Earthquake, Japan

R. Kh. Mazova¹, A. A. Martynenko², A. A. Kurkin^{1,3,✉}

¹ *Nizhny Novgorod State Technical University n. a. R. E. Alekseev, Nizhny Novgorod, Russian Federation*

² *Autonomous Non-Commercial Organization of Higher Education “Central University”, Moscow, Russian Federation*

³ *V. I. Il'ichev Pacific Oceanological Institute, Far Eastern Branch of RAS, Vladivostok, Russian Federation*

✉ aakurkin@gmail.com

Abstract

Purpose. The object of this work is to perform a comparative numerical simulation of generation and propagation of tsunami waves induced by the $M = 7.6$ earthquake on January 1, 2024 on the Noto Peninsula, Ishikawa Prefecture, Japan.

Methods and Results. Four different variants of a seismic source are simulated within framework of the earthquake source keyboard mechanism. A multi-block source is considered in which, while simulating the earthquake, a sequential motion of key-blocks was specified. It is shown that the dynamics of this process in a seismic source will determine the formation of corresponding tsunami source and wave fronts propagating from this source and that the shape of earthquake source affects the values of maximum wave heights in the water area significantly. Applying the information from the tide-gauge stations in the Sea of Japan and the Tsugaru and Tatar straits allows compare the real records of maximum values of the tsunami wave amplitudes at these stations and the computed tide-gauge ones resulted from numerical simulation of different dynamics of keyboard blocks in the seismic source.

Conclusions. This study demonstrates that the keyboard earthquake model is a viable tool for simulating complex earthquake sources, such as the one that occurred in the northwest of the Noto Peninsula and on the western coast of Honshu Island, an area home to a significant number of settlements and the largest Japanese operating nuclear power plants.

Keywords: 2024 tsunami, Noto Peninsula, Japan, earthquake source, numerical simulation

Acknowledgments: The study was supported by the Laboratory of nonlinear hydrophysics and natural disasters of POI n. a. V. I. Il'ichev, FEB of RAS, grant of the Ministry of Science and Higher Education of RF, agreement No. 075-15-2022-1127 dated July 1, 2022.

For citation: Mazova, R.Kh., Martynenko, A.A. and Kurkin, A.A., 2024. Comparative Numerical Simulation of Tsunami Waves during the January 1, 2024 Noto Peninsula Earthquake, Japan. *Physical Oceanography*, 31(5), pp. 662-678.

© 2024, R. Kh. Mazova, A. A. Martynenko, A. A. Kurkin

© 2024, Physical Oceanography

Introduction

It is well known that Japan is among ten most earthquake-prone countries in the world¹. Its location within the Pacific Ring of Fire has resulted in numerous

¹ Regan, H., Akbarzai, S., Kobayashi, C. and Maruyama, M., 2024. 'Battle against Time' to Find Quake Survivors as Japan Lifts Tsunami Warnings and Death Toll Rises. 2024. [online] Available at: <https://edition.cnn.com/2024/01/02/asia/japan-earthquake-tsunami-warnings-tuesday-intl-hnk/index.html> [Accessed: 28 February 2024].



destructive earthquakes throughout its history. One notable event occurred on 17 January 1995, when the $M = 7.3$ earthquake struck the western region of the Japanese island of Honshu resulting in over 6400 fatalities [1]. Another significant earthquake, with $M = 9$, followed by a tsunami measuring between 3 and 15 meters in height, struck the coasts of Honshu and Hokkaido islands on 11 March 2011. As a result of this natural disaster ², more than 28 thousand people died and large areas were contaminated with radioactive substances from the Fukushima I Nuclear Power Station [2, 3].

High seismic activity is stipulated by the location of the archipelago at the collision of several lithospheric plates, two of which – the Philippine and Pacific – are in motion. This leads to a significant number of intense Earth tremors usually accompanied by earthquakes and tsunamis. Several thousand earthquakes occur in Japan per year, an average of 18 earth tremors per day. However, strong earthquakes accompanied by tsunamis occur much less frequently: once every 10 years – with $M = 8$, once a year – with $M = 6$ (see ^{1, 3, 4} and [4]).

We consider a strong earthquake ($M = 7.6$) occurred on the Noto Peninsula in Ishikawa Prefecture, Japan, on 1 January 2024. As a result of a series of Earth tremors, massive destruction was caused in the towns of Suzu, Wajima, Noto and Anamizu. At the same time, significant damage was also recorded in the neighboring prefectures of Toyama and Niigata. As a result of this earthquake, a tsunami hazard was declared in several regions of Honshu Island. Japan Meteorological Agency issued a tsunami warning map, according to which, presumably, tsunami waves of 5 m in height approached the western coast of the island (Fig. 1).

This paper presents the results of numerical simulation of tsunami wave generation by a seismic source formed within the keyboard model of an earthquake source [5]. The greatest uncertainty in computation possible tsunami development scenarios is associated with the initial motion of the bottom during an earthquake. When using keyboard model, specifying the displacements and velocities of the bottom during an earthquake provides a solution to the problem of tsunami wave formation. In this case, the key-block motion is simulated according to the aftershock stage of the process. After the end of the aftershock stage, the blocks stop. During the strongest earthquakes with a rupture length of several hundred kilometers, their sources can cover many blocks.

In this paper, we consider a five-block earthquake source as well as generation of a tsunami source at different localizations of a seismic source and different kinematic

² TASS. *Chronology of Earthquakes with Fatalities in Japan*. 2024. [online] Available at: <https://tass.ru/info/19667253> [Accessed: 28 September 2024].

³ Japan Meteorological Agency. *Weather Map*. 2024. [online] Available at: <https://web.archive.org/web/20240101100413/https://www.jma.go.jp/bosai/map.html#5/38.891/141.24/&elem=warn&contents=tsunami> [Accessed: 10 May 2024].

⁴ USGS. *Latest Earthquakes*. 2024. [online] Available at: <https://earthquake.usgs.gov/earthquakes/map> [Accessed: 10 May 2024].

processes of key-block motion in the source. Analysis of wave characteristics obtained during simulation of different localizations and dynamics of the seismic source leads to conclusions about the ambiguity of the selected process model.

The work aim is a comparative numerical simulation of generation and propagation of tsunami waves induced by the $M = 7.6$ earthquake source on the Noto Peninsula, Ishikawa Prefecture, Japan, on 1 January 2024.

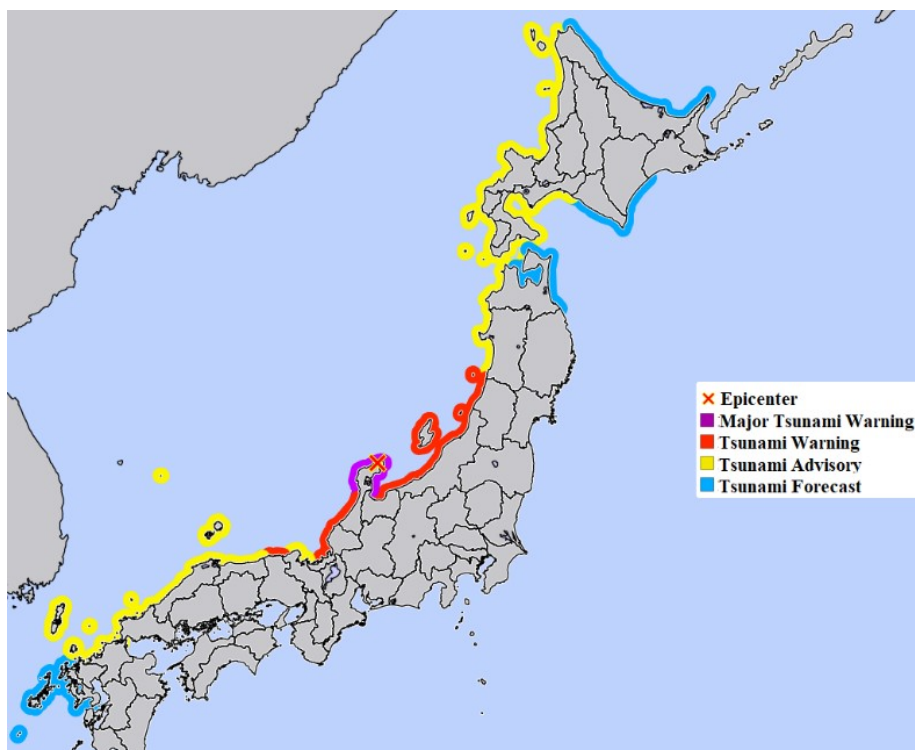


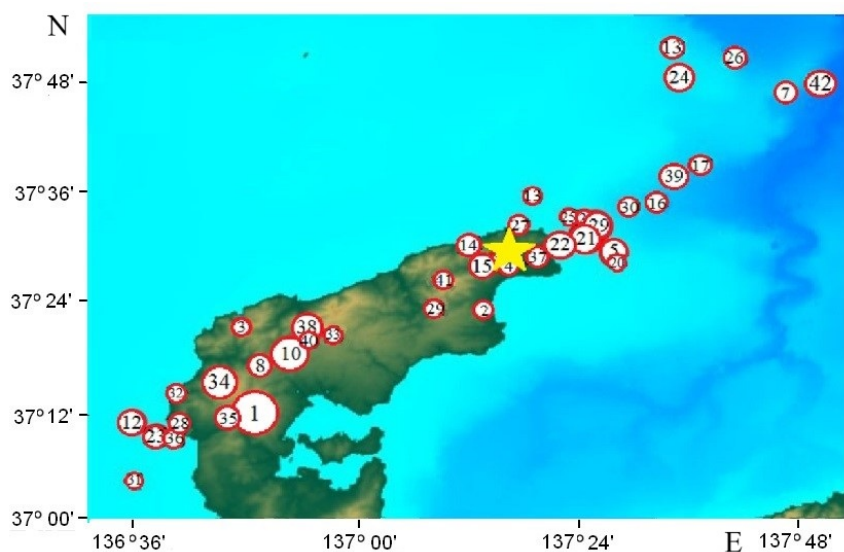
Fig. 1. Tsunami hazard map for Honshu Island published by the Japan Meteorological Agency on 1 January 2024 ³

Problem statement

Aftershock stage of the process

Using the data from [6–9], we have analyzed the sequence of the aftershock stage of earthquake process. Aftershock data were obtained from the U.S. Geological Survey ⁵ and are represented in Fig. 2. After the main earthquake shock on 01.01.2024 at 07:10:09 UTC, 42 more shocks with $M > 4.5$ occurred within three days (Table 1).

⁵ IOC. *Sea Level Station Monitoring Facility*. 2024. [online] Available at: <https://www.ioc-sealevelmonitoring.org/map.php> [Accessed: 10 May 2024].



F i g. 2. Aftershocks after the 01.01.2024 earthquake on the Noto Peninsula (yellow star is the earthquake epicenter; circles with numerals indicate the order of aftershocks ⁵⁾

T a b l e 1

All aftershocks at $M > 4.5$ from 01.01.2024 to 03.01.2024 after the earthquake on 1 January 2024

s/n	M	Time (UTC)	s/n	M	Time (UTC)	s/n	M	Time (UTC)
0	7.5	07:10:09	15	4.9	08:22:10	30	4.6	17:33:30
1	6.2	07:18:41	16	4.7	08:29:02	31	4.5	19:27:14
2	4.6	07:27:28	17	4.6	08:42:04	32	4.6	19:42:06
3	4.6	07:28:15	18	4.5	08:48:21	33	4.5	22:13:30
4	4.7	07:29:04	19	5.5	09:03:48	34	5.4	01:17:31
5	5.2	07:39:49	20	4.6	09:06:13	35	4.8	06:57:54
6	4.8	07:42:43	21	5.6	09:08:17	36	4.6	08:13:40
7	4.7	07:45:30	22	5.2	09:30:21	37	4.8	17:21:47
8	4.8	07:48:14	23	5.0	09:39:59	38	5.3	01:54:34
9	4.7	07:54:21	24	5.1	09:54:26	39	4.9	03:54:13
10	5.6	07:56:47	25	4.6	09:49:15	40	4.7	09:48:00
11	5.0	08:02:44	26	4.6	10:06:54	41	4.6	15:36:53
12	5.1	08:07:10	27	4.7	10:50:35	42	4.8	19:38:41
13	4.5	08:15:38	28	4.6	11:35:32			
14	4.8	08:17:46	29	4.5	13:19:57			

Tsunami source formation within the keyboard model of an earthquake seismic source

Since the mechanism of seismic source formation is unknown, then it is possible to calculate approximate dimensions of a seismic source and its dynamics by specifying the source mechanism from tectonic considerations based on known magnitude values of the earthquake and aftershocks and also using the distribution of $M > 4.5$ aftershocks. To calculate the source dimensions, the following formulas are applied [10]

$$\begin{cases} \lg L = 0.59M - 2.44, \\ \lg W = 0.32M - 1.01, \end{cases} \quad (1)$$

where M is earthquake magnitude; L is length of the rupture at the source, km; W is width of the rupture plane, km.

The maximum vertical displacement of the wave surface above the earthquake source is found by the formula⁶

$$\lg(H) = 0.8M - 5.6, \quad (2)$$

where H is maximum height of wave surface vertical displacement above the earthquake source, m. Estimated displacements of these characteristics applied for simulating the tsunami source⁶ [10] are presented below:

M_w	L , km	W , km	S , km ²	H , m
7.5	78 ± 18	43 ± 6	3354 ± 440	4.8

For simulating, we took source length to be 78 km and the width to be 43 km. Since the ocean surface will rise by the same value as the block on the bottom has displaced due to fluid incompressibility and pressure hydrostaticity, and from the Iida formula the displacement was obtained to be 4.8 m, then we took the maximum vertical shift of the block in the earthquake keyboard source to be 4.8 m.

Mathematical statement of the problem

The process of tsunami wave generation is considered in the shallow-water theory approximation. For simulating, we used the equations that describe a nonlinear system of shallow-water equations in a 2D formulation (see, for example,⁷ and [11]):

$$\begin{cases} \frac{\partial u}{\partial t} + u \frac{\partial u}{\partial x} + v \frac{\partial v}{\partial y} + g \frac{\partial \eta}{\partial x} = 0, \\ \frac{\partial v}{\partial t} + u \frac{\partial v}{\partial x} + v \frac{\partial v}{\partial y} + g \frac{\partial \eta}{\partial y} = 0, \\ \frac{\partial \eta}{\partial t} + \frac{\partial}{\partial x}[(\eta + H - B)u] + \frac{\partial}{\partial y}[(\eta + H - B)v] = \frac{\partial B}{\partial t}. \end{cases} \quad (3)$$

⁶ Pelinovsky, E.N., 1982. [Nonlinear Dynamics of Tsunami Waves]. Gorky: IPF AN SSSR, 226 p. (in Russian).

⁷ Voltsinger, N.E., Klevanny, K.A. and Pelinovsky, E.N., 1989. Long-Wave Dynamics of the Coastal Zone. Leningrad: Gidrometeoizdat, 272 p. (in Russian).

We assume that axis z is directed vertically upwards; x, y are spatial coordinates; $u(x, t)$, $v(y, t)$ are horizontal velocity components, $\eta(x, y, t)$ is free surface disturbance relative to the undisturbed level; H is maximum depth of the basin; function $B(x, y, t)$ determines the basin bottom change (taking into account the characteristics of the dynamic seismic source). At the initial moment of time, the parameters of dynamic seismic source (coordinates, displacement rate of the key-blocks) are specified in the solution domain. We assume that the water area with the initial bottom shape is at rest before the generation start, i.e., the velocity and disturbance of free surface were absent:

$$\eta(x, y, 0) = 0; u(x, 0) = 0; v(x, 0) = 0.$$

At the last seaward point at 5 m depth, a condition of total reflection (vertical wall) was set, which makes it possible to record the maximum and minimum wave level shift at this depth. Computational domain applied for these calculations was 125.01° – 147.00° E, 30.01° – 55.00° N with a grid of $30' \approx 759$ m step. In the numerical solution, we used a scheme constructed by analogy with the Sielecki one [3].

Numerical simulation of tsunami waves within the keyboard model of a seismic source

Figure 3 represents the computed water area with localization points of tide-gauge stations [7].

Four scenarios with different localizations of earthquake source (Fig. 4) were considered in this work. Figure 4, *a* shows scenario 1 with block 2 in the Toyama Bay area southeastwards of the Noto Peninsula. In Fig. 4, *b*, the same block is located in the Sea of Japan northwestwards of the Noto Peninsula. The location of the remaining blocks in the earthquake source is similar for these scenarios. Figure 4, *c* shows the source localization for scenario 3. It can be seen that the block located northwestwards of the peninsula took a triangular shape stretching along the entire peninsula. The shape of the remaining blocks also changed. In scenario 4, the shape of blocks 1–3 did not change, but direction of the location of blocks 4 and 5 changed. This change in the localization, size and orientation of the blocks is due to a comparison of simulation results with *in situ* data and the data from other authors. A total of 14 simulation options were carried out, with 4 of them being presented in this paper.

Table 2 shows kinematics of the key-block motion in the earthquake source. For all scenarios, the source consists of five blocks that perform sequential motion at certain time intervals. Analysis of time sequence of aftershock occurrence makes it possible to create an estimated version of key-block motion kinematics in the seismic source.

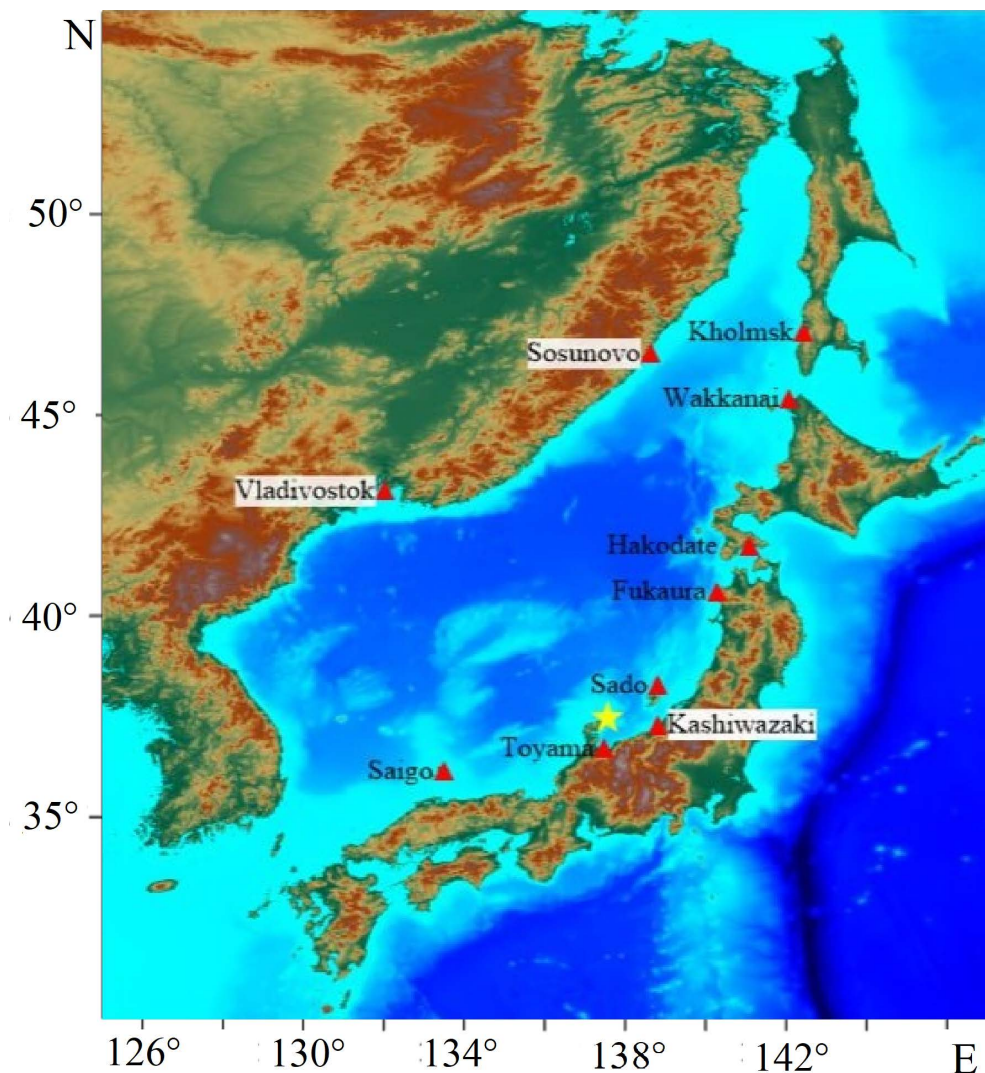


Fig. 3. Estimated water area (yellow star is the earthquake epicenter; red triangles denote the location of tide-gauge stations [7])

In scenario 1, the blocks make sequential motion at equal time intervals of 30 s. In scenario 2, the blocks make sequential motion at equal time intervals of 30 s but with negative displacement values. In scenarios 3 and 4, the block displacements in different directions remain. In scenario 3, the blocks make sequential motion at different time intervals in the range of 60–140 s. In scenario 4, the blocks make sequential motion at different time intervals from 60 to 130 s. Fig. 5 illustrates the process of tsunami source generation in scenarios 1 and 4 which clearly corresponds to the earthquake source locations shown in Fig. 4, a and d.

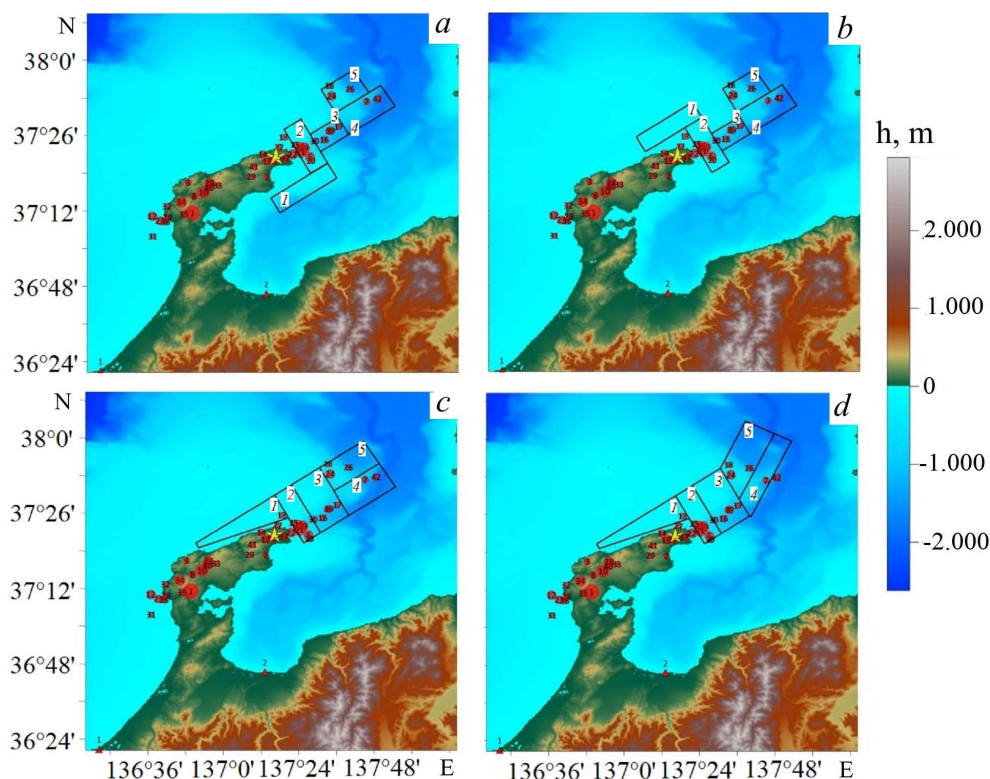


Fig. 4. Simulation of the scenarios of seismic source different locations: 1 (a); 2 (b); 3 (c); 4 (d) (1 – 5 are the key-block numbers)

Table 2

Kinematics of block motion in the earthquake source in four scenarios

Parameter	Block number				
	1	2	3	4	5
<i>Scenario 1</i>					
Displacement height, m	1.5	3	1	1	1
Start time of motion, s	30	0	90	60	120
End time of motion, s	60	30	120	90	150
<i>Scenario 2</i>					
Displacement height, m	2	1	–1	1	–1
Start time of motion, s	0	30	90	60	120
End time of motion, s	30	60	120	90	15
<i>Scenario 3</i>					
Displacement height, m	3	1.4	–1.3	1.5	1.2
Start time of motion, s	0	90	190	350	520
End time of motion, s	30	120	220	380	550
<i>Scenario 4</i>					
Displacement height, m	3.2	–1.1	–0.2	0.2	1.3
Start time of motion, s	0	90	190	350	440
End time of motion, s	30	120	220	380	470

In Fig. 5, it is seen that the water surface displacement corresponds to block displacement presented in Table 2 for scenarios 1 and 4. The main difference is associated with the change in the localization and shape of block 1 with a displacement towards the southeast (scenario 1) or northwest (scenario 4) from the Noto Peninsula. The configuration of blocks 2–5 does not differ significantly.

Fig. 6 shows the positions of wave fronts for nine points in time. It is clearly seen that 1-meter waves reach Sado Island 10 minutes after the start of generation, and the waves move in this direction faster than towards the bay; this is associated with the Toyama Trough. After 30 minutes, the wave front reached the coastal cities of Kashiwazaki and Toyama. At the 45th minute, the 0.5-meter wave front reached the northern part of Honshu Island and went around the Noto Peninsula. 1 hour 45 minutes after the earthquake, waves of ~20 cm height reached Vladivostok and the southern part of Hokkaido Island. At 05:56:30, the wave front reached Kholmsk, located in the northern part of Sakhalin Island.

The distribution of heights in Fig. 7 shows good agreement with Fig. 1 where the most hazardous areas are the coasts located in the northeastern part of the Noto Peninsula as well as the cities of Toyama, Sado and Kashiwazaki. The computation is carried out up to the 5-meter isobath.

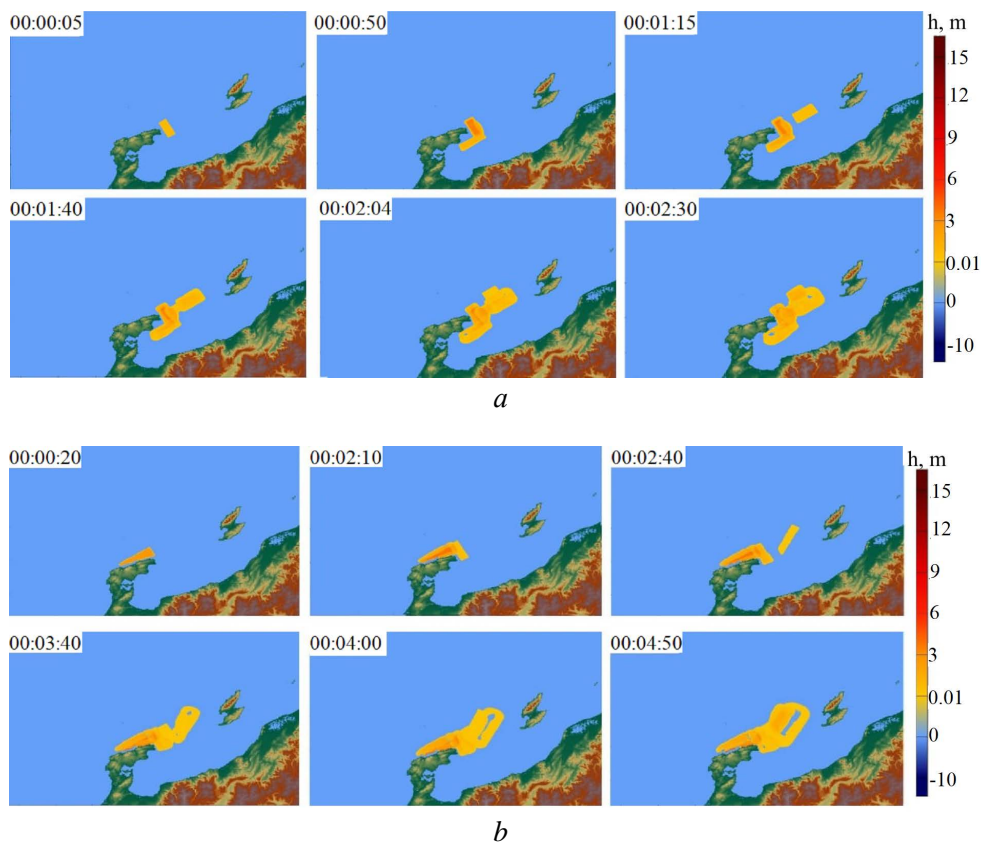


Fig. 5. Generation of a tsunami source at six time points in scenarios 1 (*a*) and 4 (*b*)

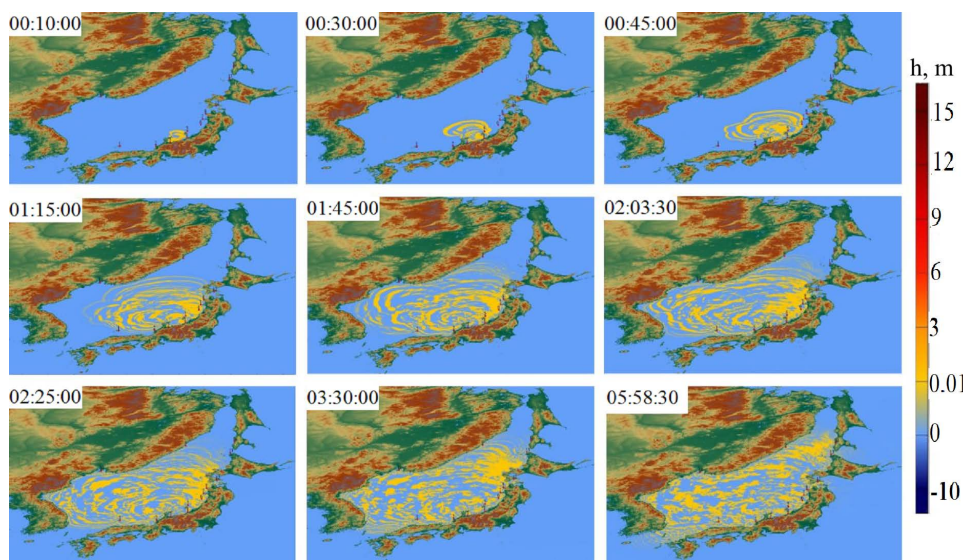


Fig. 6. Propagation of tsunami waves across the computed water area in scenario 4

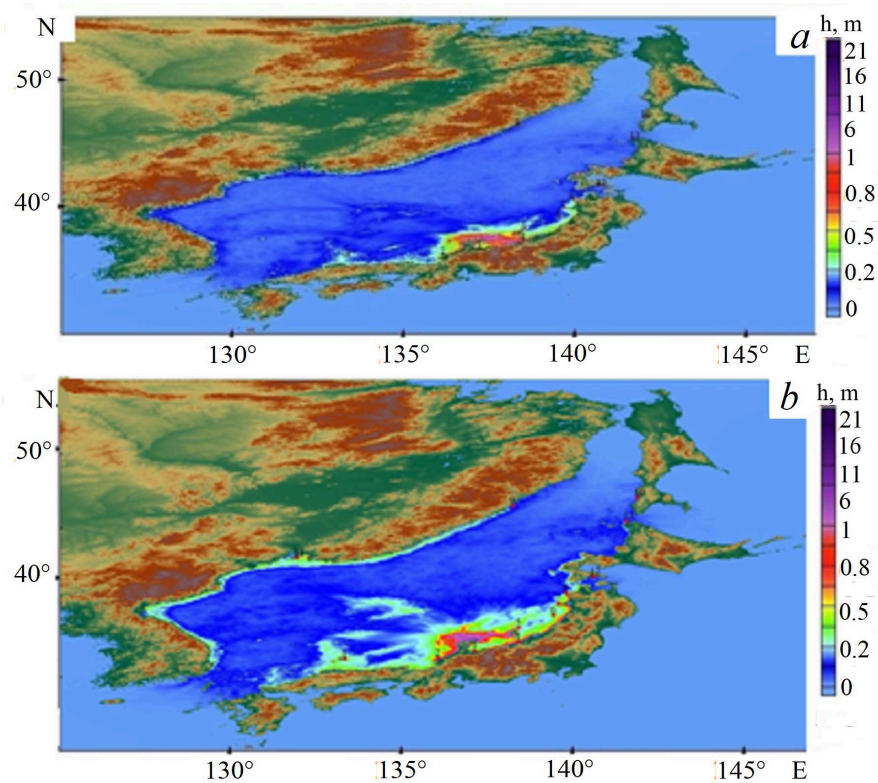


Fig. 7. Distribution of maximum wave heights across the computed water area in scenarios 1 (*a*) and 4 (*b*)

Using the computation data for scenario 4, 3D histograms of height distribution in Toyama Bay, Chuba, Tohoku, Kansai regions and Sado Island were constructed (Fig. 8). It is clearly seen that the average height of the incoming waves is 1 m in Toyama Bay and 5 m in the western part of the Noto Peninsula.

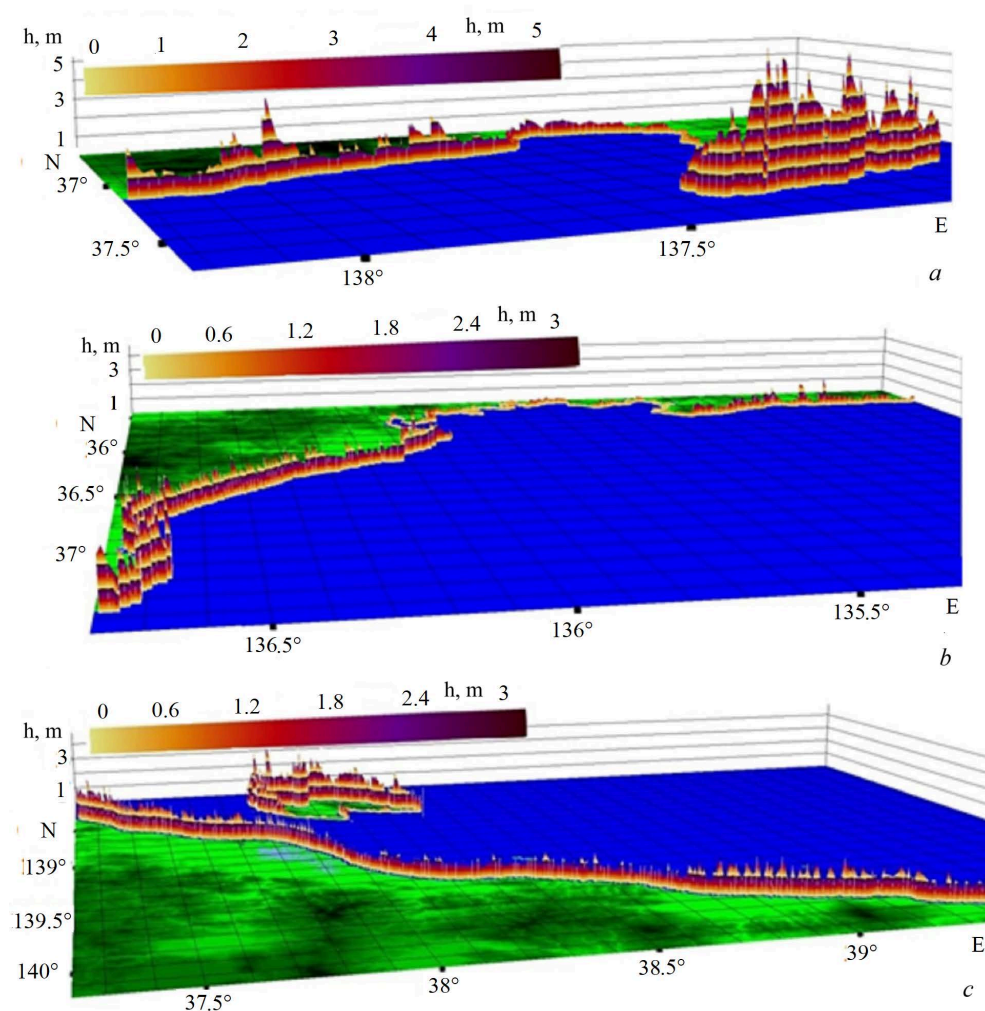


Fig. 8. 3D histograms of wave heights: *a* – Toyama Bay; *b* – Chuba and Kansai regions; *c* – Tohoku region and Sado Island (blue and green color correspond to sea and land respectively)

Fig. 8, *b* shows that the wave height was 3 m in the southern part of the Noto Peninsula and the average wave height was 1 m further in the Chuba region. Fig. 8, *c* demonstrates clearly that the average height of incoming waves in the northern part of the Tohoku region was 1 m, but the wave height in the northern part of Sado Island was 2.5 m on average.

Analysis of results of tsunami numerical simulation during the earthquake on 01.01.2024 in Japan

Fig. 9 shows 2D histograms of tsunami wave heights for different sections of the computed coasts in four scenarios under consideration.

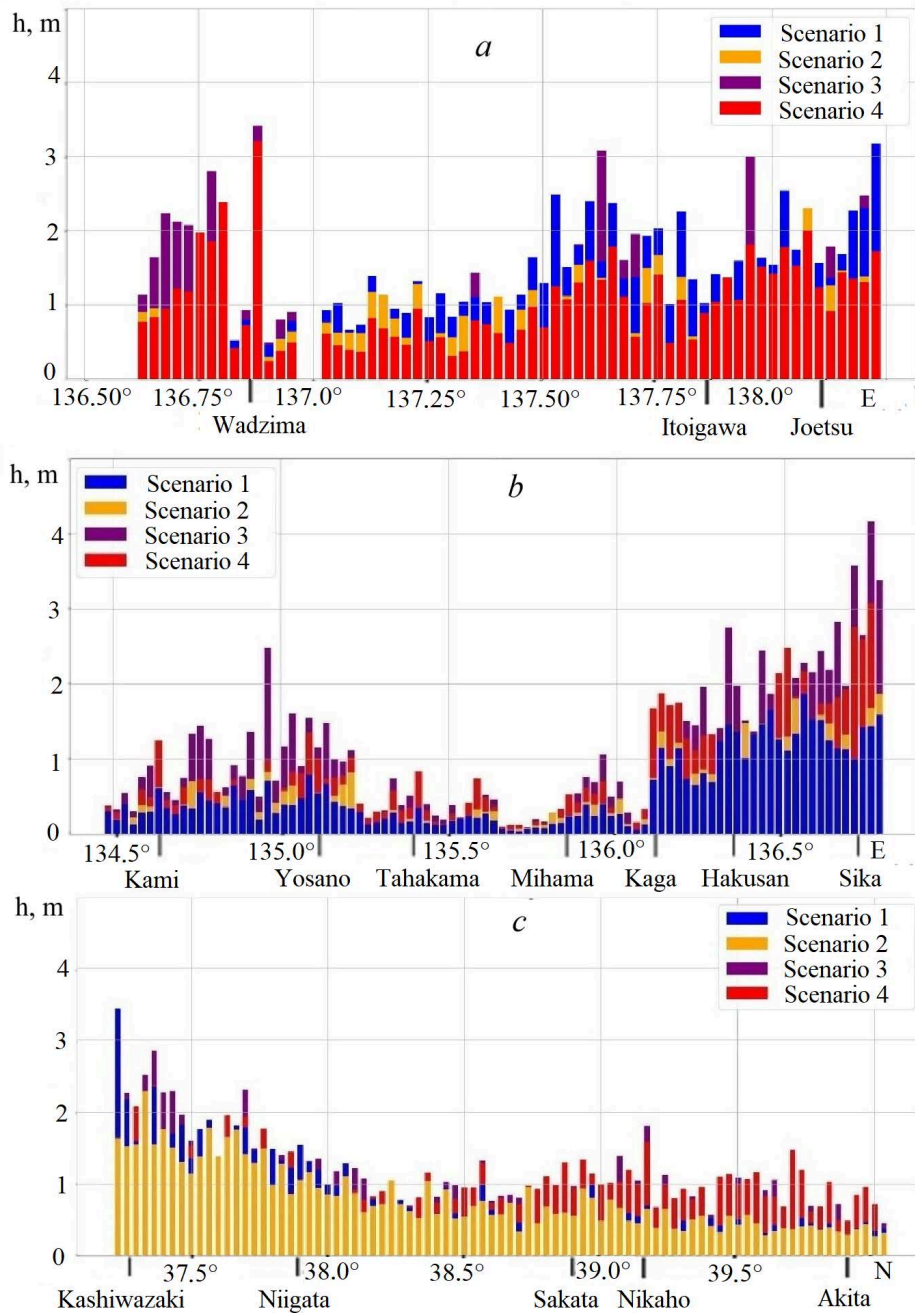


Fig. 9. 2D histograms of wave heights: *a* – Toyama Bay; *b* – Chuba and Kansai regions; *c* – Tohoku region and Sado Island

Fig. 9, a demonstrates clearly that wave height is 3 m in scenarios 3 and 4 in the area of Wadzima town; the wave height in scenario 4 is less than a meter and it is 1–1.5 m in scenarios 1, 2 and 3 in Itoigawa and Joetsu. Fig. 9, c shows that the wave heights in scenario 1 on the coasts of the Chuba and Kansai regions are on average 0.5 m less than in scenarios 3 and 4. This is due to the fact that block 1 is located inside Toyama Bay in scenario 1 and in the opposite part of the Noto Peninsula in the other scenarios. Fig. 9, c illustrates that the wave height in scenario 1 is greater than in the other scenarios near Toyama Bay (up to 38°N) and northwards of the bay the wave heights of scenario 4 predominate. This is also due to the location of the blocks, since the greatest wave heights of scenario 1 propagate from Toyama Bay and the waves of scenarios 2, 3, 4 go around Sado Island and reach the northern part of Honshu Island with large amplitudes. Table 3 provides data for all performed scenarios (scenarios 1–4) and *in situ* data from tide-gauge stations ⁵.

Table 3

**Sea level maximum rise (cm) near the settlements located
on the estimated water area coast**

Settlement	<i>In situ</i> data ⁵	Scenario 1	Scenario 2	Scenario 3	Scenario 4
Saigo	27.1	34.2	24.0	20.1	21.9
Mikuni	31.5	68.7	45.1	28.6	30.2
Toyama	79.4	124.8	81.8	78.6	85.0
Kashiwazaki	40.2	121.3	71.2	53.5	65.4
Sado	32.0	37.2	20.1	31.4	24.6
Oga	27.4	62.3	26.0	31.2	31.4
Fukauro	33.9	25.2	10.0	23.4	28.5
Vladivostok	28.0	34.0	18.4	29.5	27.8
Hakodate	9.9	2.6	1.5	3.9	3.3
Wakkanai	8.5	2.8	1.8	5.7	7.5
Sosunovo	11.4	7.1	3.5	7.6	10.7
Kholmsk	12.0	1.2	1.0	3.5	4.1

Discussion of results

The purpose of this work was to obtain wave characteristics in the Sea of Japan waters based on simulation for which 14 scenarios were considered; 4 of them with

the best wave characteristics of the process are presented in this work. Available publications on this earthquake were analyzed during the study [6–9]. A comparison of the obtained results with the data from the above publications (in most detail with the data from [6, 7] (Table 4)) performed for simulation earthquake sources, the localization of which is close to that proposed in our work, shows that the data of our numerical simulation are mainly close to the tide-gauge data at the corresponding stations with an accuracy of 5–6 cm. Where a significant difference between the tsunami amplitude and the calculated height takes place, it can be explained by complex physical processes in Toyama Bay, such as re-reflection, edge waves and bay resonance phenomena [6–9].

Table 4

Sea level maximum rise (cm) near the settlements located on the estimated water area coast (data from different sources)

Settlement	<i>In situ</i> data [7]	Scenario 4	Data from [6]
Saigo	27.1	21.9	22
Mikuni	31.5	30.2	40
Toyama	79.4	85.0	75
Kashiwazaki	40.2	65.4	60
Sado	32.0	24.6	10
Oga	27.4	31.4	18
Fukaura	33.9	28.5	19
Vladivostok	28.0	27.8	5
Hakodate	9.9	3.3	–
Wakkanai	8.5	7.5	6
Sosunovo	11.4	10.7	3
Kholmsk	12.0	4.1	3

Thus, at Kashiwazaki station, all models, both our and those used in [6, 7], overestimate the tsunami amplitude (from 89.4 to 227.1 cm). According to our computation, the data spread at this point was from 53.5 to 121.3 cm with a change in the localization and dynamics of the earthquake source. However, scenario 4, chosen as the most adequate, provided a calculated value of 65.4 cm, which also exceeded the observed maximum amplitude at this point.

According to the observations, the maximum amplitude in the Toyama station area was 79.4 cm; according to scenario 4, we obtained a maximum wave displacement of 85.0 cm, i.e., a difference of 5.6 cm. In [7], the maximum amplitude for this point was 79.4 cm according to simulation data, and in [6] – 75 cm. In other words, the difference between the calculated and *in* natural data in [6, 7] was 4.4 and 4.2 cm, respectively, i.e., 1.2 and 1.4 cm less than our corresponding data. Although the differences in both computed from [6, 7] and our are, in our opinion, within the framework of the source simulation accuracy, work [6] suggests that such a difference is possible in the presence of an additional landslide source to the seismic one, which is confirmed by the results of simulation performed by the authors of the work. The data in the remaining points in our computation have values that are quite close to the observed amplitudes, except for Wakkanai and Kholmsk. Thus, the maximum wave amplitude in Vladivostok is 28 cm and the computed values are 27.8 cm. These values are 11.4 and 10.7 cm, respectively, and their difference is 0.7 cm in Sosunovo village.

Conclusion

The computations using the block-keyboard earthquake model presented in this paper showed that it was especially important to take into account bottom geomorphology and geodynamics of tectonic processes for the earthquake that occurred in the Sea of Japan on 01.01.2024. This model permits to consider the initial stress distribution in the earthquake preparation zone as well as the dynamic transient process of forming the distribution of bottom displacements. Earthquake sources of various localizations with different shapes of the blocks that comprise it were considered. The most appropriate shape for simulating an intraplate active fault was the source with a long triangular block in the northwest of Nota Island. Numerical simulation results showed that the keyboard earthquake model made it possible to simulate adequately even such complex earthquake sources as the one that occurred in the northwest of Nota Island. A comparison of the obtained computation data with the amplitude of the maximum tsunami wave height from tide-gauge stations provided an value of less than 6 cm, except for three points.

REFERENCES

1. Holzer, T.L., 1995. The 1995 Hanshin-Awaji (Kobe), Japan, Earthquake. *GSA Today: A Publication of the Geological Society of America*, 5(8), pp. 154-167. [online] Available at: <https://rock.geosociety.org/gsatoday/archive/5/8/pdf/i1052-5173-5-8-sci.pdf> [Accessed: 28 September 2024].
2. Baranova, N.A., Kurkin, A.A., Mazova, R.Kh. and Pararas-Carayannis, G., 2015. Comparative Numerical Simulation of the Tohoku 2011 Tsunami. *Science of Tsunami Hazards*, 34(4), pp. 212-230.

3. Lobkovsky, L., Garagash, I., Baranov, B., Mazova, R. and Baranova, N., 2017. Modeling Features of Both the Rupture Process and the Local Tsunami Wave Field from the 2011 Tohoku Earthquake. *Pure and Applied Geophysics*, 174, pp. 3919-3938. <https://doi.org/10.1007/s00024-017-1539-5>
4. Simons, M., Minson, S.E., Sladen, A., Ortega, F., Jiang, J., Owen, S.E., Meng, L., Ampuero, J.-P., Wei, S. [et al.], 2011. The 2011 Magnitude 9.0 Tohoku-Oki Earthquake: Mosaicking the Megathrust from Seconds to Centuries. *Science*, 332(6036), pp. 1421-1425. <https://doi.org/10.1126/science.1206731>
5. Lobkovsky, L.I. and Baranov, B.V., 1984. A Key Model of Strong Earthquakes in Island Arcs and Active Continental Margin of Zones. *Doklady Akademii Nauk SSSR*, 275(4), pp. 843-847 (in Russian).
6. Masuda, H., Sugawara, D., Cheng, A.-C., Suppasri, A., Shigihara, Y., Kure, S. and Imamura, F., 2024. Modeling the 2024 Noto Peninsula Earthquake Tsunami: Implications for Tsunami Sources in the Eastern Margin of the Japan Sea. *Geoscience Letters*, 11, 29. <https://doi.org/10.1186/s40562-024-00344-8>
7. Fujii, Y. and Satake, K., 2024. Slip Distribution of the 2024 Noto Peninsula Earthquake (M_{JMA} 7.6) Estimated from Tsunami Waveforms and GNSS Data. *Earth, Planets and Space*, 76, 44. <https://doi.org/10.1186/s40623-024-01991-z>
8. Yuhi, M., Umeda, S., Arita, M., Ninomiya, J., Gokon, H., Arikawa, T., Baba, T., Imamura, F., Kumagai, K. [et al.], 2024. Dataset of Post-Event Survey of the 2024 Noto Peninsula Earthquake Tsunami in Japan. *Scientific Data*, 11, 786. <https://doi.org/10.1038/s41597-024-03619-z>
9. Shirai, T., Enomoto, Y., Haga, K., Tokuta, T., Arikawa, T., Mori, N. and Imamura, F., 2024. Potential for Tsunami Detection via CCTV Cameras in Northeastern Toyama Prefecture, Japan, Following the 2024 Noto Peninsula Earthquake. *Geoscience Letters*, 11, 28. <https://doi.org/10.1186/s40562-024-00343-9>
10. Wells, D.L. and Coppersmith, K.J., 1994. New Empirical Relationships among Magnitude, Rupture Length, Rupture Width, Rupture Area, and Surface Displacement. *Bulletin of the Seismological Society of America*, 84(4), pp. 974-1002. <https://doi.org/10.1785/BSSA0840040974>
11. Sielecki, A. and Wurtele, M., 1970. The Numerical Integration of the Nonlinear Shallow-Water Equations with Sloping Boundaries. *Journal of Computational Physics*, 6(2), pp. 219-236. [https://doi.org/10.1016/0021-9991\(70\)90022-7](https://doi.org/10.1016/0021-9991(70)90022-7)

Submitted 17.07.2024; approved after review 29.07.2024;
accepted for publication 12.09.2024.

About the authors:

Raisa Kh. Mazova, Professor of Applied Mathematics Department, Nizhny Novgorod State Technical University n. a. R.E. Alekseev (24 Minina Str., Nizhniy Novgorod, 603155, Russian Federation), DSc. (Phys.-Math.), Professor, **ORCID ID: 0000-0003-2443-149X**, **Scopus Author ID: 6506297372**, raissamazova@yandex.ru

Aleksandr A. Martynenko, Master's Student, Autonomous Non-Commercial Organization of Higher Education "Central University" (7, Building 1, Gasheka Str., Moscow, 123056, Russian Federation), martynenko.busy@gmail.com

Andrey A. Kurkin, Vice-Rector for Research, Nizhny Novgorod State Technical University n. a. R.E. Alekseev (24 Minina Str., Nizhniy Novgorod, 603155, Russian Federation), Leading Research Associate, V. I. Il'ichev Pacific Oceanological Institute, Far Eastern Branch of RAS, DSc. (Phys.-Math.), RAS Professor, **ORCID ID: 0000-0003-3828-6406**, **Scopus Author ID: 7003446660**, **ResearcherID: A-1972-2014**, aakurkin@gmail.com

Contribution of the co-authors:

Raisa Kh. Mazova – preparation of the paper text, problem formulation and statement, qualitative and quantitative analysis of the results

Aleksandr A. Martynenko – debugging a computer program for solving the problem, constructing drawings, participating in a discussion of paper materials

Andrey A. Kurkin – scientific supervision, data systematization, qualitative analysis of results and text revision

The authors have read and approved the final manuscript.

The authors declare that they have no conflict of interest.

Estimates of Available Potential Energy Budget in the Black Sea Using Different Schemes for Calculating Heat and Salt Advective Transport

O. A. Dymova

Marine Hydrophysical Institute of RAS, Sevastopol, Russian Federation

✉ olgadymova@mhi-ras.ru

Abstract

Purpose. The study is purposed at analyzing the available potential energy and its budget components in the Black Sea based on the results of numerical circulation modeling using a new temperature and salinity approximation scheme in the advective transport operator.

Methods and Results. Two numerical experiments were carried out based on the MHI model versions differing from each other in their approximation schemes of advective terms. The difference between the schemes is that in experiment 1, the condition of conserving temperature and salinity in the first and second degrees is satisfied, whereas in experiment 2 – temperature in the first and third degrees and salinity in the first and fifth degrees are conserved. It is found that application of the new scheme is accompanied by an increase in the available potential energy reserve by on average 30% over a year. The difference is conditioned by a decrease in both horizontal diffusion in a warm season and consumption of available potential energy through the buoyancy work in a cold season. The modeling results validated by the temperature and salinity measurement data from the MHI Oceanographic Data Bank show that application of the new approximation scheme permits to specify the density field and the energy characteristics in the Black Sea upper layer. Below the 300 m horizon, the discrepancies between the model and *in-situ* thermohaline fields in two experiments are minor, whereas the qualitative and quantitative distinctions in energy fields are significant: difference in the values of available potential energy in the basin central and periphery parts as well as the area of zones with the extreme buoyancy work values increase.

Conclusions. Application of the new approximation scheme of temperature and salinity in the advective transport operator makes it possible to specify the field density and, as a consequence, to obtain more accurate estimates of the available potential energy of sea circulation. In the Black Sea upper layer (the main pycnocline layer and above), the difference between the fields of energy characteristics calculated in two experiments is due to the differences in spatial distribution of density anomalies, at that the anomaly absolute values and the maximum energy values in the experiments are close in their magnitudes. Below the pycnocline layer, application of the new scheme is followed by the growth of available potential energy since the temperature and salinity changes lead to an increase in the gradients of density anomalies normal to the coast.

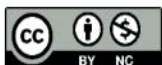
Keywords: Black Sea, modeling, circulation, available potential energy, buoyancy work, density anomaly, thermohaline characteristics

Acknowledgements: The study was carried out within the framework of the state assignment theme of FSBSI FRC MHI FNNN-2024-0001.

For citation: Dymova, O.A., 2024. Estimates of Available Potential Energy Budget in the Black Sea Using Different Schemes for Calculating Heat and Salt Advective Transport. *Physical Oceanography*, 31(5), pp. 679-693.

© 2024, O. A. Dymova

© 2024, Physical Oceanography



Introduction

Mesoscale eddy motions in the oceans and seas are one of the main mechanisms of vertical and horizontal matter and energy redistribution in marine water areas. According to classical concepts [1, 2], the formation of such eddies is associated with the release of some part of the ocean potential energy called the available potential energy (APE) and its transformation into eddy kinetic energy. The APE budget study makes it possible to estimate the role of the main physical forces in the mesoscale sea dynamics. Based on estimates of energy fluxes, it was shown in [3] that baroclinic production caused by the transfer of density anomalies by currents and potential and kinetic conversion determined by the vertical eddy flux of buoyancy force are the main mechanisms of APE transformation for the World Ocean. In [4], the results of a study of global eddy APE are presented and, in addition to [3], it is indicated that in the upper mixed layer of the ocean, diabatic mixing, atmosphere interaction at the water–air boundary and internal diffusion play a significant role in the APE budget. The literature also shows regional features of the APE distribution and evolution in large scale ocean currents. Thus, in [5], estimates of baroclinic conversion rate of APE were carried out and it was found that since it was an order of magnitude greater than the rate of barotropic conversion of eddy kinetic energy, it was this factor that explained the baroclinic nature of the Gulf Stream instability. In [6], it is shown that not the wind effect, but APE variations as a result of the thermal ocean–atmosphere interaction play a decisive role in the budget of eddy kinetic energy in the Kuroshio Extension region.

In modern conditions, numerical modeling is one of the main tools for diagnosing and predicting hydrodynamic and energy characteristics of circulation. Traditionally, the equations of the energy change rate are derived from the differential equations of ocean energy [3, 7], but their discrete analogues, which are not an exact consequence of the finite-difference equations of the ocean model, will introduce an error in the quantitative estimates of energy fluxes. In addition, to estimate APE correctly when moving from the difference equation of advection–diffusion of density to the equation of energy change rate, it is necessary to approximate the density adequately at those points of the difference template where it is not calculated directly. Taking into account the above considerations, a scheme for the approximation of the equation of APE change rate is proposed in [8]. It is obtained as a result of a strict algebraic transformation of the finite–difference equations of the model. In [9], a new scheme for the approximation of temperature and salinity on the cell edges is described (for a finite–difference template, where temperature and salinity are calculated at the cell center), which provides a divergent form of the density advection equation for an arbitrary polynomial dependence of density on temperature and salinity.

The present paper is an extended version of the report of the 14th International Conference “Waves and Vortices in Complex Media” 2023 [10] continuing the numerical analysis of the Black Sea energy [11]. To estimate how the scheme for calculating thermohaline characteristics affects the spatial and temporal variability

of energy fluxes that form APE, this paper includes a circulation modeling based on the approximations proposed in [8, 9]. All terms of the APE budget equation were calculated and analyzed and a comparison was made with previously obtained data.

Calculation method and data used

Analysis of the APE distribution features in the Black Sea is carried out using the example of circulation modeling in 2016. Numerical experiments were carried out using the eddy resolving model of Marine Hydrophysical Institute with a resolution of 1.6 km [11]. The model is constructed based on the complete system of equations of ocean thermohydrodynamics in the Boussinesq approximation and hydrostatics. The state equation is represented by a nonlinear dependence of density on temperature and salinity. Vertical turbulent mixing is parameterized by the Mellor–Yamada 2.5 closure model [12], horizontal diffusion in the heat and salt equations as well as horizontal viscosity in the equations of motion are described by the Laplace operator to the second degree with constant coefficients of the corresponding dimension. Wind stress, heat fluxes, precipitation and evaporation according to the ERA5 ¹ reanalysis data are specified as boundary conditions on the free surface. On the solid lateral sections of the boundary, the conditions of equality to zero of the normal velocity and the normal derivative of the tangential velocity as well as the equality to zero of their Laplacians are set. The equality to zero of the normal derivatives and their Laplacians are set for the temperature and salinity. On the bottom, the no-slip condition and the condition of the absence of normal heat and salt fluxes are set. The model takes into account the climatic runoff of rivers and water exchange through straits [13] and Dirichlet conditions are set on the liquid sections of the boundary. Correction of inaccuracies in the specification of the heat flux from the atmosphere to the sea surface is carried out by assimilating the satellite sea surface temperature [14]. The basin bathymetry is constructed on the basis of the EMODnet digital depth array ². The finite–difference approximation of the model equations is carried out on grid C [15]. The complete physical formulation of the problem, the coefficients used and the parameterizations are presented in detail in [11].

Two numerical experiments on the circulation modeling and the exact calculation of the APE budget were carried out in the work. The difference between them is in the method of temperature T and salinity S calculating in the finite–difference operator of advective transport which, for example, has the following form for the temperature (similarly for salinity):

¹ Hersbach, H., Bell, B., Berrisford, P., Biavati, G., Horányi, A., Muñoz Sabater, J., Nicolas, J., Peubey, C., Radu, R. [et al.], 2018. ERA5 Hourly Data on Single Levels from 1940 to Present: Data Set. In: *Copernicus Climate Change Service (C3S) Climate Data Store (CDS)*. [Accessed: 25 June 2023]. <https://doi.org/10.24381/cds.adbb2d47>

² EMODnet. *EMODnet European Marine Observation and Data Network*. [online] Available at: <https://doi.org/10.12770/ff3aff8a-cff1-44a3-a2c8-1910bf109f85> [Accessed: 27 August 2024].

$$ADV^T = [u_{i+1/2,j,k}(T_{i+1/2,j,k} - T_{i,j,k}) - u_{i-1/2,j,k}(T_{i-1/2,j,k} - T_{i,j,k})]h_x^{-1} + \\ + [v_{i,j+1/2,k}(T_{i,j+1/2,k} - T_{i,j,k}) - v_{i,j-1/2,k}(T_{i,j-1/2,k} - T_{i,j,k})]h_y^{-1} + \\ + [w_{i,j,k+1/2}(T_{i,j,k+1/2} - T_{i,j,k}) - w_{i,j,k-1/2}(T_{i,j,k-1/2} - T_{i,j,k})](h_z^k)^{-1},$$

where u, v, w are components of the current velocity vector; h is spatial step size in the corresponding direction; i, j, k are coordinates of the model grid nodes in the space of grid functions corresponding to the middle of the cell on grid C [16]. Since temperature, salinity and density on grid C are calculated at the center of the model cell [15], their values on the cell edges (half-integer indices) are, strictly speaking, unknown. It is shown in [9] that under adiabatic conditions and in the absence of external sources with a nonlinear equation of state independent of pressure, to preserve the discrete integral of density, it is advisable to use such approximations of the nonlinear terms on the cell edges so that along with T and S , T^m and S^l are preserved, where m and l are positive integers greater than 2. In experiment 1, the formula below was used to calculate T and S on the cell edges

$$T_{i+1/2,j,k} = \frac{T_{i+1,j,k} + T_{i,j,k}}{2}, \quad S_{i+1/2,j,k} = \frac{S_{i+1,j,k} + S_{i,j,k}}{2}, \quad (1)$$

and the detailed derivation of the formula in experiment 2 is shown in [9]:

$$S_{i+1/2,j,k} = \frac{4}{5} \frac{S_{i+1,j,k}^4 + S_{i+1,j,k}^3 S_{i,j,k} + S_{i+1,j,k}^2 S_{i,j,k}^2 + S_{i+1,j,k} S_{i,j,k}^3 + S_{i,j,k}^4}{S_{i+1,j,k}^3 + S_{i+1,j,k}^2 S_{i,j,k} + S_{i+1,j,k} S_{i,j,k}^2 + S_{i,j,k}^3}, \quad (2)$$

$$T_{i+1/2,j,k} = \frac{2}{3} \frac{T_{i+1,j,k}^2 + T_{i+1,j,k} T_{i,j,k} + T_{i,j,k}^2}{T_{i+1,j,k} + T_{i,j,k}}.$$

Formulas (1) and (2) describe the change in T and S along the x coordinate (for y and z similarly). For both calculation methods, the finite-difference operator of advective transport has the second order of approximation. The difference between the experiments is that T, S and T^2, S^2 were preserved in experiment 1 and T, S and T^3, S^5 in experiment 2. Approximation (2) has limitations at $|T| \ll 1^\circ\text{C}$ and/or $|S| \ll 1\text{‰}$. As for the Black Sea conditions, such a situation is practically atypical and it is not taken into account in the presented calculations.

The APE change rate was calculated using the following formula

$$\frac{\partial APE_{i,j,k}}{\partial t} + \left\{ \delta_x(u_{i,j,k} a_{i,j,k}^{pe}) + \delta_y(v_{i,j,k} a_{i,j,k}^{pe}) + \delta_z(w_{i,j,k} a_{i,j,k}^{pe}) \right\} (\delta_z \rho_k^s)^{-1} = \\ = -g \overline{w_{i,j,k}^z} \rho_{i,j,k}^* + \omega_{i,j,k} + (D_H + D_V)_{i,j,k},$$

$$APE_{i,j,k} = a_{i,j,k}^{pe} (\delta_z \rho_k^s)^{-1}, \quad a_{i,j,k}^{pe} = g \frac{(\rho_{i,j,k}^*)^2}{2}, \quad (3)$$

where APE is APE density; δ is finite-difference analogue of the differentiation operator with respect to the corresponding coordinate; g is acceleration of gravity; ρ^s is average density of sea water over the area of the k layer; ρ^* is density anomaly calculated as the difference between the local and average density over the layer; D_H ,

D_V are horizontal and vertical diffusion components of the APE budget; ω is designation of additional difference terms that have no analogue in the differential equation and result from the rigorous derivation of formula (3) from the finite-difference equations of the model. Note that ω includes terms that take into account the change in density anomalies on the cell edges and are associated with advective transport, and D is additional diffusion terms. The derivation and full form of the terms ω , D_H and D_V are presented in [8]. For ease of interpretation of the experimental results, equation (3) is rewritten in symbolic form:

$$\frac{\partial APE}{\partial t} = ADV + WRG + DIFH + DIFV,$$

where ADV is APE change due to advective transport, WRG – due to the buoyancy work, $DIFH$ and $DIFV$ – due to horizontal and vertical diffusion, respectively.

As a result of numerical experiments for each day of 2016, 3D fields of temperature, salinity, density, current velocity, density anomalies, APE field and its budget components were obtained. Validation of the results of thermohaline field modeling was carried out based on the data obtained from the MHI Oceanographic Data Bank [17]. Contact measurements of temperature and salinity were carried out by Argo profiling floats as well as during R/V *Professor Vodyanitsky* cruises in 2016. Table presents the root mean square deviations (RMSD) between the model and natural values of temperature and salinity for all available observational data. As can be seen from Table, in experiment 2, the RMSD of temperature in the 30–100 m layer decreases by 25%, and the average RMSD of salinity for horizons from 0 to 100 m decreases by 21%. The difference between the RMSD for the two experiments is insignificant for deep water horizons below 300 m.

Root mean square deviation between the model and *in-situ* temperature and salinity

Depth, m	Experiment 1		Experiment 2	
	Temperature, °C	Salinity, ‰	Temperature, °C	Salinity, ‰
0–5	0.79	0.28	0.94	0.22
5–30	1.53	0.23	1.54	0.17
30–100	1.12	0.67	0.84	0.56
100–300	0.26	0.48	0.27	0.50
300–800	0.05	0.09	0.07	0.10
800–1500	0.03	0.08	0.03	0.08

Comparison of the modeling results with *in-situ* data showed that the decrease in the RMSD in the upper 100 m layer of the Black Sea when using approximation scheme (2) from the point of view of practical hydrology was manifested in a decrease in the thickness of the upper mixed layer in the winter period and a decrease in the depth of the upper boundary of the thermocline layer in summer in the central part of the sea.

Results

Analysis of the integral and spatial distributions of the APE budget components and comparison with distribution of thermohaline and dynamic characteristics of circulation based on the results of numerical experiments were carried out. Both experiments started with the same initial conditions, and significant differences in the values of the model parameters appeared in April. It was found that, starting from spring, the volume-average APE in experiment 2 exceeded its values in experiment 1; this difference was about 30% on average per year. Since the Black Sea is characterized by strong seasonal variability of hydrophysical fields [18], summer (May–June) and winter (November–December) periods were considered for a more detailed comparison.

Fig. 1 shows the change in the volume-average *APE*, *WRG* and *DIFH* over time for two experiments in summer and winter 2016. Analysis of the change in the APE budget components over time showed that in summer season, the APE increase in experiment 2 (Fig. 1, *a*) was associated with energy loss decrease due to horizontal diffusion (Fig. 1, *b*). At the same time, the spatial distribution of the *DIFH* component indicates horizontal diffusion weakening in the coastal zone on the northwest shelf (NWS) and in the deep water part of the sea [10, p. 379, Fig. 1, *b*]. Analysis of the thermohaline characteristics on the NWS in experiment 2 revealed a decrease in horizontal salinity gradients which determines energy flux decrease due to horizontal diffusion. In the central part, the diffusion flux decreases due to a more uniform spatial distribution of the density field.

According to the mathematical formulation of the problem in the MHI model, a positive *WRG* value corresponds to the APE transformation into kinetic energy, i.e., its decrease. For the curves shown in Fig. 1, *d*, the average values of the $\langle WRG \rangle_V$ parameter are $0.15 \cdot 10^{-5}$ and $0.01 \cdot 10^{-5}$ W for experiments 1 and 2, respectively. Thus, in winter, the increase in the APE store in experiment 2 (Fig. 1, *c*) is stipulated by a smaller amount of APE spent on transformation into kinetic energy. In addition, as shown in [10, p. 380, Fig. 2], the energy flux caused by the transformation of kinetic energy into available potential energy increases in the western and southwestern parts of the continental slope in experiment 2. The *WRG* component is determined by the density and vertical velocity. Therefore, cooling and intensification of winter convection are the main reasons for the increase in APE store in winter.

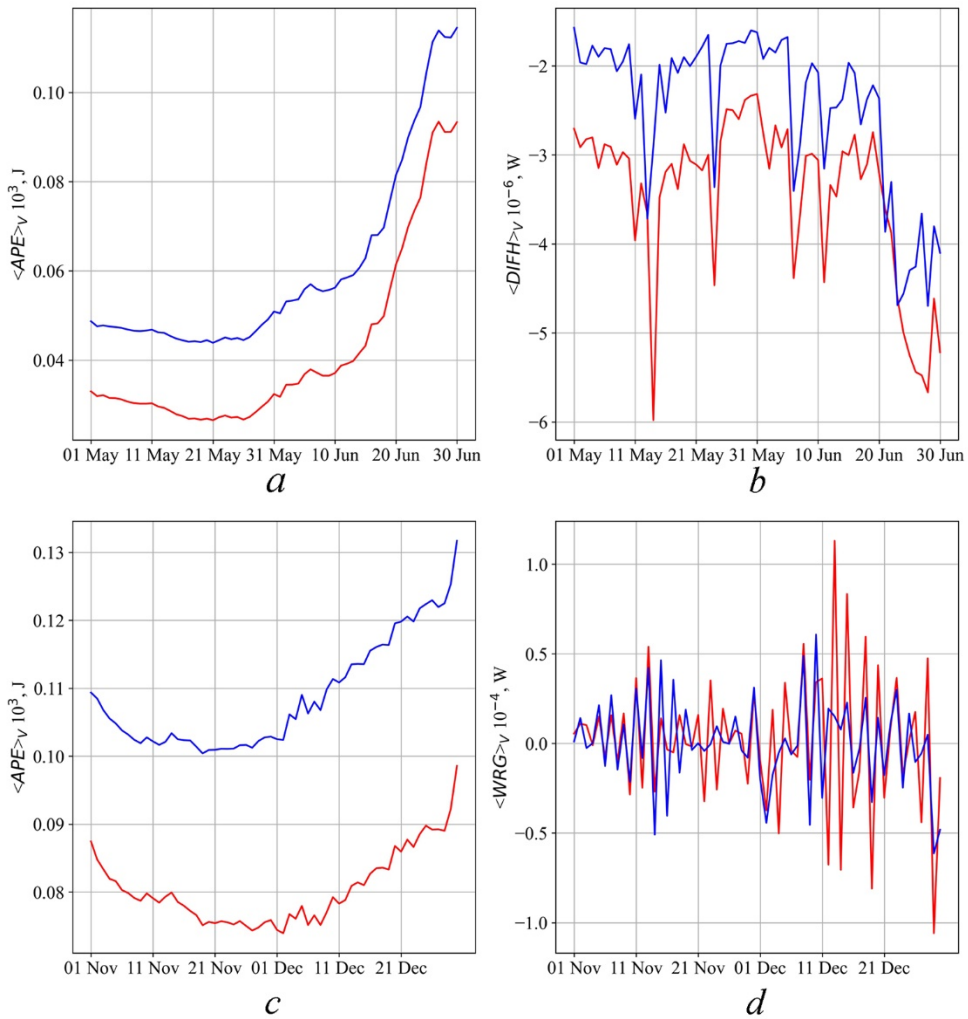


Fig. 1. Change over time of volume-average APE (*a*, *c*), horizontal diffusion of APE (*b*) and buoyancy work (*d*) for two experiments in May–June (*a*, *b*) and November–December (*c*, *d*) 2016. Red line is experiment 1, blue line is experiment 2

Comparison of the *APE* and *DIFH* curves in two experiments shown in Fig. 1 demonstrates the similarity of the temporal variability of the volume-average values of the energy characteristics. This behavior of the curves is probably due to the variability of external conditions. It was shown earlier in [19] that the upper 30 m sea layer most strongly affected by thermohaline forcing made maximum contribution to the APE store in the Black Sea. Since the boundary conditions for both experiments are the same, the variability over time of the average integral *APE* and *DIFH* values is almost identical in the experiments. The shift of the curves along the ordinate axis results from an increase in the average density anomaly due to changes in the thermohaline characteristics.

For summer and winter periods, the change in the APE store by depth was estimated for two experiments. For this purpose, the difference between the average

APE by volume of layer k in two calculations $\Delta APE_k = \langle APE_{\text{exp2}} \rangle_{V_k} - \langle APE_{\text{exp1}} \rangle_{V_k}$ was calculated in each model layer. A positive value of ΔAPE_k indicates that the APE store in layer k is higher in experiment 2. It was found that in summer, in the 5–40 m layer, the average APE was higher in experiment 1 (Fig. 2, *a*, curves 3–9). Starting from the 60 m horizon (Fig. 2, *a*, curves 11 and below), the APE in experiment 2 exceeds the values in experiment 1 reaching a maximum at layer 21 (Fig. 2, *a*, curve 21) corresponding to the 500–700 m depth.

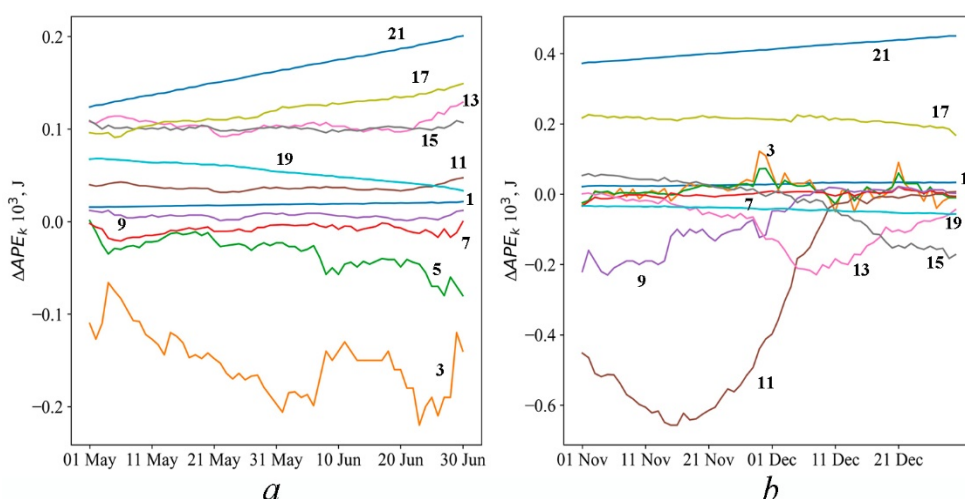


Fig. 2. Change over time of difference ΔAPE_k in May–June (*a*) and November–December (*b*) 2016. Numerals are the layer numbers (index k)

For winter season in the 40–100 m layer, the ΔAPE_k value is negative (Fig. 2, *b*, curves 9–13), therefore, the APE in the first experiment is higher than in the second one. For deep water horizons in winter, as well as in summer, the APE store in experiment 2 is higher than in experiment 1. However, the maximum difference between the calculations in winter is almost twice as large.

Discussion

Initial and boundary conditions for the numerical experiments were the same varying only in the scheme for calculating the temperature and salinity in the advective heat and salt transfer operator. No other changes to the finite-difference equations of the model or the values of the model constants were made. All the differences among the calculation results described above are directly or indirectly through a change in density due to a change in temperature and salinity advection. To determine the physical causes of the differences revealed, spatial distributions of the energy and hydrological characteristics of the circulation at different horizons in summer and winter periods will be considered in more detail. As shown above, in summer, the APE store in the upper sea layer is higher in experiment 1. Spatial distribution analysis of the APE density and local seawater

density anomaly in June shows that APE is smaller in the upper layer in experiment 2 (Fig. 3, *b*) due to the lower absolute values of the density anomaly on the NWS (Fig. 3, *d*) compared to experiment 1.

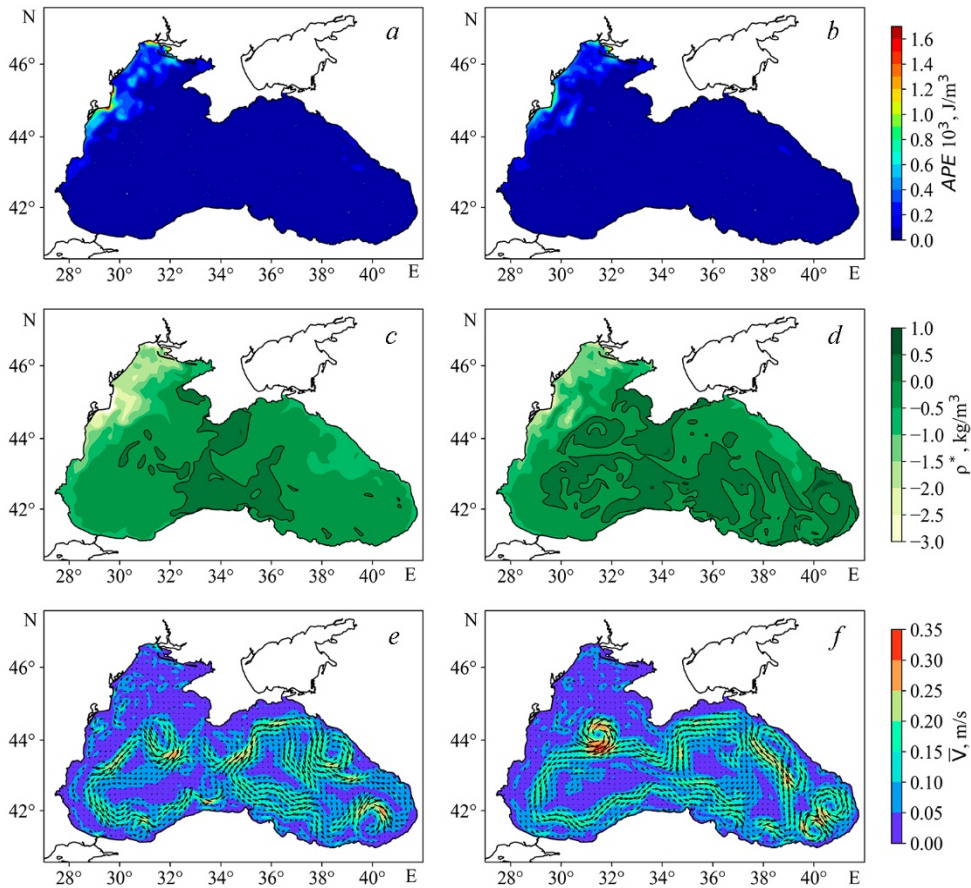


Fig. 3. Spatial distributions of APE (*a, b*), density anomaly (*c, d*) and current velocities (*e, f*) at the 5 m depth based on the results of experiments 1 (*a, c, e*) and 2 (*b, d, f*) on June 15, 2016

Decrease of the density anomaly module is due to lower temperature values and higher salinity compared to experiment 1. As can be seen from the results of the validation of thermohaline characteristics (Table), the use of the new approximation scheme (2) makes it possible to improve the reproduction of salinity in the upper 100 m layer. Since the density depends predominantly on salinity [20] in the Black Sea, it can be assumed that the density anomaly used in formula (3) was more correctly calculated in experiment 2. Consequently, the APE estimates obtained in experiment 2 are more realistic.

When comparing Figs. 3, *c* and 3, *d*, a difference in the area of positive density anomalies in the central part of the sea is observed, which has little effect on the APE spatial distribution, but shows similarity with the current velocity fields (Fig. 3, *e*

and *f*). Extensive positive anomalies correspond to denser waters within the Black Sea Rim Current in experiment 2 in summer indicating a more intense cyclonic circulation (Fig. 3, *f*) and upwelling of deep waters in the central part of the sea.

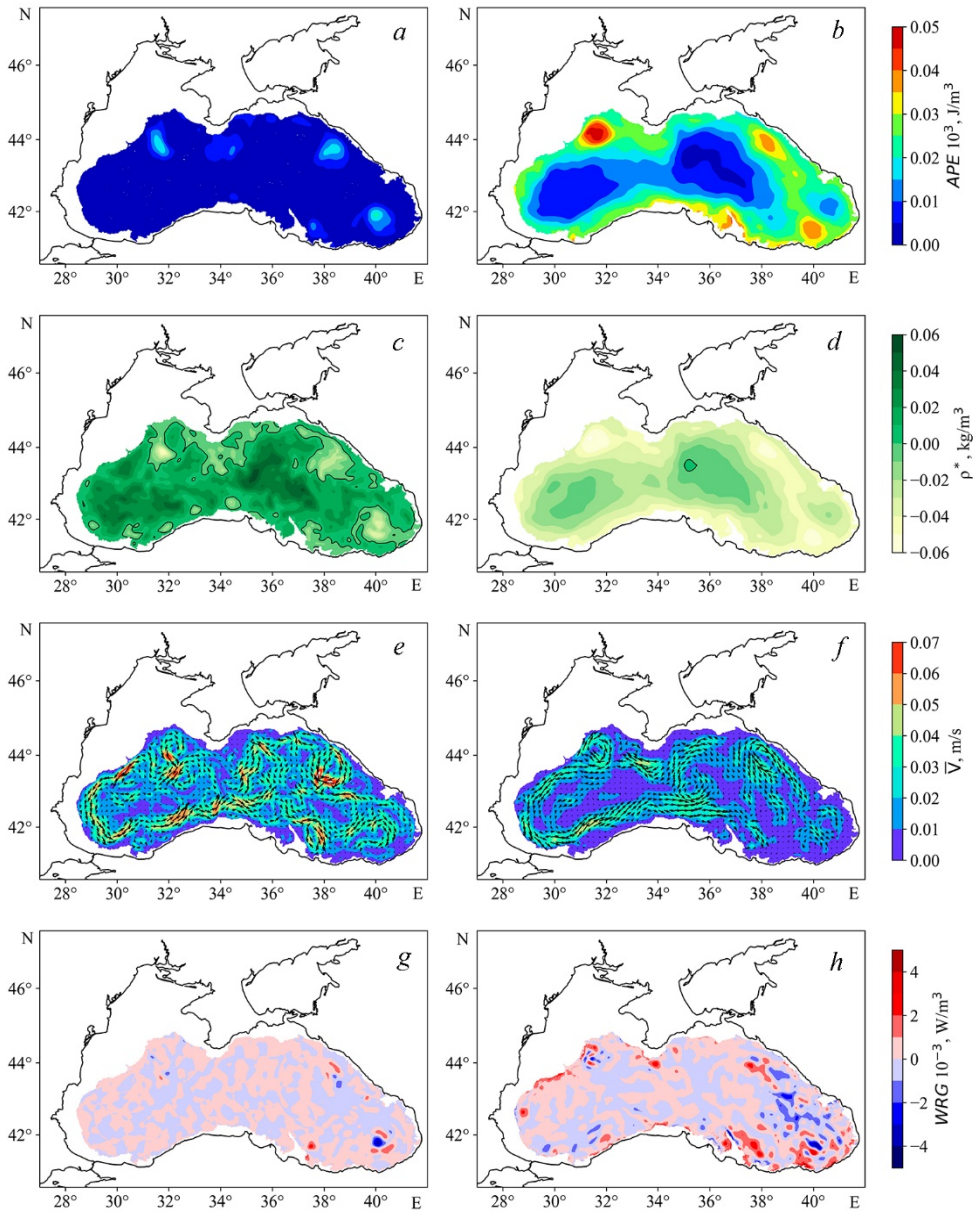


Fig. 4. Spatial distributions of APE (*a, b*), density anomaly (*c, d*), current velocities (*e, f*) and buoyancy work (*g, h*) at the 500 m depth based on the results of experiments 1 (*a, c, e, g*) and 2 (*b, d, f, h*) on June 15, 2016

At the deep horizons in summer (Fig. 4, *a, b*), the differences in the APE value are more significant than in the upper layer: firstly, the APE extremes in experiment 688

2 are approximately 2.5 times greater than in experiment 1; secondly, there is a significant difference in the APE value between the periphery and the central part of the sea. Comparison with the density anomaly fields shows that the increase in APE in experiment 2 is due to large absolute values of the density anomaly at the basin periphery (Fig. 4, *d*), whereas in experiment 1 the largest values are located in the center (Fig. 4, *c*). As shown in [19], such a structure of the APE fields and the density anomaly at the deep horizons is determined by mesoscale eddy variability. According to Fig. 4, *e* and *f*, the anticyclonic eddies near the continental slope have a clearer structure and their location coincides with the increased APE values in experiment 2. In addition, the analysis of the APE budget components showed that the contribution of the buoyancy work in the eddy zone increases in experiment 2 (Fig. 4, *h*).

For winter period, it was found that the greatest differences between the APE values in the two experiments were observed in the 40–100 m layer (Fig. 2, *b*). To identify their causes, the maps of the APE fields and density anomalies at the 50, 75, and 100 m horizons were analyzed. In accordance with Fig. 5, increased APE values are observed on the periphery of the basin in the western part of the sea in experiment 1 (Fig. 5, *a*) and these areas correspond spatially to the negative density anomalies (Fig. 5, *c*) in anticyclonic eddies. It is also evident that the spatial structure of the density anomaly fields in experiment 2 (Fig. 5, *d*) is significantly different from the experiment 1 data (Fig. 5, *c*).

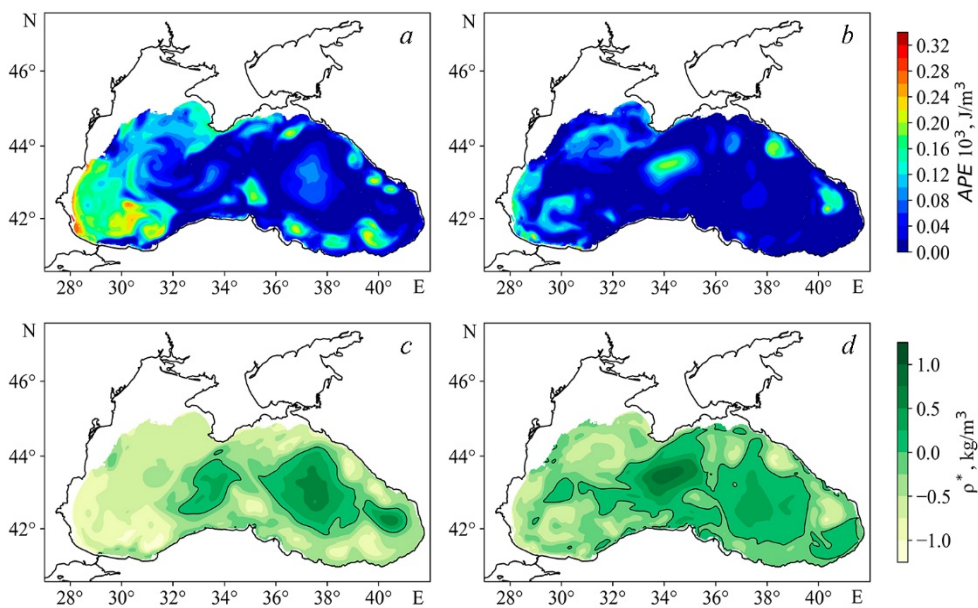


Fig. 5. Spatial distributions of APE (*a, b*) and density anomaly (*c, d*) at the 75 m depth based on the results of experiments 1 (*a, c*) and 2 (*b, d*) on December 15, 2016

Therefore, an additional estimate of the change in the temperature and salinity deviations over time from the measurement data for the southwestern part of the sea at the 50–100 m depths was carried out in winter. Three Argo profiling floats Nos. 3901852, 3901854, 3901855 were considered (the map of locations of the profiling stations is shown in Fig. 6, *a*). Fig. 6, *b* and *c* shows the model data deviations from those measured at the 75 m horizon. The average temperature deviation for 22.10.2016–28.12.2016 was -1.7 and $+0.1$ °C; the salinity deviation was 0.5 and 0.3‰ for experiments 1 and 2, respectively. As can be seen for the indicated floats in experiment 2, the deviations of the thermohaline characteristics decrease, therefore, the data are simulated more accurately than in experiment 1. Thus, for the winter season of 2016, the APE estimates obtained using the approximation schemes (2), (3) are more adequate to the real energy of the circulation.

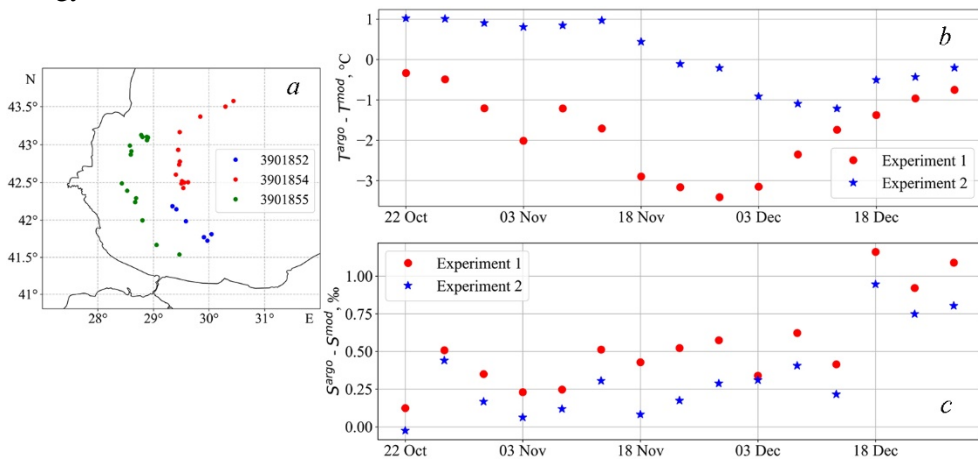


Fig. 6. Map of the locations of Argo profiling float stations (*a*), deviations of model temperature (*b*) and salinity (*c*) from the observation data at the 75 m depth in October–December 2016

For deep horizons in winter, the APE field structure is similar to that in summer, and increased values in experiment 2 are also observed on the basin periphery and by approximately two times exceed the experiment 1 data.

Conclusion

Based on the 2016 data, the paper analyses numerically the APE store and its budget components in the Black Sea obtained using a new scheme of temperature and salinity approximation in the advective transport operator for the heat and salt advection–diffusion equations in the MHI model (experiment 2). A comparison of the energy characteristics of the circulation is performed with the estimates obtained earlier based on the traditional approximation scheme (experiment 1). Differences in both integral values and spatial distribution of APE, buoyancy work and horizontal diffusion are obtained. It is found that the APE store in experiment 2 is 30%, on average per year, greater than in experiment 1. Moreover, in warm period, this

difference results from horizontal diffusion decrease, and in cold period, it is conditioned by a decrease in the APE amount spent on transformation into kinetic energy due to the buoyancy work.

As the analysis showed, the quantitative and qualitative discrepancies in the distributions of APE and its budget components between the results of the two experiments are due to differences in the fields of seawater density anomalies. In experiment 2 in the summer of 2016, the APE store in the upper layer was smaller than in experiment 1 due to a decrease in the density anomaly module on the NWS, and in winter, on the contrary, it was higher due to the formation of extensive areas of negative density anomalies in the western part of the sea corresponding to anticyclonic eddy formations. Throughout the year, the increased APE values below the 100 m horizon compared to experiment 1 are associated with an increase in density anomalies near the continental slope due to the intensification of mesoscale eddies.

As the validation of model thermohaline fields demonstrated, the use of the approximation scheme (2) permits a more accurate reproduction of salinity, and hence density, thus providing a more correct APE calculation in the Black Sea upper layer. Below the 300 m horizon, no significant discrepancies between the temperature and salinity in two calculations and observational data were found; but significant qualitative and quantitative differences were revealed for the energy characteristics: in experiment 2, the difference in APE values in the central part and on the basin periphery increases and the area of zones of extreme buoyancy work values increases.

According to the results of the study, the change in the model temperature and salinity associated with the new scheme for calculating the advective transfer of heat and salt causes a change not only in the density and APE, but also in the budget terms describing diffusion processes. The analysis showed that the areas of decreasing energy flux due to horizontal diffusion spatially correspond to the zones of decreasing horizontal salinity gradients. The indirect use of the new approximation scheme through a change in density helps to reduce the dissipation of available potential energy. It should also be noted that, according to preliminary estimates obtained in [9], a change in the temperature and salinity calculation scheme leads to an intensification of the upwelling of deep waters in the central part of the sea. Therefore, a change in advection affects vertical mixing and deep convection, however, this issue is beyond the scope of the presented work and is planned as a topic for a separate study.

The results obtained are useful for the analysis of the mechanisms of evolution of mesoscale eddies based on the estimate of the energy contributions of such physical processes as dissipation, instability, buoyancy work and pressure.

REFERENCES

1. Kamenkovich, V.M., Koshlyakov, M.N. and Monin, A.S., eds., 1986. *Synoptic Eddies in the Ocean*. Dordrecht: Springer, 444 p. <https://doi.org/10.1007/978-94-009-4502-9>
2. Gill, A.E., 1982. *Atmosphere – Ocean Dynamics*. New York: Academic Press, 662 p. [https://doi.org/10.1016/s0074-6142\(08\)x6002-4](https://doi.org/10.1016/s0074-6142(08)x6002-4)

3. Von Storch, J.-S., Eden, C., Fast, I., Haak, H., Hernandez-Deckers, D., Maier-Reimer, E., Marotzke, J. and Stammer, D., 2012. An Estimate of the Lorenz Energy Cycle for the World Ocean Based on the 1/10° STORM/NCEP Simulation. *Journal of Physical Oceanography*, 42(12), pp. 2185-2205. <https://doi.org/10.1175/JPO-D-12-079.1>
4. Guo, Y., Bishop, S., Bryan, F.O. and Bachman, S., 2022. A Global Diagnosis of Eddy Potential Energy Budget in an Eddy-Permitting Ocean Model. *Journal of Physical Oceanography*, 52(8), pp. 1731-1748. <https://doi.org/10.1175/JPO-D-22-0029.1>
5. Cronin, M. and Watts, D.R., 1996. Eddy-Mean Flow Interaction in the Gulf Stream at 68°W. Part I: Eddy Energetics. *Journal of Physical Oceanography*, 26(10), pp. 2107-2131. [https://doi.org/10.1175/1520-0485\(1996\)026<2107:EFIITG>2.0.CO;2](https://doi.org/10.1175/1520-0485(1996)026<2107:EFIITG>2.0.CO;2)
6. Yang, H., Chang, P., Qiu, B., Zhang, Q., Wu, L., Chen, Z. and Wang, H., 2019. Mesoscale Air-Sea Interaction and Its Role in Eddy Energy Dissipation in the Kuroshio Extension. *Journal of Climate*, 32(24), pp. 8659-8676. <https://doi.org/10.1175/JCLI-D-19-0155.1>
7. Holland, W.R., 1975. Energetics of Baroclinic Oceans. In: NAS, 1975. *Numerical Models of Ocean Circulation: Proceedings of a Symposium Held at Durham, New Hampshire, October 17–20, 1972*. Washington: National Academy of Sciences, pp. 168-177.
8. Demyshev, S.G., 2022. Discrete Equation for the Available Potential Energy as an Exact Consequence of the Numerical Model Equations. *Physical Oceanography*, 29(3), pp. 221-236. <https://doi.org/10.22449/1573-160X-2022-3-221-236>
9. Demyshev, S.G., 2023. Nonlinear Invariants of a Discrete System of the Sea Dynamics Equations in a Quasi-Static Approximation. *Physical Oceanography*, 30(5), pp. 523-548.
10. Demyshev, S.G. and Dymova, O.A., 2023. [Estimates of the Available Potential Energy Budget in the Black Sea Using New Approximation Schemes for the Heat and Salt Advection-Diffusion Equations]. *Multiphase Systems*, 18(4), pp. 378-381. <https://doi.org/10.21662/mfs2023.4.117> (in Russian).
11. Demyshev, S.G. and Dymova, O.A., 2022. Analysis of the Annual Mean Energy Cycle of the Black Sea Circulation for the Climatic, Basin-Scale and Eddy Regimes. *Ocean Dynamics*, 72(3-4), pp. 259-278. <https://doi.org/10.1007/s10236-022-01504-0>
12. Mellor, G.L. and Yamada, T., 1982. Development of a Turbulence Closure Model for Geophysical Fluid Problems. *Reviews of Geophysics*, 20(4), pp. 851-875. <https://doi.org/10.1029/RG020i004p00851>
13. Simonov, A.I. and Altman, E.N., eds., 1991. *Hydrometeorology and Hydrochemistry of Seas in the USSR. Vol. IV. Black Sea. Issue 1. Hydrometeorological Conditions*. Saint Petersburg: Gidrometeoizdat, 428 p. (in Russian).
14. Nardelli, B.B., Tronconi, C., Pisano, A. and Santoleri, R., 2013. High and Ultra-High Resolution Processing of Satellite Sea Surface Temperature Data over Southern European Seas in the Framework of MyOcean Project. *Remote Sensing Environment*, 129, pp. 1-16. <https://doi.org/10.1016/j.rse.2012.10.012>
15. Arakawa, A. and Lamb, V.R., 1981. A Potential Enstrophy and Energy Conserving Scheme for the Shallow Water Equations. *Monthly Weather Review*, 109(1), pp. 18-36. [https://doi.org/10.1175/1520-0493\(1981\)109<0018:APEAEC>2.0.CO;2](https://doi.org/10.1175/1520-0493(1981)109<0018:APEAEC>2.0.CO;2)
16. Bayankina, T.M., Godin, E.A., Zhuk, E.V., Ingerov, A.V., Isaeva, E.A. and Vetsalo, M.P., 2021. Information Resources of Marine Hydrophysical Institute, RAS: Current State and Development Prospects. In: T. Chaplina, ed., 2021. *Processes in GeoMedia – Volume II*. Cham: Springer, pp. 187-197. https://doi.org/10.1007/978-3-030-53521-6_22

17. Ivanov, V.A. and Belokopytov, V.N., 2013. *Oceanography of the Black Sea*. Sevastopol: ECOSI-Gidrofizika, 210 p.
18. Demyshev, S., Dymova, O. and Miklashevskaya, N., 2022. Seasonal Variability of the Dynamics and Energy Transport in the Black Sea by Simulation Data. *Water*, 14(3), 338. <https://doi.org/10.3390/w14030338>
19. Bulgakov, S.N. and Korotaev, G.K., 1984. Possible Mechanism of Stationary Circulation of Black Sea Waters. In: MHI, 1984. *Integrated Research of the Black Sea*. Sevastopol: MHI, pp. 32-40 (in Russian).

Submitted 27.03.2024; approved after review 17.04.2024;
accepted for publication 17.08.2024.

About the author:

Olga A. Dymova, Leading Researcher, Marine Hydrophysical Institute of RAS (2 Kapitanskaya Str., Sevastopol, 299011, Russian Federation), CSc. (Phys.-Math.), **ORCID ID: 0000-0003-4036-2447**, **ResearcherID: P-9669-2015**, **Scopus Author ID: 6508381809**, olgadymova@mhi-ras.ru

The author has read and approved the final manuscript.

The author declares that she has no conflict of interest.

Original article

Numerical Study of Hydrodynamic Regime of the Taganrog Bay Waters in the Sea of Azov

B. V. Divinsky

Shirshov Institute of Oceanology of RAS, Moscow, Russian Federation

✉ divin@ocean.ru

Abstract

Purpose. The work is aimed at studying the hydrodynamic conditions of formation of the sand spits in Taganrog Bay of the Azov Sea from the viewpoint of the morphological features of spits.

Methods and Results. The analysis is based on the results of numerical modeling the hydrodynamic parameters of the entire Azov Sea over 42 years, from 1979 to 2020. The generated data array consists of the hourly spatial fields of bottom current speeds and directions, as well as the wind wave significant heights and directions of their propagation. A significant difference between the hydrodynamic regimes of the sand spits of the northern coast (Belosaraysk and Krivaya spits) and the southern coast (Ochakovsk, Chumbursk, Sazalniksk and Yeysk spits) has been found.

Conclusions. In the coastal waters of Belosaraysk and Krivaya spits (the northern coast), the frequency of currents from the east prevails. Beglitsk (the northern coast), Ochakovsk and Sazalniksk (the southern coast) spits are characterized by the predominance of currents from the west. In the region of Belosaraysk and Krivaya spits, the long-term mean velocities of the currents directed to the east are slightly higher than those of the currents directed to the west. In the areas of Beglitsk spit (the northern coast), as well as Ochakovsk, Chumbursk, Sazalniksk and Yeysk spits in the southern part of the bay, the eastward directed currents dominate noticeably, both in terms of mean and maximum speeds. In the coastal waters of Belosaraysk and Krivaya spits, both the mean and maximum heights of the waves propagating to the east slightly exceed those of the waves propagating to the west. As for Beglitsk, Ochakovsk, Chumbursk, Sazalniksk and Yeysk spits, the dominating westward direction of wave propagation is, on average, a characteristic feature, whereas the waves of maximum heights develop during the eastern storms.

Keywords: Sea of Azov, sand spits, hydrodynamic conditions, numerical modeling

Acknowledgements: The work was carried out in accordance with the theme of state assignment of IO RAS (No. FMWE-2024-0027).

For citation: Divinsky, B.V., 2024. Numerical Study of Hydrodynamic Regime of the Taganrog Bay Waters in the Sea of Azov. *Physical Oceanography*, 31(5), pp. 694-706.

© 2024, B. V. Divinsky

© 2024, Physical Oceanography

Introduction

Taganrog Bay is situated in the north-eastern region of the Sea of Azov. Taganrog Bay extends for 135 km in length and has a typical width of 30 km. In comparison to the main water area of the Sea of Azov, it is relatively shallow, with



an average depth of approximately 5 m [1]. The coastal zone of the bay, as well as the entire sea, is characterised by specific geomorphological forms, namely sand spits (Fig. 1).



Fig. 1. Bathymetric map and morphometric features of Taganrog Bay in the Sea of Azov (on the top); examples of radical reshaping of spits (on the bottom)

On the northern coast, the spits of Belosaraysk, Krivaya and Beglitsk are the most developed, exhibiting significant extension into the open sea. The general direction of Belosaraysk and Krivaya spits is from east to west, whereas Beglitsk spit is oriented in the opposite direction. In the southern sector of the bay, the spits of Ochakovsk, Chumbursk, Sazalniksk and Yeysk are morphometrically oriented from west to east. However, the extremities of all spits, with the exception of Yeysk, may occasionally exhibit a tendency to extend in the opposite direction. The underwater extensions of these spits are also oriented from east to west, as is evident from Fig. 1, which illustrates the 2 m isobath. The distal portion of Dolgaya Spit, which directly borders Taganrog Bay on the southern side, bends either towards the bay or towards the open sea, depending on the prevailing hydrodynamic conditions.

It is noteworthy that a similar phenomenon was previously observed (Fig. 2). The spits directed from east to west are indicated in red in Fig. 2, while those directed from west to east are indicated in blue. The maps are ordered according to the year of publication.

Fig. 2 illustrates stability of the above-mentioned features of the morphological appearance of Taganrog Bay over a period of at least 250 years.

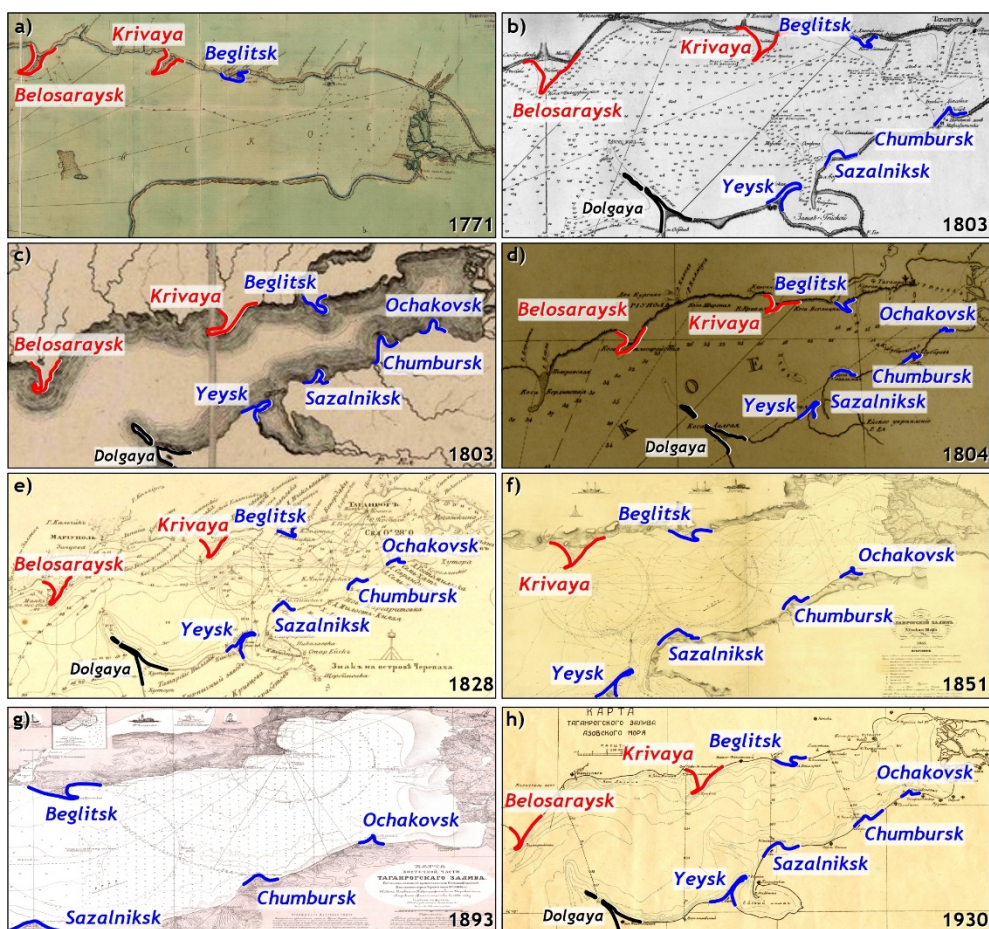


Fig. 2. Historical maps of Taganrog Bay (source: internet archives papacoma.narod.ru; www.etomesto.ru)

Spatial positions of the main Taganrog Bay spits (excluding Dolgaya Spit) are summarized in the table.

General directions of the spits in Taganrog Bay

Coast	Spit	Direction
Northern	Belosaraysk	E-W
	Krivaya	E-W
	Beglitsk	W-E
Southern	Ochakovsk *	W-E
	Chumbursk *	W-E
	Sazalniksk *	W-E

* Direction of extremity E-W, W-E.

Let us point out once again that, with the exception of Beglitsk Spit, the sand spits of the **northern** part of Taganrog Bay (Belosaraisk and Krivaya) are oriented from **east** to **west**. The **southern** coast spits (Ochakovsk, Chumbursk, Sazalniksk and Yeysk), as well as Beglitsk Spit (the northern coast), are oriented in the opposite direction – from **west** to **east**. Thus, as follows from Fig. 1, 2, certain patterns in the development of the spits of the northern and southern coasts of the bay are found. Their study is the subject of the present paper.

The formation and transformation of sand spits is influenced by morphological factors such as bedrock conditions, sediment granulometric composition and the presence or absence of beach recharge, as well as hydrodynamic factors such as sea currents, prevailing wind waves and sea level. The morpho- and lithodynamic features of the sand spits of Taganrog Bay have been the subject of considerable research. A synthesis of the findings from numerous studies [2–8] reveals that the spits are predominantly composed of fine-grained sands and coarse silts, with the proportion of aleuritic silts increasing with depth. The underwater bases of the spits, which have been traced to depths of approximately 3–4 m, consist of sands with an admixture of shells and detritus. In general, as evidenced by the findings [3], the abrasion slopes of the northern and southern coasts of the bay exhibit typological similarities.

The most extensively studied hydrodynamic characteristics of the waters of Taganrog Bay are wind surges. These surges are associated to a significant extent with the developed system of sea level observations, with data being gathered from numerous hydrological posts located along the entire coast of the Sea of Azov [9–13]. The most notable characteristic of the bay is the considerable amplitude of wind surges. To illustrate, in Taganrog, the range of sea level fluctuations exceeded 6 m between the years 1882 and 1998 [14].

The wind wave regime of Taganrog Bay (as part of the Sea of Azov) has been the subject of detailed study [15–17], with estimates of the main parameters of wind waves (heights, periods and lengths) in the water area of the entire Sea of Azov. It is regrettable that the analysis does not take into account the ice cover, which partially or completely (depending on the severity of atmospheric conditions) covers the sea area from approximately November to March. The presence of ice has a direct impact on the conditions that facilitate the development and transformation of wind waves.

The parameters of sea currents in the Taganrog Bay water area, obtained by calculation, have been subjected to analysis in several scientific manuals [6, 15]. However, the main limitation of the data is that the current fields correspond only to specified directions and certain gradations of wind speed. Consequently, there is no information regarding the estimation of climatic conditions with respect to the characteristics of the currents.

Thus, assuming a certain morphological similarity between the sand spits of Taganrog Bay, the following aims of this study are defined:

- to analyze in detail the hydrodynamic regime of the Taganrog Bay waters;

- to identify possible factors that determine the general orientation of the spits on the northern coast from east to west, and on the southern coast, in the opposite direction, from west to east;
- to propose an answer to the question "Why doesn't Beglitsk Spit of the northern coast follow the general rule and is oriented from west to east?".

It is worth noting that the renowned Soviet researcher V. P. Zenkovich ¹ noted that Krivaya and Beglitsk spits are rotated relative to each other "with an exact angle of 90°" (in reality, slightly more), but he did not inquire about the reasons for this phenomenon.

The main research method is mathematical modeling.

Materials and methods

The hydrodynamic regime of the Taganrog Bay water area is primarily influenced by three key factors: sea currents, wind waves, and sea level variations caused by storm surges and seiche oscillations. In conditions of reduced water depth, these factors are strongly interconnected. An increase in sea level results in a transformation of the fields of currents and waves. The collapse of storm waves by radiation stresses serves to adjust the magnitude and direction of currents, in addition to increasing the height of surges. The potential for ice to be present in the water area introduces an additional layer of complexity to the situation. From the perspective of simulating the ongoing hydrodynamic processes, it is evident that a separate calculation of the parameters of currents, waves and level is not entirely accurate. A more accurate methodology would be to analyse all processes within the context of a unified model. A comparable methodology was employed in the author's preceding work [18] on the investigation of the hydrodynamic regime of the entire Sea of Azov, using the following approaches:

1. Sea currents are calculated using the 5-layer σ -coordinate 3D ADCIRC model based on the solution of shallow water equations. Various modifications of the model have been effective in studies, particularly those examining extreme storm surges in the Sea of Azov (for example, in [9]).

2. Wind wave parameters are calculated using the MIKE 21 SW spectral wave model of the Danish Hydraulic Institute, which has been successfully applied to the conditions of the Azov and Black seas [19].

3. Fields of atmospheric pressure, surface wind components and ice concentration required for modeling are selected from the ERA5 global atmospheric reanalysis database. The time step is 3 h for atmospheric pressure and wind fields, and 1 day for ice concentration fields.

4. The calculation grid is formed based on a modern bathymetric map of the Sea of Azov [6].

5. The combination of models, taking into account the interaction of currents and waves, is carried out as follows: the height and current parameters determined

¹ Zenkovich, V.P., 1958. *Shores of the Black and Azov Seas*. Moscow: Geografiz, p. 164 (in Russian).

in the hydrodynamic model are used in the spectral wave model to calculate wind wave parameters; radiation stresses generated by wave breaking processes and calculated by the wave model correct the current parameters.

The combined model is validated using available experimental data on the parameters of sea currents, wind waves and sea level. The data set comprises the results of measurements obtained using a range of specialist instruments, including tide gauges, RDI ADCPs and Vector-2 probes, as well as satellite observations.

The calculations produced a database of hourly spatial fields of current and wind wave parameters covering the entire water area of the Sea of Azov, including Taganrog Bay. The calculation period was 42 years (January 1979 to December 2020).

Results and discussion

First, a few comments clarifying the features of the approach used to analyze the hydrodynamic impact on the coastal zone are to be made:

1. The data on the characteristics of sea currents and wind waves are used. Sea level fluctuations, or more specifically, storm surges, are not considered separately, since the surge process transforms both the current fields and the waves, which directly affect the bottom and coast deformations.

2. The use of a 3D hydrodynamic model allows a precise analysis of the bottom currents responsible for the initial suspension and redistribution of bottom material in the coastal zone of the sea.

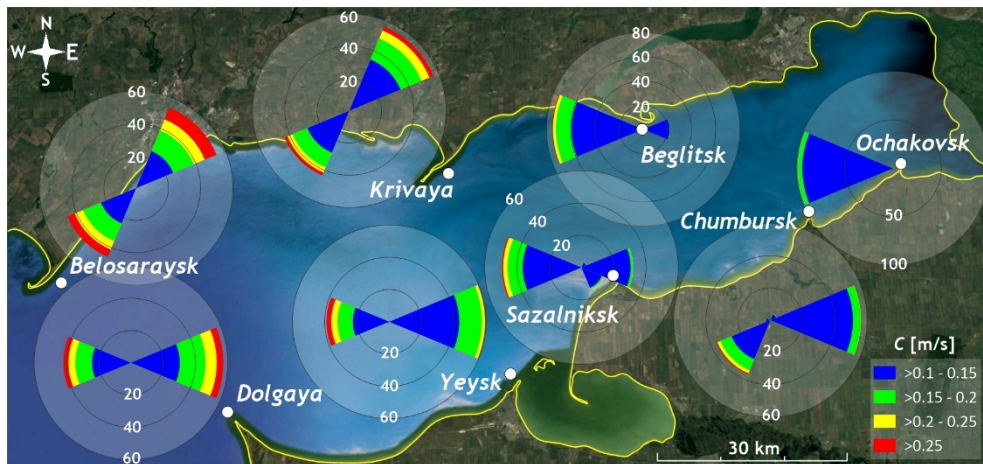


Fig. 3. Roses of bottom currents (%) in 1979–2020

Figs. 3 and 4 show bottom current and wind wave roses (in terms of significant wave heights) at several points in Taganrog Bay. Due to the climatic predominance of relatively weak currents and waves, current velocities of less than 0.1 m/s and wave heights of less than 0.1 m were not included in the data used to construct Figs. 3 and 4. The repeatability of current velocities or wave heights and directions is

presented for three spits on the northern coast (Belosaraysk, Krivaya and Beglitsk) and five on the southern coast (Ochakovsk, Chumbursk, Sazalniksk, Yeysk, and Dolgaya).

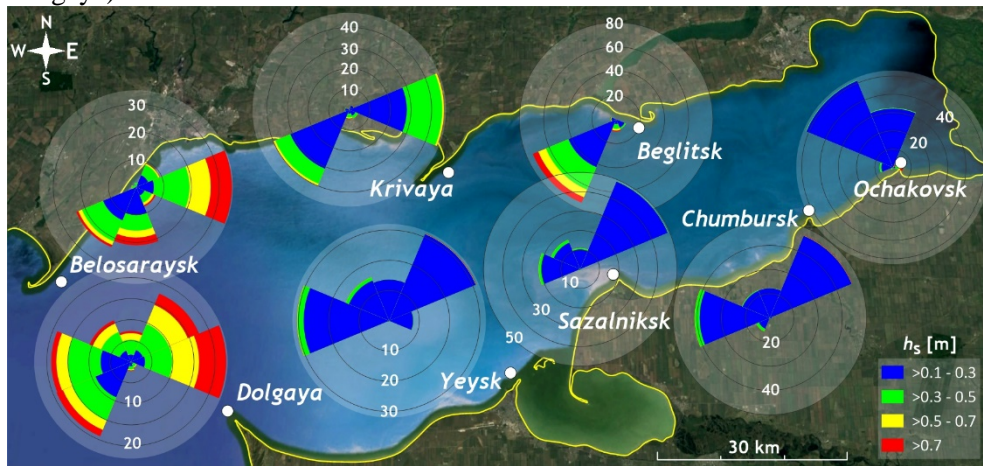


Fig. 4. Wind wave roses (%) in 1979–2020

As shown by the data in Fig. 3, in the coastal waters of Belosaraysk and Krivaya spits, the frequency of northeastern bottom currents is one and a half times higher than the frequency of southwestern currents. Beglitsk Spit is characterized by the absolute dominance (almost 80%) of western currents. In the area of Ochakovsk Spit, the currents (with the speed of more than 0.1 m/s) are almost always directed from west to east. In the waters washing Chumbursk Spit, the frequency of eastern currents is somewhat higher than that of southwestern ones (55 and 38%, respectively), but strong currents with velocities exceeding 0.2 m/s are observed precisely in the southwestern sector currents. A similar picture is specific for Yeysk Spit (60% – eastern currents, 40% – western). In addition, Yeysk Spit has a high frequency of extremely strong (more than 0.25 m/s) western currents, amounting to almost 5%. In the area of Sazalniksk Spit, western currents are observed in 50% of cases, and eastern in 30%. Dolgaya Spit is characterized by the predominance of eastern currents (58%); strong currents can form both from the open sea and from the bay.

The degree of development of wind waves depends on many factors: strength, stability in direction and time of wind flow action, acceleration length and bathymetric features. In the present case, the strongest wind waves occur at the entrance to Taganrog Bay, as well as in the area of Beglitsk Spit (Fig. 4).

The wave regime of Belosaraysk Spit is determined by waves of eastern (33%), southwestern (23%) and southern (21%) directions. Krivaya Spit is characterized by the dominance of eastern (45%) and southwestern (31%) waves. In contrast to Belosaraysk and Krivaya, the third spit of the northern coast, Beglitsk, experiences the predominant influence of storms of southwestern direction. Ochakovsk Spit, due to its location and the shallowness of the coastal zone, is best protected from strong waves; northeasterly waves make the largest contribution to the formation of

the wave regime. For the next three spits of the southern coast of the bay (Chumbursk, Sazalniksk and Yeysk), the influence of northeastern waves prevails, but the strongest storms usually come from the west. In the area of Dolgaya Spit, strong waves are possible from almost all directions, except, of course, the southern and southeastern sectors.

Some statistical characteristics of the significant wave heights and bottom current velocities should be added. Figs. 5, 6 show box plots of the distributions of wave heights and current velocities, respectively, including minimum, maximum, and average values of the parameters, as well as 5 and 95 percent quantiles of the distributions. The distributions are constructed separately for alongshore currents, conditionally directed from west to east (blue boxes), and reverse currents from east to west (red boxes). For wave heights, the statistics are similar, the only difference being that the wave sector ('west' or 'east') is determined with respect to the normal to the shoreline.

Wind waves are most developed in the strait and on the northwestern coast of the bay (Fig. 5).

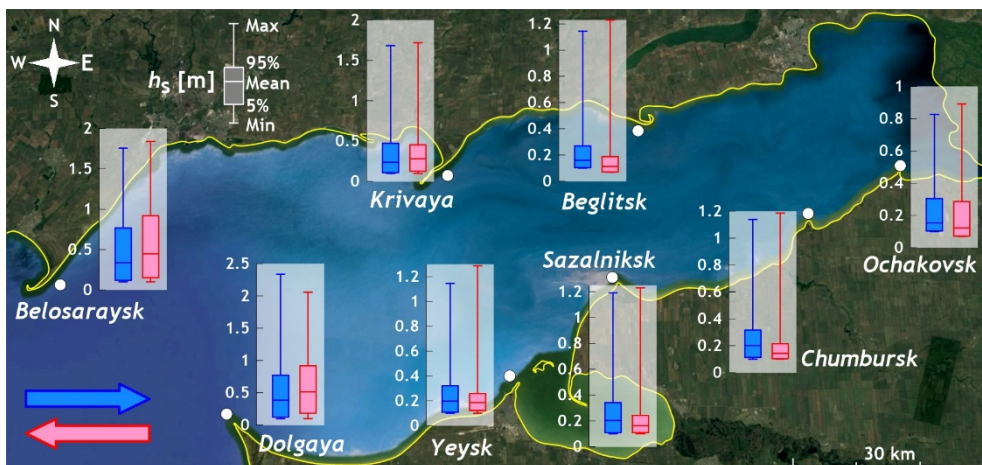


Fig. 5. Statistical characteristics of the distributions of significant wave heights (m) in 1979–2020

In the coastal waters of Belosaraysk and Krivaya spits, the wave heights of the eastern directions are observed to be higher than the average, with maximum wave heights for western direction swells also exceeding the norm. The spits of Beglitsk, Ochakovsk, Chumbursk, Sazalniksk and Yeysk are subject to comparatively weaker swells. The data indicate that, on average, these spits are subject to a predominance of western swells. However, it is notable that swells with maximum wave heights develop during eastern storms. In contrast, at Dolgaya Spit, the average wave height for eastern swells exceeds the average height characteristic of western swells. Nevertheless, maximum waves develop during storms coming from the west, from the open sea.

The strongest bottom currents with maximum velocities of ~ 0.8 m/s are formed in the western part of the bay (Fig. 6).

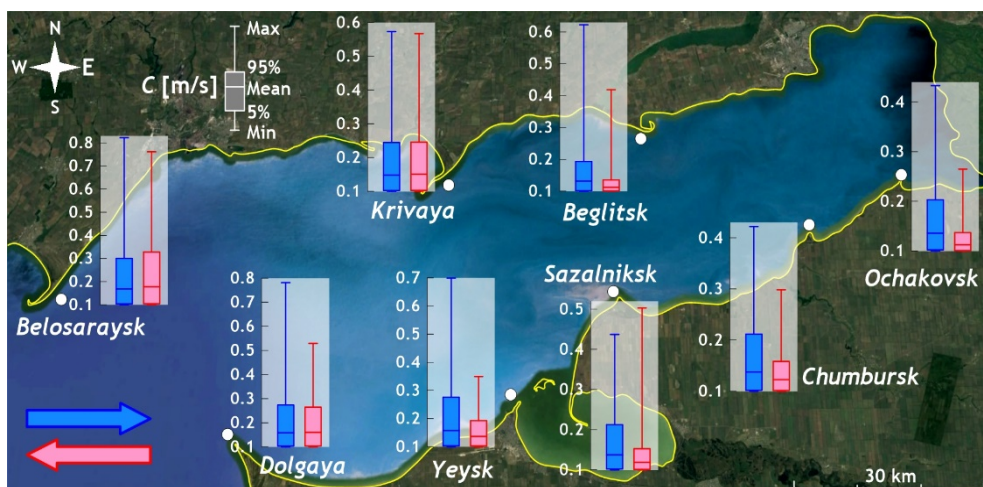


Fig. 6. Statistical characteristics of the distributions of bottom current velocities (m/s) in 1979–2020

In the coastal waters of Belosarysk and Krivaya spits, the western and eastern water flows are almost comparable in speed. However, the average long-term values of the current velocities of the eastern flows slightly exceed those of the western directions. In the area of the northern coast of Beglitsk Spit, as well as Ochakovsk, Chumbursk, Sazalniksk and Yeysk spits of the southern part of the bay, the dominance of currents from the west is evident, both in terms of average and maximum velocities. It is noteworthy that the water regime near Sazalniksk Spit exhibits a distinctive pattern, with the highest velocities occurring in the eastern currents. In the vicinity of Dolgaya Spit, the mean velocity of the eastern and western currents is equal, yet the maximum velocities of the flows are indicative of the currents from the main sea area to Taganrog Bay, exceeding the current velocities in the opposite directions by approximately 50%.

It should be noted that the spatial position of Taganrog Bay, namely its elongation along the WSW – ENE line, corresponds to the directions of the prevailing winds over the bay, which contribute to the development of surge phenomena and largely determine water circulation. As an example, Fig. 7 shows schematic maps of the magnitude and direction of bottom currents during the passage of the strong SW storm (*a*); weakening of the SW storm (*b*); development of the NE wind (*c*); weakening of the NE wind (*d*).

As shown in Fig. 7, *a*, during the passage of the SW storm, a uniform SW to NE bottom current caused by the surge is established throughout the bay. In the bays between the main bodies of Belosarysk and Krivaya spits and the mainland, small cyclonic eddies form, causing water movement in the opposite direction. As the SW wind weakens (Fig. 7, *b*), the eddy gives way to a surge and the circulation in the bay is significantly restructured. Belosarysk, Krivaya and Dolgaya spits are under the influence of NE to SW currents, while Beglitsk, Ochakovsk, Chumbursk, Sazalniksk and Yeysk are under the influence of SW to NE reverse currents.

The NE wind development (Fig. 7, *c*) near Belosaraysk, Krivaya, Sazalniksk, Yeysk and Dolgaya spits forms the alongshore flow directed towards the open sea. In the same situation, a local circulation of water is formed near Beglitsk Spit: in its western part the flow is directed to the SW, in its eastern part – to the NE. In the coastal zone of Ochakovsk and Chumbursk spits, the alongshore flow is oriented to the NE. The weakening of the NE wind (Fig. 7, *d*) leads to a weakening of the currents in almost the entire water area of the bay, with the exception of the strait waters, where significant currents develop only near Belosaraysk (SW-directed) and Dolgaya (N, NE-directed) spits. In the coastal waters of the remaining spits, local current systems are formed, usually consisting of countercurrents.

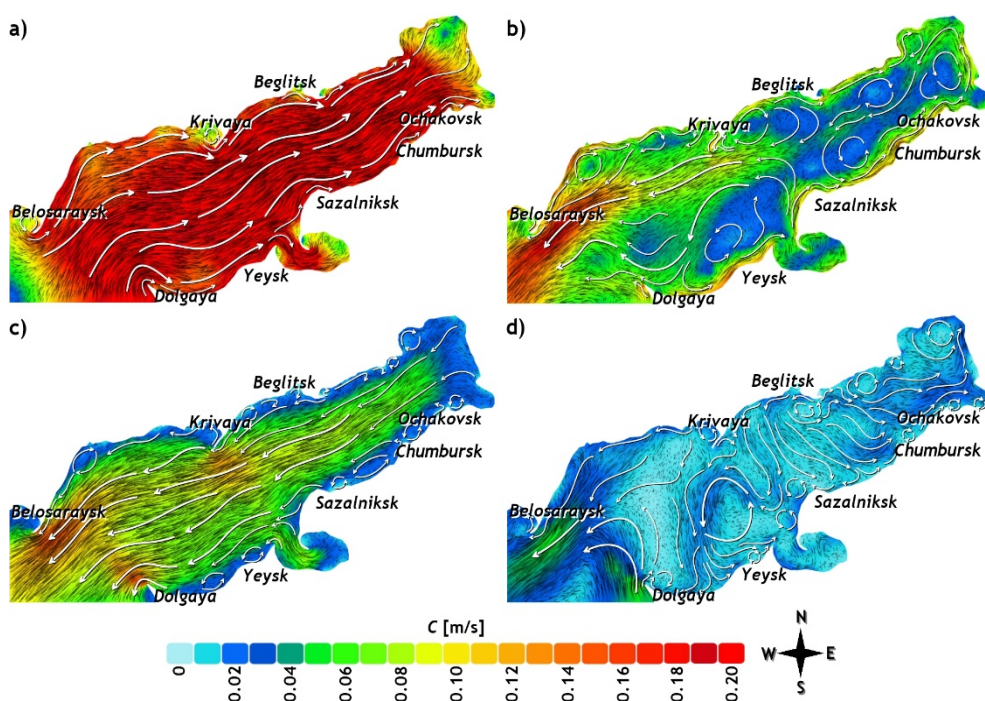


Fig. 7. Velocity fields (m/s) of bottom currents in Taganrog Bay under conditions of: *a* – strong SW wind; *b* – weakening of SW wind; *c* – strong NE wind; *d* – weakening of NE wind

It should be noted that the diagrams in Fig. 7 serve only to illustrate specific hydrodynamic situations and do not represent the full diversity of possible current structures in the bay. At the same time, Fig. 7 gives an idea of an important feature of the bottom circulation of waters: directly in the coastal zone, or more precisely in small bays between spits, countercurrents can form in relation to the general water flow in the main channel of Taganrog Bay.

Conclusions

The focus of our study is the spatial position of the sand spits of Taganrog Bay of the Azov Sea. The general direction of Belosaraysk and Krivaya spits of the northern coast is from east to west, while Beglitsk is the opposite, from west to east. The spits of the southern part of the bay, such as Ochakovsk, Chumbursk,

Sazalniksk and Yeysk, are also stretched from west to east. Accordingly, several legitimate questions arise:

1) What factors contribute to the orientation of the northern coast spits from east to west and the southern coast in the opposite direction, from west to east?

2) Why does Beglitsk Spit on the northern coast not follow the general rule and is directed from west to east?

We address these questions from a hydrodynamic perspective, examining the climatic characteristics of sea currents and wind waves that directly influence coastal formation and transformation. The potential impact of spits on the lithodynamic relation, as well as the possibility of human-induced alterations to the coastal zone (sand extraction, construction of protective structures) have not been considered.

The analysis was conducted using the results of numerical modeling of the hydrodynamic parameters of the entire Sea of Azov over a 42-year period (1979–2020). The generated data array comprises hourly spatial fields of velocity and direction of bottom currents, as well as significant heights and directions of wind waves.

As a result of the work carried out, it has been established that

1. The coastal waters of Belosaraysk and Krivaya spits (northern coast) are characterised by the recurrence of currents from the east. In the case of Beglitsk (northern coast), Ochakovsk and Sazalniksk (southern coast) spits, the dominance of currents from the west is a distinctive feature. In the waters adjacent to Chumbursk and Yeysk spits (southern coast), the recurrence of eastern currents is somewhat higher than that of southwestern ones. However, strong currents with velocities exceeding 0.2 m/s are observed with precise regularity in conjunction with currents from the west.

2. In the coastal waters of Belosaraysk and Krivaya spits (northern coast), the mean long-term values of the current velocities in the eastern directions are slightly higher than those in the western directions. In the area of Beglitsk spit of the northern coast, as well as Ochakovsk, Chumbursk, Sazalniksk and Yeysk spits of the southern part of the bay, the dominance of west currents is notable, both in terms of average and maximum velocities. However, a slight exception can be observed in the water regime near Sazalniksk spit, where the highest velocities develop with eastern currents.

3. In the coastal waters of Belosaraysk and Krivaya spits (northern coast), the height of waves originating from the east is greater than both the average and maximum heights of waves from the west. The spits of Beglitsk (northern coast), Ochakovsk, Chumbursk, Sazalniksk and Yeysk (southern coast) experience the dominance of western direction waves on average. However, waves with maximum wave heights develop during eastern storms.

It can be concluded that the hydrodynamic regime of the sand spits on the northern (Belosaraik, Krivaya) and southern (Ochakovsk, Chumbursk, Sazalniksk and Yeysk) coasts is significantly different. The climatic characteristics of the waves (to be more precise, in relation to the normal to the shore) and currents

of Beglitsk Spit in the north of the bay are similar to those of the southern coast spits, which most likely explains its elongation from east to west.

REFERENCES

1. Kosolapov, A.E., Dandara, N.T., Bepalova, L.A., Ivlieva, O.V., Lyashik, A.N., Nikanorov, V.A., Kalimanov, T.A., Dorozhkin, E.V., Klimenko, O.A. [et al.], 2012. *Gulf of Taganrog Sea of Azov: Current State and Natural Management Problems*. Rostov-on-Don: Publishing House of Southern Federal University, 554 p. (in Russian).
2. Matishov, G. and Levitus, S., eds., 2006. *Climatic Atlas of the Sea of Azov 2006*. NOAA Atlas NESDIS 59. U.S. Washington, D. C.: Government Printing Office, 103 p.
3. Bepalova, L.A. and Bepalov, A.A., 2006. Underwater Landscapes of the Azov Sea and Their Ecodiagnostics. *Ecological Bulletin of Research Centers of the Black Sea Economic Cooperation*, 3(3), pp. 23-30 (in Russian).
4. Ivlieva, O.V., 2009. [*Peculiarities of Sedimentation in the Sea of Azov in the Second Half of the 20th Century*]. Rostov-on-Don: Publishing House of Southern Federal University, 319 p. (in Russian).
5. Mayev, E.G., Myslivets, V.I. and Zverev, A.S., 2009. Structure of the Upper Sediment Layer and the Bottom Relief of the Taganrog Bay of the Azov Sea. *Moscow University Bulletin. Series 5, Geography*, (5), pp. 78-82 (in Russian).
6. Matishov, G.G., ed., 2011. *Ecological Atlas of the Sea of Azov*. Rostov-on-Don: SSC RAS Publishers, 328 p. (in Russian).
7. Matishov, G.G., Polshin, V.V., Kovaleva, G.V. and Titov, V.V., 2019. Lithology and Biostratigraphy of the Sea of Azov Holocene Deposits: Results of 15 Years Researches. *Science in the South of Russia*, 15(3), pp. 24-34. <https://doi.org/10.7868/S25000640190303> (in Russian).
8. Matishov, G. and Polshin, V., 2019. New Results on the History of the Sea of Azov in the Holocene. *Doklady Earth Sciences*, 489, pp. 1339-1344. <https://doi.org/10.1134/S1028334X19110138>
9. Fomin, V.V. and Polozok, A.A., 2013. [Technology for Modelling Storm Surges and Wind Waves in the Sea of Azov on Unstructured Grids]. In: MHI, 2013. *Ecological Safety of Coastal and Shelf Zones and Comprehensive Use of Shelf Resources*. Sevastopol: ECOSI-Gidrofizika. Iss. 27, pp. 139-145 (in Russian).
10. Matishov, G.G. and Berdnikov, S.V., 2015. Extreme Flooding in the Don River Delta in Spring 2013. *Izvestiya Rossiiskoi Akademii Nauk. Seriya Geograficheskaya*, (1), pp. 111-118. <https://doi.org/10.15356/0373-2444-2015-1-111-118> (in Russian).
11. Popov, S.K. and Lobov, A.L., 2017. [Modeling of Water Level Changes in the Sea of Azov in 2015-2016]. *Proceedings of Hydrometcentre of Russia*, (364), pp. 131-143 (in Russian).
12. Popov, S.K. and Lobov, A.L., 2018. Short-Term Forecasts of the Azov Sea Level Variations during the Iceless Period in 2017. *Hydrometeorological Research and Forecasting*, 3(369), pp. 104-118 (in Russian).
13. Bepalova, L.A., Bepalova, E.V., Misirov, S.A. and Tsygankova, A.E., 2020. Storm Surges in the Sea of Azov and Their Impact on Abrasion Processes. In: SSC RAS, 2020. *Studies of the Southern Scientific Centre of the Russian Academy of Sciences*. Rostov-on-Don: SSC RAS Publishing. Vol. 8, pp. 111-121. <https://doi.org/10.23885/1993-6621-2020-8-111-121> (in Russian).
14. Dyakov, N.N. and Fomin, V.V., 2002. [Synoptic Conditions of Occurrence of Anomalous Fluctuations in the Level of the Sea of Azov]. *Proceedings of the Ukrainian Hydrometeorological Research Institute*, (250), pp. 332-342 (in Russian).

15. Fomin, V.V., ed., 2012. [*Atlas of the Wave, Currents and Level of the Sea of Azov*]. Kiev: Marine Department of the Ukrainian Scientific Research Hydrometeorological Institute, 238 p. (in Russian).
16. Evstigneev, V.P., Naumova, V.A., Voskresenskaya, E.N., Evstigneev, M.P. and Lyubarets, E.P., 2017. *Wind and Wave Conditions of the Coastal Zone of the Azov-Black Sea Region*. Sevastopol: IPTS, 320 p. <https://doi.org/10.33075/978-5-6040795-0-8> (in Russian).
17. Yaitskaya, N., 2022. The Wave Climate of the Sea of Azov. *Water*, 14(4), 555. <https://doi.org/10.3390/w14040555>
18. Divinsky, B.V., Kosyan, R.D. and Fomin, V.V., 2021. Climatic Fields of Sea Currents and Wind Waves in the Sea of Azov. *Doklady Earth Sciences*, 501(1), pp. 976-988. <https://doi.org/10.1134/S1028334X21090087>
19. Divinsky, B. and Kosyan, R., 2018. Parameters of Wind Seas and Swell in the Black Sea Based on Numerical Modeling. *Oceanologia*, 60(3), pp. 277-287. <https://doi.org/10.1016/j.oceano.2017.11.006>

Submitted 13.05.2024; approved after review 20.05.2024;
accepted for publication 17.07.2024.

About the author:

Boris V. Divinsky, Leading Researcher, Geology and Lithodynamics Laboratory, Shirshov Institute of Oceanology of RAS (36 Nakhimovsky Ave., Moscow, 117997, Russian Federation), CSc. (Geogr.), **ORCID ID: 0000-0002-2452-1922**, **ResearcherID: C-7262-2014**, **SPIN-code: 2027-8359**, divin@ocean.ru

The author has read and approved the final manuscript.

The author declares that he has no conflict of interest.

Original article

Features of Water Exchange between the Black and Marmara Sea Basins based on the Results of Numerical Simulation with a Simplified Representation of the Strait

A. I. Mizyuk ✉, G. K. Korotaev

Marine Hydrophysical Institute of RAS, Sevastopol, Russian Federation

✉ artem.mizyuk@mhi-ras.ru

Abstract

Purpose. The study is purposed at analyzing the adequacy of reconstruction of mass, heat and salt transfer processes through the Bosphorus Strait based on the results of numerical simulation of joint circulation of the Euxine Cascade waters involving a simplified description of the strait due to the model spatial resolution.

Methods and Results. A regional configuration for the *NEMO* model (spatial resolution is about 1 km) which allows simulating the meso- and submeso-scale variability of hydrophysical fields in the Euxine Cascade seas is used. It is briefly described. The numerical experiment covers the period 2008–2009. The salinity and current velocity fields in the strait cross-section reconstructed in the experiment confirm a two-layer structure of water circulation, i.e. the presence of upper and lower Bosphorus currents. Besides, they show the availability of periods of complete or partial blocking both the upper and lower currents. Despite a somewhat rough configuration of the strait, the reconstructed salt exchange features are in good agreement with the similar ones obtained on the basis of a finite-element model with a higher spatial detailing in the strait, and as for temperature, the agreement is to some extent worse. At the same time, the reconstructed current velocities show a fairly accurate correspondence of the blocking events when compared to the earlier performed measurements.

Conclusions. The previously revealed mechanism for maintaining the upper Bosphorus Current in winter conditioned by a rise of the Black Sea level in the Bosphorus region due to the Rim Current intensification has been confirmed. The model qualitatively correctly describes the strait response to the changes both in wind forcing and seawater density in the vicinity of the northern and southern inlets to the strait. Blockings of the upper Bosphorus Current occur and can be induced by the intensification of currents in the Marmara Sea due to the wind forcing and subsequent weakening of the Black Sea Rim Current. In a winter-spring period, the Marmara Sea circulation weakens, and one can observe the reverse phenomena in which the lower Bosphorus current blockings take place.

Keywords: numerical modeling, Black Sea, Bosphorus, Sea of Marmara, salt exchange, high resolution

Acknowledgements: The study was carried out within the theme of state assignment of FSBSI FRC MHI FNN-2024-0012 “Analysis, hindcast and operational forecast of the state of hydrophysical and hydrochemical fields of marine water areas based on numerical modeling using the data of remote and *in situ* measurement methods”.

For citation: Mizyuk, A.I. and Korotaev, G.K., 2024. Features of Water Exchange between the Black and Marmara Sea Basins based on the Results of Numerical Simulation with a Simplified Representation of the Strait. *Physical Oceanography*, 31(5), pp. 707-719.

© 2024, A. I. Mizyuk, G. K. Korotaev

© 2024, Physical Oceanography

Introduction

Water exchange through the Bosphorus Strait has two effects on the Black Sea regime. Firstly, together with river runoff, precipitation and evaporation, and including the Kerch Strait, it contributes to the water and salt balance of the Black



Sea basin. The specific time scale of this process spans several hundred years, with the balance determined by the ratio of the volume of the Black Sea waters to the amount of discharge through the straits.

However, recent observations indicate that the waters entering through the straits also contribute to the mesoscale variability of the basin fields. This phenomenon is observed in the dispersion of liquid volumes that differ in their properties from the surrounding waters over considerable distances [1].

It can be assumed that the requirements for the strait model vary depending on the time scale of the phenomenon under consideration. In order to accurately model long-term changes in Black Sea stratification, it is essential to simulate the geometry of the straits with a high degree of detail, thereby enabling a precise quantitative description of water exchange. Otherwise, minor discrepancies in the simulation of salt flows through the straits over extended periods will accumulate, resulting in the distortion of the evolution trends of the basin fields. A comprehensive description of the strait geometry requires a substantial refinement of the computational grid [2]. However, in order to keep the calculation time reasonable, the authors have reduced the model resolution for the open part of the Black Sea basin in the noted work.

At the same time, to study the contribution of water exchange through the straits to the mesoscale variability of the Black Sea fields, it seems possible to use a rougher description of the straits compared to work [2].

It should also be noted that a spatial resolution of about 1 km should be sufficient to adequately simulate the dynamics of the waters of the Marmara Sea [3]. The present work aims to demonstrate that a simpler description of the strait, obtained using a grid with such a resolution, nevertheless allows the simulation of the essential features of the temporal variability of the processes of mass, heat and salt transfer in the strait. Thus, it is possible to model the contribution of water exchange through the strait to the relatively high-frequency variability of the Black Sea fields. The choice of an appropriate spatial resolution of the model allows to adequately describe the variability of the Black Sea fields caused by the spreading of saline Mediterranean waters entering through the strait.

Materials and methods

The paper uses the results obtained in the regional configuration of the interdisciplinary framework Nucleus for European Modeling of the Ocean (NEMO) [4] for modeling the components of the ocean (marine) system with high spatial resolution. It allows the simulation of meso- and submesoscale variability of hydrophysical fields in the seas of the Euxine Cascade. The computational domain is a quasi-regular grid covering the basins of the Marmara, Black and Azov Seas with steps of $1/96^\circ \times 1/69^\circ$ in the meridional and zonal directions, respectively [5]. The resolution is approximately 1.157 km in the meridional direction. In the zonal direction, the step varies uniformly from 1100 m in the north to 1230 m in the south. The bottom topography is based on the EMODnet digital bathymetry array ¹ (Fig. 1, a).

¹ European Commission. *European Marine Observation and Data Network (EMODnet)*. [online] Available at: <http://www.emodnet-bathymetry.eu> [Accessed: 16 October 2016].

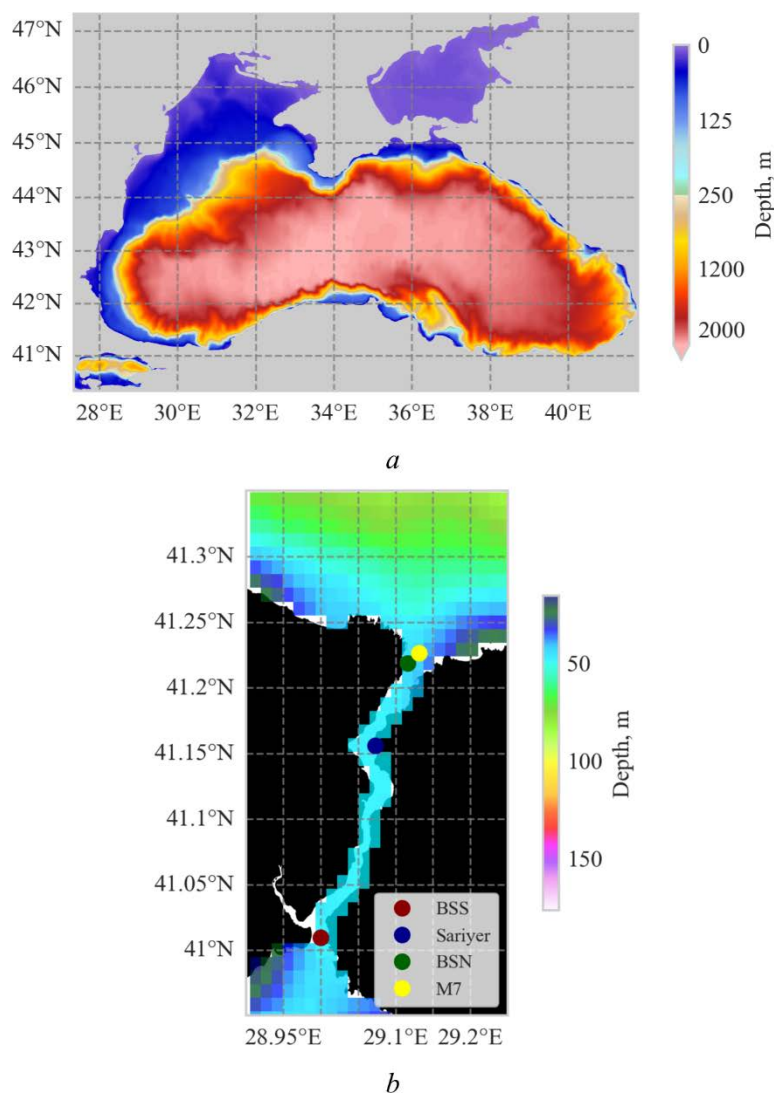


Fig. 1. Bottom topography for the *NEMO* regional configuration: for the entire numerical domain (a) and the strait water area (b). Configuration of the strait coasts is given according to the data from <https://www.openstreetmap.org/>; dots on fragment b indicate the station positions by analogy with [2]: *BSS* – *Bosphorus Strait South*, *Sariyer* – *Cape Sarrier*, *BSN* – *Bosphorus Strait North*; station *M7* is taken from [6]

Modeling the water exchange through the Bosphorus is a complex task due to the significant difference in the spatial scales of the processes occurring in the strait and in the basins it connects. However, using this framework and taking into account the spatial discretization adopted, it is possible to carry out calculations in the strait area and consider the joint dynamics of the Black and Marmara seas. In the constructed topography, the configuration of the strait was roughly taken into account (Fig. 1, b, c), only the position of the main thresholds at the northern and

southern entrances to the strait was taken into account. In this case, the depth in the strait was set at 48.5 m.

The hydrodynamic block of the framework is founded upon the system of equations of hydrothermodynamics in the Boussinesq approximation, hydrostatics and incompressibility of liquid, which are described in detail in reference [4]. The finite-difference equivalents of the equations are implemented for an arbitrary quasi-orthogonal grid in accordance with the template 'C' as defined by Arakawa. The time-discretization is performed using a modified leapfrog scheme [7].

The k - ε model of closure level 2 is employed for the description of vertical mixing processes [8]. The horizontal exchange is described by a biharmonic operator acting along the geopotential surface, with negative coefficients of viscosity and diffusion of heat and salt of equal absolute value, namely 4×10^7 and $8 \times 10^6 \text{ m}^4/\text{s}$, respectively. The UNESCO formula² is used as the equation of state. The configuration employed in this study represents a 'downscaling' of the configuration with a resolution of $1/24^\circ$ as presented in [9]. The principal distinctions between the two models lie in the parameters employed to describe the horizontal turbulent exchange and the time step, which is 60 seconds in the present study.

The boundary conditions on the surface are specified based on the air temperature and humidity fields at a height of 2 metres, the horizontal wind speed components at a height of 10 metres, the downward long-wave and short-wave radiation fluxes, and the liquid and solid precipitation, which have been obtained from the latest generation of the European Centre for Medium-Range Weather Forecasts (ECMWF) global atmospheric reanalysis, referred to as ERA5³. The product has a sufficiently high spatial ($1/4^\circ$) and temporal (1 h) resolution, which is of great significance for the simulation of short-period (intra-daily) processes and diurnal variation. The aforementioned meteorological parameters, which were initially recorded at discrete time points, were employed to calculate the total heat, mass and wind friction stress fluxes using the bulk formulas outlined in the Coordinated Ocean-ice Reference Experiments (CORE) protocol.

The objective of the present work was not to provide a comprehensive account of the process of ice formation in winter. In order to reproduce adequate temperature values on the northwestern shelf of the Black Sea and in the Sea of Azov, a heat flux correction was employed. Once the freezing temperature is reached at the surface, no heat flux condition is set, which, in effect, permits omission of any description of the formation of ice fields.

In the Marmara Sea basin situated to the west of Marmara Island (approximately along 27.38°E), the conditions characterizing an open liquid boundary are specified.

² Fofonoff, N.P. and Millard, Jr., R.C., 1983. *Algorithms for the Computation of Fundamental Properties of Seawater*. UNESCO Technical Papers in Marine Sciences; vol. 44. Paris, France: UNESCO, 53 p. <https://doi.org/10.25607/OBP-1450>

³ ERA5: Fifth Generation of ECMWF Atmospheric Reanalyses of the Global Climate. *Copernicus Climate Change Service Climate Data Store (CDS)*. 2017. [online] Available at: <https://cds.climate.copernicus.eu/> [Accessed: 22 August 2018].

The boundary conditions for temperature and salinity, level and current velocities were obtained based on the daily products of the Copernicus Marine Environment Monitoring System (CMEMS)⁴. In order to achieve this, the long-term average climate values were obtained from the analysis data for the period between 2007 and 2016 (Fig. 2). It is evident that the temperature exhibits a distinct pattern of cooling during the winter months, followed by a period of warming in spring and summer, along with the formation of the thermocline (Fig. 2, *a*).

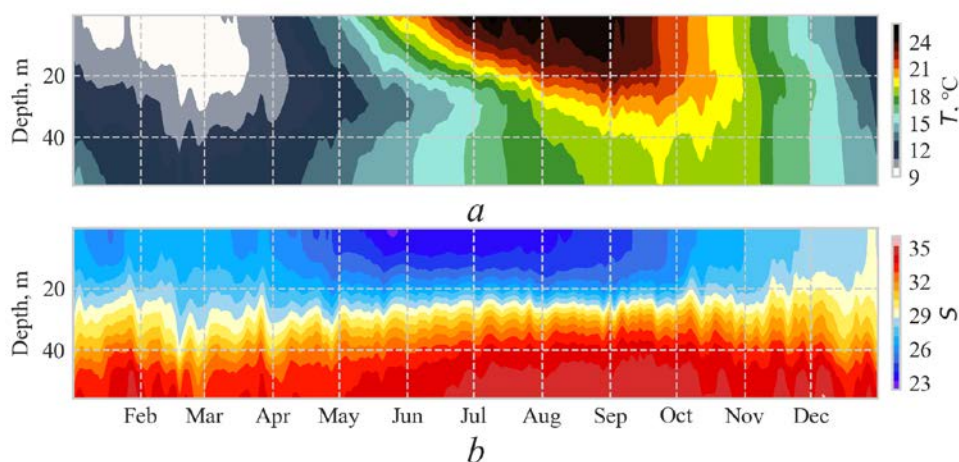


Fig. 2. Intra-annual variability of temperature (*a*) and salinity (*b*) in the Marmara Sea averaged along 27.38°E based on the CMEMS products⁴ for 2007–2016

The salinity fields according to CMEMS data demonstrate a typical vertical haline structure of waters in the Marmara basin, where the salinity of the upper layer is determined by the inflow and subsequent transformation of less saline Black Sea water masses. Salinity increases significantly with depth due to the influx of Mediterranean waters, with a salinity difference of over 12 between the deep and surface waters (Fig. 2, *b*).

In addition to the boundary conditions, the global CMEMS analysis results were also employed to establish the initial conditions of the fields. To initialize the model in the Black and Azov seas, the procedure of combining different sources, as outlined in reference [9], was employed. The temperature and salinity data for the Azov Sea were constructed using optimal interpolation of *in situ* observations. The temperature and salinity fields from the reanalysis of the hydrophysical parameters of the Black Sea Marine Forecasting Center were employed as the initial fields for the Black Sea basin [10]. Furthermore, in order to obtain the initial fields

⁴ Copernicus Marine Service. *Global Ocean 1/12° Physics Analysis and Forecast Updated Daily*. 2018. [online] Available at: http://marine.copernicus.eu/services-portfolio/access-to-products/?option=com_csw&view=details&product_id=GLOBAL_ANALYSIS_FORECAST_PHY_001_02 [Accessed: 22 August 2018].

for 15 August 2007, an adaptation calculation was conducted utilising the methodology proposed by A. S. Sarkysyan. The initial resolution of the prepared fields was $1/24^\circ$, as they were originally designed for long-term numerical experiments with a coarse resolution. Subsequently, the arrays were interpolated onto a grid of a new configuration, and a preliminary prognostic calculation of the general circulation of the cascade for the period between 15 August and 31 December 2007 was carried out in order to adapt the model to high resolution. Prior numerical experiments had demonstrated that this occurs over a period of approximately four months [11].

The principal numerical experiment using the developed configuration was conducted over the period from 1 January 2008 to 31 December 2009. The results of this study correlate temporally with the calculations presented in reference [2]. This allows for a comparison to be made, thus enabling an evaluation of the quality of the straight modeling in its schematized representation. Furthermore, the duration of the numerical experiment partially coincided with the time frame of the measurements taken from work [6], which will also be employed for comparison. The position of the M7 station, as defined in the aforementioned work, is illustrated in Fig. 1, *b*.

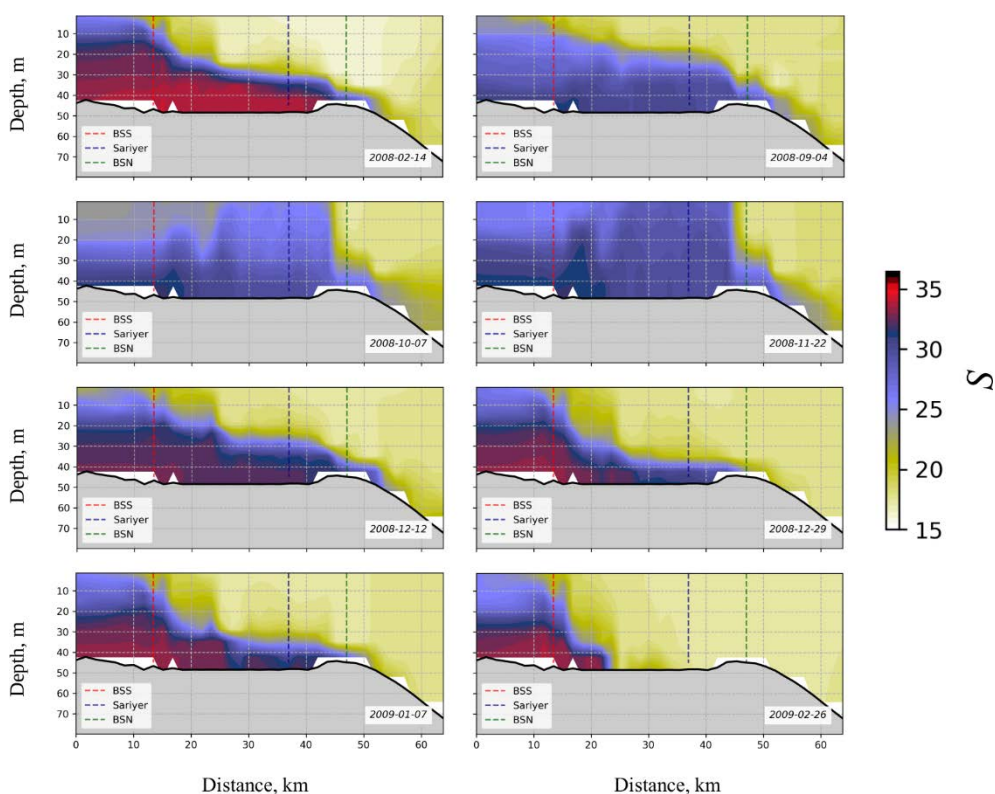


Fig. 3. Distribution of seawater salinity along the Bosphorus Strait on certain dates in 2008–2009

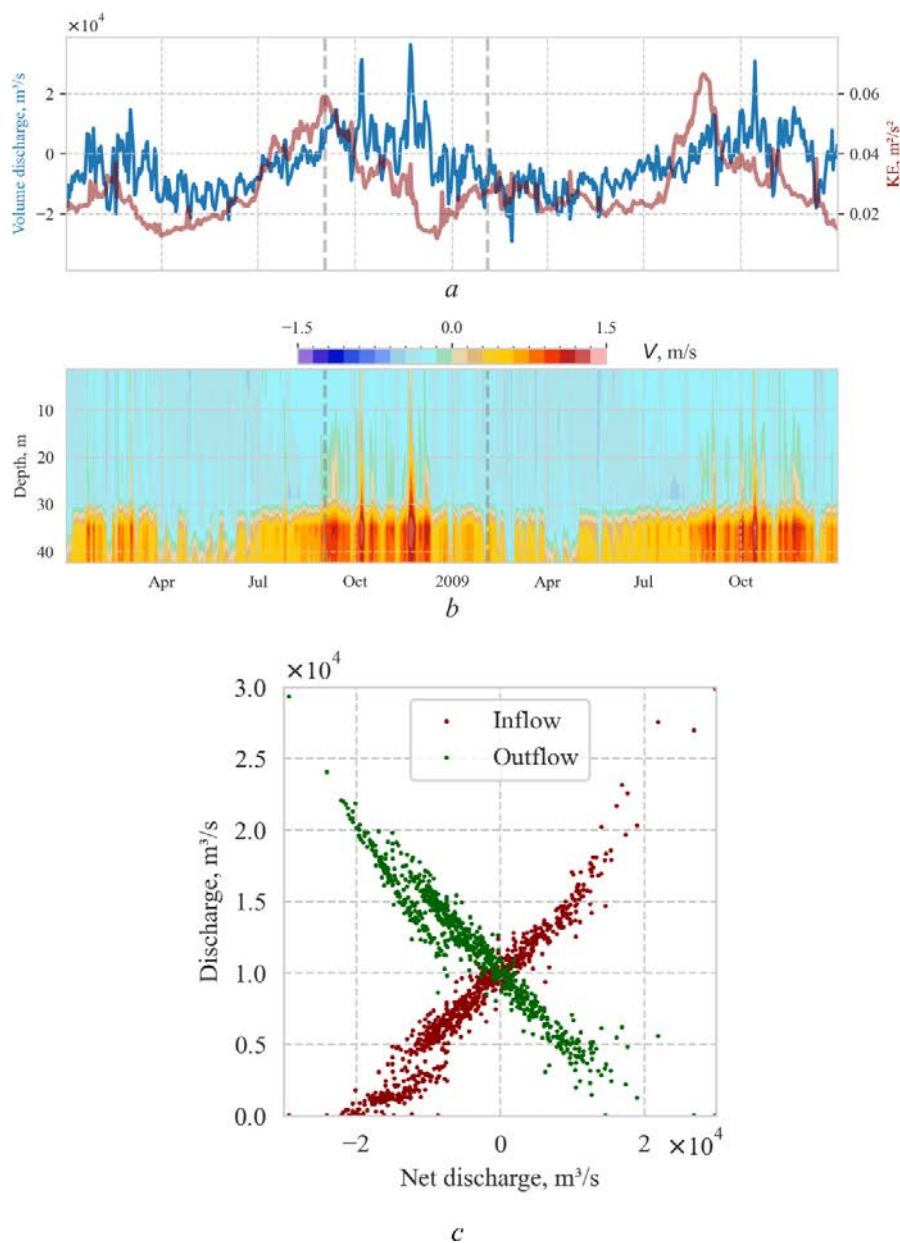


Fig. 4. Water dynamics in the Bosphorus Strait: *a* – mean kinetic energy (KE) of surface currents in the Marmara Sea and net barotropic meridional transport in the vicinity of point *BSN*; *b* – meridional currents in the northern part (*BSN*); *c* – inflow and outflow values as the functions of total transport. Vertical dashed lines indicate the period of observations from [6]

Analysis of the results

Notwithstanding the inaccuracies in the strait configuration simulation (Fig. 1, *b*), the model provides a highly plausible distribution of hydrological characteristics along the strait axis. In the thermohaline fields, two distinct layers of homogeneous water masses, separated by a thin layer of high gradients, are clearly

discernible. This is illustrated in the vertical salinity sections along the strait (Fig. 3, fragment from 14 February 2008). The locations of the stations along which the sections are constructed are illustrated in Fig. 1, *b*.

It is important to note that the calculation accurately reproduces the seasonal course of total transport through the Bosphorus Strait (Fig. 4, *a*), which is primarily influenced by the intensification of river runoff in the Black Sea during the months of May and June [12]. The ratio of the flow rates of the upper and lower Bosphorus currents is consistent with the findings presented in reference [2] (Fig. 4, *c*).

Furthermore, the currents within the strait exhibit a two-layer structure (Figs. 3 and 4, *b*). In the upper layer, the currents are directed from the Black Sea to the Marmara Sea. This layer is comprised of Black Sea waters, which undergo gradual transformation as they are transported along the strait. The current in the lower layer is oriented towards the Black Sea. The water in this layer is derived from the Marmara Sea and undergoes transformation as it is transported along the strait. However, an analysis of the meridional velocity over time reveals the occurrence of periods during which the upper Bosphorus or lower Bosphorus current is obstructed in the strait (Fig. 4, *a*, *b*).

Furthermore, our calculations confirm the mechanism for maintaining the upper Bosphorus Current during the winter period, as previously established in work [2]. The elevation of the Black Sea level in the Bosphorus region is the determining factor. This is caused by the intensification of the Black Sea Rim Current at this time (Fig. 5).

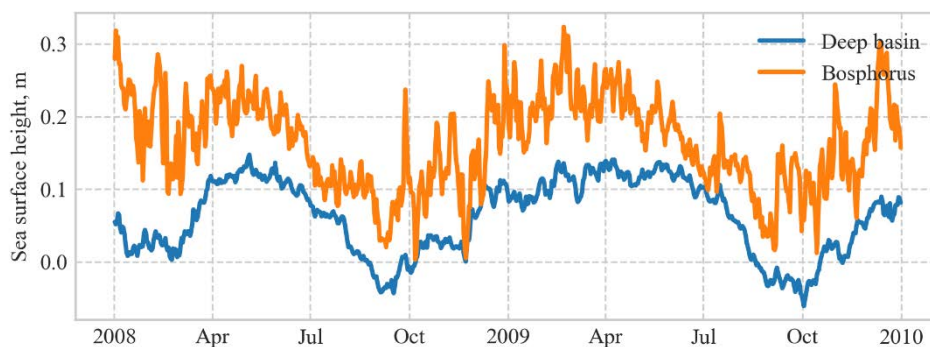


Fig. 5. The Black Sea surface level averaged over the deep-sea (deeper than 500 m) and near-Bosphorus areas

Furthermore, the salinity of the lower layer is also subject to seasonal variation in our calculations. During the winter months, the salinity can reach 30–35 (Fig. 3). In this instance, the salinity of the water reaches the threshold at the point of exit from the Bosphorus along the seabed. In general, the boundary between the layers expands and rises to the surface as the area approaches the Marmara Sea (Fig. 3). In certain periods, the salinity at the bottom reaches 25–30 (Fig. 3, fragment from 09 April 2008).

The seasonal and high-frequency variability of salinity in the lower layer of the strait can be attributed to the distinctive vertical structure of salinity in the Marmara Sea. The influx of fresher Black Sea waters into the upper layers of

the basin and highly saline Aegean Sea waters into the lower layers results in the formation of a two-layer stratification in the Marmara Sea. Fluctuations in the position of the boundary between the layers in the vicinity of the Bosphorus strait in the Marmara Sea result in alterations to the salinity of the lower layer.

In comparison with the findings of the study [2], salinity profiles along the strait on 26 October and 2 November 2008 (Fig. 6) will be considered. In comparison to the results presented in work [2], our calculations indicate that the Marmara Sea waters extended to the north to a somewhat greater extent in October. Nevertheless, as in the aforementioned work, our calculation also reveals the obstruction of Black Sea waters at the boundary with the Marmara Sea. In both calculations, there is a tendency for the boundary to rise during the October–November period. The temperature of the bottom waters in our results was found to be lower (Fig. 7). The process of incorporating more saline, yet warmer Marmara Sea waters into the Black Sea basin is less discernible in terms of temperature.

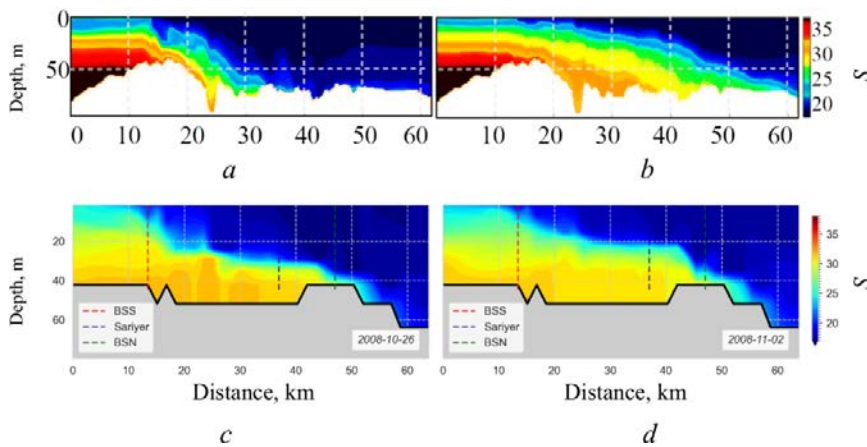


Fig. 6. Distribution of seawater salinity along the strait on 26.10.2008 and 02.11.2008 based on simulations in [2] (*a, b*) and in this paper (*c, d*)

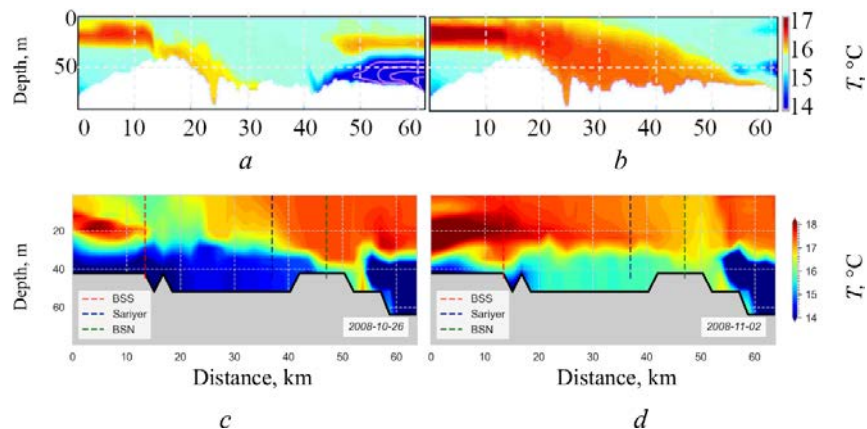


Fig. 7. Distribution of seawater temperature (°C) along the strait on 26.10.2008 and 02.11.2008 based on simulations in [2] (*a, b*) and in this paper (*c, d*)

The boundary between the layers is subject to significant fluctuations over time. On occasion, the boundary rises to the free surface, resulting in the complete obstruction of the upper Bosphorus Current (Fig. 3, fragment from 26 February 2009). In reference [6], it is demonstrated that such occurrences are linked to the wind effect. Based on direct observations of current velocity, periods during which the upper Bosphorus Current was completely blocked were identified. A comparison of the results of the present work (Fig. 8) with those of previous studies demonstrates good agreement. During the observation period, the events of blocking the upper and lower Bosphorus currents are consistent. It is important to note that the position of the boundary between these currents differs significantly due to the discrepancy between the depth of the model and the actual depth at a given station.

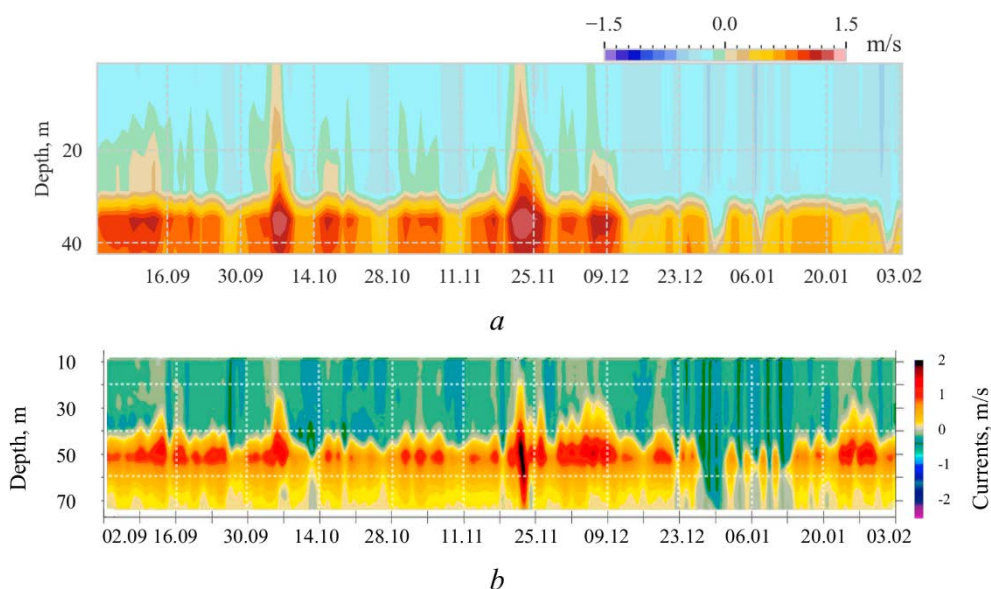


Fig. 8. Comparison with observational data: meridional currents (m/s) in the northern part of the strait in the period September 9, 2008 – February 3, 2009 based on the results of simulation (a) and measurements from [6] (b)

On approximately 7 October and 22 November 2008, the upper Bosphorus Current was observed to be blocked at both the southern and northern ends of the strait, where buoys equipped with current meters were deployed [6]. The results of the analysis indicate that on the aforementioned days, the Marmara Sea waters occupied the entire depth of the Bosphorus Strait, extending from the southern mouth to the northern end (Fig. 3, fragments from October 7 and November 22, 2008). Furthermore, the observations presented in [6] indicate that three additional instances of the upper Bosphorus current being blocked at the southern end of the strait were recorded between September 2008 and February 2009. At the same time, in the northern section of the strait, the customary transport of the Black Sea waters in the direction of the Marmara Sea was observed in the upper layer. Our calculations indicate that on these days, in the area of the southern end of the strait,

there was either a disappearance of the upper layer or a significant decrease in its thickness.

Furthermore, the observations presented in [6] demonstrated that between the end of December 2008 and mid-January 2009, a series of instances of obstruction to the lower Bosphorus Current were recorded in the northern end of the strait. As evidenced in [6], the complete obstruction of maritime traffic in the Black Sea direction was observed at the end of December (Fig. 8). The salinity sections along the strait (Fig. 3) demonstrate that at this time, the lower Bosphorus Current is entirely obstructed at its northern end.

It can be observed that between the dates of 5 and 14 January 2009, the lower Bosphorus Current in the northern section of the strait is obstructed to a significant extent, as evidenced by the findings presented in reference [6] (see Fig. 8). Our calculations indicate that the lower layer does not entirely disappear during this period, but its thickness does decrease significantly. At the same time, the calculations also demonstrate a complete blockage of the lower Bosphorus Current along the entire length of the strait (Fig. 3, fragment from 26 February 2009).

The two-year analysis of meridional currents in the strait reveals that blockages of the upper Bosphorus Current start in September (Fig. 4, *b*). This phenomenon is apparently caused by the intensification of currents in the Marmara Sea by this time (Fig. 4, *a*), which is a consequence of wind action. At the same time, the Rim Current undergoes a reduction in strength (Fig. 5). A reduction in the circulation of the Marmara Sea results in the occurrence of blockages in the lower Bosphorus Current.

Discussion

The analysis of meridional currents in the strait reveals that blockages of the upper Bosphorus Current occur from September onwards. This phenomenon may be attributed to the intensification of wind-driven currents in the Marmara Sea, which subsequently results in the weakening of the Rim Current. This results in the influx of saline Marmara waters into the Black Sea basin, leading to the formation of saltwater lenses, as demonstrated in the numerical experiment presented herewith [5]. This may also provide an explanation for the saltwater intrusions that have been detected during this period by means of profiling buoy measurements [1]. As the Marmara circulation weakens during the winter and spring, the reverse phenomenon of lower Bosphorus current blockage can be observed.

Conclusions

A comparison of the hydrophysical fields in the Bosphorus Strait with observations presented in the present paper demonstrates that the proposed model accurately reproduces the blockage of the upper Bosphorus or lower Bosphorus Current. This is in contrast to finite-element models, which allow for a more complex configuration of the strait, and which do not reproduce these situations as accurately. Furthermore, the ratios of the flow rates of the upper and lower Bosphorus currents obtained on the basis of finite-element models and according to the results of our numerical experiment are in quantitative agreement. The mechanism by which

the upper Bosphorus Current is maintained during the winter months has been confirmed. This is determined by the rise in the Black Sea level in the Bosphorus region caused by the intensification of the Rim Current.

The results of the proposed regional configuration of the NEMO model calibration indicate that the model is capable of qualitatively accurately representing the response of the strait to changes in wind action and seawater density near the northern and southern entrances.

REFERENCES

1. Falina, A., Sarafanov, A., Özsoy, E. and Turunçoğlu, U.U., 2017. Observed Basin-Wide Propagation of Mediterranean Water in the Black Sea. *Journal of Geophysical Research: Oceans*, 122(4), pp. 3141-3151. <https://doi.org/10.1002/2017JC012729>
2. Stanev, E.V., Grashorn, S. and Zhang, Y.J., 2017. Cascading Ocean Basins: Numerical Simulations of the Circulation and Interbasin Exchange in the Azov-Black-Marmara-Mediterranean Seas System. *Ocean Dynamics*, 67, pp. 1003-1025. <https://doi.org/10.1007/s10236-017-1071-2>
3. Demyshev, S.G. and Dovgaya, S.V., 2014. Numerical Modelling of the Marmara Sea Circulation in 2008 Taking into Account Wind and Water Exchange through the Straits Bosphorus and Dardanelles. *Morskoy Gidrofizicheskiy Zhurnal*, (1), pp. 68-78 (in Russian).
4. Madec, G., Bourdallé-Badie, R., Bouttier, P.-A., Bricaud, C., Bruciaferri, D., Calvert, D., Chanut, J., Clementi, E., Coward, A. [et al.], 2015. *NEMO Ocean Engine*. Notes du Pôle de Modélisation de l'Institut Pierre-Simon Laplace, No. 27. France: IPSL, 391 p. <https://doi.org/10.5281/zenodo.328739>
5. Mizyuk, A.I. and Korotaev, G.K., 2020. Black Sea Intrapycnocline Lenses According to the Results of a Numerical Simulation of Basin Circulation. *Izvestiya, Atmospheric and Oceanic Physics*, 56(1), pp. 92-100. <https://doi.org/10.1134/S0001433820010107>
6. Jarosz, E., Teague, W.J., Book, J.W. and Beşiktepe, Ş., 2011. On Flow Variability in the Bosphorus Strait. *Journal of Geophysical Research: Oceans*, 116(C8), C08038. <https://doi.org/10.1029/2010JC006861>
7. Leclair, M. and Madec, G., 2009. A Conservative Leapfrog Time Stepping Method. *Ocean Modelling*, 30(2-3), pp. 88-94. <https://doi.org/10.1016/j.ocemod.2009.06.006>
8. Rodi, W., 1987. Examples of Calculation Methods for Flow and Mixing in Stratified Fluids. *Journal of Geophysical Research: Oceans*, 92(C5), pp. 5305-5328. <https://doi.org/10.1029/JC092iC05p05305>
9. Mizyuk, A.I., Korotaev, G.K., Grigoriev, A.V., Puzina, O.S. and Lishaev P.N., 2019. Long-Term Variability of Thermohaline Characteristics of the Azov Sea Based on the Numerical Eddy-Resolving Model. *Physical Oceanography*, 26(5), pp. 438-450. <https://doi.org/10.22449/1573-160X-2019-5-438-450>
10. Korotaev, G.K., Ratner, Yu.B., Ivanchik, M.V., Kholod, A.L., and Ivanchik, A.M., 2016. Operational System for Diagnosis and Forecast of Hydrophysical Characteristics of the Black Sea. *Izvestiya, Atmospheric and Oceanic Physics*, 52(5), pp. 542-549. <https://doi.org/10.1134/S0001433816050078>
11. Mizyuk, A.I., Senderov, M.V., Korotaev, G.K. and Sarkysyan, A.S., 2016. Features of the Horizontal Variability of the Sea Surface Temperature in the Western Black Sea from High Resolution Modeling. *Izvestiya, Atmospheric and Oceanic Physics*, 52(5), pp. 570-578. <https://doi.org/10.1134/S0001433816050108>

12. Simonov, A.I. and Altman, E.N., eds., 1991. *Hydrometeorology and Hydrochemistry of Seas in the USSR. Vol. IV. Black Sea. Issue 1. Hydrometeorological Conditions*. Saint Petersburg: Gidrometeoizdat, 428 p. (in Russian).

Submitted 20.05.2024; approved after review 28.06.2024;
accepted for publication 13.07.2024.

About the authors:

Artem I. Mizyuk, Leading Researcher, Marine Hydrophysical Institute of RAS (2 Kapitanskaya Str., Sevastopol, 299011, Russian Federation), CSc. (Phys.-Math.), **ORCID ID: 0000-0003-4885-354X**, **ResearcherID: C-6125-2016**, artem.mizyuk@mhi-ras.ru

Gennady K. Korotaev, Marine Hydrophysical Institute of RAS (2 Kapitanskaya Str., Sevastopol, 299011, Russian Federation), DSc. (Phys.-Math.), Corresponding Member of the Russian Academy of Sciences, Professor, **ResearcherID: K-3408-2017**, **Scopus Author ID: 7004998153**, gkorotaev@gmail.com

Contribution of the co-authors:

Artem I. Mizyuk – investigation, methodology, validation, visualization, writing, review and editing

Gennady K. Korotaev – supervision, writing of the original draft, review, editing, conceptualization


The authors have read and approved the final manuscript.

The authors declare that they have no conflict of interest.

The Effect of Dust Aerosol on Satellite Data from Different Color Scanners

A. S. Papkova, E. B. Shybanov , D. V. Kalinskaya

Marine Hydrophysical Institute of RAS, Sevastopol, Russian Federation

 e-shybanov@mail.ru

Abstract

Purpose. The work is purposed at evaluating the errors in atmospheric correction of the satellite (*MODIS Aqua*, *MODIS Terra*, *VIIRS SNPP*, *VIIRS JPSS*, *NASA HawkEye* (*SeaHawk*) and *OLCI* (*Sentinel 3A*)) data for July 28–29, 2021 when a dust transport over the Black Sea region was recorded. **Methods and Results.** To assess the scale and intensity of the studied dust transfer, the results of *in situ* photometric measurements and satellite data were analyzed. The *in situ* measurement data on aerosol optical depth (AOD) were obtained at the western Black Sea stations *Galata Platform* and *Section_7* of the *AERONET* network (*AErosol RObotic NETwork*). The variability of sea remote sensing reflectance values during the period under study was analyzed using the additional *AERONET* – *Ocean Color* (*AERONET-OC*) data. The color scanner (*MODIS Aqua/Terra*, *VIIRS SNPP/JPSS*, *HawkEye* and *OLCI*) measurements presented in the *Ocean Color* database were used as satellite data.

Conclusions. The approximation of errors in atmospheric correction of satellite data for July 28–29, 2021 has resulted in obtaining the power-law dependencies close to λ^{-5} . This is explained by the total contribution of molecular component (λ^{-4}) and aerosol absorption (λ^{-1}). On July 29, 2021, a better pronounced power function is observed since the dust aerosol concentration increases on this day, whereas the contribution of aerosol absorption becomes close to the power dependence λ^{-2} . Also on the same day, the *CALIPSO* satellite data showed the presence of not only dust aerosol, but also the biomass burning over the region under study. Modeling the back trajectories of *HYSPLIT* air flows has shown that just on this day the aerosol masses moved towards the Black Sea from the southwest (Crete Island), that was additionally confirmed by high AOD values over the eastern Mediterranean Sea on July 29, 2021. The combination of two types of absorbing aerosols is assumed to induce even larger inaccuracies in determining the sea remote sensing reflectance for the period under study.

Keywords: *MODIS*, *VIIRS*, *HawkEye*, *Sentinel*, *SPM*, *AERONET*, *CALIPSO*, *HYSPLIT* back trajectories, dust aerosol, biomass burning, sea remote sensing reflectance, aerosol optical depth, AOD, absorption, Black Sea, atmospheric aerosol, satellite monitoring, ground monitoring, optical characteristics

Acknowledgments: The study was carried out within the framework of state assignment of FSBSI FRC MHI FNNN-2024-0012 on theme “Analysis, hindcast and operational forecast of the state of hydrophysical and hydrochemical fields of marine water areas based on numerical modeling using the data of remote and contact measurement methods”. The authors are thankful to Tom Kucsera, Brent Holben, Giuseppe Zibordi, as well as to the group of Gene Feldman from *NASA* for providing the AOD data, calculating the *BTa* data, processing the measurement results obtained at the Sevastopol *AERONET* station, and for the possibility of using high-quality photometric measurement data.

For citation: Papkova, A.S., Shybanov, E.B. and Kalinskaya, D.V., 2024. The Effect of Dust Aerosol on Satellite Data from Different Color Scanners. *Physical Oceanography*, 31(5), pp. 720-735.

© 2024, A. S. Papkova, E. B. Shybanov, D. V. Kalinskaya

© 2024, Physical Oceanography



Introduction

Mineral dust is often neglected in the analysis of anthropogenic climate change, as it is considered part of the natural aerosol. Some researchers believe that dust may be an important climate-forming component, especially over certain oceanic areas and regions where its concentrations are high [1, 2]. Although it is impossible to determine the exact impact of mineral dust on the global climate, research on this topic is interdisciplinary and relevant. Complete information on the properties of different types of aerosols (including absorbing aerosols) can be obtained by comprehensive determination of their concentration, microstructure, chemical composition and optical properties [3–5].

This study is a continuation of a series of works dedicated to the examination of optical properties of the dust aerosol over the Black Sea and its influence on *Ocean Color* products. For the region under study, the results obtained when analyzing satellite data can in many cases have large errors due to incorrect consideration of the optical properties of the aerosol [6–9]. It is worth noting that dust transports from both the African continent as well as from the Middle East and Asia are observed annually over the Black Sea region [10]. Since the MHI RAS scientists have been studying this topic for more than 10 years, there is already a certain method to identify different types of aerosols (background aerosol, smoke and dust) based on the variability of optical properties, such as aerosol optical depth (AOD), Angstrom parameter (α), single scattering albedo (SSA), size distribution and concentration of aerosol particles (fine ($PM_{2.5}$) and coarse (PM_{10}) particles), asymmetry parameter, etc. The dust aerosol identification method combines a visual analysis of satellite images, which clearly show a dust plume, and an analysis of photometric measurements of the optical properties of the aerosol. To analyze the aerosol over the Black Sea region, data from the *AERONET* network stations (*Galata_Platform, Section_7*) located in the western part of the Black Sea are used, as well as unique data from the portable SPM spectrophotometer and the ATMAS dust meter, which were measured daily on the MHI RAS territory [11–13].

It is worth noting that dust aerosol has the greatest impact not only on the variability of the optical properties of the atmosphere, but also on the *Ocean Color* satellite products. For an objective assessment of the state of the water surface and the procedure for atmospheric correction based on remote sensing data, it is necessary to carry out a comparative analysis of three types of measurement data: satellite, model and *in situ*. In [8, 14–28], it is shown that in the presence of dust, the sea remote sensing reflectance can have negative values in the shortwave range (400–443 nm). This fact indicates systematic errors in the operation of standard atmospheric correction algorithms, which are based on the principle of extrapolating aerosol properties from the near-IR part of the spectrum to the visible part [27]. In a previous work [18], it was shown analytically that in the presence of dust-absorbing aerosol in the atmosphere

above the region, the error in the atmospheric correction is expressed by a fourth-degree power function, i.e. it is close to λ^{-4} . This is due to the absorption by the aerosol of radiation scattered by the air molecules. The analytical expression describing the dependence of the error value of the standard atmospheric correction on the aerosol stratification, for small values of the optical depth of light absorption by the aerosol $a_0(\lambda)$, has the following form

$$r = \frac{p_m(\cos \gamma) \cdot \tau_m^0(\lambda)}{4\mu_0\mu} a_0(\lambda) \cdot \left(\frac{1}{\mu_0} + \frac{1}{\mu} \right) \int_0^1 \int_0^p g(x) dx \cdot dp, \quad (1)$$

$$a_0(\lambda) = (1 - \Lambda) \tau_a^0,$$

where τ_a^0 is the aerosol optical depth; Λ is the single scattering albedo; μ_0 is the cosine of the solar zenith angle; μ is the cosine of the observation zenith angle; $\cos \gamma = -\mu_1 \cdot \mu_2 + \sqrt{1 - \mu_1^2} \sqrt{1 - \mu_2^2} \cos \varphi$ is the cosine of the scattering angle; τ_m^0 is the total optical depth of the molecular atmosphere; $g(x)$ is the dust aerosol stratification function, which shows the dependence of the relative concentration of aerosol particles on atmospheric pressure at a given altitude. The first fraction in expression (1) is nothing more than the expression for the sensing reflectance of the molecular atmosphere in the linear Gordon approximation. Consequently, three factors can be identified that influence the magnitude of the atmospheric correction error. The multiplier $\frac{p_m(\cos \gamma)}{\mu_0\mu} \left(\frac{1}{\mu_0} + \frac{1}{\mu} \right)$ describes the observation geometry, and

the double integral is independent of the wavelength and takes into account stratification of the absorbing aerosol relative to the air molecules. Consequently, the spectral properties of the atmospheric correction error are described by the factors $\tau_m^0(\lambda)$ and a_0 . It is known that, according to the Rayleigh law, $\tau_m^0 \approx \lambda^{-4}$, spectral properties of aerosol absorption are determined by aerosol microphysics, which for dust aerosol depends on the dust sources and their transformation processes in the atmosphere. Until now, the spectral dependence variability a_0 has not been considered. In this paper, it is proposed to estimate for the first time the spectral behavior of the absorption properties of dust aerosol for the case of dust transfer over the Black Sea region.

Experimental regularities of the atmospheric correction error were analyzed in [18]. It was shown that the largest difference between satellite and *in situ* remotely sensed ocean reflectance data is recorded in the presence of dust aerosol in the atmosphere. For the selected 49 data obtained on dust transfer days, the principal component method with the first vector contribution estimation was used. The result showed that 86% of the variance of the *MODIS-Aqua* validation error is explained

by the first eigenvector, which is well approximated by a power law $\lambda^{-3.57 \pm 0.32}$. This confirmed the reliability of the analytical estimates [18].

The objective of this study is to estimate the magnitude of the atmospheric correction error of *MODIS-Aqua*, *MODIS-Terra*, *VIIRS-SNPP*, *VIIRS-JPSS*, *NASA HawkEye (SeaHawk)* and *OLCI-Sentinel-3A* satellite data for 28–29 July 2021, when dust transport over the Black Sea region was recorded.

The present study focuses on an analysis of the variability of the optical properties of the atmosphere on 28–29 July 2021 over the Black Sea region and the evidence (based on satellite and model data) that it is dust aerosol that is recorded over the region during the period under consideration.

The second stage is dedicated to the estimation of the impact of the absorbing dust aerosol on the size of the atmospheric correction error in the calculation of the sea remote sensing reflectance for 28 and 29 July 2021. For these dates, the largest number of different satellite measurements, synchronized with *in-situ* remote sensing sea reflectance measurements according to the *AERONET–Ocean Color (AERONET-OC)* network, were obtained. In this study, the validation error was calculated for *MODIS-Aqua/Terra*, *VIIRS-JPSS*, *Sentinel-3A* and *HawkEye (SeaHawk)*.

Instruments and materials

The photometric data from the international *AERONET (Aerosol Robotics NETwork)* were used as a source for the *in-situ* AOD measurements. The data from the *AERONET-OC* extension, which allow the measurement of radiation from underwater, were used to analyze the sea remote sensing reflectance data [29]. Currently, two stations, *Black Sea Section_7* (29.45°E, 44.45°N) and *Galata_Platform* (28.19°E, 43.05°N), provide information on seawater color. In this paper, an array of daily mean data on normalized L_{WN} level 2 (higher quality) water radiation has been analyzed. The level 1.5 data array is selected taking into account cloudiness through a series of quality tests, and the level 2 data array consists of fully cleaned data obtained after calibration and software verification. During the studies, $L_{WN}(\lambda)$ values were converted to $R_{rs}(\lambda)$ values by dividing by the solar constant $F_0(\lambda)$ [30].

To compare satellite and *in situ* measurements for 28–29 July 2021 and to correct for inaccuracies caused by variability and anomalies in atmospheric parameters, the data from the international *AERONET* photometer network, freely available at <http://aeronet.gsfc.nasa.gov> and the *MODIS-Aqua/Terra*, *VIIRS-SNPP/JPSS*, *HawkEye* and *OLCI* data, freely available at <https://OceanColor.gsfc.nasa.gov>, were selected. The *MODIS* optical properties data are the result of a combination of *Terra* and *Aqua* satellite measurements, providing near real-time information. The resolution of the *MODIS* sensor is 0.5°, the resolution of the images is 2 km, and the temporal resolution is diurnal.

A complicating factor in the study is that the wavelengths at which the *AERONET-OC* station measurements are provided do not fully match

the channels measured by the satellites, especially in the visible range. Thus, the *MODIS-Aqua/Terra* measurement channels have wavelengths of 412, 443, 469, 488, 531, 547, 555, 667 and 678 nm; *VIIRS-JPSS* – wavelengths of 411, 445, 489, 556 and 667 nm. For *HawkEye*, $R_{rs}(\lambda)$ are measured at wavelengths of 412, 488, 510, 556 and 670 nm. The problem of interpolating the sea remote sensing reflectance values obtained in the *CIMEL-318* photometer channels to the satellite channels is due to the complex shape of the seawater absorption spectrum. Scattering also affects the shape of $R_{rs}(\lambda)$. However, the corresponding spectral dependencies are monotonous and smoother, allowing the use of a second-degree polynomial in the interpolation. In the absorption spectrum, special attention is paid to the absorption of pure seawater, since it greatly affects the variability of the $R_{rs}(\lambda)$ values in the long wavelength region of the spectrum. The absorption spectrum of pure seawater introduces the largest interpolation errors.

In this study, a method was used which consists of multiplying the sea remote sensing reflectance obtained from field measurements by the seawater model absorption value:

$$a_w(\lambda_i) = a_{pw}(\lambda_i) + 0.1 \cdot C_y \cdot \exp[0.015 \cdot (400 - \lambda_i)], \quad (2)$$

where C_y is estimated by statistical relationship with color index:

$$C_y = 2.3 \cdot CI(555/510)^{2.18}. \quad (3)$$

Expression (3) was obtained based on the regression dependencies given in [31]. After multiplying the natural sea remote sensing reflectance by the model absorption, a second-degree polynomial interpolation was applied to the satellite channels. The resulting values were then divided by the model absorption value at the satellite wavelengths.

The data from the *CALIPSO* satellite were analyzed to determine the predominant aerosol type during the study period. This is an American-French research satellite launched as part of *NASA EOS (Earth Observing System)* program to study the Earth's cloud cover and the vertical structure of atmospheric aerosol. Its main instrument is a three-channel imaging radiometer (8.65, 10.6 and 12.05 μm). Aerosol types are determined by the value of the integrated backscattering coefficient and the particle depolarization coefficient. The aerosol types determined by the calculations of the *CALIPSO* algorithms are: smoke (from forest fires), dust, contaminated dust (mixtures of dust and smoke), contaminated continental and clean continental aerosol [32]. Each aerosol type is characterized by a set of lidar ratios at the 532 and 1064 nm wavelengths [33].

To obtain information on the source of the smoke aerosols, the results of the calculation of reverse trajectories of air mass transfer, obtained using the *HYSPLIT* modeling software package, were used. Reverse trajectory analysis

makes it possible to follow the movement of air flows at different altitudes and to identify the location of likely sources of pollution entering the atmosphere [34].

Results and discussion

On 28–29 July 2021, satellite data showed intense dust transport from the Arabian Peninsula and the Sahara across the Black Sea region. According to the *VIIRS* false-color satellite images, dust transport is recorded on both sides of the illuminated area, which means that the size of the dust event is more than a thousand square kilometers. All presented satellite images also clearly show the area of intense fires on the Mediterranean coast (territory of Turkey). Intense absorption due to the presence of smoke aerosol west of the island of Crete is confirmed by high AOD values over the eastern part of the Mediterranean Sea on 29 July 2021 (Fig. 1). The next step is confirming or refuting of the dust transfer event over the Black Sea region during the study period was the analysis of the reverse trajectories of the air flow movement using the *HYSPLIT* model [34] (Fig. 1, *b*, *d*). As shown in Fig. 1, dust transfer from the Sahara was recorded at the 3 km level for all days.

Table 1

Optical characteristics of atmospheric aerosol over the *AERONET-OC* stations in the Black Sea

Aerosol parameters	<i>Section-7 Platform</i>			<i>Galata Platform</i>		
	27.07.2021	28.07.2021	29.07.2021	27.07.2021	28.07.2021	29.07.2021
AOD_1020nm	0.1044	0.1594	0.15640	0.118754	0.153976	0.145702
AOD_865nm	0.1184	0.1774	0.17599	0.133570	0.169755	0.164323
AOD_779nm	0.1273	0.1888	0.18826	0.142891	0.179414	0.177168
AOD_667nm	0.1510	0.2150	0.21895	0.163671	0.200484	0.205612
AOD_620nm	0.1640	0.2299	0.23420	0.175332	0.211100	0.220486
AOD_560nm	0.1859	0.2543	0.26190	0.194556	0.230445	0.247066
AOD_510nm	0.2079	0.2793	0.29050	0.214621	0.251795	0.276285
AOD_490nm	0.2163	0.2880	0.30092	0.222911	0.259967	0.287855
AOD_443nm	0.2425	0.3173	0.33410	0.247029	0.284315	0.322171
AOD_412nm	0.2667	0.3432	0.36280	0.266241	0.303928	0.349083
AOD_400nm	0.2801	0.3569	0.37790	0.275084	0.313003	0.361403
$\alpha(440-870)$	1.1110	0.8871	0.98910	0.979185	0.782825	1.027634
$\alpha(440-675)$	1.1687	0.9532	1.06210	1.051961	0.867812	1.117899

In this paper, a comparative analysis of the aerosol optical properties at *AERONET* stations (*Galata Platform* and *Section_7 Platform*) was performed for cases of different aerosol activity, namely: for 28 July 2021 (the day of the intense dust transfer), 27 July 2021 (the day before the dust transfer in the presence of

background aerosol) and 29 July 2021 (the day after the start of the intense dust transfer). It is worth noting that in July 2021 cloudiness was often observed over the *AERONET* stations and therefore the initial monthly mean AOD values were overestimated, which is typical for summer months [35] (Table 1).

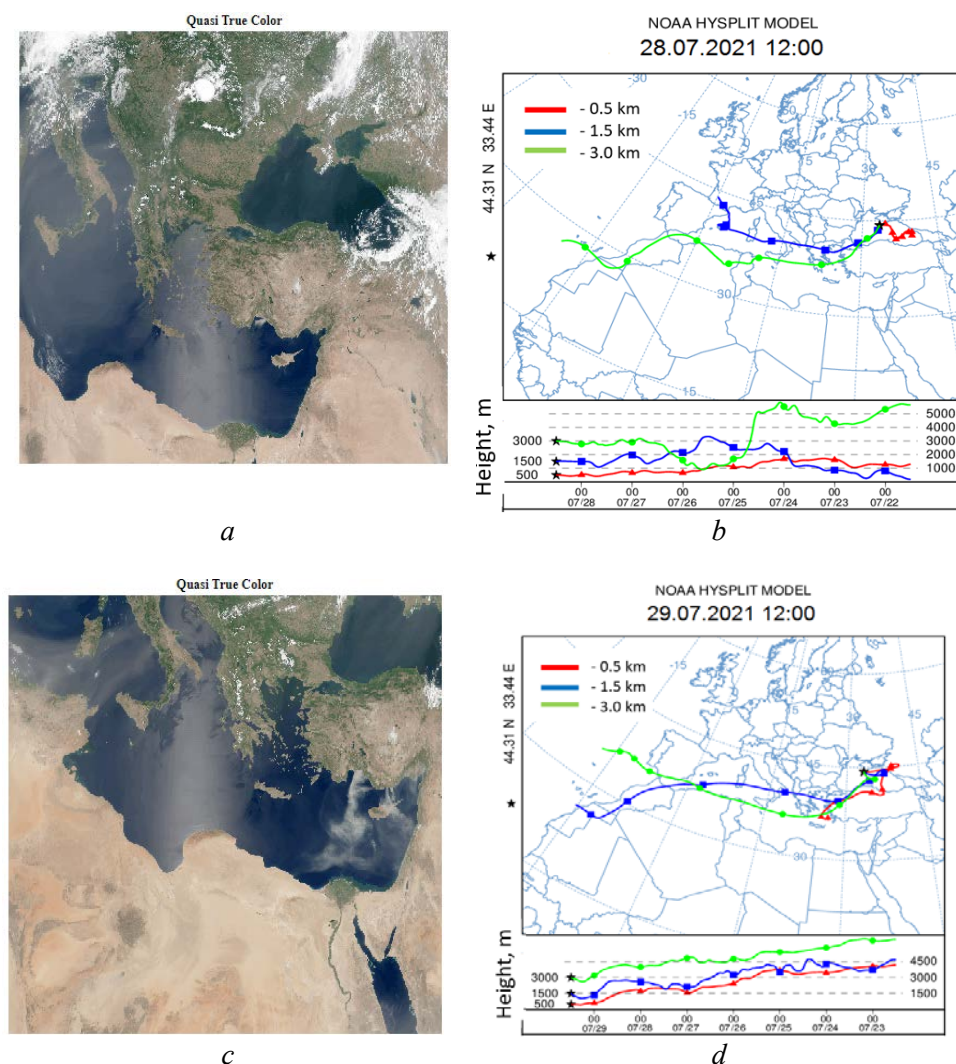


Fig. 1. Satellite images of *VIIRS-SNPP/JPSS* from 28 July 2021 (a) and 29 July 2021 (c) (source: <https://oceancolor.gsfc.nasa.gov>), and corresponding *HYSPLIT* back trajectories (b, d) (source: https://www.ready.noaa.gov/HYSPLIT_traj.php)

At both western *AERONET* stations in the Black Sea region, a large amount (compared to background values) of coarse aerosol fraction (more than $2.5 \mu\text{m}$) and low ($\text{SSA} < 1$) values of the single scattering albedo (SSA) were observed on 28 July 2021 (Fig. 2). In general, a similar situation was observed on 29 July 2021, except for higher values of the Angstrom parameter.



Fig. 2. At the *AERONET* network stations on 28 July 2021: contribution of fine (less than 2.5 mkm) and coarse particles (2.5 mkm and more) to the overall distribution of AOD at *Galata_Platform* (a) and *Section_7* (c), single scattering albedo at *Galata_Platform* (b) and *Section_7* (d), particle size distribution at two stations (e)

For the first time, an estimate of the optical depth of aerosol absorption is given for the general assessment of the absorption properties of dust aerosol:

$$a_0(\lambda) = (1 - \Lambda(\lambda))\tau_a^0(\lambda). \quad (4)$$

Consequently, the average daily variation of the power function of the optical absorption depth was analyzed for synchronous pairs of AOD and SSA measurements for *AERONET* stations (Fig. 3).

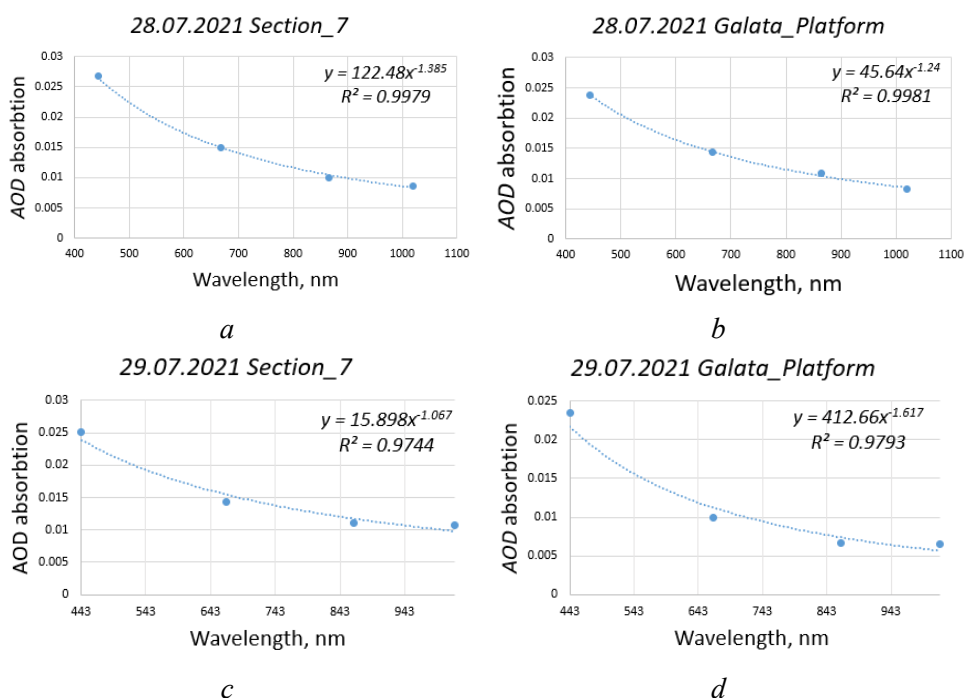
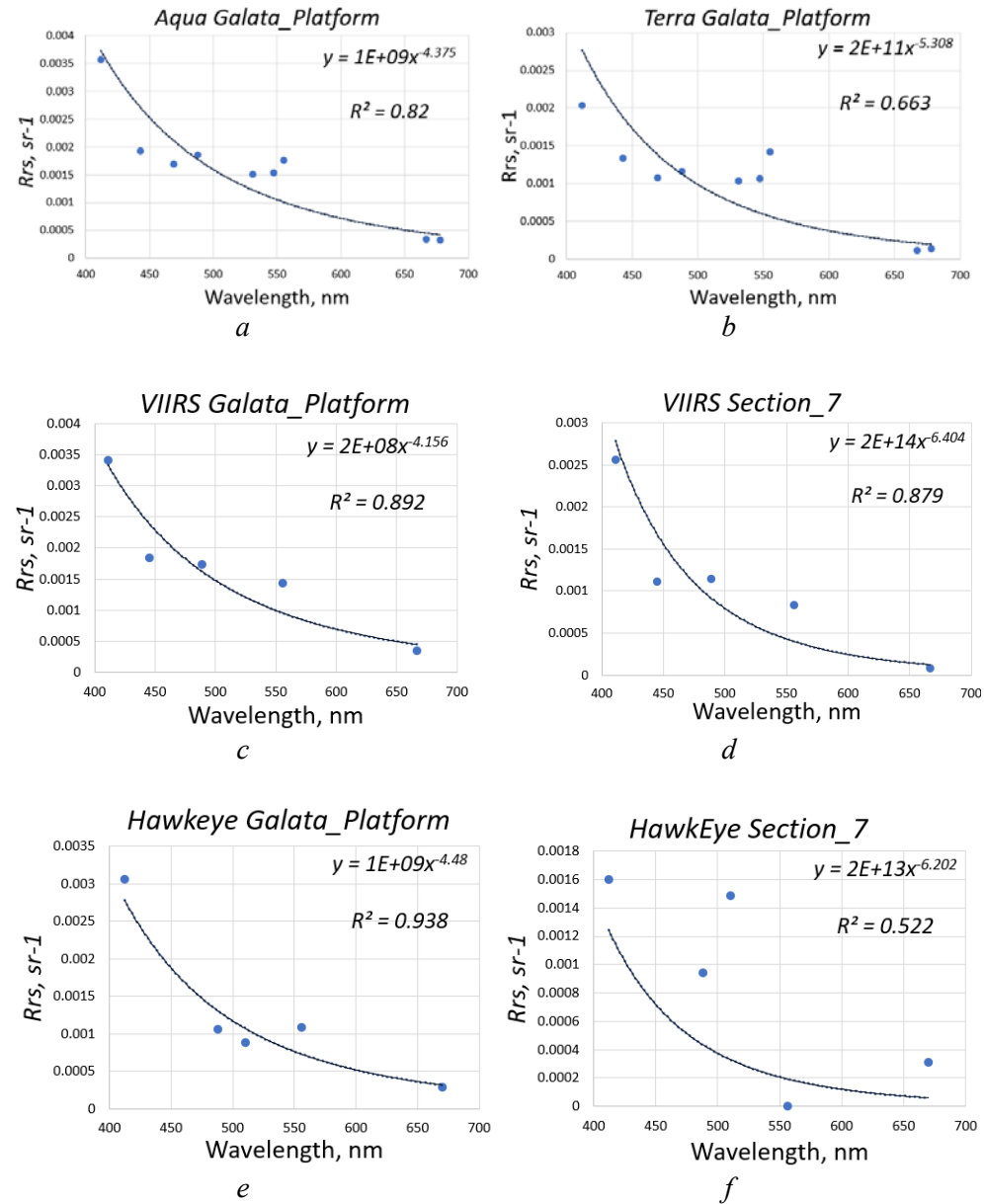


Fig. 3. Mode of the power function of aerosol absorption optical depth at *Galata_Platform* (a) and *Section_7* (b) for 28 July 2021, and at *Galata_Platform* (c) and *Section_7* (d) for 29 July 2021

From Fig. 3 it is evident that the power function is close to λ^{-1} . Consequently, the magnitude of the atmospheric correction error depends not only on the λ^{-4} factor, but also on the light absorption by the aerosol. As a result, the error of the standard atmospheric correction will increase at shorter wavelengths. It should be noted that the standard atmospheric correction procedure is not capable of qualitatively estimating the change in spectral properties of aerosol scattering under the influence of light absorption in the near IR region, due to the smallness of this effect in the long wavelength part of the spectrum. For this reason, it is necessary to use additional information about the optical properties of the underlying surface in the shortwave region. Thus, the application of standard algorithms for atmospheric correction of satellite data in the presence of absorbing dust aerosol requires an additional regional correction. The product $a_0(\lambda) \cdot \lambda^{-4}$ should be used as the interpolation function, and the proportionality coefficient is found from the conditions imposed on the sea remote sensing reflectance in the shortwave region of the spectrum.

The next stage of the study is to calculate the atmospheric correction error for the *MODIS-Aqua/Terra*, *VIIRS-SNPP/JPSS*, *HawkEye* and *Sentinel-3A* satellites for the dates considered. The validation procedure for the satellite data was similar to that used for the *SeaBASS* database: synchronous pairs of measurements with the smallest time difference within a radius of 5 km around the western Black Sea *AERONET-OC* stations were selected. Using the *SeaDAS* software package, all pixels with the following error flags were similarly excluded: *LAND*, *STRAYLIGHT*, *HIGLINT*, *HILT*, *MODGLINTATMWAR* and *NAVFAILE* [36]. Unfortunately, the *VIIRS-SNPP* satellite data for 28 July 2021 were excluded from further analysis

because all pixels within a 5 km radius of the *AERONET-OC* stations were within the satellite illumination zone. The synchronous *in situ* measurements of $Rrs(\lambda)$ at the *AERONET-OC* stations in the western Black Sea during the day changed little, namely: the standard deviation (SD) was less than 10% of the value, allowing the use of daily averages. The interpolation results constructed from the results of sea remote sensing reflectance measurements by *MODIS-Aqua*, *VIIRS-JPSS*, *Hawkeye* and *OCLI Sentinel-3A* satellites for 28 July 2021 are shown in Fig. 4.



F i g. 4. Errors of atmospheric correction and their approximation by power dependence for 28 July 2021

The atmospheric correction error was similarly calculated for 29 July 2021, when the dust aerosol AOD was higher, but the Ångström parameter was lower (Fig. 5). Unfortunately, the *Modis-Terra* and *VIIRS-SNPP* data had strong outliers and after filtering the error flags, there were no data left.

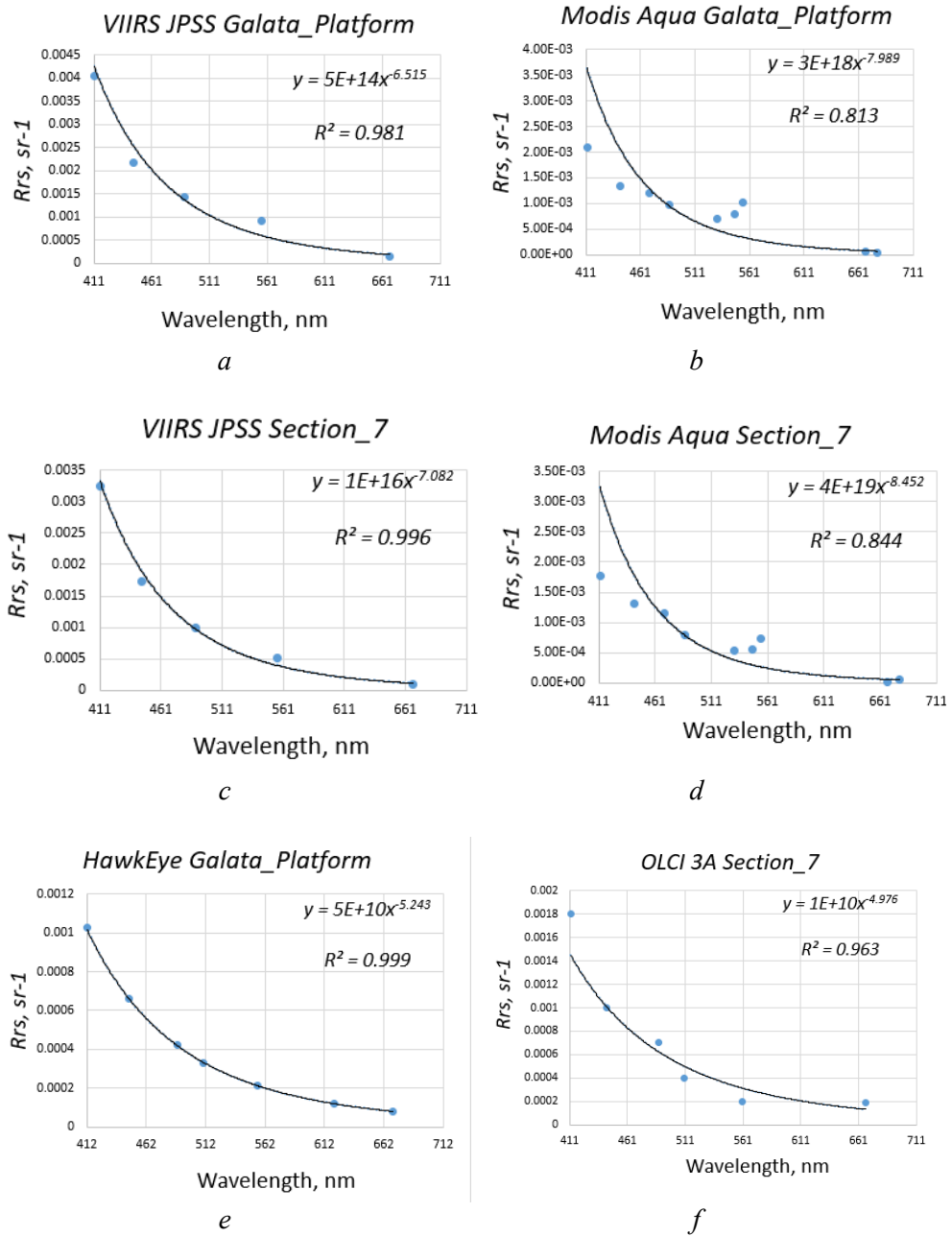


Fig. 5. Errors of atmospheric correction based on the results of measurements of sea remote sensing reflectance by satellites *MODIS-Aqua*, *VIIRS-JPSS*, *Hawkeye* and *OLCI Sentinel 3A* for the Black Sea *AERONET-OC* stations for 29 July 2021

As a result of approximation of the atmospheric correction errors for 28 July 2021, power-law dependencies close to λ^{-5} were obtained. This is explained by the total contribution of: 1) the molecular component (λ^{-4}) and 2) the aerosol absorption (λ^{-1}). Fig. 4 shows that the atmospheric correction error of the sea remote sensing reflectance for the *Galata_Platform* station, obtained from *VIIRS-JPSS* and *HawkEye* measurements, is close to the power-law dependence $\lambda^{-4} - \lambda^{-5}$, and for the *Section_7* station it has a more pronounced power-law dependence, namely λ^{-7} . A pronounced shape of the power-law function is observed on 29 July 2021, when the dust aerosol concentration increases and its aerosol absorption is already close to λ^{-2} . It is worth noting that the largest atmospheric correction errors were found for 29 July 2021 according to *MODIS-Aqua* data, whose interpolation function is close to the form λ^{-8} . We believe that this is due to underestimated R_{rs} measurements in the longwave region for this day and consequently large errors in the standard power law approximation – the logarithmic method followed by linear optimization. Using a nonlinear approximation, the power function was obtained in the form $\lambda^{-4} - \lambda^{-5}$, which also indicates large errors in the shortwave region of the spectrum. The maximum errors in the blue region are observed in Fig. 4, *a, c*; 5, *a, c*.

It is worth noting that the new *HawkEye* and *Sentinel-3A* satellites, despite their short lifetime and a low number of reprocessings and calibrations, show more accurate results. This may be due to the better spatial resolution of the new satellite instruments.

Analysis of *CALIPSO* satellite data on the stratification of different aerosol types for 28 and 29 July 2021 confirmed the presence of dust particles in the surface atmospheric column up to 5 km over the Black Sea. In addition to dust aerosol, contaminated dust and smoke aerosol were recorded on 29 July 2021, which also confirms the spatial distribution of smoke towards The Black Sea region shown in Fig. 1, *c*.

Conclusion

As a result of the approximation of the atmospheric correction errors of the satellite data for 28 July 2021, power-law dependencies close to λ^{-5} were obtained. This is explained by the total contribution of the molecular component (λ^{-4}) and the aerosol absorption (λ^{-1}). For 29 July 2021, a pronounced power-law behavior is observed as the dust aerosol concentration increases and the contribution of aerosol absorption becomes close to the λ^{-2} power-law dependence. In addition, for 29 July 2021, the presence of both dust and smoke aerosols was shown over the study region according to *CALIPSO* satellite data. According to the *HYSPLIT* air flow backtracking modeling data, the aerosol masses on this day moved from the southwest (Crete) towards the Black Sea, which is further confirmed by the high AOD values over the eastern Mediterranean on 29 July 2021. It is assumed that the combination of two absorbing aerosol types caused even greater inaccuracies in the determination of the spectral sea remote sensing reflectance for the period under study.

REFERENCES

1. Koren, I., Kaufman, Y.J., Washington, R., Todd, M.C., Rudich, Y., Martins, J.V. and Rosenfeld, D., 2006. The Bodele Depression: A Single Spot in the Sahara that Provides Most of the Mineral Dust to the Amazon Forest. *Environmental Research Letters*, 1(1), 014005. <https://doi.org/10.1088/1748-9326/1/1/014005>
2. Kubilay, N., Cokacar, T. and Oguz, T., 2003. Optical Properties of Mineral Dust Outbreaks over the Northeastern Mediterranean. *Journal of Geophysical Research: Atmospheres*, 108(D21), 4666. <https://doi.org/10.1029/2003JD003798>
3. Suslin, V.V., Slabakova, V.K., Kalinskaya, D.V., Pryakhina, S.F. and Golovko, N.I., 2016. Optical Features of the Black Sea Aerosol and the Sea Water Upper Layer Based on In Situ and Satellite Measurements. *Physical Oceanography*, (1), pp. 20-32. <https://doi.org/10.22449/1573-160X-2016-1-20-32>
4. Suslin, V.V. and Churilova, T.Ya., 2010. Simplified Method of Calculation of Spectral Diffuse Beam Attenuation Coefficient in the Black Sea Upper Layer on the Basis of Satellite Data. In: MHI, 2010. *Ecological Safety of Coastal and Shelf Zones and Comprehensive Use of Shelf Resources*. Sevastopol: ECOSI-Gidrofizika. Iss. 22, pp. 47-60 (in Russian).
5. Glukhovets, D., Salyuk, P., Sheberstov, C., Vazyulya, S., Sahling, I. and Stepochkin, I., 2021. Retrieval of the Full Complex of Optical Characteristics for Heat Content Assessing in the Southern Part of the Barents Sea in June. *Sovremennye Problemy Distantionnogo Zondirovaniya Zemli iz Kosmosa*, 18(5), pp. 214-225. <https://doi.org/10.21046/2070-7401-2021-18-5-214-225> (in Russian).
6. Korchemkina, E.N., Shybanov, E.B. and Lee, M.E., 2009. Atmospheric Correction Improvement for the Remote Sensing of Black Sea Waters. *Issledovanie Zemli iz Kosmosa*, (6), pp. 24-30 (in Russian).
7. Kopelevich, O.V., Sahling, I.V., Vazyulya, S.V., Glukhovets, D.I., Sheberstov, S.V., Burenkov, V.I., Karalli, P.G. and Yushmanova, A.V., 2018. *Bio-Optical Characteristics of the Seas, Surrounding the Western Part of Russia, from Data of the Satellite Ocean Color Scanners of 1998-2017*. Moscow: OOO "Vash Format", 140 p. (in Russian).
8. Suetin, V.S., Korolev, S.N., Suslin, V.V. and Kucheryavyi, A.A., 2004. Manifestation of Specific Features of the Optical Properties of Atmospheric Aerosol over the Black Sea in the Interpretation of SeaWiFS Data. *Physical Oceanography*, 14(1), pp. 57-65. <https://doi.org/10.1023/B:POCE.0000025370.99460.88>
9. Suetin, V.S. and Korolev, S.N., 2021. Application of Satellite Data for Retrieving the Light Absorption Characteristics in the Black Sea Waters. *Physical Oceanography*, 28(2), pp. 205-214. <https://doi.org/10.22449/1573-160X-2021-2-205-214>
10. Kabashnikov, V., Milinevsky, G., Chaikovsky, A., Miatselskaya, N., Danylevsky, V., Aculinin, A., Kalinskaya, D., Korchemkina, E., Bovchaliuk, A. [et al.], 2014. Localization of Aerosol Sources in East-European Region by Back-Trajectory Statistics. *International Journal of Remote Sensing*, 35(19), pp. 6993-7006. <https://doi.org/10.1080/01431161.2014.960621>
11. Zibordi, G., Mélin, F., Berthon, J.-F., Holben, B., Stutsker, I., Giles, D., D'Alimonte, D., Vandemark, D., Feng, H. [et al.], 2009. AERONET-OC: A Network for the Validation of Ocean Color Primary Products. *Journal of Atmospheric and Oceanic Technology*, 26(8), pp. 1634-1651. <https://doi.org/10.1175/2009JTECHO654.1>
12. Kalinskaya, D.V. and Suslin V.V., 2015. Simple Method of Determination of Ground-Based Aerosol Sources Using Back Trajectory Analysis Results. *Fundamental and Applied Hydrophysics*, 8(1), pp. 59-67 (in Russian).

13. Kalinskaya, D.V. and Papkova, A.S., 2022. Why Is It Important to Consider Dust Aerosol in the Sevastopol and Black Sea Region during Remote Sensing Tasks? A Case Study. *Remote Sensing*, 14(8), 1890. <https://doi.org/10.3390/rs14081890>
14. Wang, M., Son, S. and Harding, L.W. Jr., 2009. Retrieval of Diffuse Attenuation Coefficient in the Chesapeake Bay and Turbid Ocean Regions for Satellite Ocean Color Applications. *Journal of Geophysical Research: Oceans*, 114(C10), C10011. <https://doi.org/10.1029/2009JC005286>
15. Schollaert, S.E., Yoder, J.A., O'Reilly, J.E. and Westpha, D.L., 2003. Influence of Dust and Sulfate Aerosols on Ocean Color Spectra and Chlorophyll a Concentrations Derived from SeaWiFS off the U.S. East Coast. *Journal of Geophysical Research: Oceans*, 108(C6), 3191. <https://doi.org/10.1029/2000JC000555>
16. Suetin, V.S., Korolev, S.N. and Kucheryavy, A.A., 2014. Application of Satellite Observations for Determining Spectral Dependences of the Black Sea Waters Optical Characteristics. *Morskoy Gidrofizicheskiy Zhurnal*, (3), pp. 77-86 (in Russian).
17. Kalinskaya, D.V. and Papkova, A.S., 2023. Variability of the Water-Leaving Radiance under the Conditions of Dust Transport by the Satellite Sentinel-3 Data on the Example of the Black Sea and Sevastopol. *Physical Oceanography*, 30(3), pp. 369-383. <https://doi.org/10.29039/1573-160X-2023-3-369-383>
18. Shybanov, E.B. and Papkova, A.S., 2022. Differences in the Ocean Color Atmospheric Correction Algorithms for Remote Sensing Reflectance Retrievals for Different Atmospheric Conditions. *Sovremennye Problemy Distantionnogo Zondirovaniya Zemli iz Kosmosa*, 19(6), pp. 9-17. <https://doi.org/10.21046/2070-7401-2022-19-6-9-17> (in Russian).
19. Wei, X., Chang, N.-B., Bai, K. and Gao, W., 2020. Satellite Remote Sensing of Aerosol Optical Depth: Advances, Challenges, and Perspectives. *Critical Reviews in Environmental Science and Technology*, 50(16), pp. 1640-1725. <https://doi.org/10.1080/10643389.2019.1665944>
20. Wang, X., 2018. New Methods for Improving the Remote Sensing Estimation of Soil Organic Matter Content (SOMC) in the Ebinur Lake Wetland National Nature Reserve (ELWNNR) in Northwest China. *Remote Sensing of Environment*, 218, pp. 104-118. <https://doi.org/10.1016/j.rse.2018.09.020>
21. Gordon, H.R., 2021. Evolution of Ocean Color Atmospheric Correction: 1970–2005. *Remote Sensing*, 13(24), 5051. <https://doi.org/10.3390/rs13245051>
22. Moulin, S., Launay, M. and Guérif, M., 2001. The Crop Growth Monitoring at a Regional Scale Based on the Combination of Remote Sensing and Process-Based Models. In: K. Kobayashi, ed., 2001. *Proceedings of NIAES-STA International Workshop 2001: Crop Monitoring and Prediction at Regional Scales*. Tsukuba, Japan, pp. 187-195.
23. Korchemkina, E.N. and Kalinskaya, D.V., 2022. Algorithm of Additional Correction of Level 2 Remote Sensing Reflectance Data Using Modelling of the Optical Properties of the Black Sea Waters. *Remote Sensing*, 14(4), 831. <https://doi.org/10.3390/rs14040831>
24. Kopelevich, O.V., Burenkov, V.I. and Sheberstov, S.V., 2006. Development and Use of Regional Algorithms for Calculation of Bio-Optical Characteristics of Russian Seas Based on Satellite Color Scanner Data. *Sovremennye Problemy Distantionnogo Zondirovaniya Zemli iz Kosmosa*, 3(2), pp. 99-105 (in Russian).
25. Remer, L.A., Kahn, R.A. and Koren, I., 2009. Aerosol Indirect Effects from Satellite: Skeptics vs. Optimists. *Geochimica et Cosmochimica Acta*, 73(13), supplement A1088. <https://doi.org/10.1016/j.gca.2009.05.014>

26. Suslin, V.V., Slabakova, V.K., Kalinskaya, D.V., Pryakhina, S.F. and Golovko, N.I., 2016. Optical Features of the Black Sea Aerosol and the Sea Water Upper Layer Based on In Situ and Satellite Measurements. *Physical Oceanography*, (1), pp. 20-32. <https://doi.org/10.22449/1573-160X-2016-1-20-32>
27. Gordon, H.R. and Wang, M., 1994. Influence of Oceanic Whitecaps on Atmospheric Correction of Ocean-Color Sensors. *Applied Optics*, 33(33), pp. 7754-7763. <https://doi.org/10.1364/AO.33.007754>
28. Glantz, P., Freud, E., Johansson, C., Noone, K.J. and Tesche, M., 2019. Trends in MODIS and AERONET Derived Aerosol Optical Thickness over Northern Europe. *Tellus B: Chemical and Physical Meteorology*, 71(1), 1445379. <https://doi.org/10.1080/16000889.2018.1554414>
29. Zibordi, G., Melin, F., Berthon, J.-F. and Talone, M., 2015. In Situ Autonomous Optical Radiometry Measurements for Satellite Ocean Color Validation in the Western Black Sea. *Ocean Science*, 11(2), pp. 275-286. <https://doi.org/10.5194/os-11-275-2015>
30. Thuillier, G., Hersé, M., Labs, D., Foujols, T., Peetermans, W., Gillotay, D., Simon, P.C. and Mandel, H., 2003. The Solar Spectral Irradiance from 200 to 2400 nm as Measured by the SOLSPEC Spectrometer from the Atlas and Eureka Missions. *Solar Physics*, 214(1-22), pp. 1-22. <https://doi.org/10.1023/A:1024048429145>
31. Suetin, V.S., Kucheryavii, A.A., Suslin, V.V. and Korolev, S.N., 2000. Concentrations of Phytoplankton in the North-Western Part of the Black Sea Based on Data of Measurements by Satellite Color Scanner CZCS. *Morskoy Gidrofizicheskiy Zhurnal*, (2), pp. 74-82 (in Russian).
32. Omar, A.H., Winker, D.M., Vaughan, M.A., Hu, Y., Trepte, C.R., Ferrare, R.A., Lee, K.-P., Hostetler, C.A., Kittaka, C. [et al.], 2009. The CALIPSO Automated Aerosol Classification and Lidar Ratio Selection Algorithm. *Journal of Atmospheric and Oceanic Technology*, 26(10), pp. 1994-2014. <https://doi.org/10.1175/2009JTECHA1231.1>
33. Omar, A.H., Tackett, J. and Al-Dousari, A., 2022. CALIPSO Observations of Sand and Dust Storms and Comparisons of Source Types near Kuwait City. *Atmosphere*, 13(12), 1946. <https://doi.org/10.3390/atmos13121946>
34. Stein, A.F., Draxler, R.R., Rolph, G.D., Stunder, B.J.B., Cohen, M.D. and Ngan, F., 2015. NOAA's HYSPLIT Atmospheric Transport and Dispersion Modeling System. *Bulletin of the American Meteorological Society*, 96(12), pp. 2059-2077. <https://doi.org/10.1175/BAMS-D-14-00110.1>
35. Yakovleva, D.V., Tolkachenko, G.A., Kholben, B.N. and Smirnov, A.V., 2009. Seasonal and Interannual Variability of the Atmospheric Optical Characteristics over the Black Sea near Sevastopol in the Period 2006-2008. In: MHI, 2009. *Ecological Safety of Coastal and Shelf Zones and Comprehensive Use of Shelf Resources*. Sevastopol: ECOSI-Gidrofizika. Iss. 18, pp. 205-212 (in Russian).
36. Werdell, P.J. and Bailey, S.W., 2002. *The SeaWiFS Bio-Optical Archive and Storage System (SeaBASS): Current Architecture and Implementation*. NASA/TM 2002-211617. Greenbelt, MD, USA: Goddard Space Flight Center, 45 p.

Submitted 01.04.2024; approved after review 09.04.2024;
accepted for publication 17.07.2024.

About the authors:

Anna S. Papkova, Junior Researcher, Marine Hydrophysical Institute of RAS (2 Kapitanskaya Str., Sevastopol, 299011, Russian Federation), CSc. (Phys.-Math.), **Scopus Author ID: 57203015832**, hanna.papkova@gmail.com

Evgeniy B. Shybanov, Leading Researcher, Marine Hydrophysical Institute of RAS (2 Kapitanskaya Str., Sevastopol, 299011, Russian Federation), DSc. (Phys.-Math.), **Scopus Author ID: 6507075380**, **WoS ResearcherID: ABB-9097-2021**, e-shybanov@mail.ru

Darya V. Kalinskaya, Junior Researcher, Marine Hydrophysical Institute of RAS (2 Kapitanskaya Str., Sevastopol, 299011, Russian Federation), **Scopus Author ID: 56380591500**, kalinskaya@mhi-ras.ru

Contribution of the co-authors:

Anna S. Papkova – conceptualization, methodology, investigation, data collection, visualization and curation, preparatory drafting, review and editing

Evgeniy B. Shybanov – curation, methodology, investigation, formal analysis, editing

Darya V. Kalinskaya – methodology, data collection, investigation, visualization, preparatory drafting, editing

The authors have read and approved the final manuscript.

The authors declare that they have no conflict of interest.

Express Method for Operational Tsunami Forecasting: Possibility of its Application on the Pacific Coast of Russia

Yu. P. Korolev

*Institute of Marine Geology and Geophysics, Far Eastern Branch of RAS, Yuzhno-Sakhalinsk,
Russian Federation*
✉ *Yu_P_K@mail.ru*

Abstract

Purpose. The work is aimed at studying the possibility of short-term tsunami forecasting in the Kuril Islands based on the data on tsunamis in the open ocean.

Methods and Results. The methods underlying the actions of tsunami warning services in the northwestern Pacific Ocean are considered. The warning services relying on primary seismological information on an earthquake (magnitude criterion), produce a large number of false tsunami alarms. An adequate forecast is provided by the services that use information on a tsunami formed in the open ocean (hydrophysical methods). The problem of short-term (operational) tsunami forecasting for the Kuril Islands is described. Information on the actions of tsunami warning services during the events is provided. The process of forecasting using the express method of tsunami operational forecast is numerically simulated under the assumption of obtaining real-time information on tsunamis in the ocean. The events of 2006–2020 in the northwest Pacific Ocean are simulated. The results of numerical experiments involving actual data confirms the fact that the express method can be used for a short-term tsunami forecast in specific locations of the Kuril Islands with an advance time sufficient for taking a timely decision to declare an alarm and evacuate the population from hazardous places.

Conclusions. Development of the express method for short-term tsunami forecasting, provided that information on tsunamis in the ocean is available quickly, will make it possible to improve in future the quality of forecasting and thereby reduce the number of false tsunami alarms on the Kuril Islands. The necessity of creating own, Russian, deep-sea ocean level measurement stations is shown.

Keywords: tsunami, tsunami forecast, short-term tsunami forecast, operational tsunami forecast, tsunami alarm, false tsunami alarms, Tohoku tsunami, ocean level, ocean level measurements, tsunami warning services, Pacific Ocean, Kuril Islands

Acknowledgments: The author is grateful to the reviewers for their useful comments and suggestions, which were taken into account when finalizing the article.

For citation: Korolev, Yu.P., 2024. Express Method for Operational Tsunami Forecasting: Possibility of its Application on the Pacific Coast of Russia. *Physical Oceanography*, 31(5), pp. 736-754.

© 2024, Yu. P. Korolev

© 2024, Physical Oceanography

Introduction

Short-term (operational) tsunami forecasting still remains an unsolved problem in a number of countries in the Pacific, Indian and Atlantic Ocean basins. Tsunami warning services in these countries issue timely tsunami alarms in the event of underwater earthquakes, often false alerts [1, 2]. It is generally accepted that a false



tsunami alarm is an event in which an alarm is issued, the population is evacuated, but the waves do not cause flooding or damage [1]. False tsunami alarms, often issued too early, do not cause direct losses, but they do cause damage associated with the shutdown of production in hazardous areas, the evacuation of the population to safe zones, and the removal of ships to the open sea. In this case, all types of activity in the coastal zone stop for several hours [3].

The objective of operational (short-term) tsunami forecast is to obtain information about the expected tsunami in advance. It should include the time of arrival of the first wave, the number of waves, their amplitudes, time intervals between them, and the duration of the tsunami [4]. These characteristics of the tsunami are also listed in the definition of the concept of "tsunami forecast" formulated by the UNESCO Intergovernmental Oceanographic Commission (IOC) in 2013.¹ Based on such information, a decision should be made to declare a tsunami alarm with reasonable lead time only at those points where the tsunami poses a real threat. The lead time of the forecast is understood to be the time that passes from the moment the forecast is developed until the expected tsunami arrives at a given point.

The purpose of the operational tsunami forecast is to ensure the safety of population, movable property, sustainability of the coastal infrastructure and coastal territories functioning in conditions of a probable tsunami risk.

A review of the state of the art in the field of tsunami forecasting is given in [1, 2]. The works describe the principles underlying the actions of various tsunami warning services (TWS). The principles of operation of tsunami warning services in the northwestern Pacific Ocean are described in [3].

In the practice of tsunami warning services, two main approaches are used, based on information about an earthquake or tsunami in the open ocean. The first of them, the magnitude-geographical method, proposed about 60 years ago at the very beginning of the development of tsunami warning services, is based on empirical relationships between the magnitude of an earthquake and the intensity of a tsunami. This approach is the cause of a large number (at least 75%) of false tsunami alarms declared by all services [1, 5, 6]. Approaches based on the relationship between the magnitude of an earthquake and its probable mechanism are proposed and implemented by tsunami warning services in Japan², Australia [7], and Russia [8]. Tsunami forecasting is performed using a database of precomputed mareograms near the coast from many seismic sources with the most probable mechanism.

¹ UNESCO, 2019. *Tsunami Glossary*. Intergovernmental Oceanographic Commission. Fourth Edition. Paris: UNESCO, pp. 35-36. (IOC Technical Series; 85). [online] Available at: <https://unesdoc.unesco.org/ark:/48223/pf0000188226> [Accessed: 15 June 2024].

² UNESCO, 2019. *Users' Guide for the Northwest Pacific Tsunami Advisory Center (NWPTAC): Enhanced Products for the Pacific Tsunami Warning System*. Paris: UNESCO, 35 p. (IOC Technical Series; no. 142). [online] Available at: <https://unesdoc.unesco.org/ark:/48223/pf0000366546?posInSet=1&queryId=d1288da0-390e-47b1-8a51-a529b04abf93> [Accessed: 15 June 2024].

Another approach is associated with the development of a network of DART stations (Deep-ocean Assessment and Reporting of Tsunamis) for observing ocean levels ³. The expected tsunami is forecast using the NOAA (National Oceanic and Atmospheric Administration) hydrophysical forecasting method ³, also known as the SIFT (Short-term Inundation Forecasting for Tsunamis) method ⁴ [9, 10]. Based on ocean tsunami data, wave forms are computed at specified points in the ocean or near the coast using a pre-created giant database of synthetic mareograms. The degree of coincidence between the computed wave forms and real mareograms is not assessed during the computations ³. Tsunami forecasts using the NOAA method correspond to the UNESCO IOC definition. This real-time forecasting methodology is currently officially used by the US tsunami warning services [2]. The NOAA (SIFT) method is not applicable to areas for which there is no pre-computed database of synthetic mareograms [3].

A similar but more rigorous approach proposed in [11] identifies the most informative points for tsunami forecasting. Using a set of such points specific to each event can be useful in developing an optimal tsunami observation system. This approach assumes the possibility of operational tsunami forecasting.

The Far East coast of the Russian Federation, especially the Pacific coast of the Kuril Islands, is considered a tsunami-hazardous area ⁵.

In 2024, it was 72 years since the devastating tsunami of November 4–5, 1952, on the northern Kuril Islands. The tsunami was caused by an earthquake with a magnitude of 9 southeast of the Kamchatka Peninsula and caused flooding on the coasts of Paramushir Island and Shumshu Island (northern Kuril Islands) up to 23 m high ⁶. The city of Severo-Kurilsk and all settlements on these islands were destroyed. There are many publications dedicated to this event, for example ⁷.

After the 1952 tsunami, a tsunami warning system was created in Russia, based on information about earthquakes (magnitude and epicenter coordinates).

The strongest earthquake with a magnitude of 9.1 on March 11, 2011 east of the Honshu Island caused flooding of the Kuril Islands coast with a maximum splash height of up to 2.5 m on Paramushir Island, over 2 m on Kunashir Island and up to

³ NOAA, 2024. *NOAA Center for Tsunami Research*. [online] Available at: <http://nctr.pmel.noaa.gov/> [Accessed: 15 June 2024].

⁴ Gica, E., Spillane, M.C., Titov, V.V., Chamberlin, C.D. and Newman, J.C., 2008. *Development of the Forecast Propagation Database for NOAA's Short-Term Inundation Forecast for Tsunamis (SIFT)*. Seattle, WA: Department of Commerce, 95 p. (NOAA Technical Memorandum OAR PMEL-139).

⁵ FSBI "Sakhalin Administration for Hydrometeorology and Environmental Monitoring", 2024. *Tsunami Center*. [online] Available at: <http://sakhugms.ru/index.php/o-nas/strutura/tsentr-tsunami> [Accessed: 15 June 2024] (in Russian).

⁶ NCEI, 2024. *Hazard Tsunami Search*. [online] Available at: <https://www.ngdc.noaa.gov/hazel/view/hazards/tsunami/event-search> [Accessed: 15 June 2024].

⁷ 1952 *Tsunami, Severo-Kurilsk*. [online] Available at: http://www.sakhalin.ru/Region/Tsunami_1952/tsunami_1952.htm [Accessed: 15 June 2024] (in Russian).

2 m on Iturup Island ⁶. Based on the magnitude of the earthquake and information DART 21401 station, a tsunami alert was promptly issued for the Kuril Islands, and the population was evacuated [12].

In 2006 and 2007, two earthquakes occurred to the east of Simushir Island (central Kuril Islands). The first of them (15.11.2006) had a magnitude of 8.3, the second one (13.01.2007) – 8.1. In both cases, in all populated areas of the Kuril Islands, in accordance with the regulations based on the magnitude criterion, tsunami alerts were simultaneously issued, and the population was evacuated. The tsunami splashes were up to 21.9 m on the nearest uninhabited central Kuril Islands [13, 14]. At the same time, in populated areas the tsunamis were insignificant and did not pose a danger: for example, in Yuzhno-Kurilsk the maximum amplitudes were 0.28 m in the first event and 0.06 m in the second one ⁶.

On March 25, 2020, an earthquake with a magnitude of 7.5 occurred east of Onkotan Island (Northern Kuril Islands) at 13:49 Sakhalin time. Since information on the actions of warning services during an event is usually not published, the actions of tsunami warning services during this event are described below. This will allow you to understand the current order of actions of the TWS and assess possible changes in the future.

At 13:57 Sakhalin time, the Pacific Tsunami Warning Center (PTWC) issued a bulletin warning of dangerous tsunami waves for the coast within 1000 km from the epicenter of the earthquake. A tsunami alert for the Severo-Kurilsk district was declared by the Yuzhno-Sakhalinsk seismic station at 14:00 based on the magnitude criterion. The Tsunami Advisory Center for the Northwest Pacific Ocean, namely the Japan Meteorological Agency (JMA), also warned at 14:16 about possible destructive tsunami waves on the Kuril Islands with an amplitude of 1–3 m. The tsunami was expected to arrive in Severo-Kurilsk at 15:04. The evacuation of 400 people was completed at 14:30, half an hour before the expected arrival of the wave. The wave height at the expected time outside the settlement, according to visual assessment against the background of storm waves, was 50 cm ⁵. There is no data on the manifestation of a tsunami in the port of Severo-Kurilsk. The duration of the alarm mode was about 4 hours [15].

In the last three events, due to the small amplitude of the waves in the settlements, the alarms declared in them were clearly false.

At present, when deciding to issue a tsunami alert, Russian tsunami warning centers rely on the magnitude-geographic criterion developed about 60 years ago and warnings issued by the PTWC and JMA, which results in false tsunami alerts. The Russian tsunami warning service does not have its own deep-sea ocean level measurement stations that allow for ocean level monitoring and operational tsunami forecasting, and does not use open ocean tsunami data in its activities ⁸. For this

⁸ *Kamchatka Branch of Geophysical Survey RAS.* [online] Available at: <https://emsd.ru/conf2019/pdf/solution.pdf> [Accessed: 07 October 2024]; https://emsd.ru/files/conf2021/resolution_tsunami.pdf [Accessed: 07 October 2024]; <https://emsd.ru/files/conf2023/result.pdf> [Accessed: 07 October 2024].

reason, as well as due to the lack of modern operating forecasting methods, tsunami centers do not provide an adequate tsunami forecast for the coast of the Far East. The NOAA (SIFT) method for forecasting tsunamis on the Russian Far East coast is not applicable due to the lack of an appropriate synthetic mareograms database.

A legitimate question arises: is it possible to fundamentally improve the work of tsunami warning services, to significantly increase the quality of the forecast?

The aim of the work and the statement of the problem

For the Russian warning service, transoceanic tsunamis occurring off the coast of South America do not cause concern. The decision to declare an alarm is based on information about the manifestation of a tsunami in the Hawaiian Islands. However, the criterion for the danger of a tsunami in the Kuril Islands depending on the heights of the tsunami in the Hawaiian Islands has not been developed. Waves with amplitudes of 2 m, recorded in the Hawaiian Islands, are not considered as a factor in the occurrence of a noticeable tsunami hazard in the Kuril Islands [16, 17].

When a tsunami occurs near the Kuril Islands, the decision to declare an alarm is made based on the magnitude-geographic method. If the magnitude is above the threshold, a tsunami alarm is declared in all populated areas of the islands.

Based on the question posed above, the purpose of the work was to study the possibility of an operational, reliable tsunami forecast in the Kuril Islands based on data on tsunamis in the open ocean.

To achieve the goal, a numerical simulation of the process of operational tsunami forecasting using the express method was performed under the assumption of obtaining information about tsunamis in the ocean in real time. It was assumed that the time of forecast generation and the time of tsunami alarm announcement coincide. Information from deep-sea ocean level measuring stations of the DART system located near the Kuril Islands, which were in operation during the event, or reconstructed data from stations that were in operation earlier or installed later, were used.

The quality of the tsunami forecast is assessed by its ability to determine the degree of threat and the need to announce an alarm only in those places where a tsunami poses a real threat [3].

The method for operational (short-term) tsunami forecast

As noted, tsunami centers currently do not provide adequate tsunami forecasts for the Far East coast. Detailed information on the expected tsunami based on ocean level data could be obtained using the express method of operational forecasting [4].

The express method consists of computing the waveform of the expected tsunami at a given point A based on data on the tsunami in the ocean at point M using

the transfer function (the ratio on the right-hand side) in accordance with the relation:

$$\zeta(A, s) = \zeta(M, s) \cdot \frac{\eta(A, s)}{\eta(M, s)}. \quad (1)$$

All functions included in (1) are images (spectra) of the discrete integral Laplace transform of the corresponding data series. Expression (1) is a consequence of the similarity relation of the spectra of wave forms at points A and M of two different tsunamis (functions $\zeta(A, s)$, $\zeta(M, s)$ and functions $\eta(A, s)$, $\eta(M, s)$) with the same epicenter $\frac{\zeta(A, s)}{\zeta(M, s)} = \frac{\eta(A, s)}{\eta(M, s)}$, which is derived from the fundamental reciprocity principle [4].

If the functions $\eta(A, s)$, $\eta(M, s)$ are known for each point A , then the inverse Laplace transform of relation (1) yields the waveforms of the expected tsunami at each of these points. In practice, due to the fact that in the operational mode only the coordinates of the epicenter are known about the earthquake (the magnitude does not matter), a numerical model of waves propagating from a model (auxiliary) source in the form of an initial circular elevation of the free surface of arbitrary amplitude, for example, 10 m, with the center coinciding with the epicenter of the earthquake is adopted as the second tsunami. The diameter of the source is a characteristic transverse horizontal size of the tsunami source, 100 km. This is the main assumption of the method. It is assumed that the similarity, although approximate, is observed. The computation of waveforms from the auxiliary source at points M and A is performed during the event immediately after receiving information about the coordinates of the earthquake epicenter. In this case, there is no need to create a giant database of precomputed mareograms. Due to the approximate nature of the method, a complete match between the computed and actual waveforms is not expected. A fairly accurate forecast of the main characteristics of the expected tsunami is expected: arrival time, amplitude and duration of the head wave, arrival time and amplitude of the maximum wave.

The initial version of the method is described in [4]. Later, for operational use, it was proposed to use data on tsunamis with a duration equal to the first half-period/period of the tsunami in the ocean [18]. In [4], the success of the short-term tsunami forecast method is shown in computing waveforms at DART stations that recorded the 2006, 2007 and 2009 tsunamis in the northern Pacific Ocean. The effectiveness of the express method for forecasting transoceanic tsunamis occurring near the coast of South America, in the ocean, and near the Kuril Islands is shown in [3, 19]. The quality of tsunami forecasts for points in the ocean using the express method and the NOAA method is comparable [3].

Results

The processes of operational forecasting of the 2006, 2007 Simushir and 2020 Onokotan tsunamis, as well as the 2011 Tohoku tsunami on the Kuril Islands, were simulated.

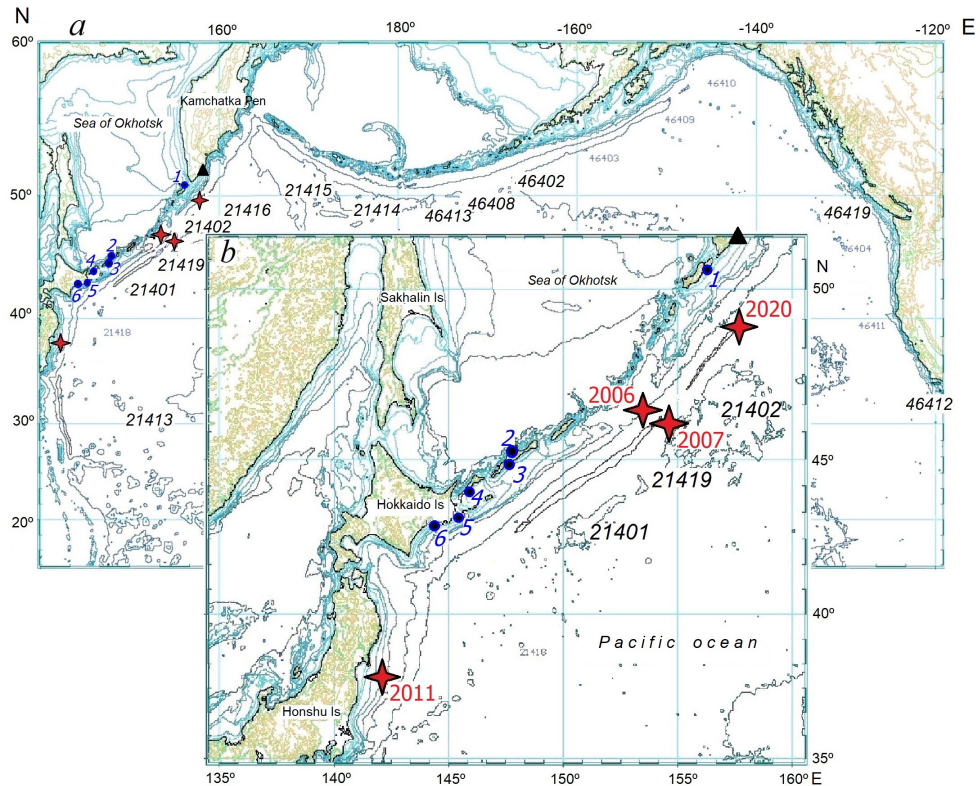


Fig. 1. Scheme of the computation areas: *a* – location of *DART* stations in the northern Pacific Ocean, the data from which are used for comparison with the calculated ones; *b* – the area near the Kuril Islands used in modeling the process of operational tsunami forecasting (black numbers indicate the location of *DART* stations; red stars – the earthquake epicenters with the year indicated; black triangle – the location of automated tide gauge “Vodopadnaya” (southeastern tip of Kamchatka); blue numbers – the settlements: 1 – Severo-Kurilsk (Paramushir Island), 2 – Kurilsk (Iturup Island), 3 – Burevestnik (Iturup Island), 4 – Yuzhno-Kurilsk (Kunashir Island), 5 – Hanasaki (Hokkaido Island) and 6 – Kushiro (Hokkaido Island))

In numerical experiments, actions similar to those that would be performed in real conditions were performed, observing the time frames: obtaining information on the coordinates of the earthquake epicenter (7–11 minutes after the main shock), constructing a transfer function immediately after receiving this information, receiving information on the sea level from the station closest to the source. The construction of the transfer function must be completed before receiving information on the level. Modern fast computation methods make it possible to do this in a short time [20]. The final computations (inverse Laplace transform) are

performed immediately after receiving information on the passage of the first quarter of the first period, half-period or full period of the tsunami through the registration point. The forecast lead time was determined. The moment of tsunami arrival at a given point was estimated as the moment of the first wave arrival (sometimes this moment is understood as the time of arrival of the first wave maximum). Subsequently, as level information is received, the forecast can be refined.

The scheme of the computation areas indicating the epicenters of earthquakes (tsunami sources), locations of DART stations and points on the coasts of the Kuril Islands and Hokkaido Island, for which the forecast was made, is shown in Fig. 1. Figure 1, a shows the locations of DART stations in the northern Pacific Ocean. The data from these stations were compared with the calculated ones to confirm the adequacy of the results. The computations were performed in spherical coordinates. The step of the difference grid covering the northern part of the Pacific Ocean is 3800 m at a latitude of 40°. Bathymetric data [21, 22] were used in computing wave propagation in the ocean. The computational domain of the Kuril Islands region (Fig. 1, b) was used to model the process of operational tsunami forecasting using the express method. The step of the difference grid of this region had a step of 900 m at a latitude of 45°.

Data from DART stations ⁹ and tide gauges ^{10, 11} were used. Tidal components and oscillations caused by the passage of seismic waves along the bottom (seismic noise) were removed from the records during the computations.

Several DART stations, installed at different times, are or were located near the Kuril Islands: DART 21401 (operating years 2009–2014), 21402 (2012–2017), 21419 (since 2009). The location of the stations is optimal for each specific case depending on the proximity to the tsunami source. For the events of 2006 and 2007, the optimal position is DART 21419, for the event of 2020 – the position of DART 21402. Due to the fact that the stations were not operating during the period of the corresponding tsunami, a preliminary reconstruction of tsunami waveforms was performed at these stations based on data from more distant stations using the express method. The original and reconstructed waveforms for each described event are given below. Based on the reconstructed data, tsunami waveforms were computed at more distant stations and near populated areas.

The lead time of tsunami forecasting is directly related to the efficiency of obtaining data on tsunamis in the ocean: using shorter time intervals for analysis

⁹ National Data Buoy Center, 2024. *Station List*. [online] Available at: https://ndbc.noaa.gov/to_station.shtml [Accessed: 15 June 2024].

¹⁰ Russian Tsunami Warning Service, 2024. *Sea Level*. [online] Available at: <http://rtws.ru/sea-level/> [Accessed: 15 April 2024] (in Russian).

¹¹ IOS, 2024. *Sea Level Station Monitoring Facility*. [online] Available at: <http://www.ioc-sealevelmonitoring.org/list.php?showall=a&output=general&order=location&dir=asc> [Accessed: 15 June 2024].

allows forecasts to be made earlier. This is especially important in cases of earthquakes occurring near the coastline. Tsunami waveforms were computed based on reconstructed data from DART 21419 for 16 minutes after the earthquake onset (including a quarter of the first wave period), 20 minutes (including half the period), 32 minutes (including one full period) and 108 minutes. The computation results were found to be virtually identical, as confirmed by comparison with actual data on the 2006 Simushir tsunami.

In subsequent numerical experiments, data from the corresponding DART station, starting from the moment of the earthquake onset and covering the first quarter of the period, were used to compute tsunami waveforms for each event.

2006 Simushir tsunami

The earthquake occurred on November 15, 2006 on the western slope of the Kuril-Kamchatka Trench⁶. The epicenter was located 90 km east of Simushir Island.

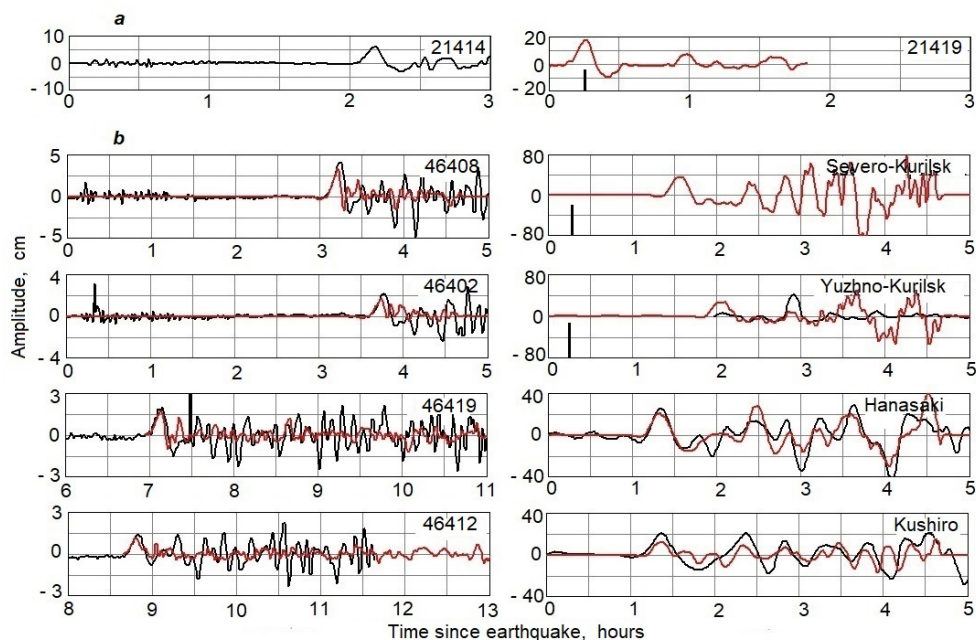


Fig. 2. Waveforms of the 2006 Simushir tsunami: *a* – recorded by DART 21414 station (left) and reconstructed at DART 21419 station (right); *b* – recorded (black line) and computed (red line) based on the reconstructed data from DART 21419 station. Here and further on, each graph is indicated by the DART station number or the settlement name, vertical black line is the boundary of the data used in forecasting, as well as the moment of forecast generation for the points on the Kuril Islands

The resulting tsunami (the epicenter is shown in Fig. 1) was recorded by DART stations located along the Aleutian Islands, the US West Coast to the California Peninsula⁹. The closest station to the Kuril Islands was DART 21414 (Fig. 1),

the tsunami travel time to which was more than 2 hours (Fig. 2, *a*). The tsunami travel time to the point where DART 21419 was installed in 2009 was 10 minutes. In this event, the station's position would have been optimal (Fig. 1). The reconstructed tsunami waveform at point 21419 based on DART 21414 station data was used for forecasting. The initial data and the reconstruction result are shown in Fig. 2, *a*.

To confirm the adequacy of the reconstructed tsunami waveform at point 21419, computations were performed at points in the ocean where more distant DART stations were located based on these data. A series of reconstructed data from DART 21419 station with a duration of 16 min from the onset of the earthquake was used (Fig. 2, *a*, on the right). The results for some stations are shown in Fig. 2, *b*, left column. Good agreement is observed between the head waves of the real and computed waveforms.

The tsunami was recorded by tide gauges in Yuzhno-Kurilsk, Hanasaki and Kushiro. The construction of transfer functions for points on the Kuril Islands and Hokkaido Island began 7–11 min after the earthquake (the moment the data on the epicenter coordinates were obtained) and was completed before the first quarter of the tsunami period passed through point 21419 (16 min after the onset of the earthquake). The forecast for selected points based on the reconstructed DART 21419 data for 16 min is shown in Fig. 2, *b*, right column.

No tsunami was recorded in Severo-Kurilsk. According to the computation, the expected tsunami did not pose a serious threat. There is no evidence of a tsunami in Severo-Kurilsk. In Yuzhno-Kurilsk, although the structures of the computed and actual waves do not match, the values of the maximum amplitudes are in good agreement, up to 0.5 m, which indicates an insignificant tsunami that does not pose a threat. Quite good agreement between the actual and computed waveforms is observed for Hanasaki and Kushiro.

The earlier arrival of the tsunami in Hanasaki and Kushiro than in Yuzhno-Kurilsk is explained by the fact that the wave in these points spreads over a deep-water basin, while in Yuzhno-Kurilsk – over a shallower shelf and strait.

When developing a forecast based on the data of the DART 21419 station at a time of 16 minutes from the onset of the earthquake, the forecast lead time for Severo-Kurilsk and Yuzhno-Kurilsk is 66 and 94 minutes, respectively.

This time is sufficient to decide on the need to declare a tsunami alarm. The moment of declaring an alarm is not regulated, but practice shows that for populated areas of the Kuril Islands, an alarm can be declared 30 minutes before the expected tsunami arrival.

2007 Simushir tsunami

Two months later, an earthquake occurred on the eastern slope of the Kuril-Kamchatka Trench approximately 170 km southeast of Simushir Island on 13.01.2007 ⁶.

In this event, the tsunami was recorded by stations along the Aleutian Islands, the US West Coast to the California Peninsula⁹. In addition, the tsunami was recorded by the DART 21413 station, located to the south of the source. Based on the data from the DART 21414 station (Fig. 3, *a*, left), the tsunami waveform was reconstructed at point 21419, where the DART 21419 station was subsequently installed, the wave travel to which is 15 minutes. The reconstruction results are shown in Fig. 3, *a*, right.

Based on the reconstructed tsunami waveform at point 21419, computations were performed at points in the ocean where more distant DART stations were located. A time series of 19 min from the onset of the earthquake was used. The results for some stations are shown in Fig. 3, *b*, left column. Good agreement was obtained between the head waves of the real and computed waveforms, both in the easterly and southerly directions from the tsunami source. In all cases, the tsunami arrival begins with a decrease in the ocean level.

The tsunami was recorded by tide gauges in Yuzhno-Kurilsk, Hanasaki and Kushiro. As for the previous event, the construction of transfer functions for points on the Kuril Islands and Hokkaido Island began 7–11 min after the earthquake occurred and was completed before the first quarter of the tsunami wave passed point 21419 (19 min after the onset of the earthquake).

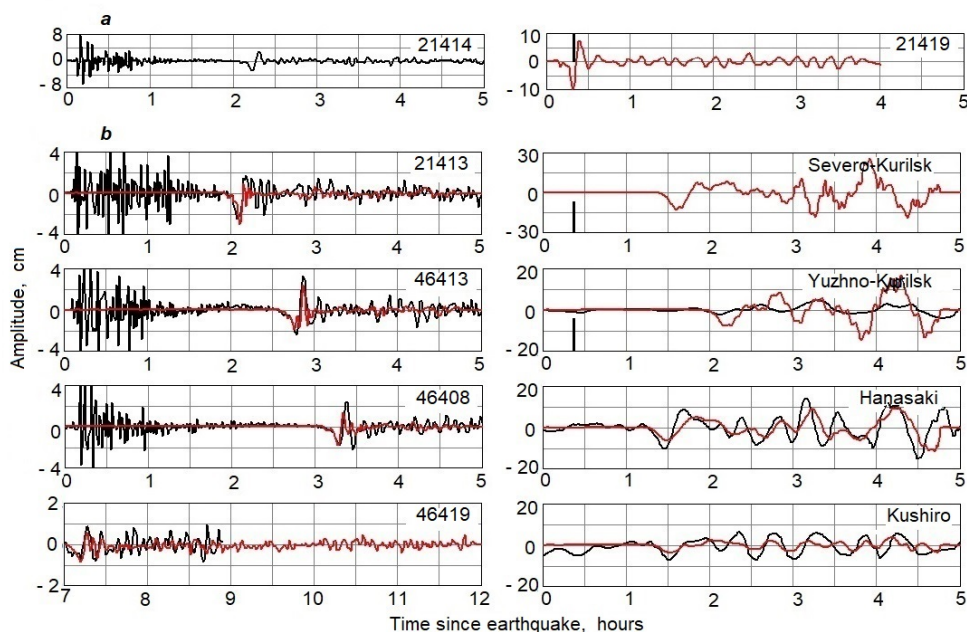


Fig. 3. Waveforms of the 2007 Simushir tsunami: *a* – recorded by the DART 21414 station (*left*) and reconstructed at DART 21419 station (*right*); *b* – recorded (black line) and computed (red line) based on the reconstructed data from DART 21419 station

In Severo-Kurilsk, as during the previous event, no tsunami was registered. According to the computation, the expected tsunami did not pose a serious danger. There is no evidence of a tsunami in the Severo-Kurilsk area. In Yuzhno-Kurilsk, although the structures of the computed and actual waves do not match, the values of the maximum amplitudes are in good agreement, up to 0.1 m, which indicates an insignificant tsunami that does not pose a danger. Quite a good match between the actual and calculated waveforms is observed for Hanasaki and Kushiro.

When generating a forecast at a time of 19 minutes from the onset of the earthquake, the forecast lead time for Severo-Kurilsk and Yuzhno-Kurilsk is 69 and 101 minutes, respectively.

2020 Onkotan tsunami

An earthquake occurred east of Onkotan Island, 220 km from Paramushir Island (Northern Kuril Islands) on March 25, 2020⁶. The resulting weak tsunami was recorded by DART stations 21415, 21416 and 21419⁹, as well as by the Vodopadnaya automated sea level measurement station¹⁰. The closest station to the source was DART 21416 (Fig. 1), the tsunami traveled to it 25 minutes. The closest to the tsunami source of those indicated in Fig. 1 is the position of the previously operating Russian station DART 21402. The tsunami traveled to this point is about 15 minutes. The tsunami forecast based on the data from this station could have been obtained earlier than based on the data from the DART 21416 station [15].

The tsunami waveform reconstruction at point 21402 was performed using the express method based on the data from the DART 21416 station (Fig. 4, *a*). The reconstructed tsunami waveform at the DART 21402 station is shown in Figure 4, *a*, on the right. The computation of the tsunami waveforms (based on the ready transfer function) at the specified points could have been performed immediately after receiving the data from the DART 21402 station on the passage of the first quarter of the tsunami period (at the 20th minute after the onset of the earthquake). The tsunami computation based on the reconstructed data series of the DART 21402 station (Fig. 4, *a*) with a duration of 20 min was performed for the DART 21415 station and the Vodopadnaya (southeast Kamchatka) (Fig. 1) and populated areas (Fig. 1). The computation results are shown in Fig. 4, *b*. A good match was obtained between the computed and recorded waves at the DART 21415 station. The oscillations preceding the tsunami in the records of this station are the effect of Rayleigh waves on the ocean floor. A good match in amplitudes was obtained between the computed waveform near the Vodopadnaya and the record obtained by this station [15].

According to the computation results, the expected time of arrival of the first wave in Severo-Kurilsk is 69 minutes after the onset of the earthquake, the computed amplitude is 15 cm. The amplitude of 15 cm was obtained at the node of

the difference grid closest to the shore, where the sea depth is 17 m. In accordance with the well-known Green's law, according to which the wave amplitude a_1 at a depth of D_1 is related to the amplitude a_0 at a depth of D_0 by the ratio $a_1/a_0 = (D_0/D_1)^{1/4}$, recalculating the amplitude of 15 cm to a point where the depth is 1 m gives an amplitude of about 30 cm. A visual estimate of the wave height (from crest to trough) of 50 cm was made 1.2 km south of the port of Severo-Kurilsk near the water's edge at a depth of about 1 m [15]. The lack of instrumental measurements of the sea level in Severo-Kurilsk, as well as on all the Kuril Islands, does not allow us to confirm either the visually estimated tsunami height of 50 cm, or the computed amplitude of 30 cm.

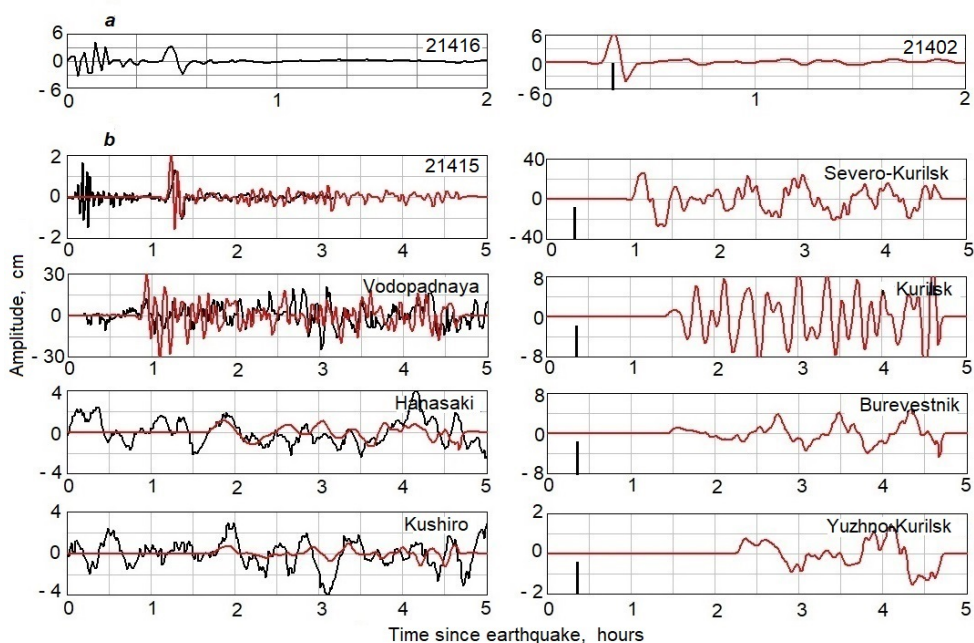


Fig. 4. Waveforms of the 2020 Onokotan tsunami: *a* – recorded by DART 21416 station (*left*) and reconstructed at DART 21402 station (*right*); *b* – recorded (black line) and computed (red line) based on the reconstructed data from DART 21402 station

According to computations, in other populated areas of the Kuril Islands, the amplitude of the expected tsunami should be insignificant.

The forecast lead time according to the DART 21402 station, which is 43 minutes for Severo-Kurilsk, 65 minutes for Kurilsk, 65 minutes for Burevestnik, and 116 minutes for Yuzhno-Kurilsk, is quite sufficient to make a decision to declare an alarm in these areas [15].

The warning issued by JMA about possible destructive waves on the Kuril Islands with amplitudes of 1–3 m was not confirmed. The event of 25.03.2020 shows

that the method of tsunami forecasting based on the magnitude criterion, preliminary computations, on which the JMA relies, cannot always give a correct forecast.

2011 Tohoku tsunami

A powerful earthquake occurred on March 11, 2011, off the northeastern coast of Honshu Island ⁶. The resulting tsunami was unusual: its amplitude exceeded the value predicted by computations for an earthquake with a magnitude of 9.0. The initial amplitude of the wave that arose after the main shock was 2 m. After 11 minutes, it unexpectedly increased to 5 m [16]. A qualitative explanation of this effect is given in [23]. Presumably, it is similar to the effect of an underwater landslide.

In the area of the Kuril Islands, the tsunami was recorded by DART 21419 and Russian DART 21401 ⁹, stations, coastal tide gauges in Kurilsk and Yuzhno-Kurilsk, as well as in Hanasaki and Kushiro on the island of Hokkaido ¹¹.

Computations were performed using data from the DART 21401 station for 68 minutes, including the first quarter of the wave period (Fig. 5).

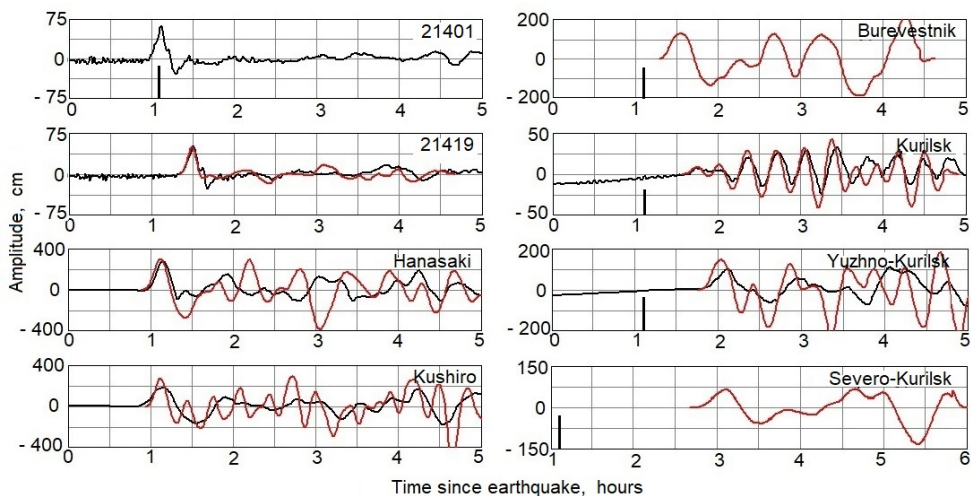


Fig. 5. Waveforms of the 2011 Tohoku tsunami: recorded (black line) and computed (red line) based on the data from *DART 21401* station

A good match was obtained between the computed and actual waveforms at the DART 21419 station closest to the islands (Fig. 5). The quality of the express forecast at this station and the quality of the tsunami waveform computations in the ocean, performed by the NOAA method, are comparable ¹².

¹² NOAA Center for Tsunami Research. *Tohoku (East Coast of Honshu) Tsunami, March 11, 2011*. [online] Available at: <http://nctr.pmel.noaa.gov/honshu20110311/> [Accessed: 19 June 2024].

The results of computing the tsunami waveform near populated areas of the Kuril Islands and Hokkaido Island are presented in Fig. 5.

The computed and recorded tsunami waveforms in Hanasaki and Kushiro are in good agreement with each other. In Yuzhno-Kurilsk, there is also agreement between the model and real waveforms. The time of tsunami arrival at the forecast point and the wave structure coincide. According to the forecast, the amplitude of the maximum wave should not exceed 1.5 m. In Kurilsk (the Okhotsk side of Iturup Island), the structure, amplitudes and characteristic periods of the waves coincide well. In Severo-Kurilsk, the computed range of water level fluctuations should not exceed 1.5 meters, which agrees with the information from ships located near Severo-Kurilsk, where the water level under the keel fluctuated from 4.2 m to 2.6 m with a difference of 1.6 m [16]. The computed wave amplitudes (up to 2 m) correspond to visual observations in the Burevestnik port point (Iturup Island) [12].

The forecast lead time is 92 minutes for Severo-Kurilsk, 37 minutes for Yuzhno-Kurilsk, and 30 minutes for Kurilsk. It is quite sufficient to make a decision on declaring a tsunami alarm. Tsunami alarms could be declared sequentially in Kurilsk, Yuzhno-Kurilsk, and Severo-Kurilsk. Due to the small amplitude of the expected wave in Kurilsk, the alarm could not be declared or cancelled in a timely manner if it was declared based on the magnitude criterion. For the Burevestnik port point, the time of wave front arrival practically coincides with the moment of forecast development. For this point, as well as points on Shikotan Island and the islands of the Small Kuril Ridge, the tsunami alarm should be declared in accordance with the current regulations, based on the magnitude criterion. In the computations performed in [18], the data from the DART 21401 station with a duration of 20 min (the first period of the wave) were used, the arrival of the tsunami was estimated as the arrival of the first wave crest. This explains the difference in the lead time estimate.

The results of the experiment confirm that, despite the anomalous mechanism of excitation of the Tohoku tsunami on March 11, 2011, the computation performed using the data from the DART 21401 level measurement station, using information only on the coordinates of the earthquake epicenter without involving additional seismological information, gives an adequate result.

Discussion

The paper shows that the tsunami forecast for the Kuril Islands based on the magnitude-geographical method used by Russian tsunami warning services is ineffective. Tsunami alarms announced simultaneously on all the Kuril Islands often turn out to be false in populated areas due to the small amplitude of the wave. However, this is not due to the actions of the Tsunami Center, but to the approved regulations based on the magnitude criterion. The Northwest Pacific Tsunami Advisory Center (JMA), relying on pre-computed mareograms from a number of

sources in tsunamigenic zones with the most probable earthquake mechanisms, also cannot always provide a correct forecast.

Currently, hydrophysical methods using information about the tsunami formed in the open ocean are effective. The NOAA (SIFT) method using DART station data is successfully used to forecast tsunamis in the USA. However, the forecast is more difficult when tsunamis occur near the coast. Often, tsunami information from DART stations comes later than the tsunami reaches the nearest coasts.

As noted above, the NOAA method cannot be used to forecast tsunamis in the Kuril Islands. For such situations, the express method of short-term tsunami forecasting can be used. To perform a forecast using the express method, seismological information is required only on the coordinates of the earthquake epicenter and tsunami information from DART stations, received in real time.

The moment of forecast generation is determined by the time (from the onset of the earthquake) of the tsunami passing through the registration point. The forecast for a specific point will be successful if its lead time is not less than the time required to evacuate the population, which is specific to each point. For points on the Kuril Islands, the forecast lead time can be estimated at no less than 30 minutes. Accordingly, a tsunami alarm can be declared 30 minutes before the expected tsunami arrival at the corresponding point. The tsunami travel time to a specific settlement is estimated in real time. If the forecast lead time is less than 30 minutes, a tsunami alarm should be declared based on the magnitude criterion. The alarm can be promptly cancelled upon receipt of information about the non-hazard of a tsunami.

The aim of the work was to study the possibility of an operational tsunami forecast for the Kuril Islands based on data on tsunamis in the open ocean. The tsunamis of 2006–2020 that occurred near the Kuril Islands are considered. It is shown that with prompt receipt of information about the coordinates of the earthquake epicenter and about tsunamis in the ocean, an operational tsunami forecast in settlements is possible with the required lead time. Despite its approximate nature, the express method allows adequately assessing the degree of danger of an expected tsunami for any part of the coast. In this case, it is sufficient to have information about the passage of a quarter of the first period of the tsunami through a registration station located in the optimal location for each event. In case of earthquakes in the area of the central Kuril Islands, the optimal position is the location of DART 21419 station. The forecast lead time for settlements of the northern and southern islands is 66–101 minutes. In case of earthquakes in the area of the northern Kuril Islands, the optimal position is the location of the previously operating Russian station DART 21402. The forecast lead time in such cases is 43–116 minutes. In the case of earthquakes off the east coast of Japan, the previously operating Russian station DART 21401 would allow forecasting to be carried out in real time. The tsunami forecast lead time for these events is 30–92 minutes for nearby and more remote settlements.

Conclusion

Many areas in the Sakhalin Region are tsunami-hazardous, especially the Kuril Islands. The problem of operational tsunami forecasting has not yet been fully resolved. The declaration of tsunami alarm on the Pacific coast of Russia is based on the magnitude method created in the middle of the last century. There are a large number (over 75%) of false alarms. These alarms, often declared too early, are accompanied by damage caused by the suspension of production and other activities in the coastal zone for a long time.

Currently, in the Russian Far East, there is no hydrophysical subsystem of the tsunami warning service that would monitor the wave regime in the ocean and assess the tsunami hazard. The tsunami warning service needs to create such a subsystem in order to increase the efficiency, reliability and accuracy of tsunami warnings.

An express method for operational tsunami forecasting can be used for the coast of the Russian Far East. Implementation of the express method for operational tsunami forecasting as a single complex, provided that information on tsunamis in the ocean is received, will improve the quality of forecasting in the future and thereby reduce the number of false tsunami alarms on the Kuril Islands. The previously operating Russian stations DART 21401 (in 2010–2014) and DART 21402 (in 2012–2017) could provide a reliable tsunami forecast for the Kuril Islands with sufficient advance notice in the event of earthquakes in the areas of the northern and central Kuril Islands and the east coast of Japan.

Russia is almost the only country in the Pacific Ocean basin that does not have deep-sea stations for measuring ocean levels, which would allow for operational tsunami forecasting. There is a need to create our own, Russian, deep-sea stations for measuring ocean levels.

REFERENCES

1. Bernard, E. and Titov, V., 2015. Evolution of Tsunami Warning Systems and Products. *Philosophical Transactions of Royal Society A*, 373, 20140371. <https://doi.org/10.1098/rsta.2014.0371>
2. Kânoğlu, U., Titov, V., Bernard, E. and Synolakis, C., 2015. Tsunamis: Bridging Science, Engineering and Society. *Philosophical Transactions of Royal Society A*, 373, 20140369. <https://doi.org/10.1098/rsta.2014.0369>
3. Korolev, Yu.P., 2023. Evaluation of the Express Method Effectiveness in Short-Term Forecasting on the Examples of the Peruvian (2007) and the Chilean (2010, 2014 and 2015) Tsunamis. *Physical Oceanography*, 30(3), pp. 315-330. <https://doi.org/10.29039/1573-160X-2023-3-315-330>
4. Korolev, Yu.P., 2011. An Approximate Method of Short-Term Tsunami Forecast and the Hindcasting of Some Recent Events. *Natural Hazards and Earth System Sciences*, 11(11), pp. 3081-3091. <https://doi.org/10.5194/nhess-11-3081-2011>

5. Gusiakov, V.K., 2011. Relationship of Tsunami Intensity to Source Earthquake Magnitude as Retrieved from Historical Data. *Pure and Applied Geophysics*, 168(11), pp. 2033-2041. <https://doi.org/10.1007/s00024-011-0286-2>
6. Gusiakov, V.K., 2016. Tsunamis on the Russian Pacific Coast: History and Current Situation. *Russian Geology and Geophysics*, 57(9), pp. 1259-1268. <https://doi.org/10.1016/j.rgg.2016.08.011>
7. Allen, S.C.R. and Greenslade, D.J.M., 2016. A Pilot Tsunami Inundation Forecast System for Australia. *Pure and Applied Geophysics*, 173, pp. 3955-3971. <https://doi.org/10.1007/s00024-016-1392-y>
8. Frolov, A.V., Kamaev, D.A., Martyshchenko, V.A., and Shershakov, V.M., 2012. Experience of the Russian Tsunami Warning System Updating. *Russian Meteorology and Hydrology*, 37(6), pp. 357-368. <https://doi.org/10.3103/S1068373912060015>
9. Percival, D.B., Denbo, D.W., Eblé, M.C., Giga, E., Mofjeld, H.O., Spillane, M.C., Tang, L. and Titov, V.V., 2011. Extraction of Tsunami Source Coefficients via Inversion of DART® Buoy Data. *Natural Hazards*, 58(1), pp. 567-590. <https://doi.org/10.1007/s11069-010-9688-1>
10. Titov, V.V., 2009. Tsunami Forecasting. In: E.N. Bernard and A.R. Robinson, eds., 2009. *Tsunamis. The Sea: Ideas and Observations on Progress in the Study of the Seas*, vol. 15. Cambridge, MA; London, England: Harvard University Press, pp. 367-396.
11. Voronina, T.A. and Voronin, V.V., 2023. Data Selection Method for Restoring a Tsunami Source Form. *Geosystems of Transition Zones*, 7(3), pp. 292-303. <https://doi.org/10.30730/gtr.2023.7.3.292-303>
12. Kaystrenko, V.M., Shevchenko, G.V. and Ivel'skaya, T.N., 2011. Manifestation of the Tohoku Tsunami of 11 March, 2011 on the Russian Pacific Ocean Coast. *Problems of Engineering Seismology*, 38(1), pp. 41-64 (in Russian).
13. Levin, B.W., Kaistrenko, V.M., Rybin, A.V., Nosov, M.A., Pinegina, T.K., Razzhigaeva, N.G., Sasorova, E.V., Ganzei, K.S., Ivel'skaya, T.N. [et al.], 2008. Manifestations of the Tsunami on November 15, 2006, on the Central Kuril Islands and Results of the Runup Heights Modeling. *Doklady Earth Sciences*, 419(1), pp. 335-338. <https://doi.org/10.1134/S1028334X08020335>
14. MacInnes, B.T., Pinegina, T.K., Bourgeois, J., Razhigaeva, N.G., Kaistrenko, V.M. and Kravchunovskaya, E.A., 2009. Field Survey and Geological Effects of the 15 November 2006 Kuril Tsunami in the Middle Kuril Islands. *Pure and Applied Geophysics*, 166, pp. 9-36. <https://doi.org/10.1007/s00024-008-0428-3>
15. Korolev, Yu.P. and Korolev, P.Yu., 2020. Simulation of the Process of Short-Term Forecasting of the 25.03.2020 Onokotan Tsunami. *Geosystems of Transition Zones*, 4(2), pp. 259-265. <https://doi.org/10.30730/gtr.2020.4.2.259-265> (in Russian).
16. Shevchenko, G.V., Ivel'skaya, T.N., Kovalev, P.D., Kovalev, D.P., Kurkin, A.A., Levin, B.V., Likhacheva, O.N., Chernov, A.G. and Shishkin, A.A., 2011. New Data about Tsunami Evidence on Russia's Pacific Coast Based on Instrumental Measurements for 2009-2010. *Doklady Earth Sciences*, 438(2), pp. 893-898. <https://doi.org/10.1134/S1028334X11060341>
17. Shevchenko, G., Ivel'skaya, T., Loskutov, A. and Shishkin, A., 2013. The 2009 Samoan and 2010 Chilean Tsunamis Recorded on the Pacific Coast of Russia. *Pure and Applied Geophysics*, 170, pp. 1511-1527. <https://doi.org/10.1007/s00024-012-0562-9>
18. Korolev, Yu.P. and Ivel'skaya, T.N., 2012. Improving Operational Tsunami Forecast and Tsunami Alarm. Analysis of Recent Tsunamis. *Issues of Risk Analysis*, 9(2), pp. 76-91 (in Russian).

19. Korolev, Y.P. and Khrumushin, V.N., 2016. Short-Term Forecast of Tsunami Occurred on April 1, 2014 on the Kuril Islands Coast. *Russian Meteorology and Hydrology*, 41(4), pp. 293-298. <https://doi.org/10.3103/S1068373916040099>
20. Lavrentiev, M., Lysakov, K., Marchuk, A., Oblaukhov, K. and Shadrin, M., 2019. Fast Evaluation of Tsunami Waves Heights around Kamchatka and Kuril Islands. *Science of Tsunami Hazards*, 38(1), pp. 1-13. Available at: <http://www.tsunamisociety.org/STHVol38N1Y2019.pdf> [Accessed: 15 April 2024].
21. Smith, W.H.F. and Sandwell, D.T., 1994. Bathymetric Prediction from Dense Satellite Altimetry and Sparse Shipboard Bathymetry. *Journal of Geophysical Research: Solid Earth*, 99(B11), pp. 21803-21824. <https://doi.org/10.1029/94JB00988>
22. Smith, W.H.F. and Sandwell, D.T., 1997. Global Sea Floor Topography from Satellite Altimetry and Ship Depth Soundings. *Science*, 277(5334), pp. 1956-1962. doi:10.1126/science.277.5334.1956
23. Pararas-Carayanis, G., 2011. Tsunamigenic Source Mechanism and Efficiency of the March 11, 2011 Sanriku Earthquake in Japan. *Science of Tsunami Hazards*, 30(2), pp. 126-152. Available at: <http://www.tsunamisociety.org/STHVol30N2Y2011.pdf> [Accessed: 15 June 2024].

Submitted 03.05.2024; approved after review 27.06.2024;
accepted for publication 17.07.2024.

About the author:

Yuri P. Korolev, Leading Research Associate, Tsunami Laboratory, Institute of Marine Geology and Geophysics, Far Eastern Branch of RAS (1b, Nauki Str., Yuzhno-Sakhalinsk, 693022, Russian Federation), CSc. (Phys.-Math.), Associate Professor, Member of the Russian Geographical Society, **ORCID ID: 0000-0002-7068-7341**, Yu_P_K@mail.ru

The author has read and approved the final manuscript.

The author declares that he has no conflict of interest.